Development of Novel Materials for High-Performance Energy Storage Devices

A thesis presented for the award of the degree of

Doctor of Philosophy

from

University of Technology Sydney

By

Xiao Tang, B. Sc., M.Sc.

July, 2020

CERTIFICATE OF AUTHORSHIP

I, Xiao Tang, certify that the work presented in this thesis has not previously been submitted for a degree nor as a part for a degree.

I also certify that the thesis has been written by me. Any help that I have received in my research work and the preparation of the thesis itself has been acknowledged. In addition, I certify that all information sources and literature used are indicated in the thesis.

This research is supported by an Australian Government Research Training Program.

Xiao Tang

Production Note:
Signature removed prior to publication.

Sydney, Australia

11/07/2020

DEDICATION

To my beloved family. Thank you for giving a different meaning of life to me.

ACKNOWLEDGEMENTS

Before writing this thesis, I dedicated myself to list all the people who deserve my sincere acknowledgment. However, I may have dropped, unintentionally, some of them; I would like to ask for their forgiveness.

Firstly, I am grateful to my supervisor, Professor Guoxiu Wang, for his kind and continuous support and invaluable advice throughout my Ph.D. study. The helps and supports from Dr. Jane Yao are also appreciated.

Thanks to Dr. Dong Zhou, who taught me many skills he knows. Under his help, I am encouraged to think outside of the box, develop ideas and implement them. We discussed with each other and co-wrote the manuscript, which should be a great memory in my life.

Special thanks are given to my colleagues at UTS, Prof. Hao Liu, Dr. Dawei Su, Dr. Bing Sun, Dr. Xin Guo, Dr. Weizhai Bao, Dr. Anjon Kumar Mondal, Dr. Jinqiang Zhang, Dr. Yufei Zhao, Dr. Pan Xiong and Dr. Huajun Tian. Their kind collaboration and assistance were helpful. In addition, I would like to thank the administrative and technical support from Dr. Ronald Shimmon, Dr. Linda Xiao, Herbert Yuan and Katie.

The financial support from UTS and China Scholarship Council (CSC) to help finish my Ph.D. study are highly appreciated.

Last but not the least, I would like to thank my parents, my girlfriend for supporting me spiritually throughout my Ph.D. study. Their accompanying always encourage me keep running in my career.

Xiao Tang

RESEARCH PUBLICATIONS

1. Xiao Tang, Dong Zhou*, Peng Li, Xin Guo, Bing Sun, Hao Liu, Kang Yan, Yury Gogotsi*, Guoxiu Wang*. MXene-based dendrite-free potassium metal batteries. **Adv. Mater.** 2020, 32 (4), 1906739.

2. Xiao Tang, Dong Zhou, Peng Li, Xin Guo, Chengyin Wang, Feiyu Kang, Baohua Li*, Guoxiu Wang*. High-performance quasi-solid-state MXene-based Li-I batteries. **ACS Cent. Sci.** 2019, 5 (2), 365-373.

3. Xiao Tang, Xin Guo, Wenjian Wu, Guoxiu Wang*. 2D metal carbides and nitrides (MXenes) as high-performance electrode materials for lithium-based batteries. **Adv. Energy Mater.** 2018, 8 (33), 1801897.

4. Weizhai Bao, Xiao Tang, Xin Guo, Sinho Choi, Chengyin Wang, Yury Gogotsi*, Guoxiu Wang*. Porous cryo-dried MXene for efficient capacitive deionization. **Joule** 2018, 2 (4), 778-787.

5. Dong Zhou, Xiao Tang, Xin Guo, Peng Li, Devaraj Shanmukaraj, Hao Liu, Xiaochun Gao, Yizhou Wang, Teofilo Rojo, Michel Armand, Guoxiu Wang*. Polyolefin-based Janus separator for rechargeable sodium batteries. **Angew. Chem. Int. Ed.** 2020, DOI: 10.1002/anie.202007008.

6. Dong Zhou, Anastasia Tkacheva, Xiao Tang, Bing Sun, Devaraj Shanmukaraj, Peng Li, Fan Zhang, Michel Armand, Guoxiu Wang*. Stable conversion chemistry-based lithium metal batteries enabled by hierarchical multifunctional polymer electrolytes with near-single ion conduction. **Angew. Chem. Int. Ed.** 2019, 58 (18), 6001-6006.

TABLE OF CONTENTS

LIST OF TABLES

LIST OF FIGURES

ABSTRACT

Recently, tremendous efforts have been devoted to the development of novel materials for advanced energy storage devices that simultaneously possess high energy density and power density. Two-dimensional (2D) materials have been considered to be promising in the field of large-scale energy storage. After the discovery of graphene, a large family of two-dimensional transition metal carbides/nitrides (MXenes), derived from MAX phase precursors, have attracted extensive attention owing to the superior physical and chemical properties, which includes excellent electrical conductivity, high mechanical strength, hydrophilic features, multiple possible surface functional groups, superior specific surface area, and the ability to accommodate intercalants. In this thesis, the preparation strategies, structures, properties, and applications of MXene materials in lithium-based and potassium-based batteries have been systematically reviewed. Moreover, we rationally design various MXene materials for lithium-iodine, potassium metal, and aqueous lithium-sulfur batteries. The usage of MXene materials can effectively enhance the electrochemical performances of these energy storage devices. This thesis may provide an insight into the development of two-dimensional MXene materials for large-scale energy storage.

Chapter 1. Introduction

Recently, the energy shortage is one of the biggest obstacles that severely restrain the development of modern society. The development of electrification of road transportation and power grid requires high-performance energy storage technologies.[1] Thus, various types of energy storage systems with high energy density and low cost have been proposed, such as alkali metal-ion batteries (including lithium-ion, sodium-ion, and potassium-ion batteries, *etc.*), batteries based on conversion chemistry (including lithium-sulfur, lithium-iodine, and potassium-sulfur batteries, *etc.*) and capacitors.

Two-dimensional (2D) materials such as graphene[2, 3], graphene oxide (GO)[4, 5], phosphorene[6], exfoliated nanosheets of metal-organic frameworks (MOFs)[7], and transition metal dichalcogenides (TMDs)[8, 9], have attracted extensive research attention due to their unique physical and chemical properties. Beyond these 2D materials, a family of transition metal carbides and nitrides, MXenes, have been developed for energy storage devices in recent years.[10] MXenes can be prepared by selectively etching the reactive "A" layers in laminated carbides or carbonitrides (also known as "MAX" phases). The MAX phases have the form $M_{n+1}AX_n$ (n = 1-3), where "M" represents a transition metal, "A" usually represents a group IIIA or IVA element (such as Al, Ga, Si, or Ge), and "X" represents carbon and/or nitrogen. During the etching process, surface functional groups (*e.g.* -O, -OH and –F) can be attached on the surface of MXenes. Terminated MXenes have a general formula of $M_{n+1}X_nT_x$, where T represents the surface functional groups and x is the fraction of such functional groups. So far, more than thirty MXenes, including $Ti_3C_2T_x$[11, 12], Ti_2CT_x[13], $Mo_2TiC_2T_x$[14] and $Nb_4C_3T_x$[15], have been successfully synthesized for various applications, with more predicted to exist according to theoretical calculations.[16-23]

MXenes have been reported to be highly efficient electrode materials for energy conversion devices (such as triboelectric nanogenerators[24] and water splitting devices[25-27]) and energy storage devices (including supercapacitors[28-33] and batteries[34-37]) as well as for other applications (*e.g.*, capacitive desalination[38] and electromagnetic interference shielding[39]). To date, more than two hundred of literatures about MXenes for energy storage have been published, which indicates that MXene materials have great promise in the field of energy storage.

This thesis mainly focuses on the development of transition-metal carbides/nitrides (MXene) materials for energy storage devices (including lithium-based battery and potassium-based battery). Contents of chapters in this doctoral work are outlined as followed:

Chapter 2: Literature review. This chapter reviews the latest advances of transition-metal carbides/nitrides (MXene) materials for energy storage devices, including lithium-based batteries (such as lithium-ion batteries and lithium-sulfur batteries) and potassium-based batteries. The preparation methods, structures, and properties of MXene materials are also discussed in this chapter.

Chapter 3: The material preparations, characterizations, and the electrochemical investigations methods are summarized in this chapter. Particularly, drop-filtration method, and infusion method, *etc.* were used to synthesize various electrode materials in this doctoral work. The morphologies of the as-prepared materials were characterized by field emission scanning electron microscopy (FE-SEM), transmission electron microscopy (TEM), and High angle annular dark field (HAADF)-scanning transmission electron microscopy (STEM). The structures, phases, chemical compositions of the materials were investigated by X-ray diffraction (XRD), nitrogen adsorption-desorption, Raman Spectroscopy, X-ray photoelectron spectroscopy (XPS), and

thermogravimetric analysis. This chapter also presents the cell assembly and electrochemical testing techniques.

Chapter 4: Here we successfully develop a quasi-solid-state Li-I battery enabled by a MXene-based iodine cathode and a composite polymer electrolyte (CPE) containing $NaNO_3$ particles dispersing in a pentaerythritol tetraacrylate (PETEA)-based gel polymer electrolyte. As verified by experimental characterizations and first-principle calculations, the abundant functional groups on the surface of MXene sheets provide strong chemical binding to iodine species, and therefore immobilize their shuttling. The PETEA-based polymer matrix simultaneously suppresses the diffusion of iodine species and stabilizes the Li anode/CPE interface against dendrite growth. The $NaNO_3$ particles act as an effective catalyst to facilitate the transformation kinetics of LiI_3 on the cathode. Owing to such synergistic optimization, the as-developed Li-I batteries deliver high energy/power density with long cycling stability and good flexibility. This work opens up a new avenue to improve the performance of Li-I batteries.

Chapter 5: Herein, we report a high-performance potassium anode achieved by confining potassium metal into a titanium-deficient nitrogen-containing MXene/carbon nanotube free-standing scaffold. The high electronic transport and fast potassium diffusion of this scaffold enable reduced local current density and homogeneous ionic flux during plating/stripping process. Furthermore, as verified by theoretical calculations and experimental investigations, such MXene sheets with “potassium-philic” characteristic can induce the nucleation of potassium, and guide potassium to uniformly distribute in the scaffold upon cycling. Consequently, the as-developed potassium metal anodes exhibit a dendrite-free morphology with high Coulombic efficiency and long cycle life during plating/stripping process. Such anodes also deliver significantly improved

electrochemical performances in potassium-sulfur batteries compared with bare potassium metal anodes. This work could provide a new avenue for developing potassium metal-based batteries.

Chapter 6: In this chapter, we report the development of the high-performance aqueous lithium-sulfur/ion batteries enabled by the highly concentrated electrolyte and MXene interlayer. The concentrated electrolyte not only enhance the voltage window, but also suppress the dissolution of short-chain lithium polysulfides. In the meanwhile, the free-standing MXene interlayer can significantly restrain the shuttling of the intermediate products by physical/chemical adsorption. Therefore, the as-assembled batteries can provide a high specific capacity of ~715 mAh g^{-1} at a current density of 0.2 C. Furthermore, an improved cycling performance can be achieved by using MXene interlayer. This work can open a new path to inspire the development of the aqueous rechargeable batteries based on conversion chemistry.

Chapter 7: In this chapter, advantages of MXene and MXene-based composites have been summarized. Furthermore, challenges and perspectives have also been proposed for the future development of MXenes and their composites for energy storage devices.

Chapter 2. Literature Review

The development of two-dimensional (2D) materials for energy storage has received intensive attention in recent years.[1, 40] Among them, MXene materials, which are derived from MAX phase precursors, have been frequently adopted in many energy storage/conversion devices. The outstanding physical/chemical properties of MXenes include abundant surface terminations, excellent electrical conductivity, high mechanical strength, hydrophilic features, and the ability to accommodate intercalants. When employed as electrodes in energy storage devices, MXene materials can demonstrate excellent performance. This chapter summarizes the recent progress of MXenes and MXene-based composites in terms of synthesis strategies, morphology engineering, physical/chemical properties and their applications in energy storage devices (*e.g.* lithium-based batteries and potassium-based batteries).

2.1 Synthesis of the MXene materials

Chemical exfoliation method is usually adopted to prepare MXene materials because "M" elements (transition metal) can form a strong metallic bond with "A" elements (such as Al, Si, *etc.*). Therefore, such a bond can be hardly broken by mechanical exfoliation. According to previous literatures, the M-A bond is more active compared with the metal-carbon/nitrogen bond, which makes the cleavage of M-A bonds possible.[20, 41] Chemical exfoliation of MAX phases by using hydrofluoric acid (HF) was first reported in 2011 by Coleman *et. al*. The preparation of MXene can be described in the following equation (2-1):

$$Ti_3AlC_2 + 3HF = AlF_3 + 3/2H_2 + Ti_3C_2 \quad (2\text{-}1)$$

As shown in Figure 2.1a, the A elements can be selectively etched in the exfoliation procedure, during which surface functional groups such as oxygen (=O), hydroxyl (-OH), and fluorine (-F)

can be attached on MXene layers. As for the experimental conditions (*e.g.* reaction time, temperature, and concentration of etchant) usually changes with the type of the MXene. For example, Ti_2CT_x MXene was prepared by using 10 wt% HF acid to etch the Ti_2AlC MAX material for 10 hours. In contrast, exfoliation of V_2AlC MAX requires reaction time of 90 hours with 50 wt% HF acid to obtain the corresponding MXene.[13]

Noticeably, the etched MXene usually present an accordion-like particle morphology instead of the 2D sheets/flakes. Sonication under inert atmosphere can be employed to separate the MXene particles to single/few-layered MXene sheets. However, the strong interlayer forces may facilitate the restacking of the MXene. Therefore, organic molecules were intercalated into the layered structure of MXene, enabling an enhanced interlayer spacing.[42] Because of the larger interlayer distance and weakened interlayer forces, the intercalated MXenes can be easily delaminated. This strategy can significantly improve the yield of the single/few-layered MXenes and boost the development of the MXene materials.[43] Till now, different types of organic molecules, such as urea, isopropyl amine, dimethyl sulfoxide (DMSO), and tetrabutylammonium hydroxide (TBAOH) have been applied to insert into MXenes, which effectively enhances the interlayer spacing and prevents the restacking of MXene.[44, 45]

Beyond the utilization of HF acid, MXenes can also be synthesized by employments of HF-containing (NH_4HF_2) or HF-forming (LiF + HCl) etchants. It is worth noticing that employments of those etchants are much safer than using concentrated HF acid. Furthermore, during the exfoliation process, NH_4^+/Li^+ cations can simultaneously insert into the layered structure of MXenes, which facilitates the delamination of MXene from accordion-like particles to sheets/flakes.[29] After the discovery of Al-containing MAX, Si-containing MAX materials have also been developed. However, as Si element has higher reduction potential compared with Al, HF

and HF-containing etchants can hardly exfoliate the Si-containing MAX phase. Noticeably, Si can be etched in the mixture of HF and oxidant by a two-step reaction. Briefly, oxidants can spontaneously oxidize silicon to silicon oxide that tends to dissolve in the HF. Hence, an oxidant-assisted selective etching strategy was reported by Alhabeb *et al*. to synthesize the MXene from Si-containing MAX phase (Figure 2.1b).[46] This new preparation strategy gave a new insight into the preparation of MXenes.

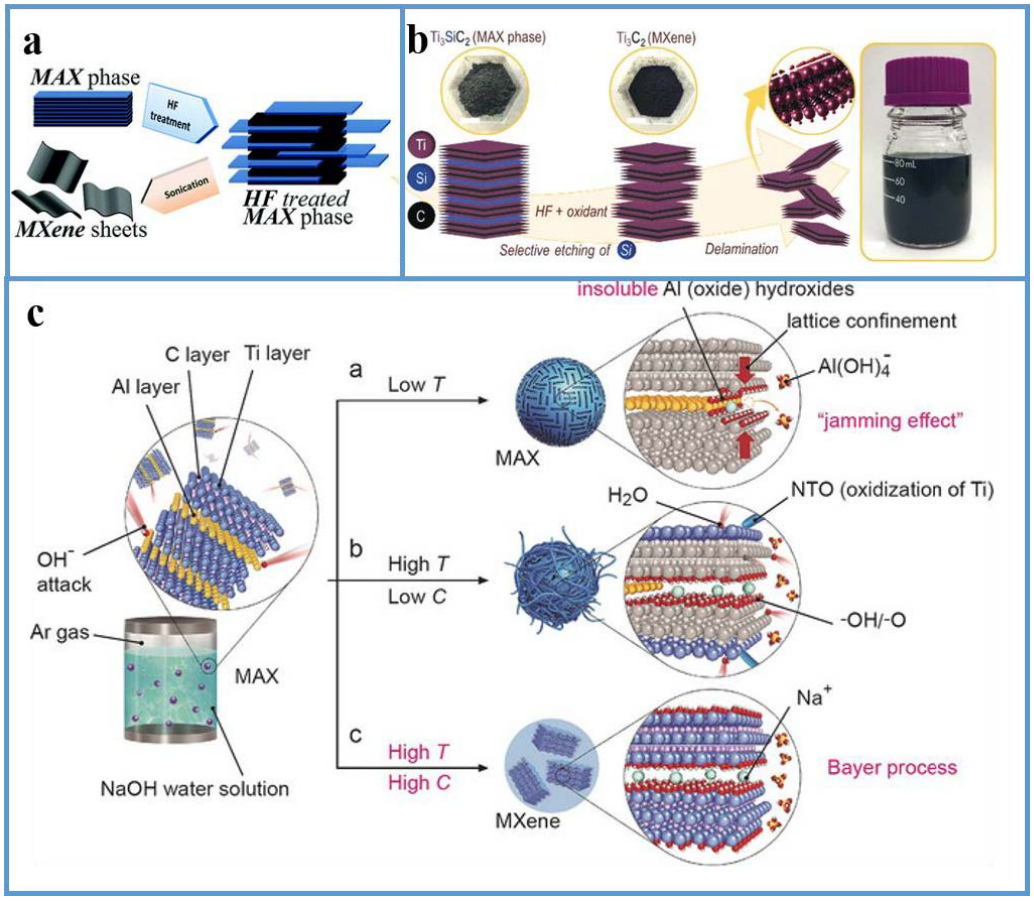

Figure 2.1. a) *Schematic for the exfoliation process of MAX phases and the formation of MXenes. Reproduced with permission.[13] Copyright 2014, American Chemical Society.* ***b)*** *Schematic for the exfoliation of Ti_3SiC_2 and the formation of Ti_3C_2 MXene using an etching solution consisting of HF and an oxidant. Reproduced with permission.[46] Copyright 2018, Wiley-VCH.* ***c)*** *Schematic for the exfoliation of the MAX phase by alkali (NaOH) treatment. Reproduced with permission.[47] Copyright 2018, Wiley-VCH.*

The experimental conditions (*e.g.* reaction time, temperature, and concentration of etchant) have a significant influence on the properties and performance of the as-obtained MXene.[48, 49] For example, it was found that the concentration of the etchant can affect the defects concentration on the surface of MXene materials.[50] Lower concentrations, shorter reaction times and sonication-free delamination may lead to less defects and larger lateral sizes, which results in higher electronic conductivity of the MXene. In addition, MXene sheets prepared by HF-forming etchant usually possess larger lateral size and less defects.[23] Thus, mild etching conditions are preferentially adopted to prepare MXenes for batteries. However, it should be noted that diluted HF, HF-forming etchant, and short reaction time may reduce the yield of the MXene.

In spite of the usage of acidic etchants, the organic-based tetramethylammonium hydroxide (TMAOH) and alkali-based sodium hydroxide (NaOH) were also employed as effective etchants to prepare MXene materials. TMAOH is a major ingredient in commercial Al etchants, which can effectively facilitate the transfer from Al to $Al(OH)_4^-$. The reaction mechanism is described as followed (2-2):

$$2Al + 2OH^- + 6H_2O = 2Al(OH)_4^- + 3H_2 \quad (2\text{-}2)$$

Such a $Al(OH)_4^-$ act as a titanium-mediation moiety on the surface of MXene layers ($Ti_3C_2T_x$, T=$Al(OH)_4^-$).[51] Additionally, as shown in Figure 2.1c, alkali-based sodium hydroxide (NaOH) can also act as a etchant to prepare MXene materials.[47] Interestingly, the Al atoms in the MAX phase can dissolve in 27.5 M NaOH solution under a high temperature of 270 ºC. Different from the previously reported strategies, this method not only prepares the fluorine-free MXene with only oxygen and hydroxyl terminations, but also eliminates safety concerns in the preparation of MXenes.

Aparting from chemical exfoliation methods, other methods (including salt-templated methods, molten-salt methods, and chemical vapor deposition (CVD)) were also proposed to synthesize MXenes.[52-54] However, these methods have yet to be widely adopted as only few MXenes can be obtained till now. Further investigations are highly desired to accelerate the large-scale preparation of MXene materials.

Table 2. 1. *Summary of MXenes produced by wet etching methods and related exfoliation parameters.*

Precursors	MXenes	Etchants	Conditions		c-lattice constant (nm)		Yield	Ref
			T	time	before	after		
		50 % HF	RT	2 h	1.842	2.051	100 %	[11]
		3 M LiF + 6 M HCl	35 °C	24 h	1.842	2.8	100 %	[55]
Ti_3AlC_2	$Ti_3C_2T_x$	NH_4HF_2	RT	11 h	1.86	2.47	NA	[56]
		KHF_2	60 °C	24 h	1.86	2.48	NA	[57]
		27.5 M NaOH	270 °C	12 h	1.86	2.4	92 %	[47]
Ti_2AlC	Ti_2CT_x	10 % HF	RT	10 h	1.36	1.504	60 %	[13]
TiNbAlC	$TiNbCT_x$	50 % HF	RT	28 h	1.379	1.488	80 %	[13]
$(V_{0.5}Cr_{0.5})_3AlC_2$	$(V_{0.5}Cr_{0.5})_3C_2T_x$	50 % HF	RT	69 h	1.773	2.426	NA	[13]
Ta_4AlC_3	$Ta_4C_3T_x$	50 % HF	RT	72 h	2.408	3.034	90 %	[13]
Ti_3AlCN	Ti_3CNT_x	30 % HF	RT	18 h	1.841	2.228	80 %	[13]
Nb_4AlC_3	$Nb_4C_3T_x$	50 % HF	RT	96 h	2.422	3.059	77 %	[15]
$(Nb_{0.8}Ti_{0.2})_4AlC_3$	$(Nb_{0.8}Ti_{0.2})_4C_3T_x$	50 % HF	50 °C	96 h	2.417	2.969	NA	[58]
$(Nb_{0.8}Zr_{0.2})_4AlC_3$	$(Nb_{0.8}Zr_{0.2})_4C_3T_x$	LiF +12 M HCl	50 °C	168 h	2.441	3.477	NA	[58]
Mo_2Ga_2C	Mo_2CT_x	3 M LiF +12 M HCl	35 °C	384 h	1.81	2.31	NA	[59]
		14 M HF	55 °C	160 h	1.81	2.12	NA	[59]
Mo_2TiAlC_2	$Mo_2TiC_2T_x$	50 % HF	RT	48 h	1.86	2.58	100 %	[14]

$Mo_2Ti_2AlC_3$	$Mo_2Ti_2C_3T_x$	50 % HF	55 °C	90 h	2.36	~2.9	100 %	[14]
Cr_2TiAlC_2	$Cr_2TiC_2T_x$	5 M LiF + 6 M HCl	55 °C	42 h	1.87	2.43	~80 %	[14]
Nb_2AlC	Nb_2CT_x	50 % HF	RT	90 h	1.388	2.234	100 %	[60]
V_2AlC	V_2CT_x	50 % HF	RT	90 h	1.31	1.973	60 %	[60]
Zr_3AlC_5	$Zr_3C_2T_x$	50 % HF	RT	72 h	2.773	3.253	NA	[61]
$Hf_3[Al(Si)]_4C_6$	$Hf_3C_2T_x$	35 % HF	RT	60 h	3.188	3.270	73 %	[62]
Ti_3SiC_2	$Ti_3C_2T_x$	1.17 M H_2O_2 +15 M HCl	40 °C	45 h	0.995	1.443	NA	[46]

2.2 Structural characteristics and properties of MXenes

2.2.1 Structural properties and surface terminations

Investigations on the MXene structure play a crucial role in understanding the properties of MXenes. Similar to their precursor MAX phases, crystalline MXenes possess a hexagonal close-packed structure. Transition metal atoms in MXenes are situated in a close-packed structure, while carbon/nitrogen atoms fill the octahedral interstitial sites. The ordering of transition metal atoms changes with the value of n in the MXenes. For example, in M_2C, transition metal atoms have a hexagonal close-packed stacking, while transition metal atoms in M_3C_2 follow face-centered cubic stacking.[18] M. Naguib *et al*. proposed the first structural model of stacked $Ti_3C_2(OH)_2$ MXene via a density functional theory (DFT) simulation.[11] The c-lattice parameter obtained from the XRD pattern closely matches the calculated value of the geometry-optimized structure of $Ti_3C_2(OH)_2$. A more precise DFT model and the ground state of multilayer $Ti_3C_2(OH)_2$ MXene have been discovered later by Mochalin *et al.*.[36] In reality, the real structures of MXenes are more complicated because of the co-existence of mixed -OH, -O and/or -F terminations.[63] Notably, -OH terminations are unstable because the hydrogen atoms on the end of -OH terminations tend to be

replaced by alkali metals or transition metals. Moreover, -OH terminations are readily converted to -O terminations at a high temperature, which causes MXenes to decompose to metal oxides through the adsorption of multivalent metal atoms. Tang *et al.* found three possible configurations based on the orientations of the surface functional groups (including -F and -OH) in $Ti_3C_2T_2$ as shown in Figure 2.2a-d.[64] In configuration I, surface functional groups are positioned above the hollow sites surrounded by three neighboring carbon atoms and aligned toward the middle Ti atoms. In configuration II, the surface functional groups tend to occupy the top sites of carbon atoms. Configuration III is a mixed structure, where one side is in configuration I and the opposing side is in configuration II. Based on their relative DFT total energies, configuration I is energetically the most favourable, while configuration II is unstable and usually transforms to configurations I or III. However, in previous research, configurations II and III were shown to retain their MXene structures. This is mainly because the carbon atoms near the surface functional groups can provide electrons in configurations II and III.[65-67]

As an adjunct to theoretical calculations, experimental studies on surface terminations of MXenes have been carried out by many researchers. For example, Persson's group observed individual $Ti_3C_2T_x$ MXene sheets at atomic resolution, which revealed the uneven coverage of oxygen-based surface functional groups and oxidized titanium adatom complexes.[68] Meanwhile, Wang *et al.* reported that the top sites of the Ti (c) atoms and the carbon atoms of the MXene monolayer are the most favourable locations for the functional groups and the intercalated sodium ions, respectively.[21] In addition, nuclear magnetic resonance (NMR) spectroscopy was employed to study terminations on the surface of MXenes. The ^{1}H NMR spectrum shows that the -OH groups on the surface of the MXene are bonded to the hydrogen of water molecules. An unusual ^{19}F NMR spectrum was observed, which can be ascribed to strong interactions between the

metallic/semiconducting MXene and -F groups.[69] The combination of multilevel structural modelling and Neutron scattering data also discloses structural details of MXenes.[70] These results afford further insights into the surface structure of MXenes at the atomic level, which is beneficial for material design and applications.

2.2.2 Physical properties

Physical properties have a significant effect on the electrochemical performance of MXene electrodes in lithium-based batteries. Hence, prior to applying MXenes as electrodes in batteries, the physical properties (including dielectric properties[71], electronic properties[72-75] and mechanical properties[76-79]) were extensively studied by theoretical calculations and experimental characterizations.

Figure 2.2e, f demonstrates the electron density of states (DOS) of two MXenes and the corresponding MAX phase precursors. In Figure 2.2e, the Fermi level of the Ti_2AlC MAX phase is dominated by M 3d orbitals. The valence states below the Fermi level comprise sub-bands A and B, where A is composed of hybridized Ti 3d-Al 3p orbitals and B consists of hybridized Ti 3d-C 2p/Ti 3d-Al 3s orbitals. After etching the "A" layers, the Ti-Al bonds break, and Ti-Ti metallic-like bonding states appear near the Fermi level, leading to a higher electron DOS around the Fermi level in bare Ti_2C MXene.[72] Although bare MXene monolayers possess metallic conductivity with a high electron density near the Fermi level, some functionalized MXenes are predicted to become semiconductors with reduced Fermi levels and small bandgaps. Furthermore, the electronic properties of MXenes depend not only on the types of surface functional groups but also on the orientations of the surface groups. For instance, -F/-OH-terminated Ti_3C_2 MXene in configuration I has been proven to be a semiconductor with a small bandgap while the MXene with -F/-OH terminations in configuration II is predicted to possess metallic conductivity.[64] In

addition to the surface groups, the electronic properties also rely on the type of "M" atoms. For example, the calculated results show that Ti_2CO_2 MXene has an indirect bandgap of 0.24 eV, while Hf_2CO_2 MXene possesses an indirect bandgap of 1.0 eV.[80] The "X" atoms determine the properties of MXenes as well. Ti_2C and Ti_2N MXenes with the same terminations exhibit different electron DOSs, mainly because nitrogen atoms have more electrons than carbon atoms.

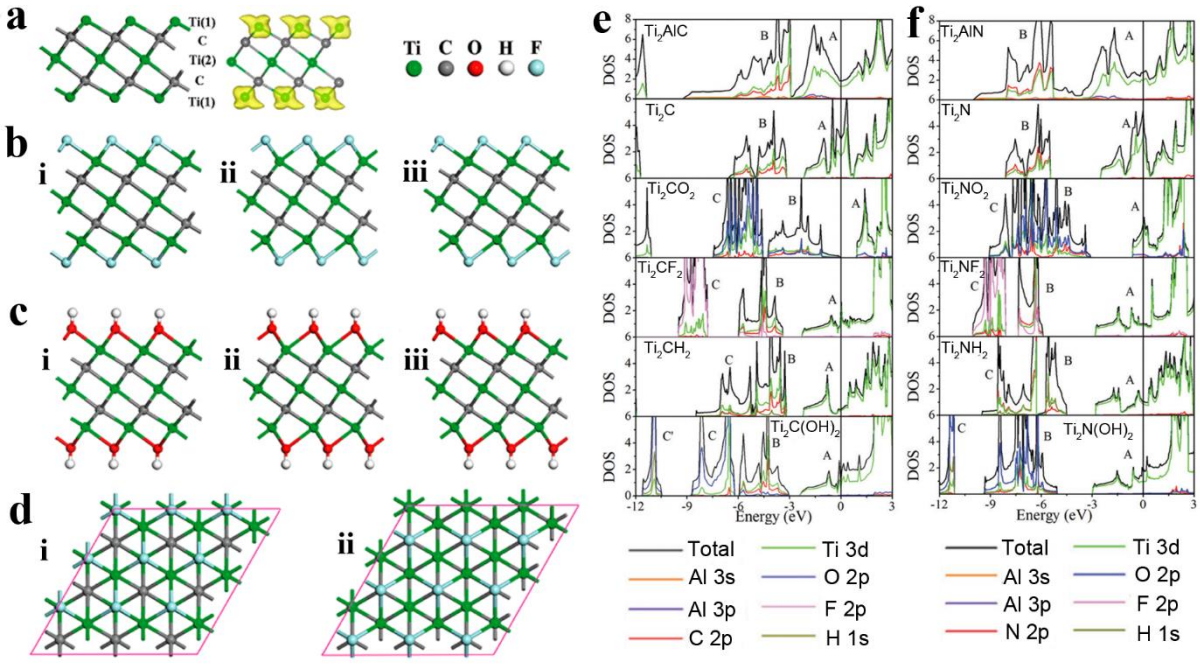

Figure 2.2. *Optimized geometries of bare Ti_3C_2 MXene and its functionalized derivatives with different configurations. Side views of* ***a)*** *bare Ti_3C_2;* ***b)*** *$Ti_3C_2F_2$: i)I-$Ti_3C_2F_2$, ii) II-$Ti_3C_2F_2$, and iii) III-$Ti_3C_2F_2$;* ***c)*** *$Ti_3C_2(OH)_2$: i) I-$Ti_3C_2(OH)_2$, ii) II-$Ti_3C_2(OH)_2$, and iii) III-$Ti_3C_2(OH)_2$; top views of* ***d)*** *$Ti_3C_2F_2$: i) I-$Ti_3C_2F_2$ and ii) II-$Ti_3C_2F_2$. Because configuration III is a mixture of configurations I and II, the top view of configuration III is not shown.*[64] *Reproduced with permission. Copyright 2012, American Chemical Society. Total and partial density of states of* ***e)*** *Ti_2CT_2 and* ***f)*** *Ti_2NT_2 MXene, and related MAX phases calculated using the HSE06 functional.*[72] *Reproduced with permission. Copyright 2013, American Physical Society.*

To date, some theoretical predictions have been verified by experimental investigations. Individual $Ti_3C_2T_2$ particulates were experimentally proven to be highly anisotropic by *in situ* I−V measurements.[81] In addition, MXene films prepared by a spin-casting method exhibited superior conductivity due to a high degree of coplanar alignment of individual nanosheets and a metal-like

free-electron density.[82] Two-dimensional $Ti_3C_2T_x$ thin films with different thicknesses were also prepared by an interfacial film formation technique to study their electrical and optical properties.[83, 84] In particular, a $Ti_3C_2T_x$ film with a thickness of ~17 nm showed metallic conductivity and negative magnetoresistance below 100 K.[56] Xie *et al.* reported that the zeta potential of the obtained $Ti_3C_2T_x$ MXene was -63.3 mV, suggesting that they can easily absorb other materials with positive zeta potential by physical adsorption.[85] Apart from $Ti_3C_2T_x$ MXene, other MXenes such as Ti_2CT_x,[59, 63] Nb_2CT_x,[86] and Mo_2CT_x[59] have been studied experimentally. In accordance with the above discussions, all computational and experimental results demonstrate that MXenes have excellent electronic properties, which can facilitate electron transport during discharge/charge processes and hence contribute to the electrochemical performances of lithium-based batteries.

2.3 Application of MXenes for lithium-based batteries

In 2013, Naguib et al. reported that a steady-state capacity can be achieved when Li^+ ions are intercalated into MXenes. Moreover, Li^+ ions are predicted to diffuse quickly on the surface of MXenes, resulting in a large storage capacity and outstanding high rate capability.[87, 88] Hence, MXenes are considered as promising anode materials for lithium-ion batteries. On the other hand, MXenes with functional groups on the surface are capable of efficiently trapping polysulfides by chemical and physical adsorption, suppressing the shuttle effect in lithium-sulfur batteries.[89] Therefore, research on MXenes in lithium-sulfur batteries is attracting extensive attention. Herein, we review the latest advances of MXenes and their composites for lithium-based batteries, including lithium-ion batteries and lithium-sulfur batteries.

2.3.1 Lithium-ion batteries

Lithium-ion batteries (LIBs), which are the state-of-the-art energy storage technology in current society, are widely used in industry. Nevertheless, commercial graphite anodes, which have relatively low capacity, cannot meet the soaring demand for energy storage in the future. Thus, it is urgent to develop novel electrode materials with both high power density and high energy density for lithium-ion batteries. MXenes and MXene-based composites have shown great potential as anode materials for lithium-ion batteries because of their metallic conductivity (or narrow band gap semiconducting characteristics), open structure, weak interlayer forces and high specific surface area.

2.3.1.1 Bare MXenes for lithium-ion batteries

Most MXenes and their fluorinated/hydroxylated derivatives have excellent electronic conductivity, which can facilitate their practical applications in lithium-ion batteries.[64] In 2011, Naguib *et al.* first proposed that the multilayered structure of $Ti_3C_2T_x$ MXene can be used as an anode for lithium storage.[11] According to DFT calculations, the intercalated lithium ions bond into the spaces vacated by aluminum atoms, as described in reaction (2-3):

$$Ti_3C_2 + 2Li = Ti_3C_2Li_2 \quad (2\text{-}3)$$

Since then, investigations into MXene electrodes for lithium-ion batteries have been carried out both experimentally and computationally. The first utilization of Ti_2CT_x MXene in lithium-ion batteries was published in 2012 by Naguib *et al.*.[87] The exfoliated Ti_2CT_x MXene was observed to deliver a high reversible capacity of 225 mAh g^{-1} at a current density of C/25 (based on one lithium ion per Ti_2CO_x formula unit). In addition, a stable capacity of 110 mAh g^{-1} was retained after 80 charge-discharge cycles at 1 C. This result opens a door for other researchers to study MXenes as

Li^+ intercalation hosts for lithium-ion batteries. In addition, according to the equation $I = av^b$ (where I represents the measured current, v represents the scan rate, and a and b are adjustable parameters), Come *et al.* demonstrated that the insertion/extraction of lithium ions of Ti_2CT_x is not a mass transport-limited process at a slow scan rate ($v \leq 5$ mV/s, $b \approx 1$). This means that lithium ions have easy access to the active sites below the scan rate of 5 mV/s.[88] Thereafter, Kajiyama *et al.* reported a Ti_2CT_x MXene with steric chloride terminations, which can increase the interlayer spacing between the individual MXene units. The increased interlayer spacing can efficiently improve the lithium ions accessibility and afford more active sites, thus improving the electrochemical performances of lithium-ion batteries.[90]

Because Ti_2CT_x has a higher surface energy than $Ti_3C_2T_x$, Ti_2CT_x layers tend to adsorb each other to decrease energy and establish a stable structure, which leads to a smaller c-lattice parameter (interlayer spacing) for lithium ions storage. Thus, $Ti_3C_2T_x$ MXene is considered as a better candidate anode material for lithium-ion batteries. DFT calculations were used to study the electronic properties and possible lithium storage capability of $Ti_3C_2T_x$ MXene. Tang *et al.* discussed the diffusion and adsorption of lithium ions on bare Ti_3C_2 and $Ti_3C_2T_x$ (-OH, -F) monolayers and concluded that lithium ions can migrate more easily on bare Ti_3C_2 because of the lower energy barrier and shorter diffusion pathway compared with its fluorinated or hydroxylated derivatives.[64] Er *et al.* found that the theoretically calculated capacity for Li^+ intercalating into Ti_3C_2 is 447.8 mAh g^{-1}, which is higher than that of its Na^+, K^+ and Ca^{2+} counterparts.[91] Additionally, Xie *et al.* found that extra lithium layers can be adsorbed on the outer layer of lithiated, oxygen-terminated MXenes, which may further enhance the Li storage capacity.[36] In 2013, $Ti_3C_2T_x$ "paper" was prepared by intercalation with hydrazine monohydrate (HM) dissolved in N,N-dimethylformamide (DMF) followed by filtration (shown in Figure 2.3a). XRD data

(Figure 2.3b and c) reveal the successful intercalation of small molecules and Figure 2.3d and e display the morphologies of $Ti_3C_2T_x$ MXene before and after the intercalation treatment, confirming that the porous structure is retained after intercalation. Similarly, $Ti_3C_2T_x$ can be intercalated and delaminated by DMSO (Figure 2.3f). The as-obtained $Ti_3C_2T_x$ "paper" can deliver a high reversible capacity of 410 mAh g^{-1} at a 1 C rate, which is remarkably higher than that of etched-$Ti_3C_2T_x$ MXene (Figure 2.3g).[42, 92] The cold pressing method was employed to prepare $Ti_3C_2T_x$/carbon black free-standing binder-less electrodes, exhibiting a high areal capacity of 1.58 mAh cm^{-2} even at 2.7 C.[93]

Apart from the Ti-based MXene, Naguib *et al.* reported niobium carbides (Nb_2CT_x) and vanadium carbides (V_2CT_x) as electrode materials for lithium-ion batteries in 2013, which exhibited reversible capacities of 170 and 260 mAh g^{-1} at 1 C, respectively. High reversible capacities of 110 mAh g^{-1} for Nb_2CT_x electrodes and 125 mAh g^{-1} for V_2CT_x electrodes can be achieved even at 10 C. Both Nb_2CT_x and V_2CT_x demonstrated excellent rate performances, suggesting fast transport of Li^+ between MXene layers.[60] Similarly, due to its excellent electronic conductivity and enhanced interlayer spacing, $Nb_4C_3T_x$ MXene delivers a remarkable capacity of 380 mAh g^{-1} at a current density of 100 mA g^{-1} when applied as an anode for lithium-ion batteries. The capacity increased from 116 mAh g^{-1} to 320 mAh g^{-1} after 1000 cycles at a current density of 1000 mA g^{-1}, which can be attributed to the enhanced interlayer spacing during the cycling processes.[58, 94] More recently, $(Nb_{0.8}, Ti_{0.2})_4C_3T_x$ and $(Nb_{0.8},Zr_{0.2})_4C_3T_x$ were prepared for the first time in 2015. After 20 cycles at C/4, $(Nb_{0.8}, Ti_{0.2})_4C_3T_x$ and $(Nb_{0.8}, Zr_{0.2})_4C_3T_x$ electrodes still retained specific capacities of 158 and 132 mAh g^{-1}, respectively.[58]

Eames *et al.* performed a global screening of the capacities and insertion voltages for different intercalation ions in various M_2C-based compounds (including Ti_2CT_x, V_2CT_x, Nb_2CT_x, and

Ta_2CT_x) with -OH, -O, -F and -H functional terminations on the surface of the MXene. Their calculations indicated that the functional terminations and transition metal species significantly affect the cell voltages and specific capacities of MXenes. In particular, -O terminations tend to enhance the specific capacity, while -OH and -F terminations should be avoided because they lead to a relatively lower capacity. Furthermore, the authors proposed that the most promising MXene anode materials are M_2C compounds containing light transition metals with no functional groups or -O terminations. Additionally, the specific capacities originating from intercalated Li^+ or Mg^{2+} are higher than those originating from Na^+ or K^+. Thus, these results provide valuable guides for exploring M_2C-based compounds for practical applications in energy storage. Interestingly, Hu *et al.* obtained similar results when investigating V_2C and V_2CX_2 (X = F, OH) monolayers.[95]

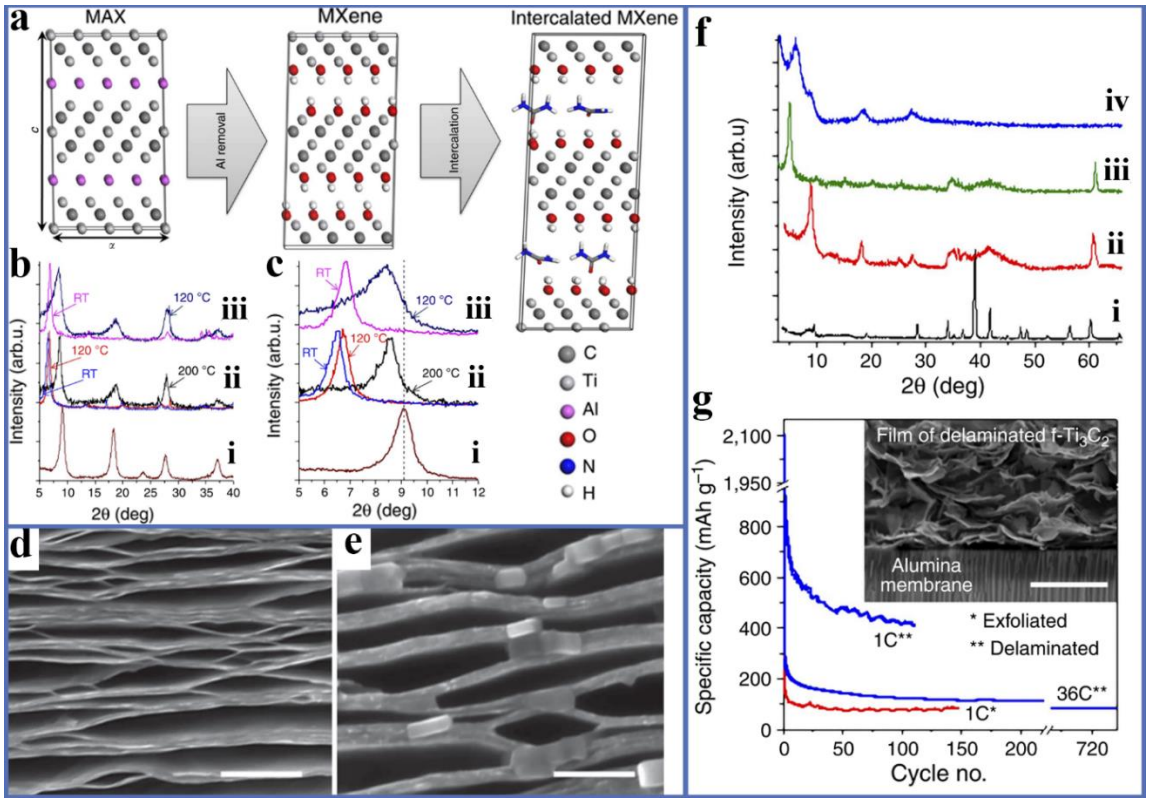

Figure 2.3. a) *Schematic illustration for the preparation of intercalated MXene by the intercalation of urea molecules.* ***b)*** *XRD patterns of surface-functionalized Ti_3C_2: i) before treatment, ii) after intercalation treatment followed by washing with DMF, and iii) after intercalation treatment, washing with ethanol and*

drying under different conditions. ***c)*** *Magnified view of c in the 5-12° 2θ range showing the (0002) peaks. SEM images of* Ti_3C_2 ***d)*** *before and* ***e)*** *after intercalation.* ***f)*** *XRD patterns of i)* Ti_3AlC_2*, ii) exfoliated* Ti_3C_2*, iii) DMSO intercalated* Ti_3C_2 *and iv) delaminated* Ti_3C_2*.* ***g)*** *Comparison of the performances of exfoliated and delaminated functionalized* Ti_3C_2 *in lithium-ion batteries. The inset is an SEM image of the delaminated* Ti_3C_2 *film. Scale bars: 200 nm in d), e).*[42] *Reproduced with permission. Copyright 2013, Macmillan Publishers Ltd.*

The high chemical diversity and structural complexity of MAX phases motivated the exploration of new MXenes; for this purpose, Anasori *et al.* synthesized $Mo_2TiC_2T_x$, $Mo_2Ti_2C_3T_x$ and $Cr_2TiC_xT_x$ in 2015.[14] **Figure 2.4**a and b shows the transformation mechanisms of Mo_2TiAlC_2 to Mo_2TiC_2Tx and $Mo_2Ti_2AlC_3$ to $Mo_2Ti_2C_3T_x$. Obtained from theoretical calculations, Figure 2.4c shows the energy differences between Mo_2TiC_2 MXenes with fully ordered and partially ordered configurations. In particular, ordered Mo_2TiC_2 MXene with Ti atoms in the middle layer and Mo-Ti-Mo stacking is energetically the most favorable. The SEM and transmission electron microscopy (TEM) images shown in Figure 2.4d reveal the co-existence of Mo and Ti elements. $Mo_2TiC_2T_x$ MXene can also be delaminated by intercalation with DMSO followed by sonication. After that, a $Mo_2TiC_2T_x$ "paper" electrode can be prepared by filtration, as shown in Figure 2.4e. The $Mo_2TiC_2T_x$ MXene achieves a reversible capacity of 269 mAh g^{-1}, which is notably higher than that of $Ti_3C_2T_x$ and Ti_2CT_x (Figure 2.4f). The different electrochemical behaviors of $Mo_2TiC_2T_x$ and $Ti_3C_2T_x$ indicate that the properties and performances of $Mo_2TiC_2T_x$ MXene are determined by the surface Mo atoms.

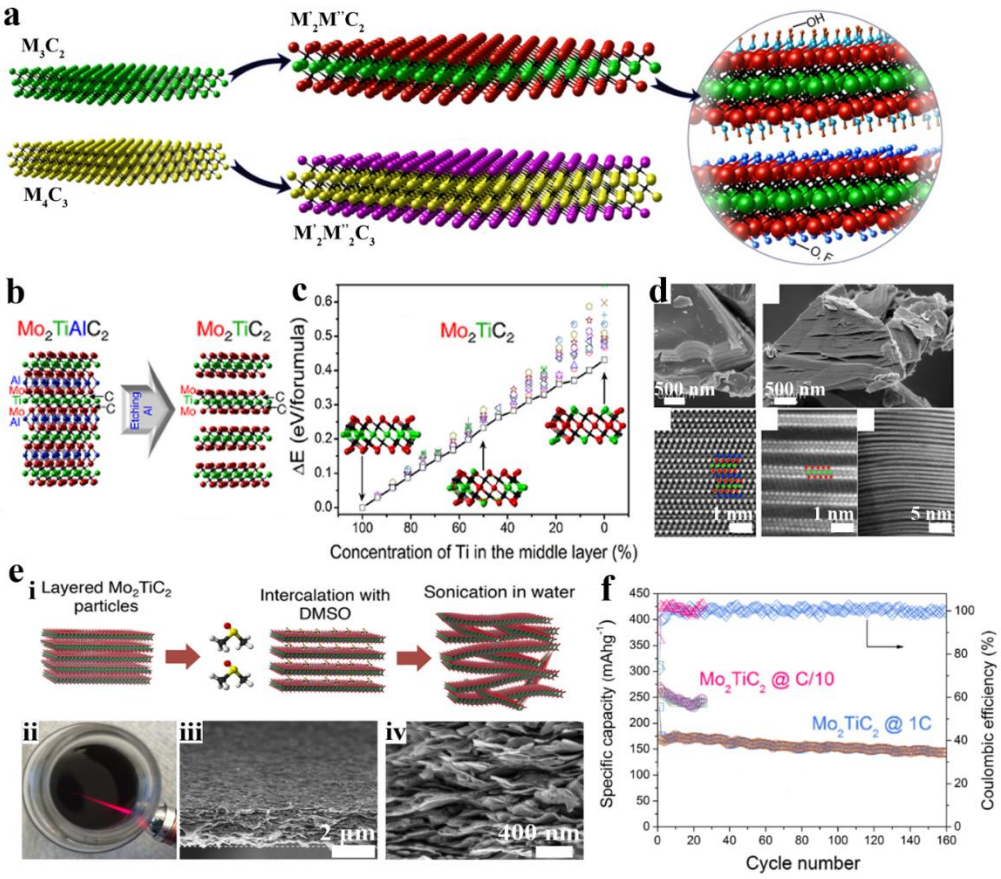

Figure 2.4. a) *Schematic illustration for the preparation of $M'_2M''C_2/M'_2M''_2C_3$ MXene structures.* ***b)*** *Transformation mechanism of Mo_2TiAlC_2 to $Mo_2TiC_2T_x$.* ***c)*** *Total energy diagram of the Mo_2TiC_2 monolayer as a function of Ti concentration in the middle layer.* ***d)*** *SEM and TEM images of the $Mo_2TiC_2T_x$ MXene and Mo_2TiAlC_2 MAX phases.* ***e)*** *Delaminated $Mo_2TiC_2T_x$ MXene: i) schematic illustration for the preparation of delaminated $Mo_2TiC_2T_x$; ii) Tyndall effect on $Mo_2TiC_2T_x$ aqueous solution; iii) low-resolution and iv) high-resolution SEM images of $Mo_2TiC_2T_x$ "paper".* ***f)*** *Cycling performances of $Mo_2TiC_2T_x$ paper at C/10 and 1 C rates. (green circles: Ti atoms, red circles: Mo atoms, black circles: C atoms, blue circles: Al atoms).*[14] *Reproduced with permission. Copyright 2015, American Chemical Society.*

Although MXenes possess many advantages, such as good electronic conductivity and open structures, there are some challenges in the practical application of MXene electrodes. For example, the serious restacking of MXene sheets during electrode fabrication still cannot be avoided, which limits ion transport and degrades device performance. Thus, the prevention of MXenes from restacking is critical for fully realizing the benefits of MXenes. Recently, Xia *et al.* prepared

vertically aligned MXene sheets by mechanical shearing of a discotic MXene lamellar liquid crystal (Figure 2.5a, b).[96] The vertical alignment of MXene flakes enabled directional ion transport (Figure 2.5c), which can lead to thickness-independent electrochemical performance in a thick film up to 200 μm. Zhao *et al.* fabricated 2D MXene flakes into 3D hollow spherical architectures via a sacrificing template approach (Figure 2.5d).[97] The as-prepared macroporous MXene films were free standing and highly conductive, which can facilitate ion and electron transport in the electrodes (Figure 2.5e). These morphologies can be further extended to lithium-ion batteries, which are expected to result in good electrochemical performances.

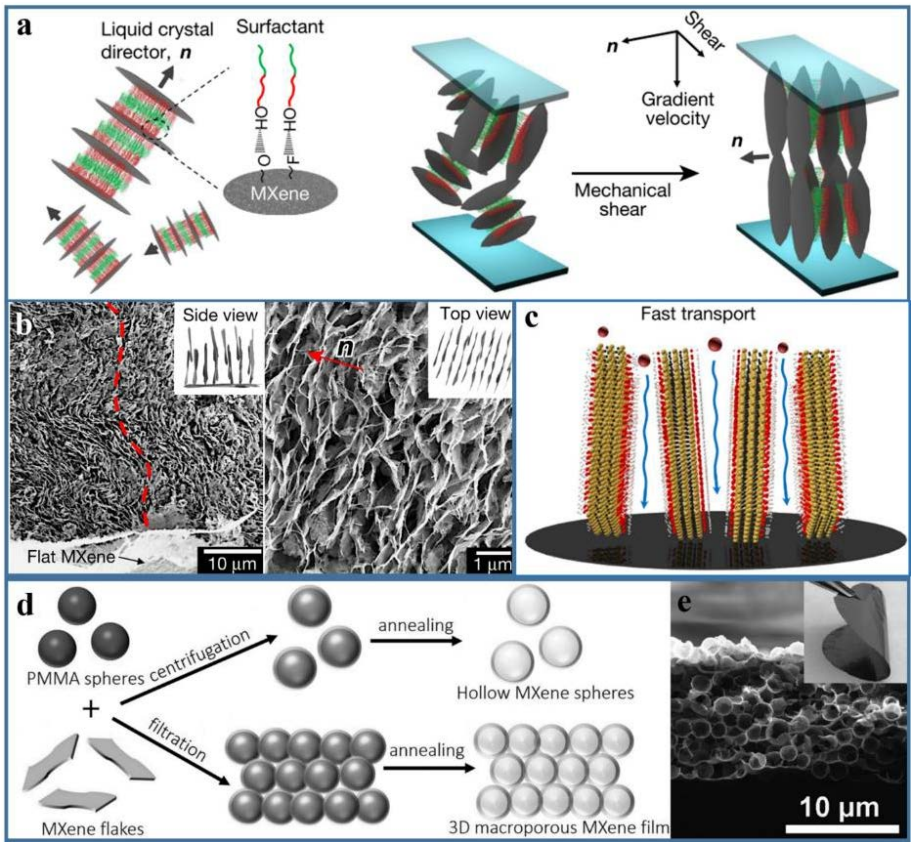

Figure 2.5. *Two examples of the MXene architectures construction.* ***a)*** *Illustration for the preparation of vertical alignment by mechanical shearing of a discotic lamellar liquid-crystal phase of $Ti_3C_2T_x$;* ***b)*** *Side view and top view of SEM images of the MXLLC;* ***c)*** *Schematic of ion transport in the vertically aligned MXene film. Reproduced with permission.[96] Copyright 2018, Nature publishing group.* ***d)*** *Schematic showing the fabrication of hollow MXene spheres and 3D macroporous MXene frameworks;* ***e)*** *Cross-*

sectional SEM image and digital image (inset) of a 3D macroporous film. Reproduced with permission.[97] *Copyright 2017, Wiley-VCH.*

2.3.1.2 MXene-based composites for lithium-ion batteries

MXenes have received tremendous attention because of their high volumetric capacity and superior electronic conductivity. However, due to the electrostatic forces between the layers, MXene layers tend to restack, leading to a severe decrease in electrical conductivity and surface area.[30] Thus, carbon nanofibers (CNFs) were grown on the surface of MXene layers by CVD treatment to prevent the restacking of MXene layers (as shown in Figure 2.6a). Figure 2.6b and c displays the SEM images of bare $Ti_3C_2T_x$ and Ti_3C_2/CNF composites, respectively, showing that the interlayer spacing of the composites was enhanced due to the presence of the CNF spacers. Compared with bare $Ti_3C_2T_x$, the as-obtained Ti_3C_2/CNF composite delivered enhanced capacities of ~320 and ~100 mAh g^{-1} at 1 C and 100 C, respectively (shown in Figure 2.6d). Moreover, the Ti_3C_2/CNF composites also show excellent long-term cycling stability and superior rate capability. These values are remarkably higher than those of bare $Ti_3C_2T_x$.[98] Similar strategies can be further extended to produce Nb_2CT_x@carbon nanotube (CNT)[99], CNTs@$Ti_3C_2T_x$[100] and porous-$Ti_3C_2T_x$@CNT[55] composites for high-performance lithium-ion batteries. For example, as shown in Figure 2.6e, delaminated Nb_2CT_x flakes can be prepared by intercalating isopropylamine (i-PrA) molecules, followed by sonication. The obtained flakes (Figure 2.6f) were filtered with and without carbon nanotubes to prepare the Nb_2CT_x@CNT composite and Nb_2CT_x paper, respectively (shown in Figure 2.6g, h). The MXene/CNT composites are also promising for hybrid ion batteries. The flexible and free-standing $Ti_3C_2T_x$@CNT paper electrodes achieved capacities of approximately 100 mAh g^{-1} at 0.1 C and 50 mAh g^{-1} at 10 C when applied as cathodes for hybrid magnesium/lithium-ion batteries.[101] In addition to CNTs, other carbon-based materials such as reduced graphene oxide (RGO)[102] and poly(3,4-ethylenedioxythiophene) (PEDOT)[103], have also

been combined with MXenes and demonstrated superior electrochemical performance in lithium-ion batteries.

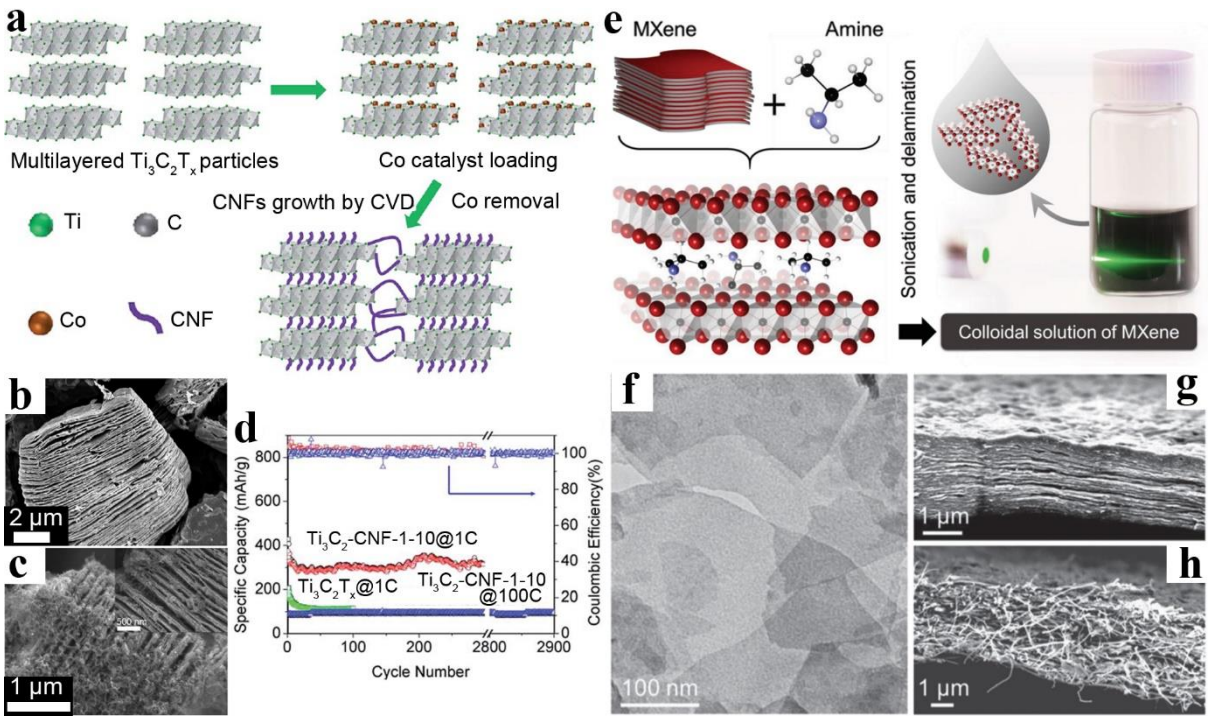

Figure 2.6. a) *Schematic illustration for the preparation of MXene/CNF hybrid particles, SEM images of* ***b)*** *the as-etched $Ti_3C_2T_x$ and* ***c)*** *the Ti_3C_2/CNF composite.* ***d)*** *Cycling stability of the $Ti_3C_2T_x$ sample at 1 C and the $Ti_3C_2T_x$/CNF sample at 1 C and 100 C.*[104] *Reproduced with permission. Copyright 2015, The Royal Society of Chemistry.* ***e)*** *Schematic illustration for the preparation of delaminated Nb_2CT_x.* ***f)*** *TEM image of delaminated Nb_2CT_x flakes. Cross-sectional SEM images of* ***g)*** *bare Nb_2CT_x and* ***h)*** *Nb_2CT_x/CNT composite paper.*[105] *Reproduced with permission. Copyright 2015, WILEY-VCH.*

Since the relatively low theoretical capacities of MXene anodes impede their application in lithium-ion batteries, Sn nanoparticles were introduced to decorate $Ti_3C_2T_x$ MXene through a simple surfactant-assisted method. Figure 2.7a shows the SEM image of the PVP-Sn(IV)@$Ti_3C_2T_x$ composite, in which the Sn nanoparticles are loaded into the MXene layers. The enhanced interlayer spacing can improve the adsorption and intercalation of lithium ions; in contrast, the restacked MXene layers with limited interlayer spacing lead to a substantial decrease in electrochemical performance. Hence, owing to the possible "pillar effect" and synergistic optimization, the nanocomposites show great rate and cycling capability (Figure 2.7b and c). These

results suggest that PVP-Sn(IV)@$Ti_3C_2T_x$ nanocomposites are promising for lithium-ion batteries.[106, 107] Similarly, as shown in Figure 2.7d, Ag nanoparticles were also introduced and combined with $Ti_3C_2T_x$ MXene to improve the electrochemical performance. MXene/Ag composites were prepared by the direct reduction of $AgNO_3$ in $Ti_3C_2T_x$ aqueous solution. The as-prepared composites have two advantages: i) Ag spacers can prevent the restacking of $Ti_3C_2T_x$ MXene layers, permitting more stable chemical properties and ii) Ag metal particles on the surface of the MXene can improve the electrical conductivity of the composite. As demonstrated in Figure 2.7e, the MXene/Ag electrodes show high reversible capacities of 310 mAh g^{-1}, 260 mAh g^{-1} and 150 mAh g^{-1} at 1 C, 10 C and 50 C, respectively. In addition, the electrodes deliver stable capacities without fading even after 5000 cycles at 1~50 C (Figure 2.7f). The ultra-long life span is attributed to the reduced interfacial resistance and the transformation of Ti(II) to Ti(III) during the cycling process.[108]

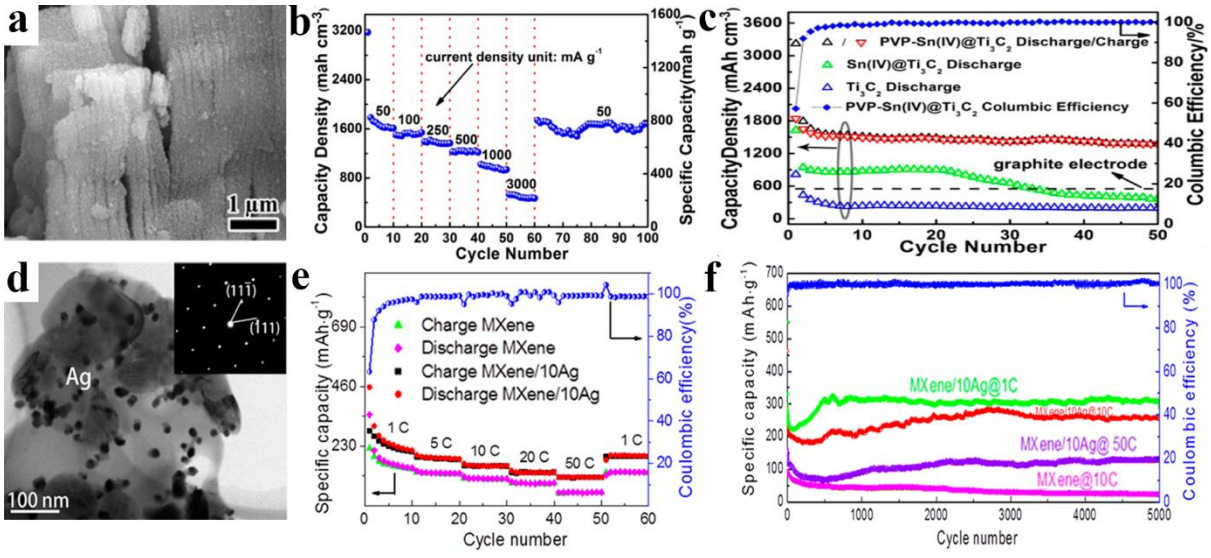

Figure 2.7. a) *SEM image of PVP-Sn(IV)@Ti_3C_2 nanocomposites;* ***b)*** *Rate performance of the PVP-Sn(IV)@Ti_3C_2 nanocomposite;* ***c)*** *Cycling performances of different electrodes.[106] Reproduced with permission. Copyright 2016, American Chemical Society.* ***d)*** *TEM image of the MXene/10Ag composite;* ***e)*** *Rate performances of an MXene/Ag electrode and an MXene electrode;* ***f)*** *Cycling performances of an*

MXene/10Ag electrode and an MXene electrode.[108] *Reproduced with permission. Copyright 2016, American Chemical Society.*

The incorporation of nanomaterials with complementary properties is an effective strategy to develop advanced electrode materials for energy storage devices. Thus, the combination of transition metal oxides (TMOs) with high capacity and 2D MXenes with good electronic conductivity is promising for batteries because of the possible synergistic optimization between the MXenes and TMOs. In 2016, Nb_2O_5@$Nb_4C_3T_x$ (and Nb_2O_5@Nb_2CT_x and TiO_2@$Ti_3C_2T_x$) hierarchical composites were prepared via a facile one-step oxidation process (shown in Figure 2.8a). As displayed in the SEM images (Figure 2.8b and d), Nb_2O_5 (TiO_2) can be grown *in situ* on the surface of $Nb_4C_3T_x$ (or $Ti_3C_2T_x$) MXene. As demonstrated in Figure 2.8c and e, the composites deliver much higher capacities than those of bare MXenes, which can be ascribed to the synergistic and electron "bridge" effects of the disordered carbon.[109, 110] Furthermore, Zhao *et al.* reported a flexible free-standing $Ti_3C_2T_x$/$NiCo_2O_4$ (or Co_3O_4) hybrid film as an anode for lithium-ion batteries (Figure 2.8f). The hybrid film combines the high specific capacity of $NiCo_2O_4$ (or Co_3O_4) and superior conductivity of $Ti_3C_2T_x$ MXene, exhibiting good rate capability and high capacity for lithium ion storage. Typically, high reversible capacities of 1330, 650 and 350 mAh g^{-1} can be achieved by high-performance $Ti_3C_2T_x$/$NiCo_2O_4$ hybrid film anodes at 0.1, 5 and 10 C, respectively, without capacity loss even after hundreds of cycles.[111] The atomic layer deposition (ALD) technique was also applied to synthesize $Ti_3C_2T_x$/SnO_2 hybrid anodes as shown in Figure 2.8g. In this architecture, MXene layers provide excellent electronic conductivity, and the SnO_2 particles act as spacers to prevent the restacking of the MXene layers, which leads to good electrochemical performances.[112] Recently, Huang *et al.* reported novel sandwich-like $Na_{0.23}TiO_2$/$Ti_3C_2T_x$ nanocomposites via a one-step transformation reaction of $Ti_3C_2T_x$ MXene.[113] The 2D nanosheets and 3D architecture synergistically relieve the strain of the electrode during

charge and discharge processes, preventing aggregation of the electrode materials. When applied as anode materials for lithium/sodium-ion batteries, the $Na_{0.23}TiO_2/Ti_3C_2T_x$ nanocomposites present excellent cycling stability and rate capability.

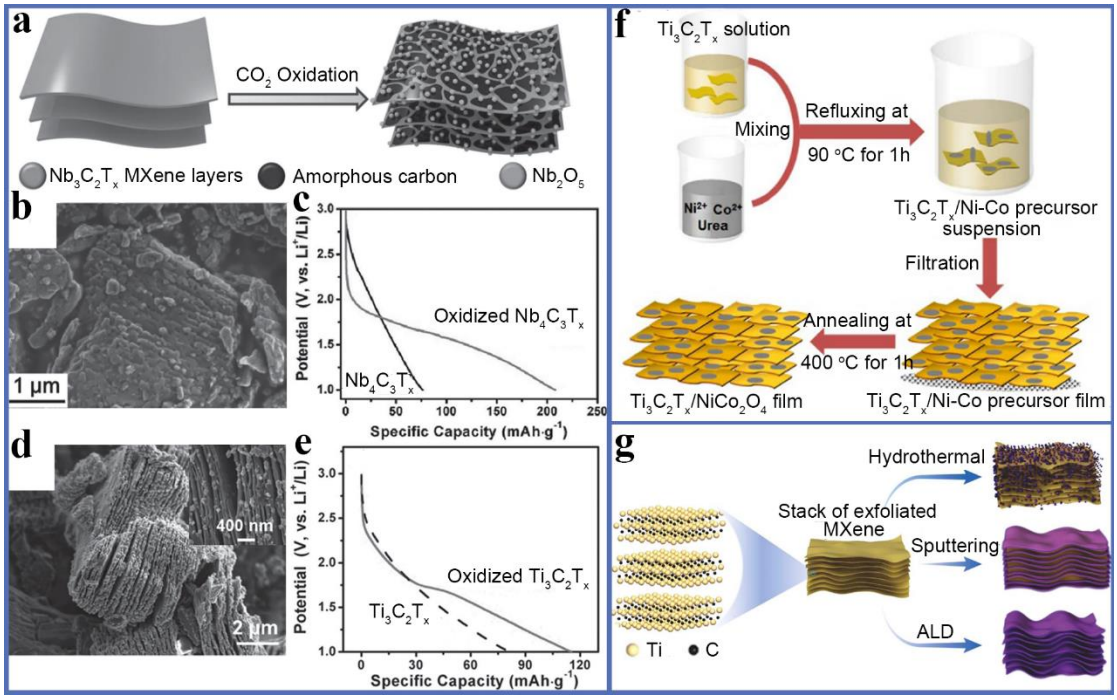

Figure 2.8. a) *Schematic illustration of the structure of composites before and after oxidation.* ***b)*** *SEM image of the $Nb_2O_5@Nb_4C_3T_x$ composite.* ***c)*** *Discharge profiles of the $Nb_2O_5@Nb_4C_3T_x$ and $Nb_4C_3T_x$ electrodes collected at 50 mA g^{-1}.* ***d)*** *SEM image of the $TiO_2@Ti_3C_2T_x$ composite. The inset shows a higher magnification SEM image.* ***e)*** *Discharge profiles of the $TiO_2@Ti_3C_2T_x$ and $Ti_3C_2T_x$ electrodes collected at 50 mA g^{-1}.*[109] *Reproduced with permission. Copyright 2016, WILEY-VCH.* ***f)*** *Schematic illustration for the in situ growth procedures of a $Ti_3C_2T_x/NiCo_2O_4$ hybrid film.*[111] *Reproduced with permission. Copyright 2016, Elsevier.* ***g)*** *Schematic illustration of different methods applied to deposit SnO_2 onto MXene.*[112] *Reproduced with permission. Copyright 2017, Elsevier.*

Transition metal dichalcogenides such as MoS_2[114-116] and SnS_2[117], have also been combined with MXenes to form high-performance anodes for lithium-ion batteries. The presence of MXenes leads to enhanced lithium ions adsorption during the intercalation and conversion processes. For example, Chen *et al.* reported 2D MoS_2-on-MXene heterostructures prepared by *in situ* sulfidation of $Mo_2TiC_2T_x$ MXene. Figure 2.9a shows a schematic illustration for the preparation of MoS_2-on-MXene hybrid materials. The SEM image (Figure 2.9b) and TEM image (Figure 2.9c) confirm the

successful synthesis of macroporous MoS_2/MXene hybrid materials. Due to synergistic effects, the $MoS_2/Mo_2TiC_2T_x$-500 (500 indicates that the heating temperature was 500 ºC) electrode shows a superior reversible capacity of 554 mAh g^{-1} at a current density of 100 mA g^{-1} and retains a capacity of 509 mAh g^{-1} after 100 cycles (Figure 2.9d). When the current density was increased to 200, 500, 1000 and 2000 mA g^{-1}, the $MoS_2/Mo_2TiC_2T_x$-500 electrode exhibited capacities of 484, 407, 315 and 182 mAh g^{-1}, respectively. Even at a high current density of 5000 mA g^{-1}, the $MoS_2/Mo_2TiC_2T_x$-500 electrode still delivered a capacity of 90 mAh g^{-1}. Theoretical calculations show three possible sites for lithium adsorption on the surface of MoS_2 and $MoS_2/Mo_2TiC_2T_x$ (Figure 2.9e and f). Site I in the $MoS_2/Mo_2TiC_2T_x$ composite is the most energetically favorable (Figure 2.9g). Furthermore, the $MoS_2/Mo_2TiC_2T_x$ composite exhibited stronger Li_2S adsorption with lower binding energy than bare MoS_2, which endows $MoS_2/Mo_2TiC_2T_x$ with superior cycling performance (Figure 2.9h and i). Moreover, the computational results reveal that the 2D heterostructures possess metallic properties, which further improve the electrochemical performance of lithium-ion batteries.[114] We summarize the electrochemical performances of lithium-ion batteries with MXene (or MXene composite) electrodes in Table 2.2. The MXene composites deliver better electrochemical performance than bare MXenes, which can be attributed to the synergistic effects of the composites and the purposefully designed material architectures.

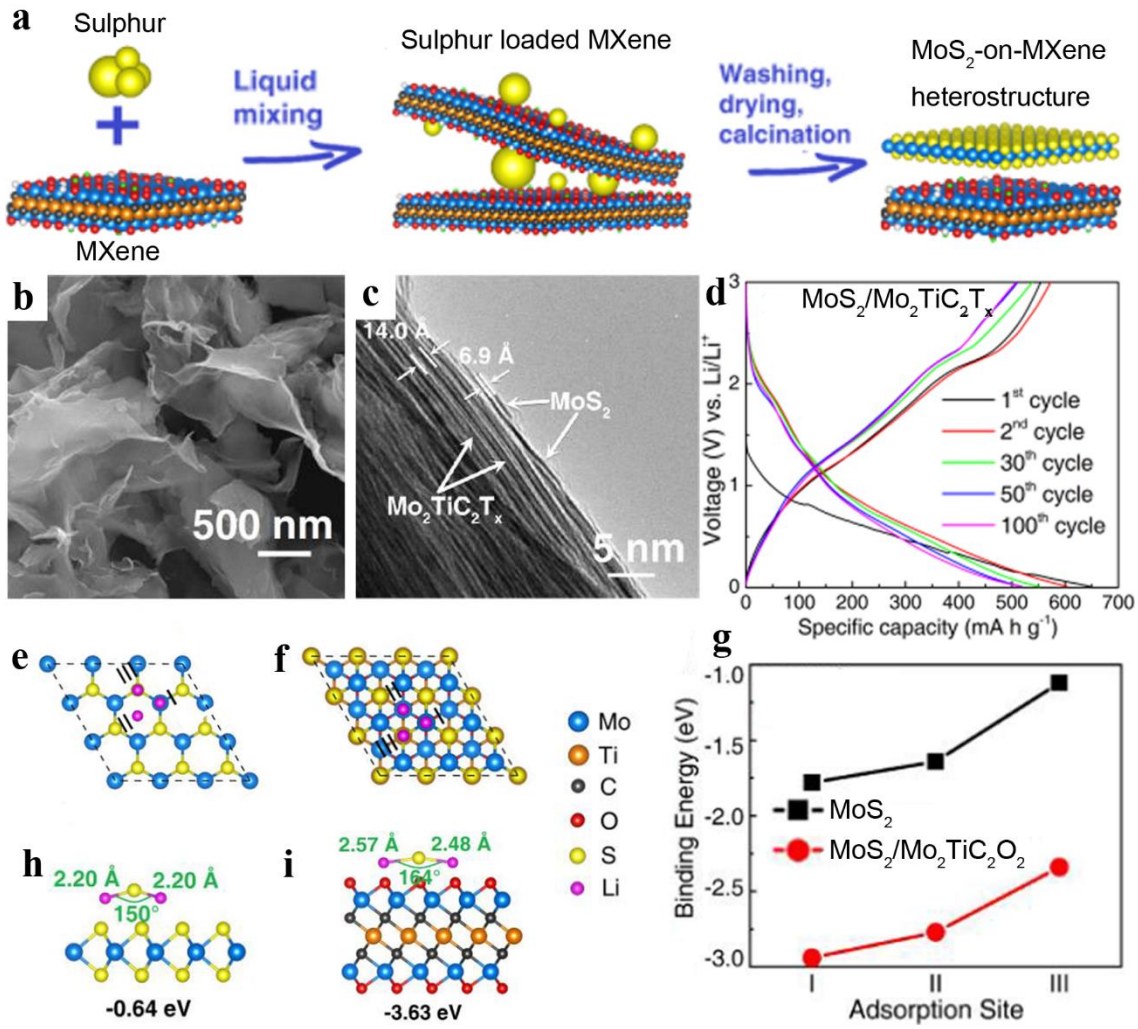

***Figure 2.9. a**) Schematic illustration for the preparation of MoS_2/MXene hybrids. SEM image **b**) and TEM image **c**) of $MoS_2/Mo_2TiC_2T_x$-500. **d**) Galvanostatic charge/discharge profiles of $MoS_2/Mo_2TiC_2T_x$-500 at 100 mA g^{-1}. Adsorption sites of lithium ions on (**e**) MoS_2 and (**f**) $MoS_2/Mo_2TiC_2O_2$. (**g**) Binding energies of lithium ions on the surface of MoS_2 and $MoS_2/Mo_2TiC_2O_2$. The most stable adsorption configurations and binding energies of Li_2S on (**h**) MoS_2 and (**i**) $Mo_2TiC_2O_2$.[114] Reproduced with permission. Copyright 2017, WILEY-VCH.*

Table 2.2. *Summary of electrochemical performances of MXene and MXene-based composites for lithium-ion batteries.*

Materials	Architecture	Reversible Capacity	Rate and Cycling capability	Ref.
Ti_2CT_x	Exfoliated graphite-like morphology	225 mAh g^{-1} at C/25	70 mAh g^{-1} at 10 C after 200 cycles	[87]
V_2CT_x	Exfoliated graphite-like morphology	288 mAh g^{-1} at 1 C	125 mAh g^{-1} at 10 C after 150 cycles	[60]
Nb_2CT_x	Exfoliated graphite-like morphology	250 mAh g^{-1} at 1 C	110 mAh g^{-1} at 10 C after 150 cycles	[60]
$Ti_3C_2T_x$	Accordion-like layer structure	123 mAh g^{-1} at 1C	69 mAh g^{-1} at 10 C after 100 cycles	[92]
$Ti_3C_2T_x$	Cold-pressed Free-standing discs	15 mAh cm^{-2} at C/3	5.9 mAh cm^{-2} at C/3 after 50 cycles	[93]
Nb_2CT_x	Cold-pressed Free-standing discs	16 mAh cm^{-2} at C/3	6.7 mAh cm^{-2} at C/3 after 50 cycles	[93]
Ti_3C_2/CNF	CNF bridged layered sheets	320 mAh g^{-1} at 1 C	97 mAh g^{-1} at 100 C after 2900 cycles	[104]
Nb_2CT_x/CNT	Composite paper	420 mAh g^{-1} at 0.5 C	370 mA mAh g^{-1} at 2.5 C after 100 cycles	[105]
Ti_2C/TiO_2	TiO_2 nanocrystals on the MXene surface	389 mAh g^{-1} at 0.1 A g^{-1}	280 mA mAh g^{-1} at 1 A g^{-1} after 1000 cycles	[110]
Sn(IV)@Ti_3C_2	Sn(IV) nanocomplex anchored on MXene	635 mAh g^{-1} at 0.1 A g^{-1}	544 mAh g^{-1} at 0.5 A g^{-1} after 200 cycles	[106]
$Ti_3C_2T_x$/CNT	Porous sheets and CNT composite film	1250 mAh g^{-1} at 0.1 C	500 mAh g^{-1} at 0.5 C after 100 cycles	[55]
$Nb_4C_3T_x$	Exfoliated graphite-like morphology	380 mAh g^{-1} at 0.1 A g^{-1}	320 mAh g^{-1} at 1 A g^{-1} after 1000 cycles	[94]
Nb_2O_5@$Nb_4C_3T_x$ (Voltage: 1~3 V)	Nb_2O_5 nanoparticles decorated on MXene	208 mAh g^{-1} at 0.25 C	133 mAh g^{-1} at 0.5 A g^{-1} after 400 cycles	[109]
$Ti_3C_2T_x/NiCo_2O_4$	Layer-by-layer hybrid film	1330 mAh g^{-1} at 0.1 C	1200 mAh g^{-1} at 1 C after 100 cycles	[111]
$Ti_3C_2T_x$/Ag	Ag nanoparticles distribute on MXene	310 mAh g^{-1} at 1 C	260 mAh g^{-1} at 10 C after 5000 cycles	[108]

SnO_2/ $Ti_3C_2T_x$	SnO_2 crystallites on MXene flake	1041 mAh g^{-1} at 0.1 A g^{-1}	451 mAh g^{-1} at 0.5 A g^{-1} after 50 cycles	[112]
SnO_2/ $Ti_3C_2T_x$	SnO_2 particles on the MXene layer	354 mAh g^{-1} at 0.1 A g^{-1}	347 mAh g^{-1} at 0.3 A g^{-1} after 300 cycles	[118]
Ti_3CNT_x	Powder consisting of fluffy flakes	343 mAh g^{-1} at 0.05 A g^{-1}	300 mAh g^{-1} at 0.5 A g^{-1} after 1000 cycles	[119]
MoS_2@ $Ti_3C_2T_x$	MoS_2 nanoparticles grown on the MXene	843 mAh g^{-1} at 0.05 A g^{-1}	132 mAh g^{-1} at 1 A g^{-1} after 200 cycles	[116]
MoS_2/$Ti_3C_2T_x$-MXene@C	MoS_2 nanoplates on MXene@C	1210 mAh g^{-1} at 0.2 A g^{-1}	551 mAh g^{-1} at 20 A g^{-1} after 3000 cycles	[120]
MoS_2/$Mo_2TiC_2T_x$	Porous open structure	554 mAh g^{-1} at 0.1 A g^{-1}	509 mAh g^{-1} at 0.1 A g^{-1} after 100 cycles	[114]
MoS_2/partially oxidized $Ti_3C_2T_x$	MoS_2 nanosheets grown on MXene	490 mAh g^{-1} at 0.1 A g^{-1}	230 mAh g^{-1} at 0.5 A g^{-1} after 50 cycles	[115]

2.3.2 Lithium-sulfur batteries

2.3.2.1 MXene-based materials as sulfur hosts for lithium-sulfur batteries

Lithium-sulfur batteries are a promising system to satisfy the rising demand for energy storage due to their high energy density of ~2567 Wh kg^{-1}. However, several challenges still need to be overcome before their practical application. For example, during the charge-discharge process, conversion between sulfur and Li_2S_{2-x} ($x \leqslant 1$) involves a series of soluble intermediates known as polysulfides (LiPSs), which tend to shuttle between the cathode and anode and result in low Coulombic efficiency and severe capacity fading. Hence, preventing the "shuttle effect" and maintaining a high sulfur loading are the main issues for practical applications. Cathode matrices with strong sulfur/polysulfide adsorption have been widely investigated to address these issues. Because of their inherently excellent electrical conductivity and surface functional groups, 2D MXenes can also be applied as sulfur hosts in lithium-sulfur batteries.[121]

In 2015, Liang *et al.* reported, for the first time, that Ti_2CT_x MXene is a highly effective matrix for lithium-sulfur batteries. As shown in Figure 2.10a, the hydroxy surface groups can be replaced by sulfur and/or sulfide species to form a strong Ti-S interaction, effectively suppressing the polysulfide "shuttle effect". Figure 2.10b and c reveals the mechanism of sulfur binding via chemical adsorption by X-ray photoelectron spectroscopy (XPS) analysis. Delaminated Ti_2CT_x MXene-S composites exhibit a stable cycling performance (723 mAh g^{-1} after 650 cycles at C/2). Furthermore, even at 1 C, a high capacity of 1000 mAh g^{-1} can be achieved, indicating excellent rate capability. In fact, the as-obtained Ti_2CT_x MXene nanosheets have neither a high specific surface area nor a well-ordered porous architecture. However, owing to the existence of S-Ti-C bonding, Ti_2CT_x/S cathodes clearly show great performance, suggesting that the "shuttle effect" can be efficiently suppressed.[89]

Restacking MXene nanosheets limit the accessibility of active ions and impede the utilization of MXene surfaces. To address this challenge, Bao *et al.* reported a MOF-derived mesoporous carbon/$Ti_3C_2T_x$ composite as a cathode host that demonstrates enhanced electrochemical performance for lithium-sulfur batteries.[122] The hydrophilic surface groups of delaminated-$Ti_3C_2T_x$ MXene nanosheets can efficiently trap polysulfides, and the mesoporous carbon matrix can slow the diffusion of polysulfides during the charge-discharge process. Theoretical calculations were carried out for $Ti_3C_2T_x$ MXene to investigate the adsorption energies of polysulfides. DFT calculations clearly show that there is specific bonding between lithium polysulfides (*e.g.*, Li_2S and Li_2S_4) and the $Ti_3C_2F_2$ monolayer with adsorption energies of -0.29 and -0.38 eV, respectively, indicating the strong ionic attraction between Ti and S cations. Based on this mechanism of trapping polysulfides, $Ti_3C_2T_x$/reduced graphene oxide (RGO)-S hybrid materials were also investigated as high-performance cathodes for lithium-sulfur batteries.[123]

In 2017, Linda Nazar's group reported that hydroxyl groups on the surface of Ti_3C_2 and Ti_3CN MXene tend to be consumed by the polysulfides before the formation of Ti-S bonds through a Lewis acid-based interaction (shown in Figure 2.10d). Figure 2.10e shows the adsorption configurations of Li_2S_4 on the surface of $Ti_3C_2(OH)_2$, $Ti_3C_2(OH)_2$ (show one hydroxyl vacancy), and fully exposed Ti_3C_2, respectively. The binding energies of polysulfides increase as the number of hydroxyl groups on the surface of MXene decreases. The fully exposed Ti_3C_2 MXene shows the highest binding energy, which means that the polysulfides rather than the hydroxyl groups serve as the terminations in the MXene nanosheets. This dual-mode behavior (Lewis acid-base interaction and thiosulfate/polythionate conversion) further confirms the mechanism of trapping polysulfides and endows MXene-based hosts with excellent cycling performance for lithium-sulfur batteries. Since MXenes have superior adsorption capability, which prevents the shuttle effect of polysulfides, sandwich-like MXene/CNT-S nanocomposites exhibit a high capacity of ~1260 mAh g^{-1} and only a 0.043% capacity fading rate per cycle for up to 1200 cycles. Such outstanding performance can be attributed to the improved conductivity across the nanosheet basal planes and the pillar effect between the MXene layers and CNTs.[124] Furthermore, Ti_2C MXene with -F and -O terminations as sulfur hosts for lithium-sulfur batteries were studied by DFT calculations. Both Ti_2CF_x and Ti_2CO_x were found to suppress the shuttle effect of polysulfides. However, MXene with -F terminations traps polysulfides through a strong interaction, while MXene with -O terminations suppresses shuttle effects by converting the soluble polysulfide species to insoluble sulfur.[125-127] In addition, the redox reaction of polysulfides occurs on the surface of MXene due to the metallic conductivity of MXene after absorbing polysulfides.[125]

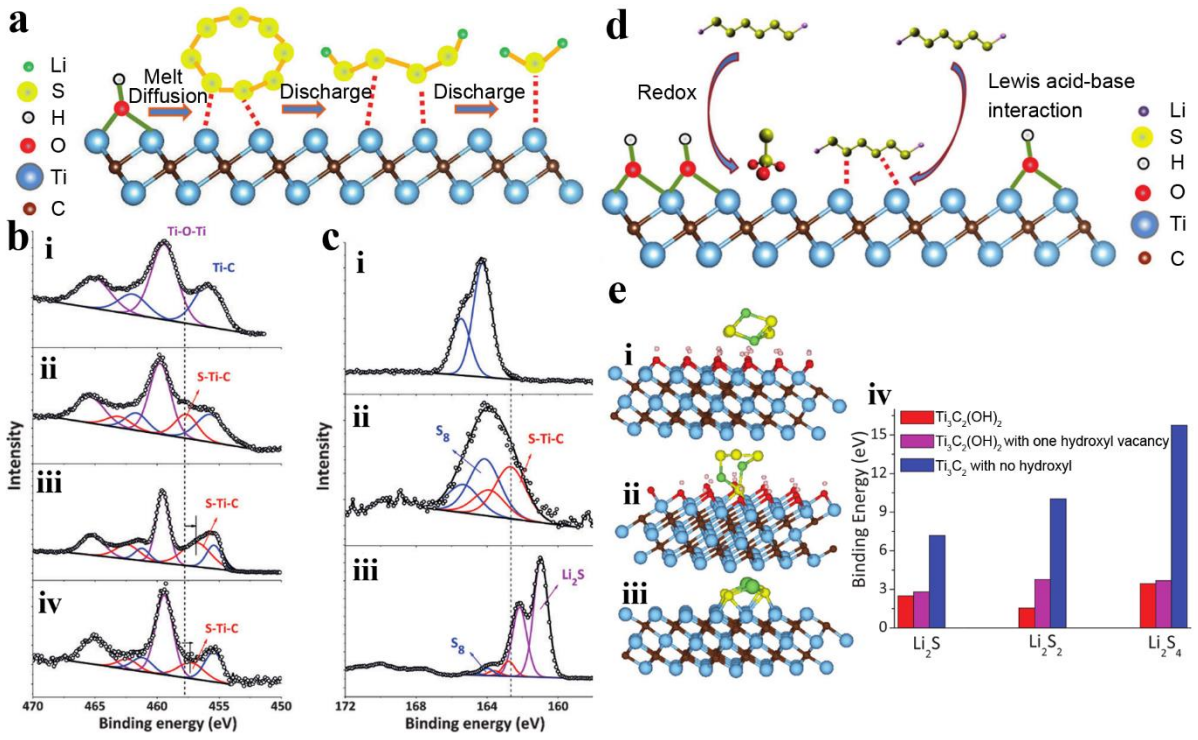

Figure 2.10. a*) Schematic illustration for the replacement mechanism of the Ti-OH bond by a S-Ti-C bond via heat treatment or direct contact with polysulfides. XPS analysis of the Ti_2C sheets and S/Ti_2C composite.* ***b****) Ti 2p spectra of the i) Ti_2C sheets and ii) 70S/Ti_2C composite, iii) Li_2S_4-Ti_2C and iv) 70S/Ti_2C electrode discharged to 1.8 V at C/20.* ***c****) S 2p spectra of i) elemental sulfur, ii) 70S/Ti_2C composite, and iii) 70S/Ti_2C electrode discharged to 1.8 V at C/20.*[89] *Reproduced with permission. Copyright 2015, WILEY-VCH.* ***d****) Schematic illustration for the two-step interaction between polysulfides and MXene with -OH terminations.* ***e****) Theoretical calculations for the interaction between polysulfide Li_2S_4 and Ti_3C_2 MXene: i) $Ti_3C_2(OH)_2$, ii) $Ti_3C_2(OH)_2$ with one hydroxyl vacancy, and iii) fully exposed Ti_3C_2, along with iv) the differences in the binding energies of polysulfide molecules (e.g., Li_2S, Li_2S_2, and Li_2S_4) to the different matrices.*[124] *Reproduced with permission. Copyright 2017, WILEY-VCH.*

Notably, nitrogen doping in carbonaceous materials can enhance the electrochemical performance of lithium-sulfur batteries.[128] Inspired by previous studies, nitrogen-doped $Ti_3C_2T_x$ MXene (N-$Ti_3C_2T_x$) nanosheets were prepared by a novel one-step approach (**Figure 2.11**a). Figure 2.11b demonstrates the morphologies of crumpled N-$Ti_3C_2T_x$ nanosheets and N-$Ti_3C_2T_x$/S composites, which clearly confirms the successful loading of sulfur onto crumpled N-$Ti_3C_2T_x$ nanosheets. Ultraviolet/visible (UV-vis) adsorption spectra were obtained to confirm the strong adsorption of representative polysulfides (Li_2S_6) on N-$Ti_3C_2T_x$ as shown in Figure 2.11c. In particular, a high sulfur mass loading of 5.1 mg cm^{-2} was achieved by N-$Ti_3C_2T_x$ nanosheets. The

existence of heteroatomic nitrogen can efficiently improve the capability for dual physical and chemical adsorption of polysulfides. Furthermore, since the unique porous architecture with physical confinement can suppress the shuttle effect and dissolution of polysulfides, N-$Ti_3C_2T_x$/S cathodes show a high reversible capacity of 1144 mAh g^{-1} at a current density of 0.2 C and a superior cycling performance (610 mAh g^{-1} at 2 C after 1000 cycles).[129]

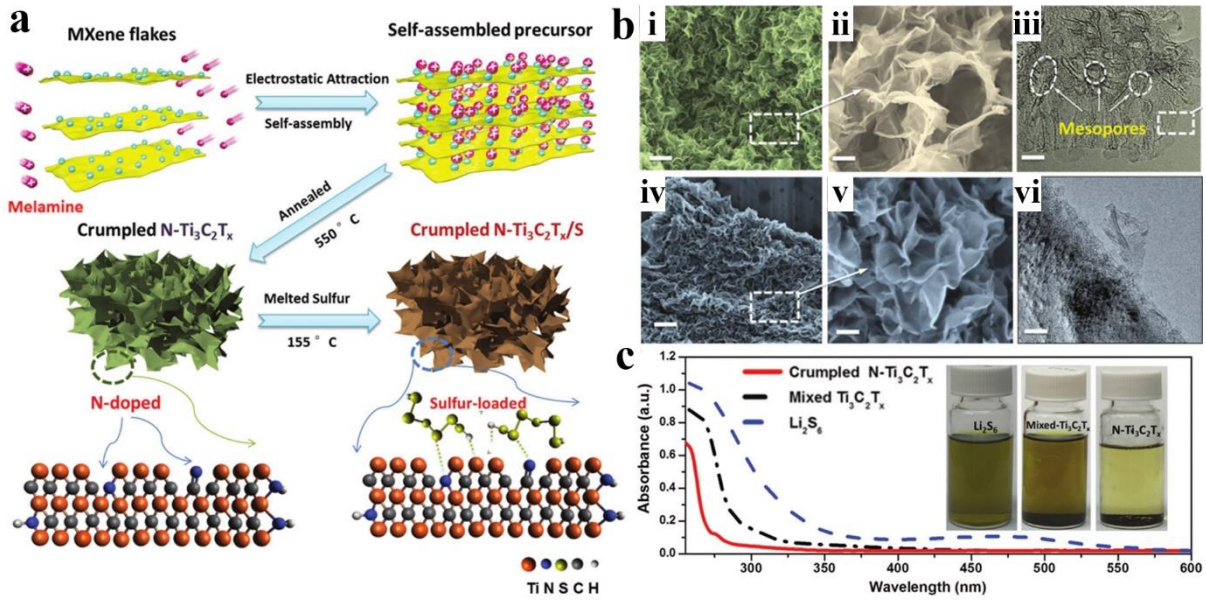

Figure 2.11. a) *Schematic illustration for the synthesis procedure of crumpled N-$Ti_3C_2T_x$/S composites.* ***b)*** *Morphologies of crumpled N-$Ti_3C_2T_x$ nanosheets and crumpled N-$Ti_3C_2T_x$ /S composites: i, ii) FE-SEM image of crumpled N-$Ti_3C_2T_x$ nanosheets. iii) HRTEM image of crumpled N-$Ti_3C_2T_x$ nanosheets. iv, v) FE-SEM image of crumpled N-$Ti_3C_2T_x$ /S composites. vi) HRTEM image of crumpled N-$Ti_3C_2T_x$/S composites. Scale bars: 2 μm (i, iv), 200 nm (ii, v) and 100 nm (iii, vi).* ***c)*** *Ultraviolet/visible adsorption spectra and digital images (inset) of a Li_2S_6 solution before and after adding crumpled N-$Ti_3C_2T_x$ and mixed-$Ti_3C_2T_x$.[129] Reproduced with permission. Copyright 2018, WILEY-VCH.*

2.3.2.2 Separators modified by MXenes for lithium-sulfur batteries

Due to the dissolution of polysulfides and the shuttle effect, the short cycle life of lithium-sulfur batteries hinders their practical application. Recently, tremendous efforts have been made to modify separators to prevent the migration of polysulfides between the cathode and anode.[130] Introducing a functional interlayer between the separator and sulfur cathode or coating a layer on

the cathode side of the separator can effectively suppress the shuttle effect, leading to good cycling performance. Hence, Song *et al.* reported a method to trap polysulfides by coating $Ti_3C_2T_x$ MXene nanosheets on commercial Celgard™ membranes.[131] As shown in Figure 2.12a, the porous polypropylene (PP) separator is beneficial for the rapid transport of ions in conventional cells but allows soluble polysulfides to shuttle to the anode and react with lithium foil, leading to the loss of active materials and capacity fading. In contrast, MXene-modified polypropylene (MPP) separators effectively restrict the migration of soluble polysulfides by dual physical and chemical adsorption. In addition, $Ti_3C_2T_x$ MXene nanosheets, which show excellent conductivity, greatly decrease the internal resistance of the cells. Thus, MPP separators remarkably improve the electrochemical performance of lithium-sulfur batteries (Figure 2.12b). [131] Similar results were also obtained on $Ti_3C_2T_x$ MXene modified glass fiber separators. Moreover, theoretical calculations were performed to calculate the binding energies between $Ti_3C_2T_x$ MXene and polysulfides (Figure 2.12c and d). Based on the calculations, fully exposed MXene shows strong interactions with polysulfides, indicating that the polysulfides can be effectively trapped as individual molecules. This result was also verified by the diffusion experiments of polysulfides shown in Figure 2.12e and f.[132] Moreover, the MXene materials can also trap the iodide species.[133] According to theoretical calculations and experimental investigations, MXene not only shows strong chemical binding with iodine species, but also boosts the redox reactions. Therefore, a porous $Ti_3C_2T_x$ MXene foam was employed as a cathode-electrolyte interface layer in lithium-iodine batteries, which enables superior rate performance and cycling stability.

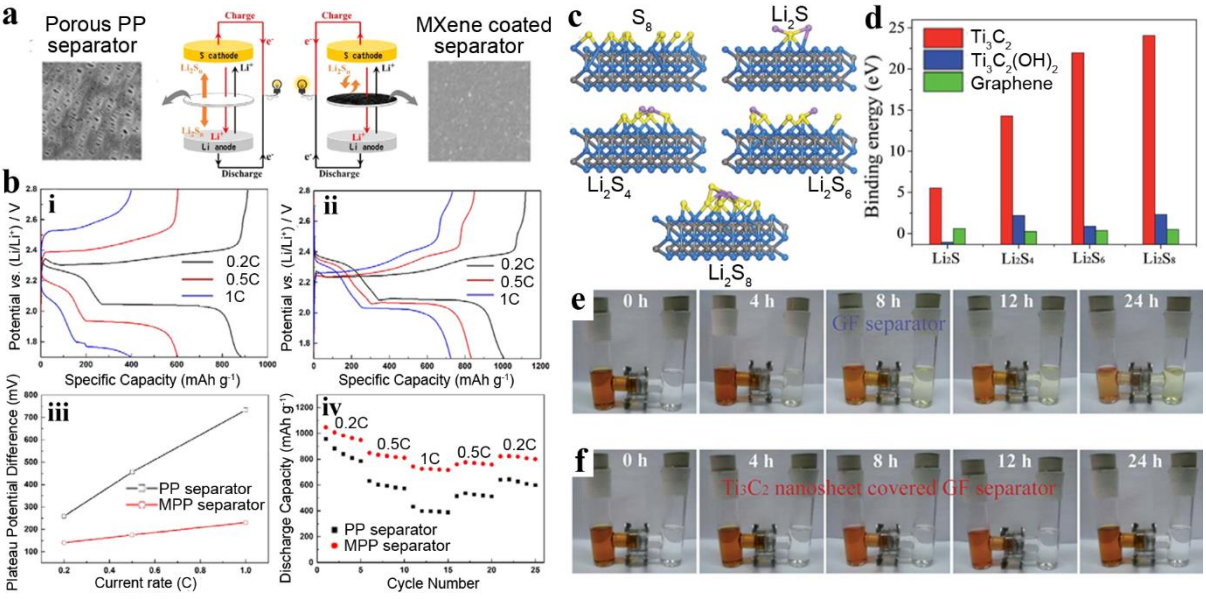

Figure 2.12. a) *Schematic illustration of the configurations of lithium-sulfur batteries using a porous PP separator and an MXene-coated PP separator.* ***b)*** *Electrochemical characterizations of two lithium-sulfur batteries with PP and MPP separators: The initial voltage profiles of cells with i) a PP separator and ii) an MPP separator at 0.2, 0.5, and 1 C. iii) Comparative analysis of the potential difference of two cells between the charge and discharge plateaus at 0.2, 0.5, and 1 C. iv) Rate performances of above two cells.*[131] *Reproduced with permission. Copyright 2016, American Chemical Society.* ***c)*** *Configurations of S_8, Li_2S, Li_2S_4, Li_2S_6 and Li_2S_8 on Ti_3C_2 MXene.* ***d)*** *Binding energies of Li_2S, Li_2S_4, Li_2S_6 and Li_2S_8 on graphene, $Ti_3C_2(OH)_2$ MXene, and Ti_3C_2 MXene. Digital images of the diffusion of polysulfides: H-type cells with* ***e)*** *a glass fiber separator and* ***f)*** *a Ti_3C_2 MXene-covered glass fiber composite separator.*[132] *Reproduced with permission. Copyright 2016, The Royal Society of Chemistry.*

2.3.3 Lithium metal anode

Owing to the high theoretical capacity of 3860 mAh g^{-1} and low electrochemical potential of ~ -3.04 V versus the standard hydrogen electrode (SHE), metallic lithium is considered as the most promising anode material for rechargeable lithium-based batteries, including lithium-ion, lithium-sulfur, and lithium-oxygen batteries. Nevertheless, large volume changes and uncontrollable growth of lithium dendrites, which may lead to short life spans and serious safety hazards, need to be circumvented to promote their practical applications.

Several strategies have been adopted to optimize lithium metal anodes. These include i) pre-forming rigid solid electrolyte interface films on the surface of the lithium anode, ii) utilization of

separators with high strength to prevent being pierced by lithium dendrites, and iii) depositing lithium metal into matrices to mitigate the volumetric change of the lithium anode and suppress the growth of lithium dendrites. Significantly, the third strategy has proven to be the most effective method to prevent the vertical growth of lithium dendrites. Ti_3C_2 MXene was selected to act as a host to fabricate lamellar structured Ti_3C_2 MXene-Li films by a roll-to-roll mechanical method.[134] As shown in the synthesis procedure (Figure 2.13a), the Ti_3C_2 MXene nanosheets were rolled with lithium metal to fabricate an elongated film, which was then folded to increase the number of layers. The as-obtained Ti_3C_2 MXene-Li hybrid film possesses good flexibility and mechanical strength. Figure 2.13b and c shows the top view and cross-sectional views of the hybrid film, indicating that lithium metal is evenly distributed between the MXene layers. The multilayered Ti_3C_2 MXene-Li hybrid film electrode shows flat voltage profiles, a reduced overpotential (32 mV at 1.0 mA cm^{-2}) and superior cycling performance (Figure 2.13d). Furthermore, a lithium-sulfur battery based on a Ti_3C_2 MXene-Li film anode and a sulfur-carbon cathode delivers a reversible capacity of 948 mAh g^{-1}. Even after 100 cycles, a capacity of 841 mAh g^{-1} is retained. A high energy density of ~ 656 Wh kg^{-1} can also be achieved in Ti_3C_2-Li-S batteries. *In situ* TEM analysis (Figure 2.13e and f) reveals that the superior electrochemical performance can be attributed to the existence of nucleation sites on MXene nanosheets, which facilitate the deposition of lithium metal into the gaps of the MXene layers.[134] As discussed above, MXenes indeed improve the electrochemical performance of lithium-sulfur batteries, as summarized in Table 2.3.

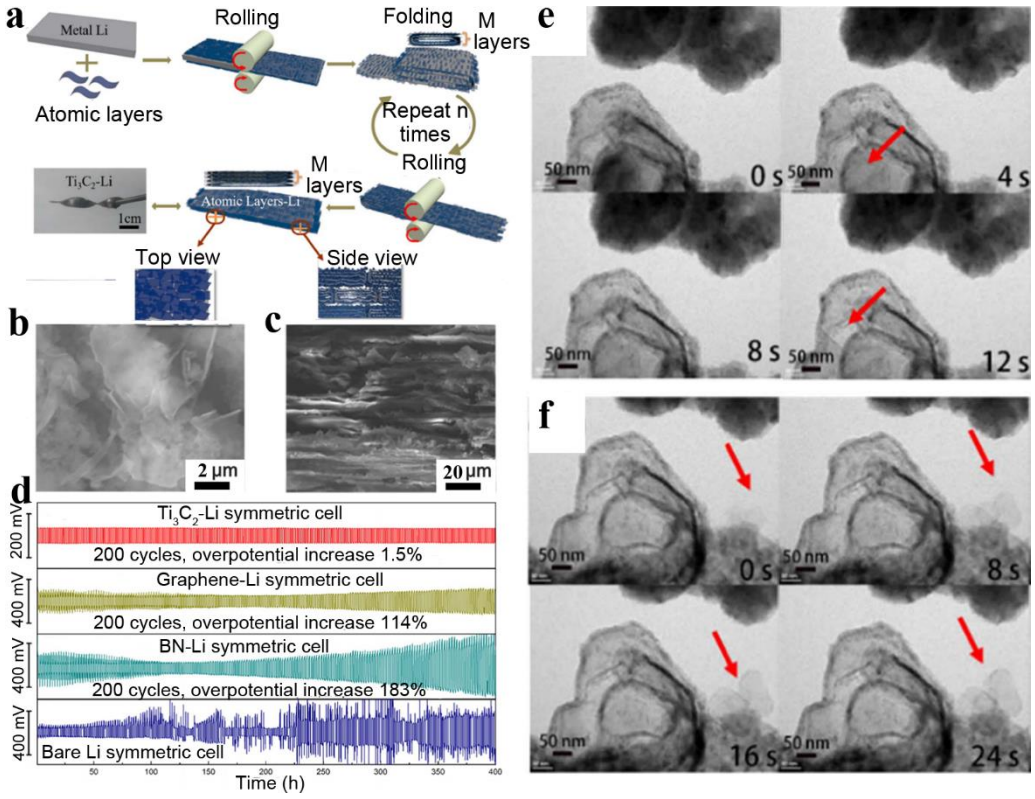

Figure 2.13. *Fabrication of flexible lamellar-structured Ti_3C_2 MXene-Li films.* ***a)*** *Schematic illustration for the preparation procedures of Ti_3C_2 MXene-Li films.* ***b)*** *Top and* ***c)*** *cross-sectional SEM images of a Ti_3C_2 MXene-Li hybrid film with a layered structure.* ***d)*** *Cycle performances of symmetric cells of Ti_3C_2-Li, Graphene-Li, BN-Li and bare Li at a constant current density of 1.0 mA cm^{-2}.* ***e)*** *In situ TEM images of growing lithium into the Ti_3C_2 MXene-Li films.* ***f)*** *In situ TEM images of growing lithium dendrites outside of the Ti_3C_2 MXene-Li films.*[134] *Reproduced with permission. Copyright 2017, Elsevier.*

Table 2.3. *Summary of electrochemical performances of MXene and MXene-based composites in lithium-sulfur batteries.*

Materials	Application	S content	Initial reversible capacity	Cycle life	Capacity decay rate	Ref.
Ti_2CT_x	Cathode host	70 wt%	1200 mAh g^{-1} at C/5	650 cycles at C/2	0.05 % per cycle	89
$Ti_3C_2T_x$@ Meso-C	Cathode host	73 wt%	1225 mAh g^{-1} at C/2	300 cycles at C/2	0.14 % per cycle	122
$Ti_3C_2T_x$	Interlayer on separator	100 wt%	1225 mAh g^{-1} at 0.5 A g^{-1}	100 cycles at 0.5 A g^{-1}	0.12 % per cycle	132

$Ti_3C_2T_x$	Interlayer on separator	68 wt%	1047 mAh g^{-1} at C/5	500 cycles at 1C	0.062 % per cycle	131
$Ti_3C_2T_x$/ RGO	Cathode host	70 wt%	1144 mAh g^{-1} at C/2	300 cycles at C/2	0.077 % per cycle	123
MXene/ CNT	Cathode host	83 wt%	1263 mAh g^{-1} at C/20	1200 cycles at C/2	0.043 % per cycle	92
N-doped $Ti_3C_2T_x$	Cathode host	74 wt%	1144 mAh g^{-1} at C/5	1000 cycles at 2C	0.026 % per cycle	96
$Ti_3C_2T_x$ nanoribbon	Cathode host and interlayer	68 wt%	1062 mAh g^{-1} at C/5	200 cycles at C/2	0.24 % per cycle	101
$Ti_3C_2T_x$/ MoS_2-C	Cathode host	79.6 wt%	1195 mAh g^{-1} at C/10	300 cycles at C/2	0.07 % per cycle	102

2. 4 Application of MXenes for potassium-based batteries

Recently, lithium-ion batteries have achieved tremendous successes in commercial applications. However, the development of lithium-based batteries is hampered by limited and unevenly distributed lithium resources in the earth's crust.[2] Potassium (K)-based batteries are considered as high-performance and low-cost alternatives to lithium-based batteries due to abundant potassium resources.[3] Furthermore, Potassium-based batteries also possess high operating voltage and energy density (low redox potential of K/K^+ couple), as well as fast diffusion kinetics (higher transference number and ionic conductivity).[5] However, the research on potassium-based batteries is still in infant state, and several challenges should be solved before the practical applications. Compared with lithium ion, potassium ion has larger radius, which impedes the fast and reversible K ion insertion/extraction during the cycling, leading to inferior capacity and poor cycling performance. In order to improve the electrochemical performance of the potassium-based batteries, it is highly

necessary to develop new-generation of electrode materials with high capacity and good conductivity.

Due to the metallic conductivity, large interlayer space, and unique open morphologies, MXene might be an ideal candidate for potassium storage. In 2013, Lukatskaya et. al., for the first time, found that the non-lithium-ion (including K ions) can intercalate into the terminated MXene materials in aqueous electrolytes, which provides insight into K ion storage mechanisms in 2D MXene.[28] This work opens the possibility to use MXene materials as electrode for potassium-based batteries. Subsequently, several researches on MXene and MXene-based materials as electrodes for potassium storage have been published. In this part, we review the latest progress of MXenes and MXene-based materials for potassium-based batteries.

In 2014, Er et. al. investigated the adsorption of four ions (Li, Na, K, and Ca) on Ti_3C_2 MXene by using first-principles density functional calculations, and they also found that the calculated capacity for K ions on MXene is about 191 mAh g^{-1}.[91] Later in this year, another group of researchers verified the intercalation of K-ion into terminated MXenes in organic electrolyte by experimental measurements.[35] Although the potassium shows the relatively smaller adsorption energy compared with those of Li and Na, the Ti_2CO_2 still shows a high capacity of 264 mAh g^{-1} for potassium storage. This high capacity obviously endows the MXene materials as a promising electrode for potassium storage. Additionally, the potassium-intercalated MXene presents enhanced capability for Li and Na storage, which results from the enlarged MXene interlayer due to the potassium "pillar".[135] Besides the titanium carbides, titanium carbonitride, niobium carbide, and vanadium carbide were also used as anode materials for potassium-ion batteries. The as-prepared Ti_3CN MXene can deliver a stable capacity of 90 mAh g^{-1} at the current density of 10 mA g^{-1}, while the capacity of Nb_2C MXene drops very fast during the cycling.[136] Interestingly, the

V_2C MXene obtained by dual acid/alkali treatment is able to deliver a good performance, showing a capacity of 152 mAh g^{-1} at a current density of 100 mA g^{-1}.[137]

Morphology modification is a useful method to improve the electrochemical performance of the MXene materials for potassium-ion storage. For example, by preparing the MXene in aqueous KOH solution, the as-obtained alkalized Ti_3C_2 presents a nanoribbon morphology. This interconnected 3D framework not only enhances the surface area and active sites, leading to a superior reaction kinetics, but also provide electron pathway, which effectively improves the electronic conductivity. Thus, when employed as anode materials, the nanoribbon MXene displayed a reversible capacity of 136 mAh g^{-1} at the current density of 20 mA g^{-1} in potassium-ion batteries.[138] Doping strategy can also be used on MXene materials for potassium-ion storage. Zhu et. al. demonstrates the feasibility of the replacement of –O and –OH terminations by Si and P elements. By theoretical calculations, the modified MXene can present a surprising potassium capacity of 711 mAh g^{-1}.[139]

As MXene materials possess high electronic conductivity, fabrication of MXene-based materials as electrode for potassium-ion batteries is also proposed by a group of researchers. It is well known that the K ion can intercalate into the carbon materials. However, considering the large radius of K ion, the structure stability and reaction kinetics are obstacles that hinder the practical application of carbon materials for potassium-ion batteries. MXene can be employed to combine with carbon materials to form high-performance electrode due to their unique properties. The MXene/carbon hybrid not only possesses large surface area, but also present stable cycling performance due to the suppressed volume change resulted from the intimate contact between MXene and carbon materials.[140, 141] Furthermore, the as-obtained 3D free-standing electrode can eliminate the current collector, thus leading to a higher energy density of the batteries.[141] Other materials, such as MoS_2,

$MoSe_2$, and metal Sb are also used to decorate the MXene materials.[142-144] For example, $MoSe_2$/MXene@C composite have been developed as an anode material for potassium-ion batteries. Due to the synergistically optimization effect, the as-developed anode shows 355 mAh g^{-1} at the current density of 200 mA g^{-1} after 100 cycles. [143] As discussed above, although some progress has been achieved, the development of MXene on potassium-ion batteries is still in its infant state. The electrochemical performances of potassium-based batteries with MXene (or MXene composite) electrodes are summarized in Table 2.4.

Table 2.4. *Summary of electrochemical performances of MXene and MXene-based composites for potassium-based batteries.*

Materials	Architecture	Reversible Capacity	Rate and Cycling capability	Ref.
Ti_3C_2	Exfoliated graphite-like morphology	146 mAh g^{-1}	/	35
Ti_3CN	Accordion-like layer structure	90 mAh g^{-1} at 10 mA g^{-1}	75 mAh g^{-1} at 20 mA g^{-1} after 100 cycles	136
Nb_2C	Accordion-like layer structure	80 mAh g^{-1} at 10 mA g^{-1}	30 mAh g^{-1} at 20 mA g^{-1} after 50 cycles	136
V_2C	Accordion-like layer structure	152 mAh g^{-1} at 100 mA g^{-1}	~125 mAh g^{-1} at 100 mA g^{-1} after 150 cycles	137
Ti_3C_2 ribbons	Nanoribbons	136 mAh g^{-1} at 20 mA g^{-1}	42 mAh g^{-1} at 200 mA g^{-1} after 500 cycles	138
Ti_3C_2/NPCNs	network structure	583.6 mAh g^{-1} at 100 mA g^{-1}	252 mAh g^{-1} at 1 A g^{-1} after 2000 cycles	140
MXene-bonded HC film	Composite paper	270 mAh g^{-1} at at 30 mA g^{-1}	210 mAh g^{-1} at 50 mA g^{-1} after 100 cycles	141
MoS_2/MXene	Accordion-like structure	290 mAh g^{-1} at at 50 mA g^{-1}	206 mAh g^{-1} at 50 mA g^{-1} after 100 cycles	142
$MoSe_2$/MXene@C	Composite nanosheets	183 mAh g^{-1} at at 10 A g^{-1}	355 mAh g^{-1} at 200 mA g^{-1} after 100 cycles	143

MXene/Sb	Composite paper	503 mAh g^{-1} at at 50 mA g^{-1}	472 mAh g^{-1} at 50 mA g^{-1} after 100 cycles	[144]

Chapter 3 Experimental

3.1 Overview

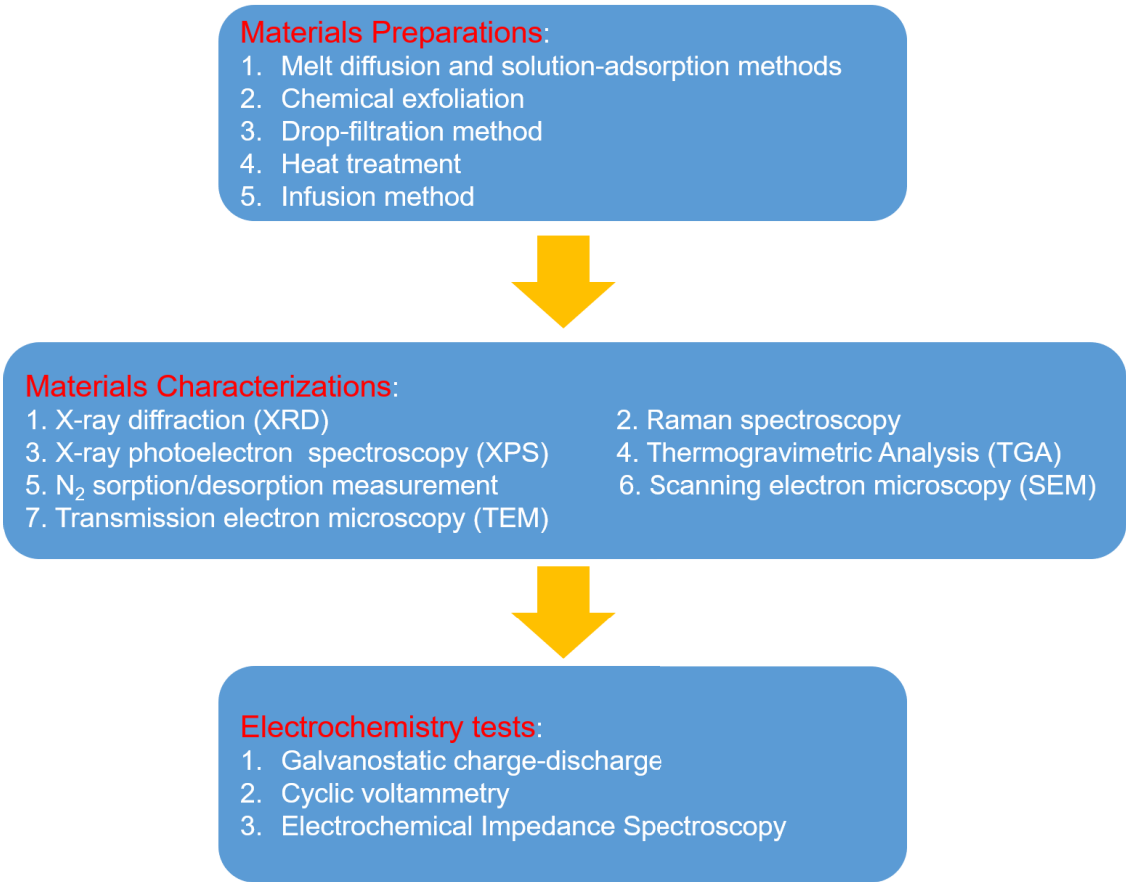

Figure 3.1. *The diagram that demonstrates the procedures of the experiments.*

Figure 3.1 summarizes the materials preparation, materials characterization, and electrochemical test methods utilized in this thesis. Generally, the materials in this thesis are usually prepared by melt diffusion method, solution-adsorption method, chemical exfoliation, drop-filtration method, heat treatment, infusion method. Additionally, all the chemicals related to this work are listed in Table 3.1.

Table 3.1. *Chemicals details in the research project.*

Chemicals	Formula	Purity	Supplier
Carbon additive (carbon black)	C	100 %	Sigma-Aldrich
Poly(vinylidene difluoride) (PVdF)	$(CH_2CF_2)_n$	-	Sigma-Aldrich
Sulfur	S		Sigma-Aldrich
Ethanol	CH_3CH_2OH	95 %	Chem Supply
Ethylene carbonate (EC)	$(CH_2)_2CO_3$	99 %	Sigma-Aldrich
Graphite (natural flakes)	C	75 %	Sigma-Aldrich
Hydrochloric Acid	HCl	37 %	Fisher Scientific
hexadecyltrimethyl ammonium bromide	$CH_3(CH_2)_{15}N(Br)(CH_3)_3$	99 %	Sigma-Aldrich
$KHCO_3$	$KHCO_3$	99%	Sigma-Aldrich
N-methyl pyrrolidinone (NMP, anhydrous)	C_5H_9NO	99.5 %	Sigma-Aldrich
iodine	I	99 %	Sigma-Aldrich
Carbon cloth	C	-	Sigma-Aldrich
Lithium foil	Li	99.999 %	Hohsen Corporation Japan
diethyl carbonate (DEC)	$C_5H_{10}O_3$	100 %	Sigma-Aldrich
Glass fiber	-	-	whatman
Polypropylene separator	$(C_3H_6)_n$	100 %	Celgard
Sodium nitrate	$NaNO_3$	99 %	Sigma-Aldrich
Lithium Fluorine	LiF	98 %	Alfa Aesar
Dimethoxymethane (DME)	$CH_2(OCH_3)_2$	99%	Sigma-Aldrich
Bis(trifluoromethane)sulfonimide lithium salt (LiTFSI)	$CF_3SO_2NLiSO_2CF_3$	99%	Sigma-Aldrich
Lithium trifluoromethanesulfonate (LiOTf)	CF_3SO_3Li	99%	Sigma-Aldrich

Carbon nanotube (CNT)	C	-	Shenzhen Nanotech Port Co. Ltd.
Potassium	K	99%	Sigma-Aldrich
Polytetrafluoroethylene (PTFE)	$(C_2F_4)_n$	60 % solution	Sigma-Aldrich

Before testing the electrochemical performance of the as-prepared materials, various characterizations (including X-ray diffraction (XRD), X-ray photoelectron spectroscopy, Raman spectroscopy, thermogravimetric analysis (TGA), N_2 sorption/desorption measurements, scanning electron microscopy (SEM), and transmission electron microscopy (TEM), *etc.*) should be conducted to study the physical, structure, and morphology properties of the as-prepared materials.

Finally, electrochemical tests, such as galvanostatic charge-discharge, cyclic voltammetry, and electrochemical impedance spectroscopy, have been performed to study the electrochemical performance of the as-assembled MXene-based energy storage devices. Furthermore, *In situ* (*ex situ*) XRD, *in situ* microscopy, and *ex situ* SEM were also adopted to study the underlying mechanisms existed in the as-developed energy system.

3.2 Materials preparation

3.2.1 Melt diffusion and solution-adsorption methods

In this thesis, the sulfur containing materials and iodine containing materials can be prepared by melt diffusion method and solution-adsorption method, respectively. As sulfur possess relatively low melting point at ~155ºC, the melt diffusion method is one of the favourable strategy to develop sulfur composite electrode materials. Generally, the sulfur powder (99.99%, Sigma-Aldrich) and

the as-obtained host materials were homogenously mixed with a certain mass ratio. Then, the sulfur-containing materials can be obtained by heating the mixture at 155 ºC, in which sulfur was incorporated into the matrix by melt diffusion. The solution-adsorption method is a simple method to prepare the iodine containing materials. As iodine is slight soluble in the water and host materials shows a strong adsorption ability towards iodine, the iodine in the water can be slowly adsorbed on the host materials, and the solid iodine tend to dissolve to retain the iodine concentration in the water. In chapter 4, a piece of commercial carbon cloth was cleaned by diluted hydrochloride acid and distilled water, and then put into distilled water with a certain amount of iodine powder, followed by continuously stirring until the solution turns clear. Finally, the iodine containing materials can be obtained by drying at 80 ºC in vacuum oven for 12 hours.

3.2.2 Chemical exfoliation

Two-dimensional materials have been becoming a very promising materials in the field of energy storage and energy transformation due to their unique properties including good electronic conductivity, large surface area, and flexibility. However, direct synthesis of two-dimensional nanosheets or nanoflakes is relatively difficult and expensive. Therefore, chemical exfoliation technique is usually preferred to exfoliate the bulk materials with layered structure to two-dimensional nanosheets or nanoflakes. In this doctoral work, the chemical exfoliation was used to etch the Al layers in the MAX phase to obtain the MXene sheets for the energy storage devices.

3.2.3 Drop-filtration method

In this study, drop-filtration method is used to prepare the MXene-wrapped electrode materials and free-standing MXene papers. Briefly, the as-obtained homogeneous dispersion is dropwise

added onto the electrode materials under vacuum filtration. This step could be repeated for several times until the desired mass loading is obtained.

3.2.4 Heat treatment

Heat treatment techniques used in industrial production mainly include annealing, hardening and softening, tempering, carburizing, normalizing, and quenching, *etc.* Generally, the mixed reactants are put in tube oven and heated to a needed temperature under inert atmosphere (or hydrogen). The heating programs are set up depending on the certain conditions. In this thesis, the heat treatment techniques were used to prepare sulfur-poly(acrylonitrile) (SPAN) and carbon materials.

3.2.5 Infusion method

Alkali metal anode usually possess relatively lower melting points (180 ºC for Li, 97 ºC for Na, and 63 ºC for K) compared with other metals. Therefore, Li, Na, and K metal can be easily melted into liquid-state, and then adsorbed by the as-prepared host materials. After that, the liquid-state metal will be cool down quickly and remain in the host materials to form a metal anode. By applying infusion method in chapter 5, metallic K anode can be prepared within a short time.

3.3 Materials characterization

3.3.1 X-ray Diffraction (XRD)

In this thesis, the X-ray Diffraction (XRD) was conducted to investigate the phase and crystallographic structure of the as-synthesized materials. The interaction of the incident X-rays with the sample produces constructive interference (and diffracted rays) when conditions satisfy Bragg's Law:

$$2d \sin \theta = n\lambda$$

where d is the interplanar spacing, θ is the glancing angle, n is the positive integer and λ is the wavelength of the incident X-ray. By comparing the obtained XRD patterns with the standard diffraction lines in the Joint Committee on Powder Diffraction Standards (JCPDS) database, the crystal phase can be identified.

3.3.2 Raman Spectroscopy

Raman Spectroscopy is one of the most important chemical analysis techniques. Raman spectroscopy is based upon the interaction between the light and the chemical bonds within a material. The chemical bonds and symmetry present specific vibrational information in Raman spectroscopy which can help to investigate the chemical structure, phase, crystallinity and molecular interactions of the as-prepared materials. In this doctoral study, this technique was employed not only to identify the chemical bonds that verifies the composite of the materials, but also to detect defect information of carbon materials.

3.3.3 *In situ* microscope

In the field of the metal anode, *in situ* microscope is a common technique to probe the surface morphology of the electrode during the cycling of battery systems. The schematic illustration of the *in situ* cell is presented in **Figure 2.2**. In this thesis, *in situ* microscope was applied to study the growth of the potassium metal dendrites during the plating process (Chapter 5).

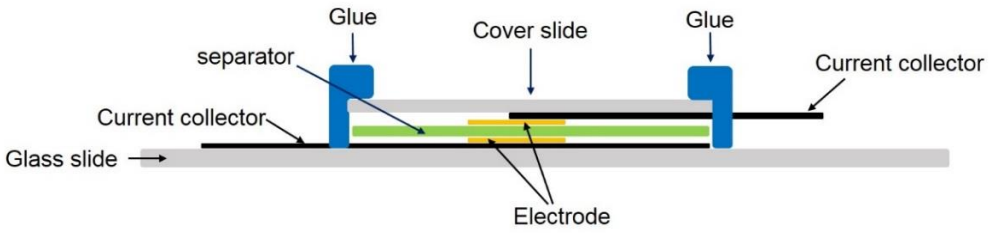

Figure 3.2. *the schematic illustration of as-assembled cell for in situ microscope.*

3.3.4 X-ray photoelectron spectroscopy (XPS)

X-ray photoelectron spectroscopy (XPS) is a surface-sensitive quantitative spectroscopic technique that measures the electronic/chemical state, and elemental composition. XPS spectra are obtained by irradiating a material with a beam of X-rays while simultaneously measuring the kinetic energy and number of electrons. By analyzing the binding energies, the information about the electronic/chemical state, and elemental composition can be obtained. In chapter 4-6, XPS measurements were adopted to study the chemical states of MXene-based and carbon materials.

3.3.5 N_2 sorption/desorption measurement

Surface area is a very important criterion for the new-generation of materials as the surface area relates to the kinetics and capacitance. In this thesis, we conducted the N_2 sorption/desorption measurements by using a Micromeritics 3Flex analyzer to measure the surface area, pore size and pore volume of the materials. The Brunauer-Emmett-Teller (BET) method was used to calculate surface areas of the as-produced samples by using the experimental points at a relative pressure of P/P_0 = 0.05-0.25. The pore size distribution was calculated by the Barret-Joyner-Halenda (BJH) method.

3.3.6 Thermogravimetric Analysis (TGA)

Thermogravimetric analysis (TGA) is a technique that measures mass losing of the materials as a function of the increasing temperature. TGA can be carried out in either N_2 or air atmosphere, and the temperature and heating rate are set up depending on the conditions. In chapter 4, the TGA was measured to quantify the iodine contents in the electrodes.

3.3.7 Scanning Electron Microscopy (SEM)

A scanning electron microscope (SEM) is a type of electron microscope that can provide surface morphology of a specimen by detecting the surface with a focused beam of electrons. The electrons interact with atoms within the materials, providing signals that contain morphology and composition information of the material. In this thesis, SEM images were obtained by using high resolution SEM (Zeiss Supra 55VP, operated with an acceleration voltage of 5-15 kV). Sample preparation method for morphology probing includes 1) put sample powder directly onto a carbon tape; 2) mix sample powder with isopropanol, and drop the dispersion onto silicon foil followed by drying process. The Supra 55VP is also equipped with Oxford energy dispersive spectroscopy (EDS), which enables components and elements analysis.

3.3.8 Transmission Electron Microscopy (TEM)

Transmission electron microscopy (TEM) is a microscopy technique in which a beam of electrons is transmitted through a specimen to form an image. Additionally, the interplanar image can be obtained by using high resolution TEM (HRTEM). Moreover, atom arrangements of specimen can be obtained by using high angle annular dark field (HAADF)-scanning transmission electron

microscopy (STEM). Comparing the changes on the atom arrangements, the lattice distortion can be observed.

3.4 Electrode preparation and battery assembly

3.4.1 Electrode preparation

For powder electrode materials, there are two methods to prepare electrode depending on the type of the electrolytes. For the materials tested in organic electrolyte, the electrodes were developed by mixing active materials, carbon black, and PVDF with a mass ratio of 8:1:1 to form slurry, which was then coated on the copper/aluminium foil, followed by overnight drying. Generally, the mass loading of active materials was about 1~2 mg cm^{-2}. For the materials tested in aqueous electrolyte, the active materials were mixed with carbon black, and PTFE with a mass ratio of 8:1:1. The mixture was dried and compressed to a thin film, which was cut into small disks followed by overnight drying. These small disks were then pressed onto stainless steel/titanium mesh as electrodes for batteries. For the freestanding electrode materials (*e.g.* CC-I, CC-I/MXene, MXene/CNT, and K@MXene/CNT electrode), the as-developed materials were used directly as cathode or anode in the batteries without further process.

3.4.2 Cell assembly

Electrochemical tests of the as-prepared electrodes were conducted by using two-electrode configuration. The CR2032-type coin cells were assembled in an argon-filled glove box, where both the moisture and oxygen contents are less than 0.1 ppm. For lithium-based half-cell tests, the as-developed electrodes were assembled into coin cells with lithium metal foil as counter/reference electrode and Celgard 2400 as separator. As for potassium-based half-cell tests, the as-developed

electrodes were assembled into coin cells with potassium metal foil as counter/reference electrode and glass fiber membrane (Whatman GF/A) as separator. For symmetric cells assembled in chapter 4 and 5, two identical metal foils were used to assemble a coin cell. The electrolytes used in this thesis is ranging from 1 mol kg^{-1} LiTFSI in water, 21 mol kg^{-1} LiTFSI with addition of 7 mol kg^{-1} LiOTf in water, 1 M LiTFSI in 1,2-dioxolane (DOL)/dimethoxymethane (DME) (1:1, v/v), 0.8 M KPF_6 in ethylene carbonate (EC)/diethyl carbonate (DEC) (1:1, v/v), 0.8 M KFSI in ethylene carbonate/diethyl carbonate (1:1, v/v), to composite polymer electrolyte.

3.5 Electrochemical measurements

In this thesis, the electrochemical performance of batteries were studied by carrying out galvanostatic charge-discharge, cyclic voltammetry (CV), and electrochemical impedance spectroscopy (EIS) techniques.

3.5.1 Galvanostatic charge-discharge

Galvanostatic charge-discharge is usually conducted on Neware battery testing system or VMP3 electrochemical workstation at a constant current density within a certain voltage window. The specific capacities (Q, mAh g^{-1}) of electrode materials can be calculated by the equation 3-1:

$$Q = I * t \qquad (3\text{-}1)$$

where I is the current density (unit: mA g^{-1}) and t is the charge/discharge time (unit: h). Rate performances of the electrodes can be collected by performing galvanostatic charge-discharge measurements at different current densities. Additionally, the cycling performances of electrodes can be obtained by repeating galvanostatic charge-discharge measurements. All of the specific capacity, rate performance, and cycling performance are the important criteria for battery systems.

3.5.2 Cyclic voltammetry (CV)

CV is an electrochemical technique which measures the current of an electrochemical cell under a certain scan rate (mV s^{-1}). The workstation (VMP3 or CHI 660D) apply a potential on the electrochemical cell and monitor the current during the test. Redox peaks can be observed if there are reduction or oxidation reactions on the working electrode. Hence, CV curves can provide information about the redox potential and the electrochemical reaction rates of the electrode materials.

3.5.3 Electrochemical Impedance Spectroscopy (EIS)

EIS is an electrochemical measurement to study the transduction in electrochemical systems.[145] The as-obtained Nyquist plots consist of several sub-component sections, which are explained as followed:

Ohmic resistance R_Ω (or bulk resistance R_b) comes from the sum of the resistances of electrolyte, electrode, and separator. The depressed semi-circle in the high frequency area is usually related to the solid electrolyte interface (SEI) layer, which is formed on the surface of the electrode at the initial cycle. The depressed semi-circle in the medium frequency area suggests the resistance of charge transfer at the electrolyte/electrode interface. Finally, the straight line at low frequencies corresponds to the diffusion processes within the active material.

In this thesis, Nyquist plots of various electrodes were collected to gain the further insight into the kinetics of electrodes.

Chapter 4 A High-performance Li-I battery enabled by a MXene wrapped carbon cloth-iodine electrode and a composite polymer electrolyte

4.1 Introduction

In modern society, the development of new generation rechargeable batteries with high energy density, high power density and low cost is highly desired due to soaring demand for utilising renewable energy and reducing air pollution.[146] As a promising alternative to lithium (Li)-ion batteries, rechargeable lithium-iodine (Li-I) batteries based on a conversion mechanism (I_2 + 2 Li ↔ 2 LiI) have drawn intensive attention owing to their high theoretical capacity (1040 mAh cm^{-3} and 211 mAh g^{-1}), superior rate performance, degassing-free battery chemistry, and the low cost of iodine.[147, 148] However, currently, the development of Li-I batteries has been stunted by many intrinsic obstacles. Iodine-based electrodes usually suffer from poor electrical conductivity of the elemental iodine (I_2).[149] More severely, iodine species (*i.e.* I_2, I_3^- and I^-) are highly dissoluble in organic electrolyte solvents. This not only results in serious self-discharge due to their shuttle effect, but also leads to increased internal resistance together with decreased Li^+ transport kinetics.[150, 151] Furthermore, uncontrollable dendrite growth on the Li anode during cycling deteriorates the Li/electrolyte interface and causes safety hazards.[152, 153]

To improve the performance of Li-I batteries, many efforts have been devoted to confine iodine in carbon (C) matrices (such as graphene,[149, 154] carbon microtubes,[155] porous carbon[147, 156, 157] and heteroatom-doped carbon[158, 159]) with the aim of enhancing electronic conductivity and suppressing the dissolution/diffusion of iodine species. However, the physical adsorption of iodine species in these carbon matrices is insufficient to prohibit the shuttle effect. Therefore, it is highly desired to develop a novel iodine-based cathode simultaneously possessing high iodine loading and strong chemical binding of iodine species. As for the electrolyte, replacing organic liquid

electrolyte (LE) with solid electrolyte can synergistically restrain the diffusion of dissolved iodine species and eliminate safety issues (fire and explosion, *etc.*), which could result from the leakage of flammable electrolyte solvents.[160] However, the low ionic conductivity of solid electrolyte and the unstable electrode/solid electrolyte interface greatly limit their applications in Li-I batteries.

Recently, we have proposed a versatile technique for the preparation of MXene-based electrode materials,[38, 129] and an intensive investigation on the liquid/polymer electrolytes[161, 162] for conversion mechanism-based alkali metal batteries. Based on these, for the first time, we successfully develop a flexible quasi-solid-state Li-I battery integrated with a $Ti_3C_2T_x$ (T represents surface functional group, and x is number of such groups) MXene wrapped carbon cloth-iodine (CC-I/MXene) cathode and a composite polymer electrolyte (CPE) composed of catalytic $NaNO_3$ particles dispersing in a pentaerythritol tetraacrylate (PETEA)-based gel polymer electrolyte. As verified by theoretical calculations and experimental investigations, the $Ti_3C_2T_x$ MXene sheets with abundant surface functional groups can effectively confine the iodine species inside the cathode, therefore restrain the shuttle effect. In the *in-situ* prepared CPE, the PETEA-based polymer matrix can efficiently suppress the diffusion of iodine species, and benefit for the formation of a stable Li anode/CPE interface without dendrite growth. Meanwhile, the $NaNO_3$ particles not only greatly enhance the mechanical strength of CPE, but also effectively increase the kinetic transformation of LiI_3 on the cathode. The as-developed quasi-solid-state Li-I batteries exhibit a high energy density with stable cycling performance and excellent flexibility.

4.2 Experimental section

4.2.1 Synthesis of the $Ti_3C_2T_x$ MXene

Ti_3AlC_2 with a particle size of < 38 μm was synthesized according to the previous report.[32] Subsequently, 3 g as-prepared Ti_3AlC_2 powder was etched in a mixture of 3 g lithium fluoride (LiF, Alfa Aesar) and 30 mL 9 M hydrochloric acid (HCl, Fisher Scientific) at ~35 °C for 24 hours to extract the Al atoms and obtain multilayered $Ti_3C_2T_x$ suspension. The obtained suspension was repeatedly rinsed with distilled water and centrifuged (3500 rpm) until the pH of the supernatant was higher than 5.

4.2.2 Preparation and characterization of the CC-I/MXene electrode

Firstly, CC-I electrodes can be prepared by a "solution-adsorption" process.[157] A piece of commercial carbon cloth was cleaned by diluted hydrochloride acid and distilled water, and then put into distilled water with a certain amount of iodine powder, followed by continuously stirring until the solution turns clear. Finally, the as-obtained samples were dried at 80 ºC in vacuum oven for 12 hours. The areal mass loading of iodine is set as ~ 5, ~7.5 and ~10 mg cm^{-2}, respectively. The CC-I/MXene electrodes can be prepared though a simple "drop-filtration" method. Briefly, the as-obtained MXene dispersion was first sonicated under Ar atmosphere for 20 min, and then dropwise added onto CC-I electrode under vacuum filtration. This step was repeated for several times until the desired mass loading was obtained. The as-prepared electrode was then transferred to vacuum oven followed by overnight drying at 50 ºC. The mass loading of MXene on the CC-I electrode was measured by weighting the mass change before and after the "drop-filtration" process, which is estimated to be ~0.8 mg cm^{-2}.

The XRD patterns of the as-prepared samples were collected by using Bruker D8 discover XRD with Cu Kα radiation (40 KV and 40 mA). Raman spectra of samples were measured using a Renishaw inVia Raman spectrometer system (Gloucestershire, UK). The specific surface area was determined by the gas sorption technique using a Micromeritics 3Flex analyser based on the Brunauer-Emmett-Teller (BET) method. The content of iodine in each electrode was estimated by thermogravimetric analysis (TGA) with heating rate of 10 ºC min^{-1} under nitrogen atmosphere. X-ray photoelectron spectroscopy (XPS) measurements were performed on a Kratos XSAM-800 spectrometer. The morphology of the samples was observed using a field emission scanning electron microscope (FE-SEM, Zeiss Supra 55VP). FT-IR spectra were recorded on a Nicolet Magna 6700 FT-IR spectrometer with 0.9 cm^{-1} standard optical resolution by using a KBr beam splitter.

4.2.3 Preparation and characterization of the CPE

The CPE was prepared via *in-situ* polymerization of a precursor solution. Firstly, anhydrous $NaNO_3$ (≥99%, Sigma-Aldrich) was added into a solution of PVDF-HFP (M_n ~130,000, Sigma-Aldrich) in 1 M LiTFSI (99.95 %, Sigma-Aldrich) in DOL (99.8 %, Sigma-Aldrich): DME (99.9 %, Sigma-Aldrich) (1: 1, v/v) electrolyte. Then the mixture was subjected to a stirring process until crushing the bulky $NaNO_3$ to small particles and forming a homogeneous suspension. After that, PETEA monomer together with 2-hydroxy-2-methyl-1-phenyl-1-propanone (HMPP, 97 %, Sigma-Aldrich) photo-initiator were dissolved into such suspension to get a precursor solution, and then exposed to UV-irradiation from a Hg UV lamp (with an irradiation peak intensity of ~2000 mW cm^{-2}) for 15 min to ensure the PETEA monomer fully polymerized in the electrolyte and obtain a milky white CPE. The weight ratio of PETEA: PVDF-HFP: $NaNO_3$: HMPP: LE was set as 1.5: 1.5: 2: 0.1: 94.9 in the CPE. For comparation, a PETEA-based gel polymer electrolyte

(GPE) was prepared by *in-situ* polymerizing a solution of 1.5 wt% PETEA monomer with 1.5 wt% PVDF-HFP and 0.1 wt % HMPP in 1 M LiTFSI in DOL: DME electrolyte. All procedures for electrolyte preparation were carried out in an Ar-filled glove box (Universal 2440/750) with the concentrations of moisture and oxygen below 0.1 ppm. To separate and purify the PEATEA-based polymer matrix from the CPE, the CPE was mashed into pieces and washed with acetone and then deionized water for three times. Subsequently, the obtained mixture was dialyzed against deionized water for 3 days to further remove the residual ions. The as-prepared precipitates were then vacuum-dried at 120 ºC for 6 h to obtain the separated PETEA-based copolymer matrix.

The performances of the prepared CPE were characterized using following methods and instruments. The ionic conductivity of the CPE was measured via electrochemical impedance spectrum (EIS) from 100 kHz to 1 Hz with an alternating current amplitude of 5 mV on a VMP3 (Bio Logic Science Instruments) multichannel electrochemical station. The test cell was a small piece of CPE film sandwiched between two stainless steel blocking electrodes. The cell was kept at each test temperature (from 0 ºC to 90 ºC) for at least half an hour to reach thermal equilibrium before the EIS measurements. The Li ion transference number (T_{Li}^{+}) of the CPE was tested by the method described by Abraham et al.[163] A symmetric Li|CPE|Li cell was assembled and then the polarization currents (including the initial (I^{o}) and steady-state (I^{ss}) current values) under a small polarization potential (ΔV) at 10 mV were recorded. Simultaneously, the initial and steady-state values of the bulk resistances (R_b^{o} and R_b^{ss}) and electrode/electrolyte interfacial resistances (R_i^{o} and R_i^{ss}) were examined by EISs before and after the potentiostatic polarization. The T_{Li}^{+} was calculated as following equation:

$$T_{Li}^{+} = \frac{I^{ss} R_b^{ss} (\Delta V - I^{o} R_i^{o})}{I^{o} R_b^{o} (\Delta V - I^{ss} R_i^{ss})} \qquad (5\text{-}1)$$

The compatibility of CPE with Li metal electrode was characterized by galvanostatic cycling measurement composed of repeated 3 h charge and 3 h discharge cycles, which was performed on a symmetric Li|CPE in a Celgard 2400 separator|Li cell at a current density of 0.5 mA cm^{-2}. To evaluate the durability of the CPE, its weight loss in an open environment was tested as a function of aging time at 25 ºC. The formation and diffusion of iodine in electrolytes along with aging time at 25 ºC was visually observed after adding same amounts of iodine (10 mg) into the electrolytes.

4.2.4 Assembly and testing of quasi-solid-state Li-I batteries

CR2032 coin cells were assembled in an Ar-filled glove box. CC-I and CC-I/MXene electrodes were used as cathode directly without further process. The precursor solution containing 1.5 wt% PETEA, 1.5 wt% PVDF-HFP, 2 wt% $NaNO_3$ and 0.1 wt% HMPP in 1 M LiTFSI in DOL: DME electrolyte was injected into a Celgard 2400 separator on the surface of CC-I/MXene cathode and *in-situ* polymerized under UV-irradiation, and subsequently integrated with Li metal anode to construct the quasi-solid-state Li-I cells. The electrolyte/iodine ratio in each cell was uniformly set at ~20 μL mg^{-1}. For comparison, the Li|LE|CC-I/MXene (Li|LE|CC-I, Li|LE|CC and Li|LE|CC/MXene) cells were assembled by using 1 M LiTFSI in DOL: DME electrolyte. The assembled Li-I cells were cycled between 2.0 and 3.6 V at various charge/discharge rates (1 C = 211 mA g^{-1} based on the mass of iodine) on a Land 2001 A battery testing system at 25 ºC. Cyclic voltammograms (CVs) of the assembled cells were tested using the VMP3 electrochemical working station at a scanning rate of 0.1 mV s^{-1}. Electrochemical impedance spectra (EISs) of cells were examined using the VMP3 multichannel electrochemical station in a frequency range of 10^{-2} to 10^5 Hz by applying a disturbance amplitude of 5 mV. The cells after designated cycling tests were transferred into a glove box and dissembled for postmortem analysis. Flexible soft packing Li-I batteries were assembled as follow. The compositions of electrodes and precursor solution

were same as the above-mentioned coin cells. Aluminium and nickel strips were joined to the side of cathode and anode as the electrode tabs, respectively. The CPE was firstly in-situ obtained in the separator covered on the CC-I/MXene cathode, and then laminated together with Li foil to form the battery core and assembled into aluminum-plastic film packages. After that, these packages were sealed under vacuum to get the soft packing batteries.

4.2.5 Theoretical calculations

All structure relaxation and electronic structure calculations were performed with density functional theory with the projector-augmented wave method. The exchange-correlation functional of Perdew, Burke, and Enzerhof (PBE) was employed to analyze the exchange and correlation potentials. The cut-off energy level was set as 500 eV, the SCF tolerance level was set as 1.0×10^{-5} au in geometry optimization, while the SCF tolerance was set as 1.0×10^{-6} for energy calculation. The semi-empirical London dispersion corrections of Grimme et al. were applied to take the dispersion interactions of van der Waals into consideration.[164]

4.3 Results and discussion

Figure 4.1 illustrates the preparation of the Li|CPE|CC-I/MXene batteries. Iodine can be facilely loaded onto the porous carbon cloth (CC) by a simple "solution-adsorption" method to obtain the flexible carbon cloth-iodine (CC-I) electrodes. Delaminated $Ti_3C_2T_x$ MXene was prepared by selectively etching Al atoms in Ti_3AlC_2 (MAX) precursor materials followed by sonication. As shown in Figure 4.2a, the delaminated MXene sheets shows a crumple architecture with an average sheet size of ~50 μm. The EDS elemental mappings in Figure 4.2b-e exhibit the uniform presence of Ti, C, O, and F elements, confirming a successful synthesis of the MXene sheets. A sharp peak at around 6º appears in the XRD pattern (Figure 4.2f), which can be assigned to the typical MXene (002) peak.[38] Raman spectrum of the as-prepared MXene sheets is displayed in Figure 4.2g. The

peaks at ~200, ~378, and ~607 cm^{-1} correspond to specific $Ti_3C_2T_x$ MXene bands. There is no peak of anatase phase titanium dioxide (usually at ~144 cm^{-1}) in the Raman spectrum of MXene sheets, indicating no compositional change during the preparation process. By adopting a "drop-filtration" process, the CC-I electrodes can be tightly wrapped by the MXene sheets (Figure 4.1, upper panels), which can greatly improve the stability of iodine due to the strong interaction. As shown in Figure 4.3a, compared with pure iodine and CC-I samples, CC-I/MXene sample shows highest on-set evaporation temperature at around 195 ºC, suggesting that MXene sheets can effectively improve the thermal stability of iodine in the sample. Furthermore, the on-set evaporation temperature of iodine in CC-I/MXene samples decreases from 195 ºC to 175 ºC and 160 ºC as the areal mass loading of iodine increases from 5 mg cm^{-2} to 7.5 mg cm^{-2} and 10 mg cm^{-2}, respectively (Figure 4.3b).

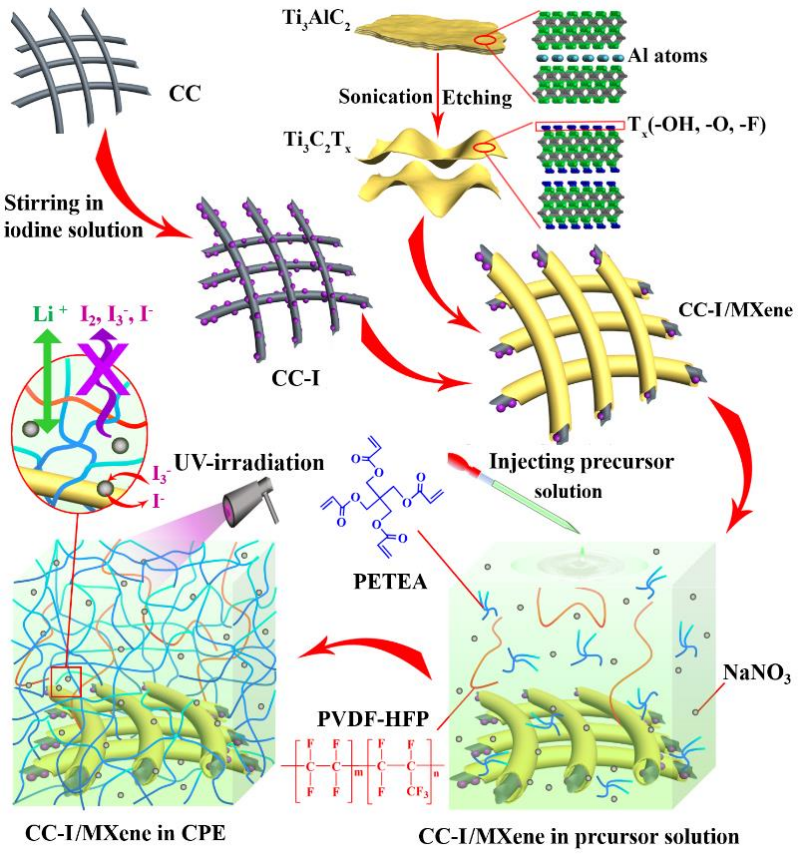

Figure 4.1. *Schematic illustration of the preparation of MXene wrapped carbon cloth-iodine cathodes and composite polymer electrolyte.*

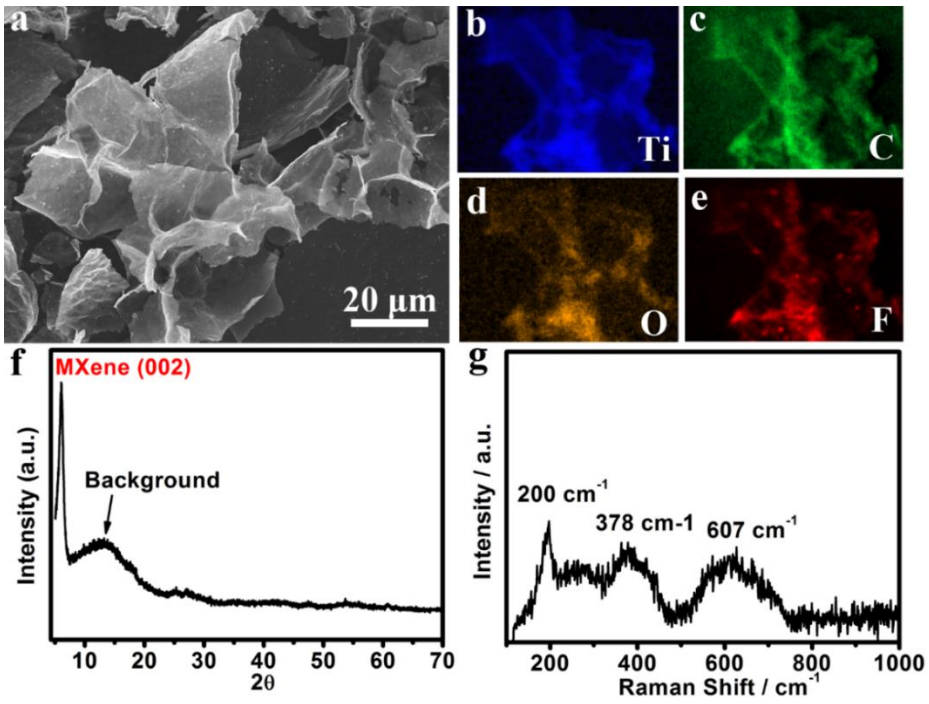

Figure 4.2. *Characterizations of the delaminated MXene sheets. (a) FE-SEM image of the delaminated MXene sheets. (b-e) EDS elemental mapping of elemental Ti, C, O and F of the delaminated MXene sheets. (f) XRD pattern and (g) Raman spectrum of the delaminated MXene sheets.*

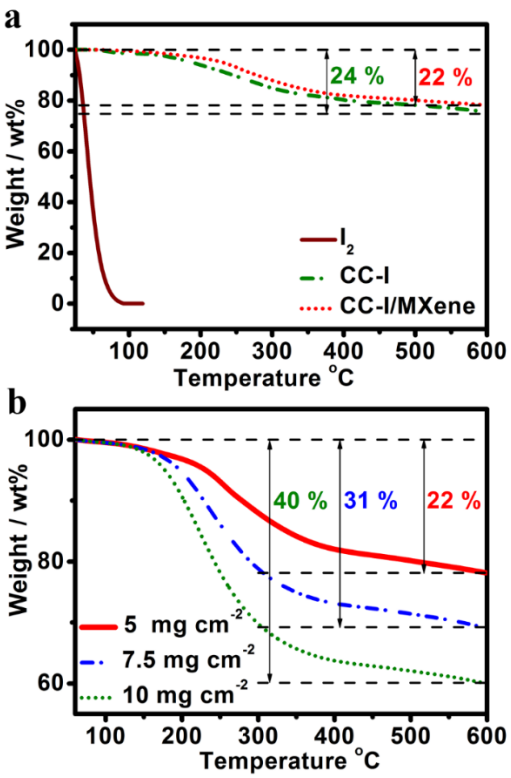

Figure 4.3. *(a) TGA curves of the pure iodine, CC-I, and CC-I/MXene samples under N_2 flow from room temperature to 600 °C. (b) Thermogravimetric analysis curves of the CC-I/MXene electrode with different areal mass loading of iodine.*

To further enhance the electrochemical performance of CC-I/MXene cathodes in batteries, optimization of electrolyte has been conducted. Based on previous research, it is believed that the addition of $LiNO_3$ in ether-based electrolytes benefits for the formation of a passive film on the Li anode, and therefore suppresses its corrosion from dissolved iodine species.[164] However, as shown in Figure 4.4, a Li anode pre-cycled in a $LiNO_3$-containing liquid electrolyte (LE) cannot suppress the serious self-discharge, while Li-I cells using a suspension of insoluble $NaNO_3$ in LE can deliver a negligible self-discharge, which is comparable to that of the $LiNO_3$-containing LE. Therefore, we present a new understanding on the role of nitrates in Li-I batteries. We suggest that $NaNO_3$ can catalyze the conversion from I_3^- to elemental I_2 near the end of the charging process. Thus, we

prepared a composite polymer electrolyte consisting of 2 wt% $NaNO_3$ homogeneously dispersing in a PETEA-based gel polymer electrolyte. Firstly, $NaNO_3$ particles were dispersed in 1 M bis(trifluoromethane) sulfonamide lithium (LiTFSI) in 1,2-dioxolane (DOL): dimethoxymethane (DME) (1: 1, v/v) electrolyte (in which a small amount of PVDF-HFP was dissolved to improve the dispersion of $NaNO_3$ particles) to form a suspension, and then PETEA monomer together with 2-hydroxy-2-methyl-1-phenyl-1-propanone (HMPP) photo-initiator were dissolved into the suspension to obtain a precursor solution. After that, the precursor solution was subjected to an ultraviolet light (UV)-irradiation to initiate a radical polymerization of C=C bonds on the monomers, and thereafter the cross-linked CPE was *in-situ* constructed on the surface of the CC-I/MXene cathode (Figure 4.1, lower panels). In such CPE, the PETEA-based polymer matrix with strong chemical interaction with iodine species can efficiently suppress their shuttle effect and simultaneously stabilize the Li anode/CPE interface. Furthermore, as shown in Figure 4.5, the precursor solution of CPE presents an appearance as a homogeneous suspending liquid. After the gelation process, the GPE without $NaNO_3$ exhibits an extremely low mechanical strength that cannot form a freestanding mass (Figure 4.5c, e). On sharp contrast, with the addition of $NaNO_3$ particles, the strength of the obtained CPE remarkably increases. It can maintain integrity under the pressure of a 100 g weight (Figure 4.5d, f). $NaNO_3$ particles can not only greatly enhance the mechanical strength of the CPE, but also act as an effective catalyst on the iodine cathode/CPE interface. Such collaborative optimization on electrode and electrolyte is expected to achieve a superior cycling stability for the Li-I batteries.

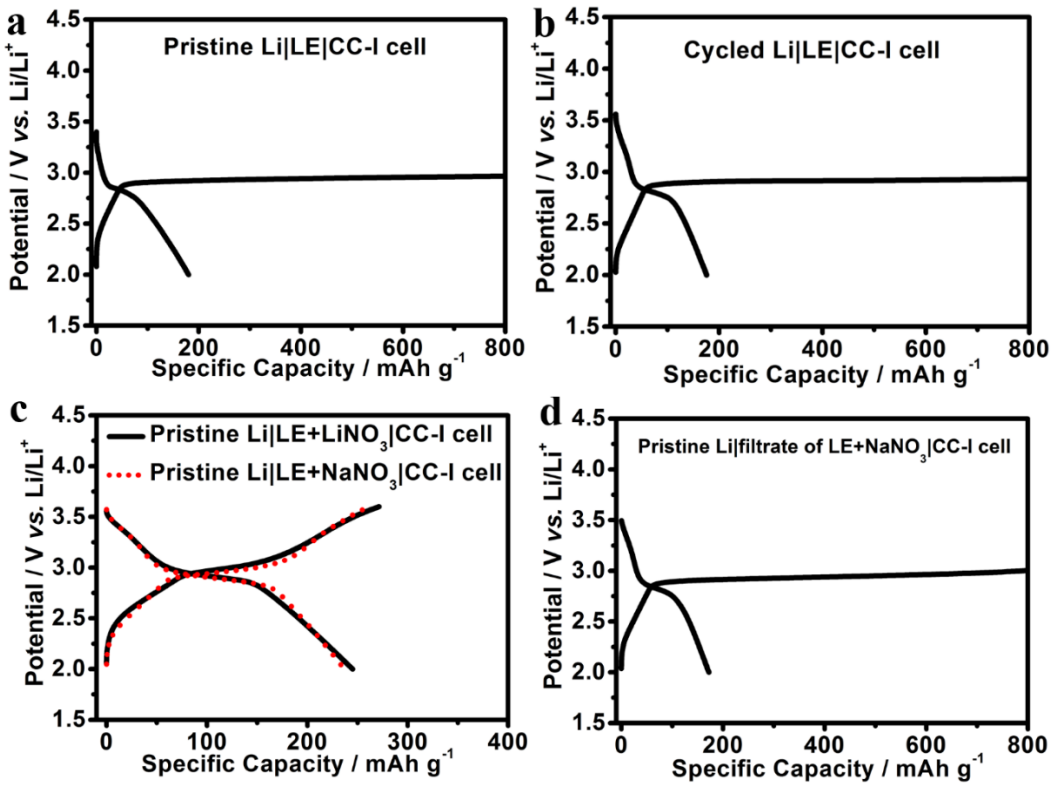

Figure 4.4. *The initial discharge/charge curves at 0.5 C of (a) pristine Li|1 M LiTFSI in DOL: DME (LE)|CC-I cathode cell; (b) cycled Li|LE|CC-I cathode cell, the cycled Li anode was obtained from a CC-I cathode|LE with 1 wt% $LiNO_3$ additive|pristine Li cell after 5 cycles at 0.5 C; (c) pristine Li|LE with 2 wt% $LiNO_3$ additive|CC-I cathode and pristine Li|suspension of 2 wt% $NaNO_3$ in LE additive|CC-I cathode cells, and (d) pristine Li|the filtrate of a suspension of 2 wt% $NaNO_3$ in LE|CC-I cathode cell.*

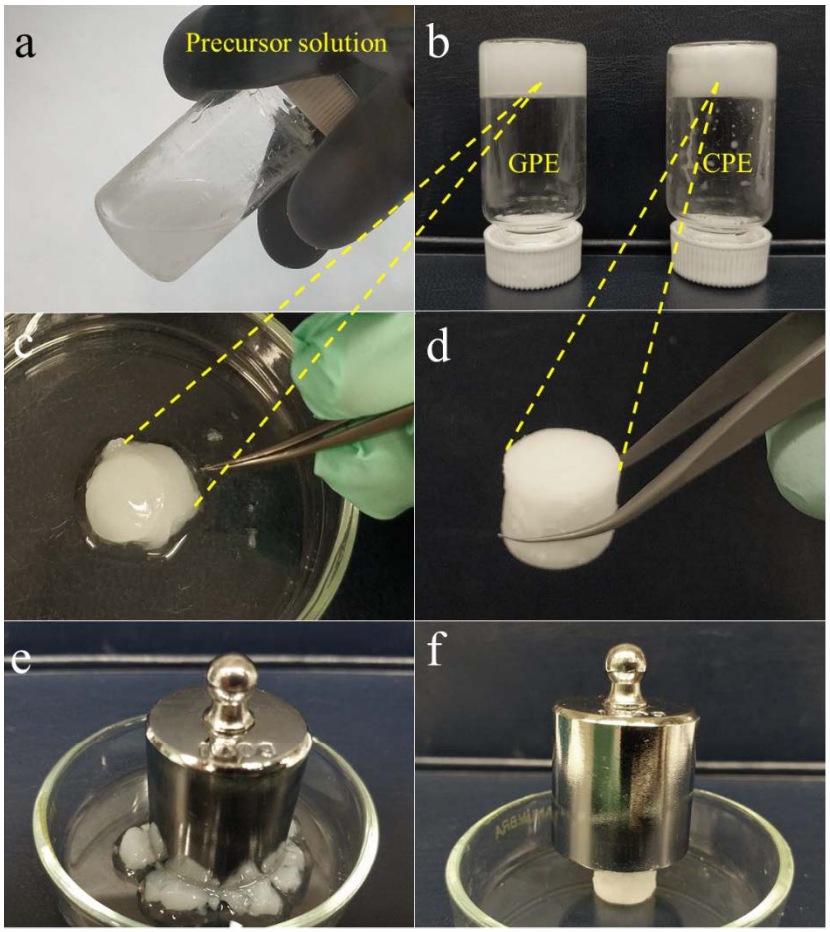

Figure 4.5. *Optical images of (a) the precursor solution of CPE, and (b-d) GPE and CPE. (e) GPE and (f) CPE under the pressure of a 100 g weight.*

As shown in Figure 4.6a, the carbon cloth shows a morphology of tidily knitted carbon fibres. No any structural change is observed after absorbing iodine (Figure 4.6b). For the CC-I/MXene electrode, it is clearly seen that the iodine-loaded carbon fibres are well-wrapped by the MXene sheets (Figure 4.7a and Figure 4.8a-b). This is further confirmed by the uniform distribution of elemental titanium (Ti), carbon (C) and iodine (I) in the energy dispersive spectrometer (EDS) images of a CC-I/MXene electrode (Figure 4.7b). Furthermore, no characteristic peak of iodine can be observed in the X-ray diffraction (XRD) pattern (Figure 4.8c) and Raman spectrum (Figure

4.8d) of the MXene-wrapped electrode, indicating the formation of amorphous iodine during the solution-adsorption process, which is consistent with previous reports.[158] X-ray photoelectron spectroscopy (XPS) was applied to investigate the chemical composition of the CC-I/MXene electrode. The Ti 2p spectrum (Figure 4.7c) shows two Ti $2p_{3/2}$ doublets at 455.1 and 458.7 eV, and two Ti $2p_{1/2}$ doublets at 461.1 and 464.4 eV, respectively. As for the Ti $2p_{3/2}$, three deconvoluted peaks at 455.1, 456.5 and 458.7 eV can be assigned to Ti-C bonds, Ti-X bonds and Ti-O surface bonds, respectively. Similarly, three deconvoluted peaks at 460.9, 461.9 and 464.4 eV are observed in the Ti $2p_{1/2}$.[38, 165] Such Ti 2p spectrum result confirms the successful wrapping of MXene sheets on the electrode without any compositional change. Figure 4.7d exhibits the XPS spectrum of I 3d in the CC-I/MXene electrode, in which peaks located at around 619.9 and 631.2 eV are associated with I $3d_{5/2}$ and I $3d_{3/2}$, respectively.[166] Noticeably, a peak located at around 623 eV can be ascribed to the chemical adsorption between iodine and the -O/-OH terminations of MXene.[166] Such O-I chemical bonding is further validated by the O 1s XPS spectrum (Figure 4.9). Figure 4.9b shows the O 1s XPS spectrum of the CC-I/MXene electrode, which can be deconvoluted into four peaks centred at 530.2, 531.2, 532.8 and 533.1 eV, corresponding to I-O, Ti-O_x, Ti-OH and H-O (hydroxide), respectively.[124, 166] The O-I bonding is expected to confine the iodine in the cathode and suppress its dissolution. To estimate the adsorption ability of MXene for iodides, ultraviolet-visible (UV-vis) spectra of a 2 mL 0.005 M LiI_3 (prepared by dissolving LiI and I_2 with a stoichiometric ratio of 1:1)-DOL solution were measured. As shown in Figure 4.7e, after adding 1 mg MXene, the characteristic peaks of I_3^- at around 286 nm and 365 nm[167] decrease gradually with the aging time. After 2 days adsorption, the solution turned clear (the inset in Figure 4.7e), which illustrates a strong adsorption of iodides by the MXene. The initial discharge/charge curves of Li-I cells using CC-I and CC-I/MXene electrodes in nitrate-free LE (1 M LiTFSI in

DOL/DME) are shown in Figure 4.7f. The CC-I cathodes show extremely low Coulombic efficiency and cannot be charged to above 3 V, which can be attributed to the severe shuttling of dissolvable iodine species. In sharp contrast, after wrapping with MXene sheets, the CC-I/MXene cathodes exhibit a significantly enhanced Coulombic efficiency (~73%) and reversible capacity (~219 mAh g^{-1}), indicating an effective immobilization of iodine species by the MXene sheets.

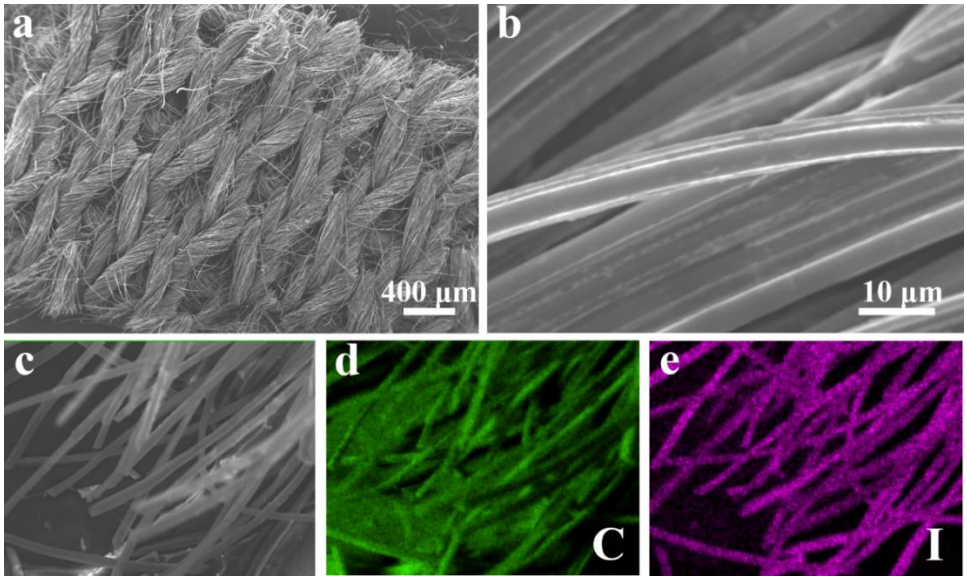

Figure 4.6. *Characterizations of the carbon cloth-iodine electrode. (a-b) FE-SEM images of the CC-I electrode. (c-e) EDS Elemental mapping of the CC-I electrode. The elemental mapping analysis of the CC-I sample in Figure 4.6c-e demonstrates that I and C elements are evenly distributed, confirming the successful loading of iodine into the pores of carbon fibres.*

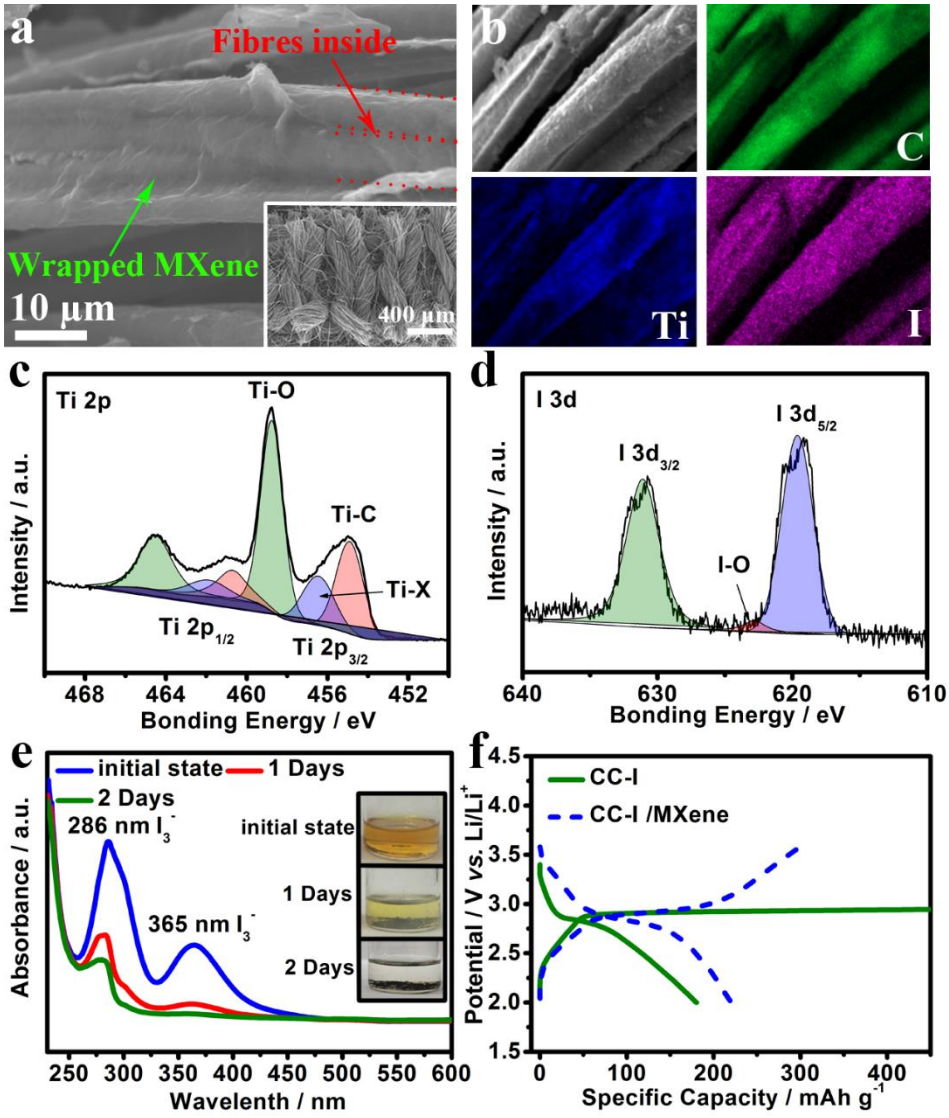

Figure 4.7*. Characterizations of CC-I/MXene electrodes. (a) FE-SEM images and (b) EDS mappings of elemental Ti, C and I on a CC-I/MXene electrode; High resolution XPS spectra of (c) Ti 2p and (d) I 3d in a CC-I/MXene electrode; (e) UV-vis spectra and corresponding digital images of 10 mM LiI_3 solution before and after loading MXene sheets; (f) The initial discharge/charge curves of Li|LE|CC-I and a Li|LE|CC-I/MXene cells at 0.5C.*

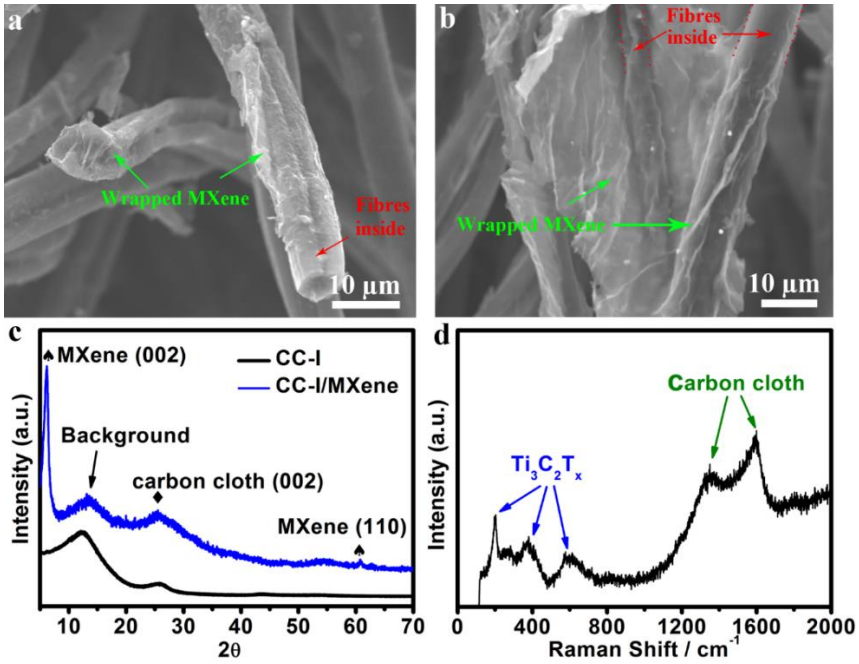

Figure 4.8. *Characterizations of the MXene wrapped carbon cloth-iodine electrode. (a-b) FE-SEM images of CC-I/MXene electrode. (c) XRD patterns of CC-I and CC-I/MXene electrodes. The MXene (002) peak at around 6° peak indicates the successful preparation of the CC-I/MXene electrode without any compositional change. (d) Raman spectrum of CC-I/MXene electrode. The peaks located at ~200, ~378, and ~607 cm^{-1} can be assigned to specific Ti_3C_2Tx MXene bands while two peaks at ~1355 and ~1600 cm^{-1} can be ascribed to the D band and G band of carbon cloth, respectively.*[168]

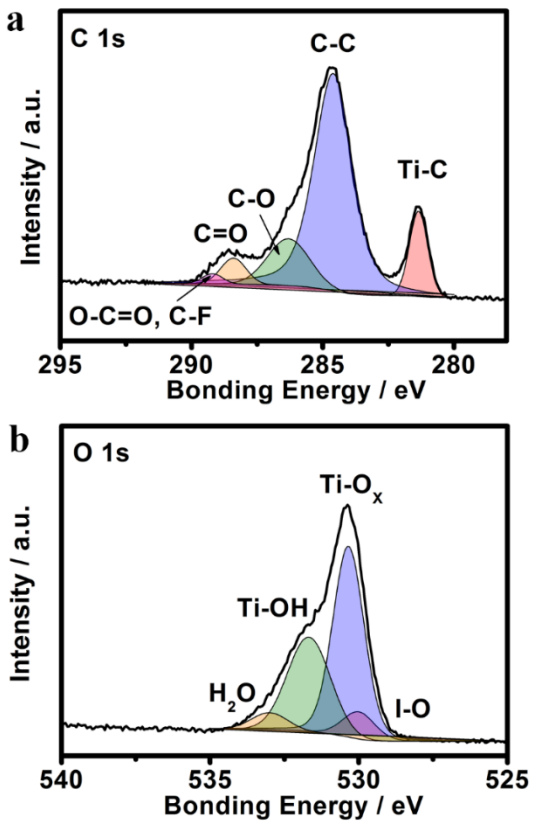

Figure 4.9. *(a) C 1s and (b) O 1s XPS spectra of the as-prepared CC-I/MXene electrode. The C 1s XPS spectrum of CC-I/MXene electrode in Figure 4.9a can be deconvoluted into five peaks at 281.7, 284.8, 286.3, 288.3 and 289.2 eV. The peak at 281.7 eV can be assigned to the C-Ti bond. The peaks at 284.8 eV and 286.3 eV relate to C-C and C-O, respectively. The other two peaks appearing at 288.3 and 289.2 eV can be indexed to the signals of C=O and O-C=O/C-F, respectively.*[124]

The Fourier transform infrared spectroscopy (FTIR) spectra of the PETEA monomer and the PETEA-based polymer matrix separated from CPE is shown in Figure 4.10. Peaks at 1404 and 1468 cm^{-1} (CH_2 bending), and 1722 cm^{-1} (C=O stretching) appear in the spectra of PETEA monomer. It is seen that the peak at approximately 1633 cm^{-1} assigned to the stretching vibration of C=C bonds nearly disappears in the spectrum of PETEA-based polymer matrix, which verifies that the monomers have been successfully polymerized in the $NaNO_3$ suspension with a high degree of conversion.[162] The ionic conductivities of the LE, LE suspended with $NaNO_3$ and CPE as a function of temperature from 0 to 90 ºC are shown in Figure 4.11a. The plots of log σ versus

T^{-1} for all electrolyte samples deliver a non-linear relationship, which can be well-described by the Vogel–Tamman–Fulcher (VTF) empirical equation:[169]

$$\sigma=\sigma_o T^{-1/2} \exp(-\frac{E_a}{R(T-T_o)}) \quad (5\text{-}2)$$

where E_a is the activation energy, σ_o is the pre-exponential factor, R is the ideal gas constant, and T_o is a parameter correlated to the glass transition temperature. It is worth noting that the E_a value (which indicates the barrier for ionic conduction) for the CPE obtained from the VTF fitting (8.92×10^{-3} eV) is quite close to that for the LE (7.37×10^{-3} eV, Table 4.1), indicating that in the CPE, the adverse influence from small amounts of non-conductive additive components (*i.e.* polymers and $NaNO_3$) on ionic conduction is negligible. As a result, the CPE shows an extremely high conductivity of 9.50×10^{-3} S cm^{-1} at 25 °C, which is almost the same as that of the LE (1.18×10^{-2} S cm^{-1} at 25 °C). Such a high ionic conductivity value is sufficient to meet the requirement for Li-I batteries with high power density.

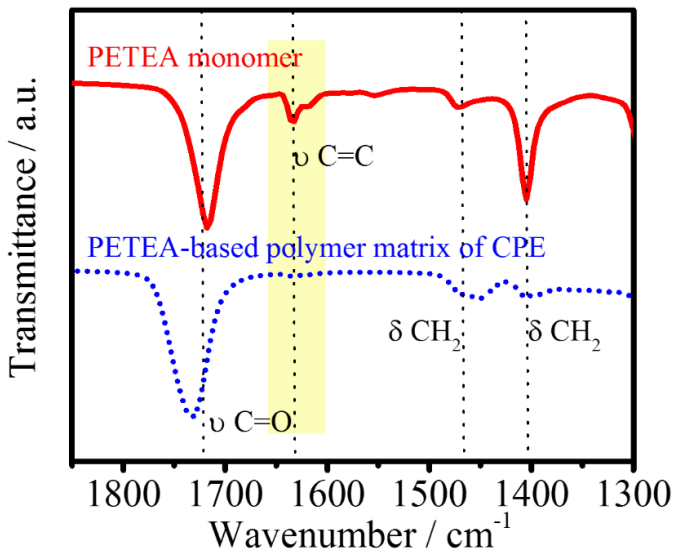

Figure 4.10. *FTIR spectra of PETEA monomer and the PETEA-based polymer matrix of CPE.*

The Li ion transference number (t_{Li}^{+}) is a crucial parameter for electrolytes, since a low t_{Li}^{+} results in an increase in electrode polarization.[170] It is seen that the t_{Li}^{+} of CPE reaches 0.52 (Figure 4.11b), which is much higher than that of the LE (0.33, Figure 4.12). This can be ascribed to the fact that the polymerized PETEA framework significantly immobilizes the anions.[161] Such enhanced t_{Li}^{+} is expected to not only diminish the polarization of batteries, but also restrains the dendrite growth on Li anodes.[171] This is confirmed by galvanostatic cycling measurements on a symmetric Li|Li cell at a current density of 0.5 mA cm^{-2}. For the Li|LE|Li cell, the voltage hysteresis between the voltages of Li stripping and plating dramatically increases after ~240 h, demonstrating a deteriorated Li/LE interface, resulting from an accumulated thick solid electrolyte interface (SEI) and Li dendrite growth (Figure 4.11c).[172] The Li|CPE|Li cell, in sharp contrast, delivers a much lower voltage fluctuation and maintains stability up to 300 h. This validates a uniform Li deposition with a stable Li/CPE interface. Therefore, the safety risks caused by dendrite growth have been successfully mitigated.

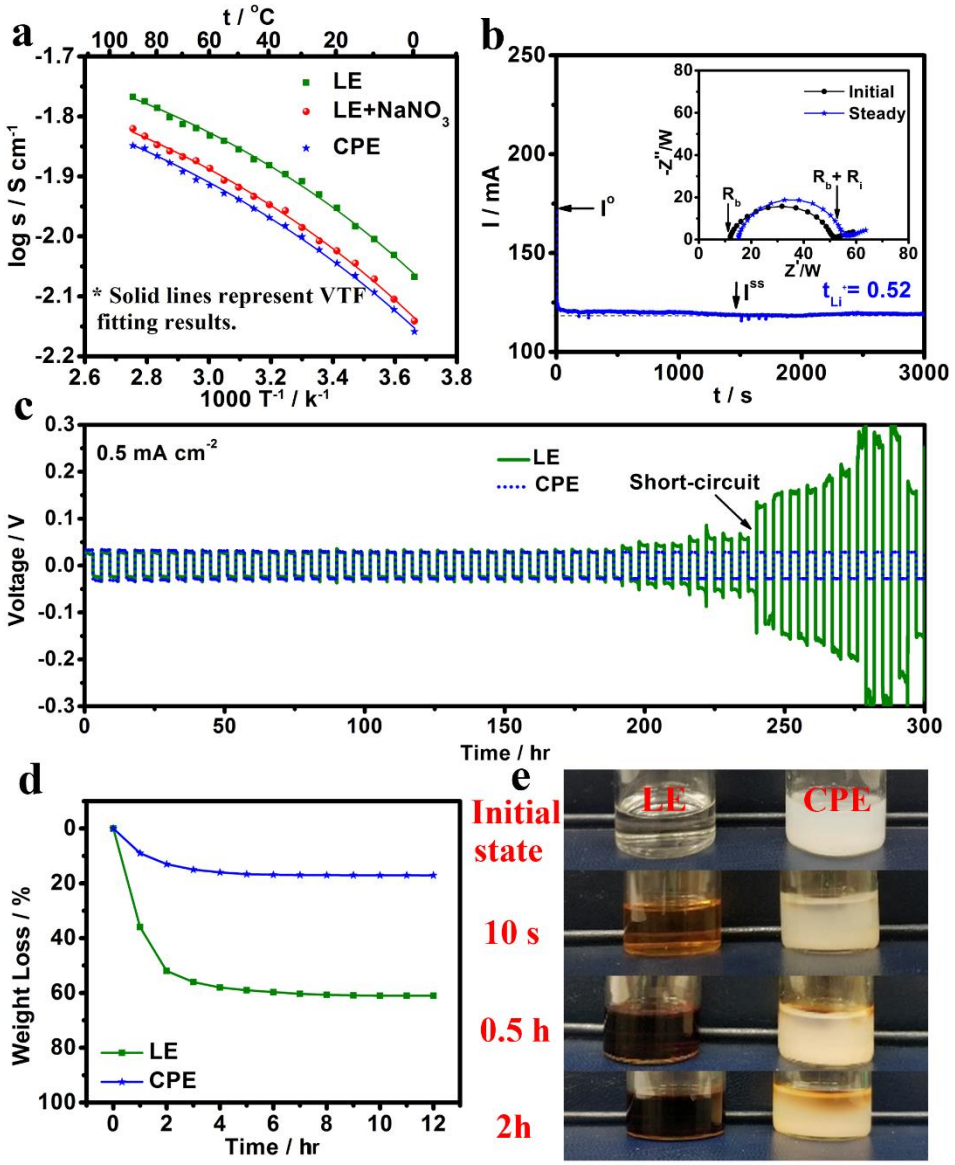

Figure 4.11. *Characterizations of the CPE. (a) The ionic conductivities of 1 M LiTFSI in DOL: DME (1: 1, v/ v) LE, LE suspended with $NaNO_3$ and CPE as a function of temperature. The plots represent the experimental data meanwhile the solid lines represent VTF fitting results. (b) The chronoamperometry profile of a symmetric Li|CPE|Li cell under a polarization voltage of 10 mV. The corresponding EISs before and after the polarization are shown in inset. (c) Galvanostatic cycling curves of Li|Li symmetrical cells using LE or CPE at a current density of 0.5 mA cm^{-2} with cutoff capacity of 1.5 mAh cm^{-2}; (d) Weight loss of LE and CPE along with aging time at 25 °C. (e) Visual observation of iodine dissolution/diffusion in LE and CPE with different aging times.*

Table 4.1. *The values of VTF fitting parameters in Figure 4.11a.*

Sample	σ at 25 °C (S cm^{-1})	σ_o (S cm^{-1} K$^{-1/2}$)	E_a (eV)	T_o (K)
LE	1.18×10^{-2}	0.871	7.37×10^{-3}	164.1
LE + $NaNO_3$	9.83×10^{-3}	0.838	8.23×10^{-3}	159.5
CPE	9.50×10^{-3}	0.837	8.92×10^{-3}	152.5

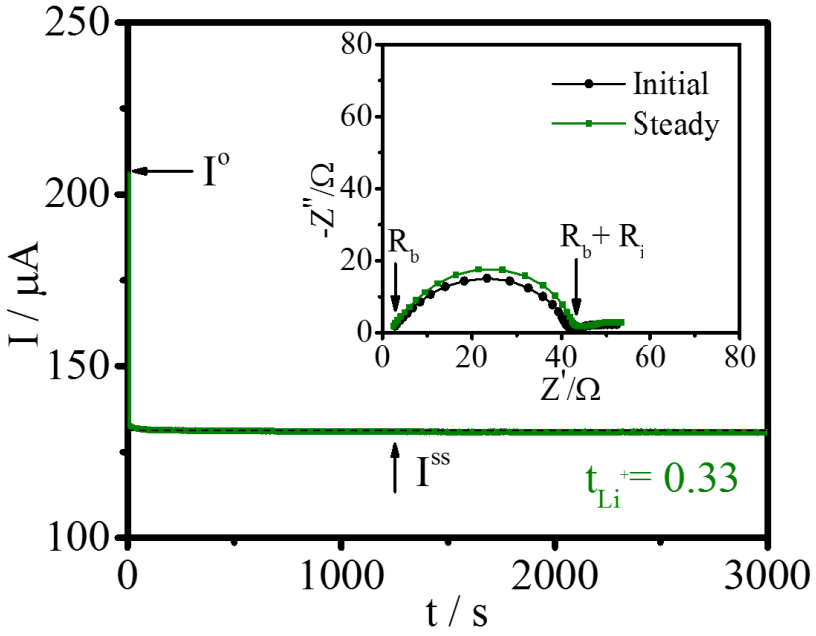

Figure 4.12. *The chronoamperometry profile of symmetric Li|LE|Li cell under a polarization voltage of 10 mV. The corresponding EISs before and after the polarization are shown in inset.*

The durability and safety of the CPE are elucidated by measuring its weight loss in an open environment as a function of aging time at room temperature. As shown in Figure 4.11d, the CPE exhibits a slight weight loss with aging time (17 wt% after 12 h) due to the volatilization of electrolyte solvent, which is much lower than that of the LE (61 wt% after 12 h). Therefore, the

CPE shows a much enhanced safety characteristic compared to LE. To directly characterize the dissolution and diffusion of iodine species in electrolytes, we performed visual observation on the same amount of iodine powder soaked in LE and CPE. The LE immediately turns dark brown after adding the iodine (Figure 4.11e, left), implying that the iodine powder massively dissolves in the LE. However, the CPE remains milky white with a light-yellow skin layer during the aging process (Figure 4.11e, right), indicating that the dissolution of iodine has been significantly alleviated in the CPE.[172]

To investigate the electrochemical characteristics of the as-assembled Li-I batteries, the performances of CC-I/MXene electrodes using LE, $NaNO_3$-containing LE, and CPE were tested. As shown from the self-discharge phenomena (Figure 4.13), the potential of the Li|LE|CC-I/MXene cell decreases rapidly due to the dissolution of active material and shuttle effect; While the cell with CPE achieves a negligible self-discharge after aging for 48 hours, indicating the strong immobilization of iodine species by the CPE. The Li|LE|CC-I/MXene cell can deliver an initial discharge capacity of 219 mAh g^{-1} (based on the mass of iodine) at 0.5 C with a Coulombic efficiency of 73 % (Figure 4.14a). It should be noticed that such a capacity value is higher than the theoretical capacity of Li-I batteries (211 mAh g^{-1}), since the MXene sheets as well as porous carbon cloth substrates can also impart capacity. As shown in Figure 4.15, bare carbon cloth and MXene wrapped carbon cloth deliver capacities of ~40 and ~46 mAh g^{-1} at 0.2 mA cm^{-2}, respectively. The linear charge-discharge profiles indicate the capacitive behaviour of MXene sheets as well as porous carbon cloth substrates. After adding $NaNO_3$ into the LE, an enhanced capacity (301 mAh g^{-1}) and Coulombic efficiency (~92 %) are achieved at 0.5 C, suggesting that $NaNO_3$ can greatly enhance the transformation kinetics due to catalytic effect (Figure 4.16a). The capacity of CC-I/MXene electrodes in Li-I batteries can be further improved to ~330 mAh g^{-1} at

0.5 C by using CPE, since the cross-linked monomers in electrolyte can effectively immobilize the iodine species and prevent loss of active materials. The Li|CPE|CC-I/MXene cells also exhibit superior long-term cycling stability with 85 % capacity retention after 1000 cycles, which is much higher than those with LE (57 %, 50 cycles) and $NaNO_3$-containing LE (67%, 1000 cycles) (Figure 4.14b and Figure 4.16b, respectively).

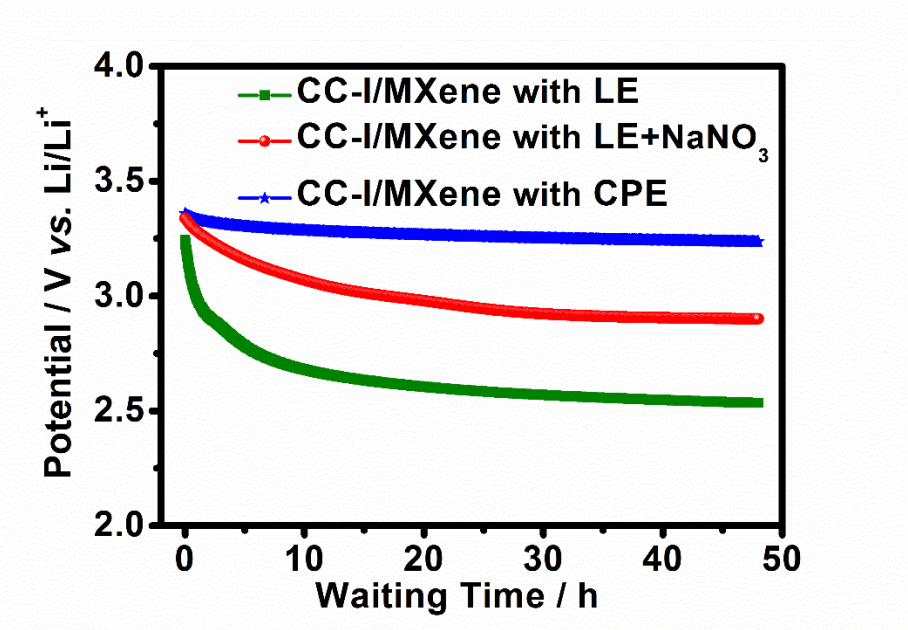

Figure 4.13. *The potential change of Li|LE|CC-I/MXene, Li|LE+$NaNO_3$|CC-I/MXene, and Li|CPE|CC-I/MXene cells over standing time.*

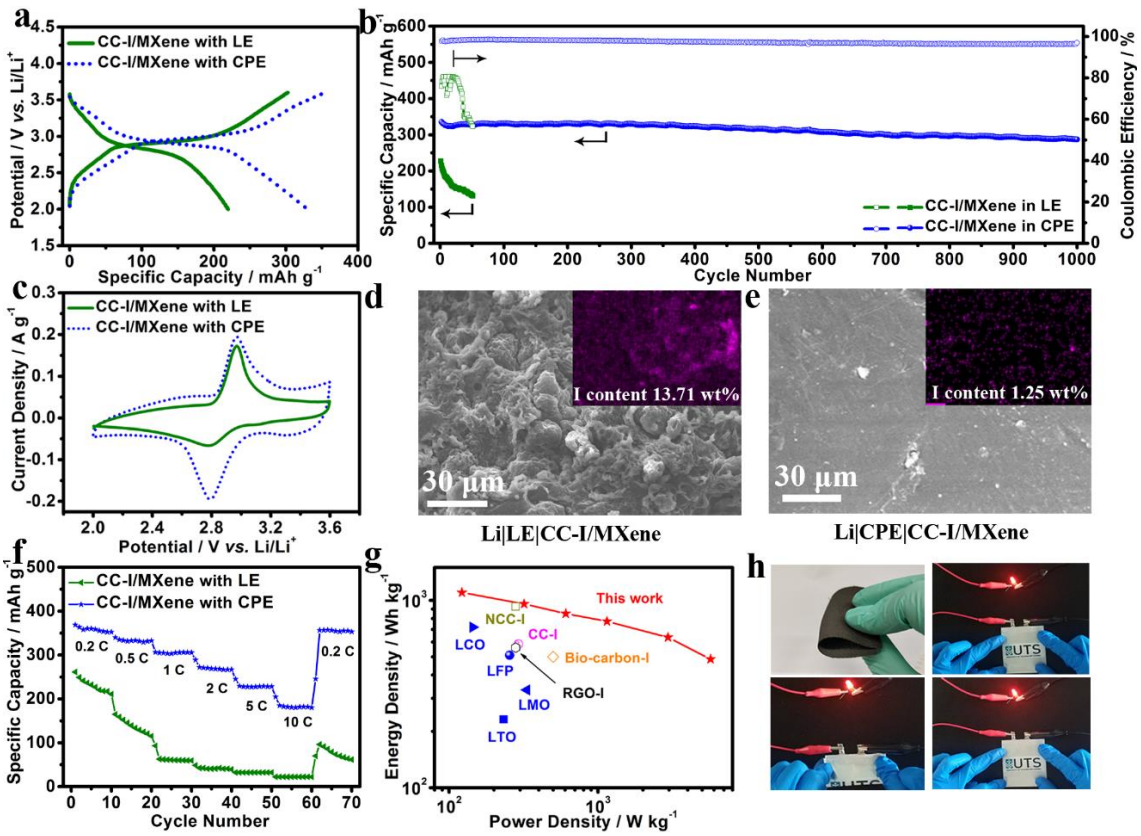

Figure 4.14. *Electrochemical characterizations of Li-I cells. (a) The initial charge/discharge curves and (b) cycling performances of Li|LE|CC-I/MXene and Li|CPE|CC-I/MXene cells at 0.5 C, and (c) CV curves at 0.1 mV* s^{-1}*. The morphologies and corresponding EDS mappings of iodine (shown in insets) of Li anodes obtained from the (d) Li|LE|CC-I/MXene and (e) Li|CPE|CC-I/MXene cells after 50 cycles at 0.5 C. (f) The Rate performances of above two Li-I cells; (g) Ragone plot of the as-assembled Li|CPE|CC-I/MXene battery compared with previously reported Li-I batteries*[149, 156, 158] *(hollow symbols) and representative Li-ion batteries*[173] *(solid symbols). (h) Digital images of an as-prepared CC-I/MXene cathode (upper right), and a red LED powered by a flexible Li|CPE|CC-I/MXene cell under flat–bent–flat states.*

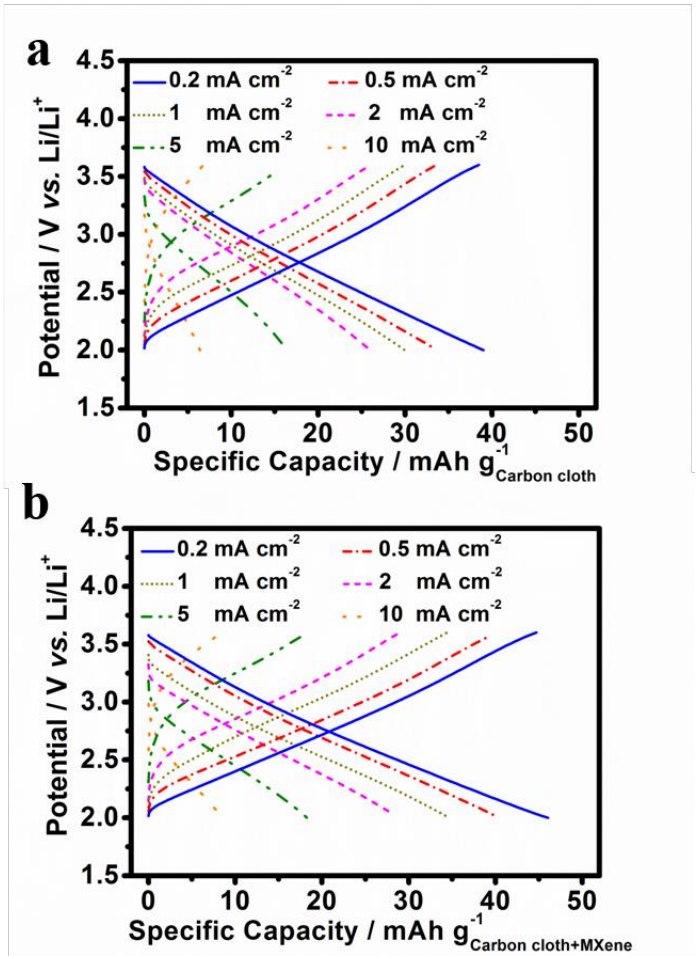

Figure 4.15. *Charge/discharge curves of (a) Li|LE|carbon cloth and (b) Li|LE|MXene wrapped carbon cloth cells at different current densities.*

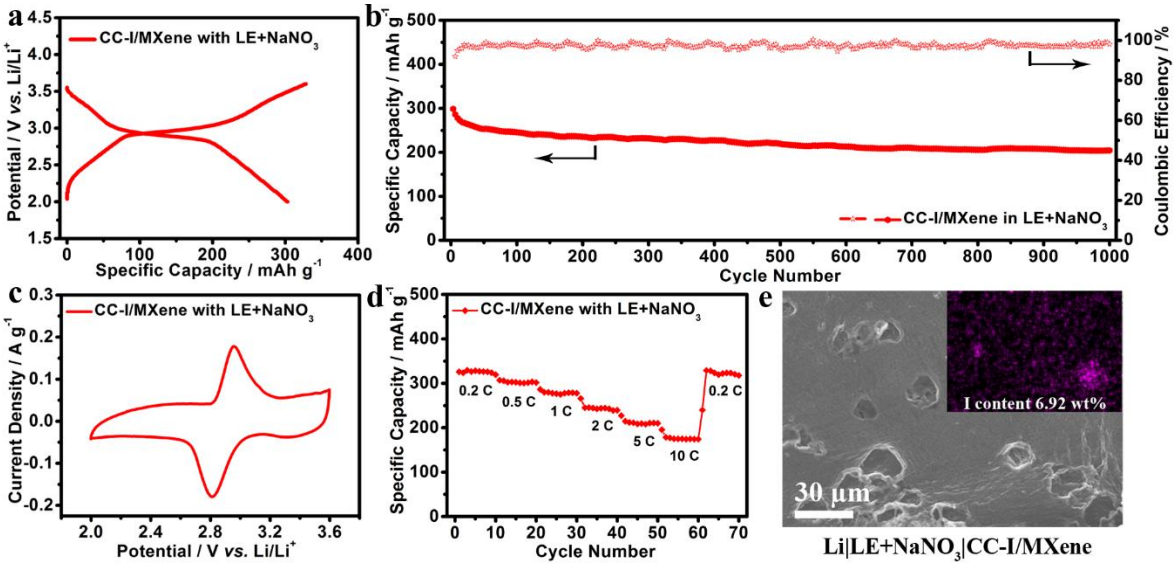

Figure 4.16. *Electrochemical characterizations of the Li|LE+$NaNO_3$|CC-I/MXene cell. (a) The initial charge/discharge curves and (b) cycling performance at 0.5 C, and (c) CV curves at 0.1 mV s^{-1}. (d) The Rate performance of the Li|LE+$NaNO_3$|CC-I/MXene cell; e) The morphology and corresponding EDS mapping of iodine (shown in insets) of Li anodes obtained from the Li|LE+$NaNO_3$|CC-I/MXene cell after 50 cycles at 0.5 C.*

Cyclic voltammetry (CV) was also performed for understanding the chemistry of Li|LE|CC-I/MXene, Li|LE+$NaNO_3$|CC-I/MXene and Li|CPE|CC-I/MXene cells. As shown in Figure 4.14c and Figure 4.16c, a Li-I cell with the $NaNO_3$-containing LE exhibits enhanced current density and reduced potential gap between the main anodic and cathodic peaks than that of the cell with the LE, which indicates the catalytic effect of $NaNO_3$ particles. Moreover, the Li-I cell using CPE shows the highest peak current density, signifying a lower polarization contributed by the synergistic optimization of the catalytic $NaNO_3$ and PETEA-based polymer matrix. For the Li|CPE|CC-I/MXene cells, the capacity contribution from different behaviours can be studied by analysing the CV curves at different scan rates. Figure 4.17a shows the initial five CV curves of Li|CPE|CC-I/MXene cell at 0.1 mV s^{-1}, in which the negligible capacity fading can be observed from the first cycle to fifth cycle, which is consistent with the excellent cycling performance of the Li|CPE|CC-I/MXene cell in Figure 4.14b. Figure 4.17b displays the CV curves of the Li-I cell

at various scan rates from 0.1 to 2 mV s^{-1}. From these CV curves, we can obtain a plot of log(peak current) as function of log(scan rate) based on equation (5-3) and (5-4)[149, 174]:

$$i = av^b \tag{5-3}$$

$$\log(i) = b\log(v) + \log(a) \tag{5-4}$$

where the i is peak current, the v is scan rate, a and b are adjustable parameters. The value of b is determined by the slope in the log(v)-log(i) plots. The b values in Figure 4.17c are calculated to be ~0.61 and ~0.65 for cathodic and anodic processes, respectively, indicating that the capacity at peak voltage is dominated by the non-capacitive behaviour.

We can also separate the non-capacitive and capacitive currents based on equation (5-5) and (5-6):[174]

$$i\,(V) = k_1 v + k_2 v^{0.5} \tag{5-5}$$

$$i\,(V)/v^{0.5} = k_1 v^{0.5} + k_2 \tag{5-6}$$

where the i(V), $k_1 v$, $k_2 v^{0.5}$, and v represent the current at a fixed voltage, the capacitive and non-capacitive currents, and scan rate, respectively. According to equation (5-5) and (5-6), by plotting $v^{0.5}$ versus $i(V)/v^{0.5}$, k_1 can be determined by the slope in the straight line while the k_2 can be obtained by the intersection of the diagram with the Y-axis.[85] Thus, non-capacitive current ($k_2 v^{0.5}$) versus voltage can be plotted in Figure 4.17d as the shadow area.

By applying the capacity separation method,[151] the non-capacitive capacity contribution can be obtained as displayed in the shadowed area of the CV curve (Figure 4.17). It is seen that during the cathodic scan, a small hump emerges at ~3.3 V *vs.* Li/Li^+, indicating the conversion of I_2 to I_3^-. And the peak at ~2.8 V can be assigned to the reaction from I_3^- to I^-. The anodic scan is a reversible

process, in which the peak at ~3.0 V indicates that I^- was oxidized to I_3^- and I_3^- was further oxidized to I_2 at ~3.3 V.[149] Noticeably, the current sharply increased from ~3.5 V vs Li/Li^+, which could be attributed to the oxidation of the NO_3^- anions, as described in the equation (5-7):[175]

$$NO_3^- - e \rightarrow NO_3 \qquad (5\text{-}7)$$

Such NO_3 has been reported to be widely exist in nature with a short life-span,[176, 177] and usually forms as a reaction intermediate in electrochemical synthesis.[178] It is speculated that, in Li-I batteries, the NO_3 radicals tend to be consumed instantly by the I_3^- anions as described in the following equation (5-8):

$$2\ NO_3 + 2\ I_3^- \rightarrow 2\ NO_3^- + 3\ I_2 \qquad (5\text{-}8)$$

Thus, $NaNO_3$ as the catalyst can effectively enhance the conversion kinetics and the transformation of I_3^- to I_2. This is well consistent with the corresponding *ex situ* Raman spectra in Figure 4.18a, in which the Raman peak of I_3^- (at ~120 cm^{-1})[179, 180] disappears at the end of the charge process (3.6 V), demonstrating a complete oxidization of I_3^- to I_2. For comparison, due to poor kinetics, the peak of I_3^- in the Li|LE|CC-I/MXene cell still exists at the end of the charge process, which means that I_3^- cannot fully revert to I_2 (Figure S15b), resulting in the limited Coulombic efficiency as shown in Figure 4.14a.

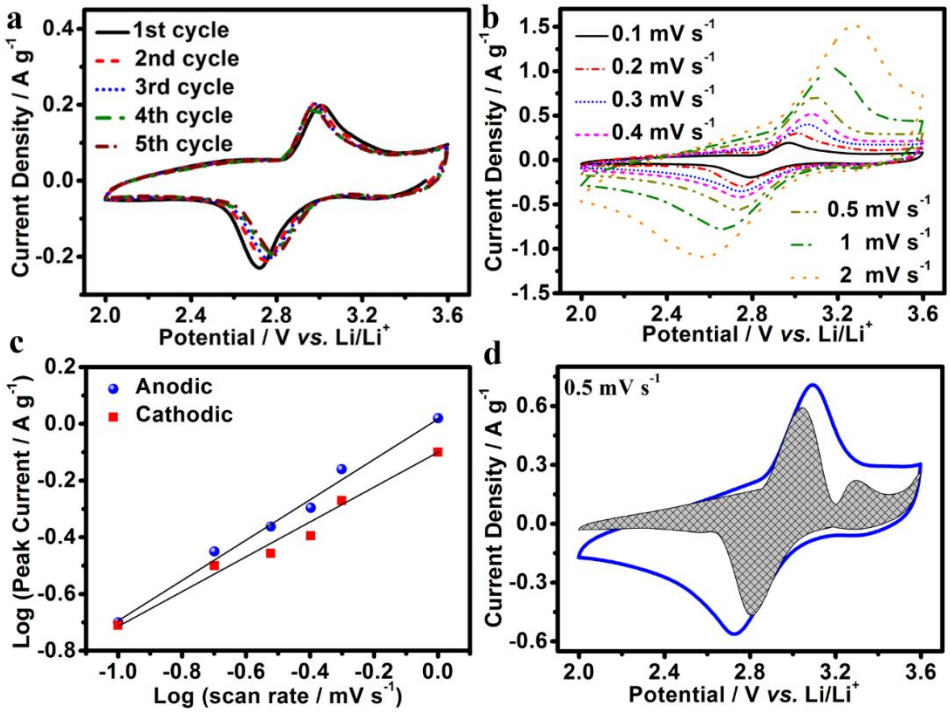

Figure 4.17. *(a) The initial five CV curves of Li|CPE|CC-I/MXene cell at 0.1 mV s^{-1}; (b) CV curves of Li|CPE|CC-I/MXene cell at different scan rates. (c) Plot of log(peak current) as function of log(scan rate) obtained from Figure S14b. (d) The calculated non-capacitive behaviour and total current in Li|CPE|CC-I/MXene cell at 0.5 mV s^{-1}.*

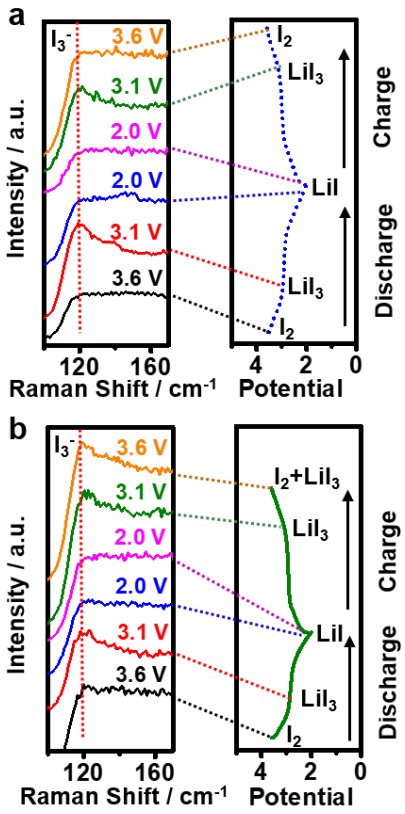

***Figure 4.18**. Ex situ Raman spectrum at various charge/discharge states and the corresponding charge/discharge curves at 0.2 C of the (a) Li|CPE|CC-I/MXene and (b) Li|LE|CC-I/MXene cells.*

Electrochemical impedance spectroscopy (EIS) was conducted to further investigate the interfacial behavior and reversibility of Li-I cells. Figure 4.19a-b present the EIS results for Li-I cells after different cycles at 0.5 C. The EIS spectra can be well-simulated via an equivalent circuit as shown in Figure 4.19c, and the simulation results are summarized in Table 4.2. According to the simulated equivalent circuit shown in the inset of Figure 4.19c, the intersection of the diagram with the real axis refers to a bulk resistance (R_b), reflecting the resistance of electrodes and electrolyte/separator. The depressed semicircle at high frequency area is ascribed to the interfacial resistance (R_f) and *CPE1*, while the depressed semicircle at medium frequency area can be attributed to the charge transfer resistance (R_{ct}) and *CPE2*. Instead of capacitance of the passivation layer (C_f) and double-layer capacitance (C_{dl}), *CPE1* and *CPE2* (the constant phase elements) have been applied in the simulated equivalent circuit to take the roughness of the surface into account. The slope line at low frequency area is equivalent to the Warburg impedance (Z_w), which is related to the kenitics transformation.[181] For the Li|LE|CC-I/MXene cell, the solid electrolyte interface resistance (R_f) sharply rises from 98.1 Ω to 187.2 Ω after 50 cycles, which correlates with the unstable SEI film and dendrite growth on the anode as well as the severe shuttle effect in the cathode.[162] In sharp contrast, after replacing the LE with CPE, the values of R_f are much lower (21.7 Ω after 1 cycle), and maintain steady with limited variation during cycling (40.0 Ω after 50 cycles). This implies an inhibition of the shuttle of iodine species and a stable electrode/CPE interface, which contribute to the significantly improved cycling performance in Figure 4.14b. The Li anodes disassembled from Li-I cells after 50 cycles were observed by FE-SEM. Massive dendrite structures and micro-sized precipitates can be found on the surface of the Li anode

disassembled from the Li|LE|CC-I/MXene cell, and the iodine content on such anode is as high as 13.71 wt% (Figure 4.14d, corresponding to the digital image in Figure 4.20). The Li anode from the Li|LE+$NaNO_3$|CC-I/MXene cell shows an iodine content of 6.92 wt% (Figure 4.16e). With the CPE, the surface of Li anode tends to be smooth and the growth of Li dendrite has been remarkably suppressed. The iodine content of this Li anode is as low as 1.25 wt% (Figure 4.14e), confirming the successful suppression of shuttle effect.

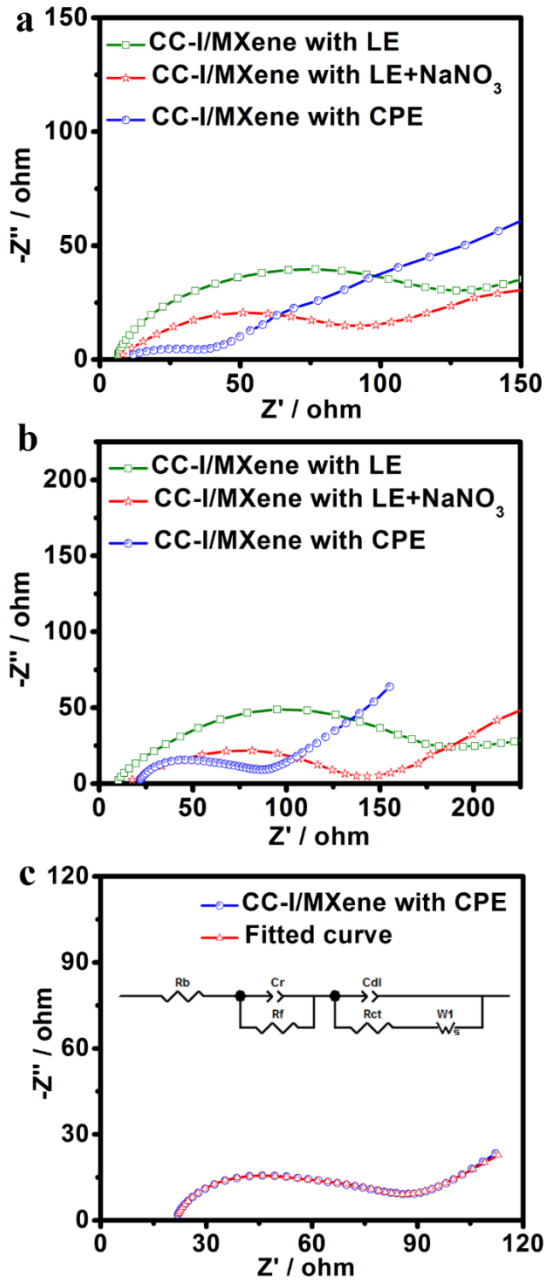

Figure 4.19. *EISs of Li|CPE|CC-I/MXene, Li|LE+$NaNO_3$|CC-I/MXene, and Li|LE|CC-I/MXene cells. (a) after the 1st cycle and (b) after the 50th cycle at 0.5 C, measured in the half charged state; (c) Experimental and simulation EIS curves of the Li|LE|CC-I/MXene cell using an equivalent circuit shown in inset.*[181]

Table 4.2. *EIS simulation results from Figure 4.19.*

Battery sample	After 1st cycle			After 50th cycle		
	R_b (Ω)	R_{ct} (Ω)	R_f (Ω)	R_b (Ω)	R_{ct} (Ω)	R_f (Ω)
Li|LE|CC-I/MXene	6.0	39.6	98.1	10.1	37.9	187.2
Li|LE+$NaNO_3$| CC-I/MXene	8.2	33.2	63.8	17.7	30.5	100.5
Li|CPE|CC-I/MXene	10.1	21.2	21.7	21.9	22.8	40.0

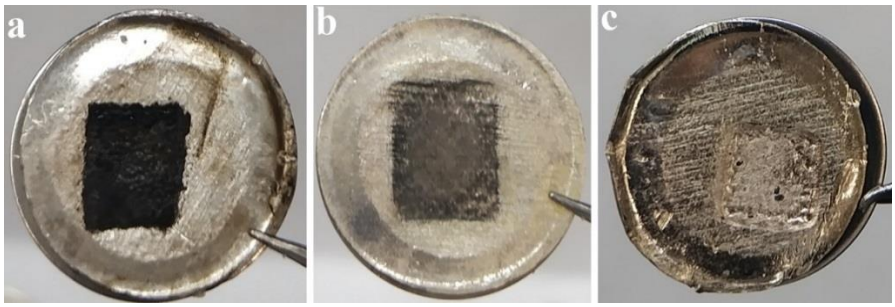

Figure 4.20. *Digital images of Li anodes obtained from (a) Li|LE|CC-I/MXene, (b) Li|LE+$NaNO_3$|CC-I/MXene and (c) Li|CPE|CC-I/MXene cells after 50 cycles at 0.5 C.*

The rate performances of Li-I batteries are shown in Figure 4.14f and Figure 4.16d. Meanwhile, the corresponding voltage profiles are presented in Figure 4.21. The Li|CPE|CC-I/MXene cell delivered specific capacities of 358, 332, 303, 268 and 227 mAh g^{-1} at 0.2 C, 0.5 C, 1 C, 2 C and 5 C, respectively. Even at a high current density of 10 C, the cell can still maintain a capacity of 182 mAh g^{-1}, which is higher than Li|LE|CC-I/MXene and Li|LE+$NaNO_3$|CC-I/MXene cells. Furthermore, the charge/discharge potential gap of the cell with CPE is smaller than that of the cell with LE, which agrees very well with CV curves in Figure 4.14c. Li|CPE|CC-I/MXene cells

with different areal mass loadings of iodine in the cathodes were further cycled at 0.5 C. With high iodine loadings of 7.5 and 10 mg cm^{-2}, the cell still can achieve capacities of 243 and 160 mAh g^{-1} after 350 cycles, respectively (Figure 4.22). Ragone plots (Figure 4.14g) have been used to compare the power densities and energy densities of the as-developed Li|CPE|CC-I/MXene battery with previously reported Li-I batteries and representative Li-ion batteries. Obviously, the novel MXene-based Li-I battery delivers high energy densities (1050 Wh kg^{-1} at 0.2 C and 485 Wh kg^{-1} at 10 C) and power densities (125 W kg^{-1} at 0.2 C and 5700 W kg^{-1}at 10 C; Table 4.3), which are much higher than most of the previously reported Li-I batteries (*e.g.* Li||RGO-I: 560 Wh kg^{-1} at 1 C; Li||CC-I: 580 Wh kg^{-1} at 100 mA g^{-1}; Li||NCC-I: 920 Wh kg^{-1} at 100 mA g^{-1}; Li||Bio-carbon-I: 500 Wh kg^{-1} at 1 C)[149, 156, 158] and representative lithium-ion batteries (*e.g.* Li||$LiFePO_4$: ~510 Wh kg^{-1}, *etc.*).[173]

To explore the potential application of the CC-I/MXene electrode and CPE in flexible devices, a soft packed Li-I battery was fabricated (Figure 4.14h). The Li|CPE|CC-I/MXene battery can readily power a red light-emitting diode (LED) lamp under a repeated flat–bent–flat test. This demonstrates that the CC-I/MXene electrode can maintain structural integrity and the electrode/CPE interfaces can keep tight adhesion under a dramatic shape deformation.

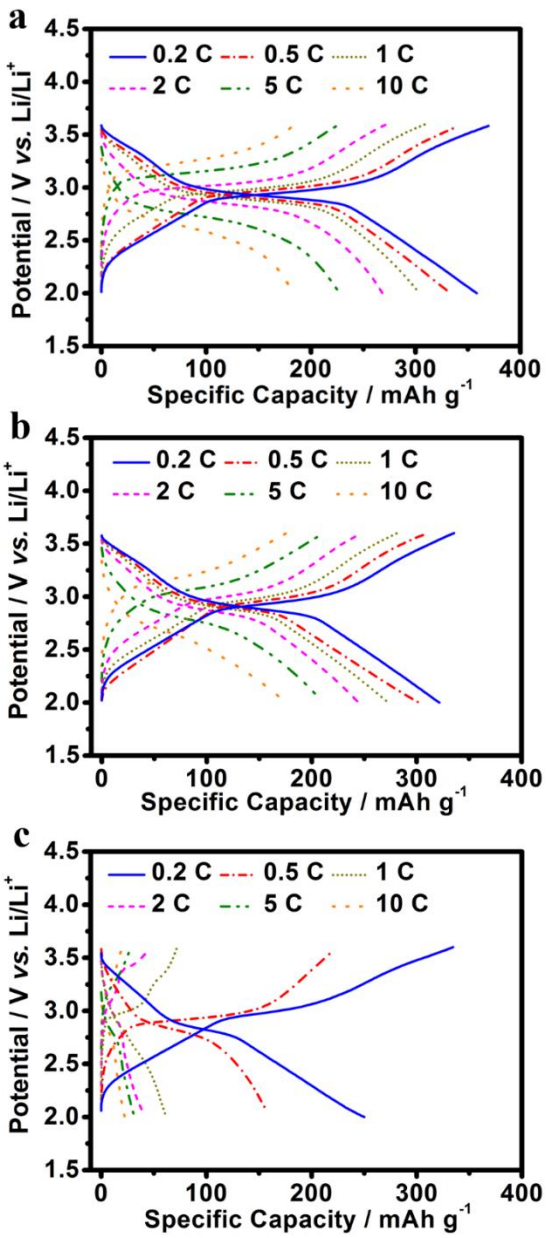

Figure 4.21. *Charge/discharge curves of (a) Li|CPE|CC-I/MXene, (b) Li|LE+$NaNO_3$|CC-I/MXene, and (c) Li|LE|CC-I/MXene cells at different current densities.*

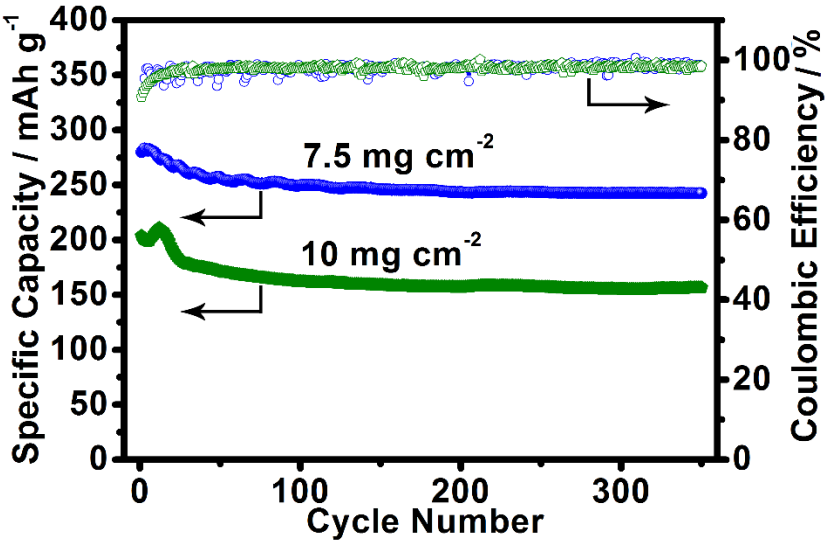

Figure 4.22. *Cycling performances of the Li|CPE|CC-I/MXene cell at 0.5 C with different areal mass loading of iodine in the cathode.*

Table 4.3. *The power densities and energy densities of the Li|CPE|CC-I/MXene cell.*

Current Density	0.2 C	0.5 C	1C	2C	5C	10 C
Power Density ($W\ kg^{-1}$)	125	320	610	1150	2710	5700
Energy Density ($Wh\ kg^{-1}$)	1050	960	850	775	540	485

Theoretical calculations were conducted to further investigate the interaction between iodides (LiI_3 was selected as a representative of iodides) and MXenes as well as electrolyte. Figure 4.23a-b reveals that the binding energies of DOL-LiI_3 and DME-LiI_3 are calculated to be -0.99 and -1.16 eV, respectively, which are stronger than that of graphene-LiI_3 (-0.79 eV).[155] Thus, the LiI_3 molecules prefer to dissolve into these electrolyte solvents and shuttle to the anode. In contrast, the binding energy of PETEA-LiI_3 is around -1.86 eV. Consequently, LiI_3 molecules are

preferentially immobilized by the functional groups in the polymer matrix of CPE, leading to its low solubility and slow diffusion in the CPE. This is highly consistent with the experimental results shown in Figure 4.11e. Furthermore, as shown in Figure 4.23d-f, binding energies of LiI_3 with $Ti_3C_2T_x$ MXenes (-1.76 eV for $Ti_3C_2F_2$ (Figure 4.23d), -1.95 eV for $Ti_3C_2O_2$ (Figure 4.23e), and -2.1 eV for $Ti_3C_2(OH)_2$ (Figure 4.23f) are also much stronger than those of LiI_3 with electrolyte solvents, indicating that LiI_3 molecules prefer to adhere to the cathode/CPE surface rather than dissolve into the electrolyte. Notably, the difference in charge density of LiI_3 adsorbed on $Ti_3C_2T_x$ MXenes (Figure 4.23g-h and Figure 4.24) shows apparent charge transfer from MXenes to LiI_3, verifying the strong chemical interactions between LiI_3 and MXene, which leads to the enhanced binding energy as mentioned above. Therefore, the above-mentioned theoretical calculation results convincingly prove that MXene and CPE can cooperatively suppress the shuttle of iodine species and therefore improve the performance of Li-I batteries.

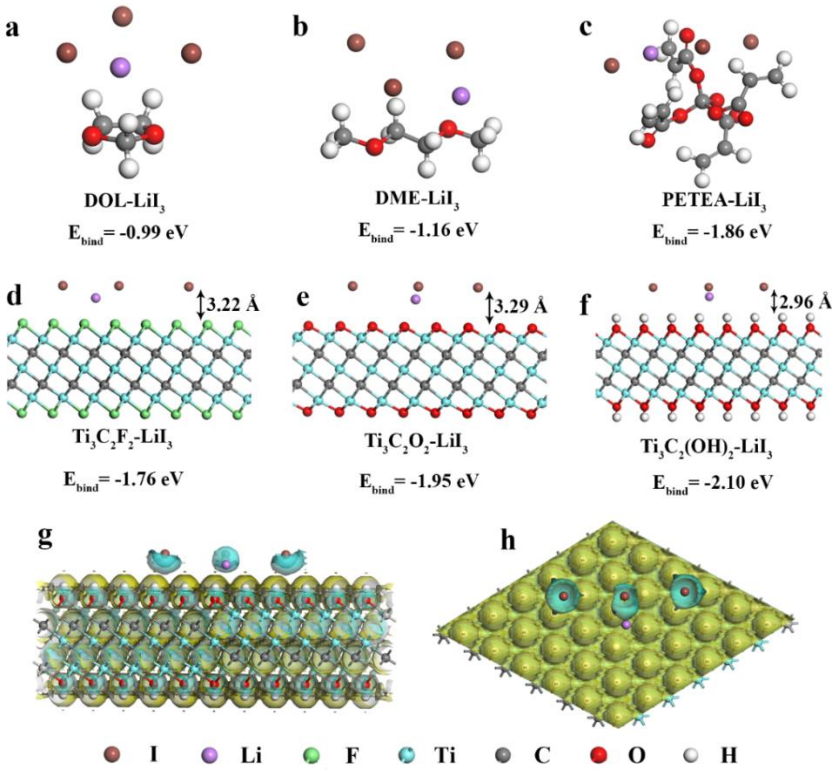

Figure 4.23. *Theoretical calculations. Molecular models and calculated binding energies of LiI_3 with (a) DOL; (b) DME; (c) PETEA monomer and (d) $Ti_3C_2F_2$; (e) $Ti_3C_2O_2$; (f) $Ti_3C_2(OH)_2$ as $Ti_3C_2T_x$ MXenes. g) Side view and h) top view of the difference in charge density for the optimized structure of LiI_3 adsorbed on $Ti_3C_2(OH)_2$ MXene. Yellow and blue color indicate the charge depletion and accumulation, respectively.*

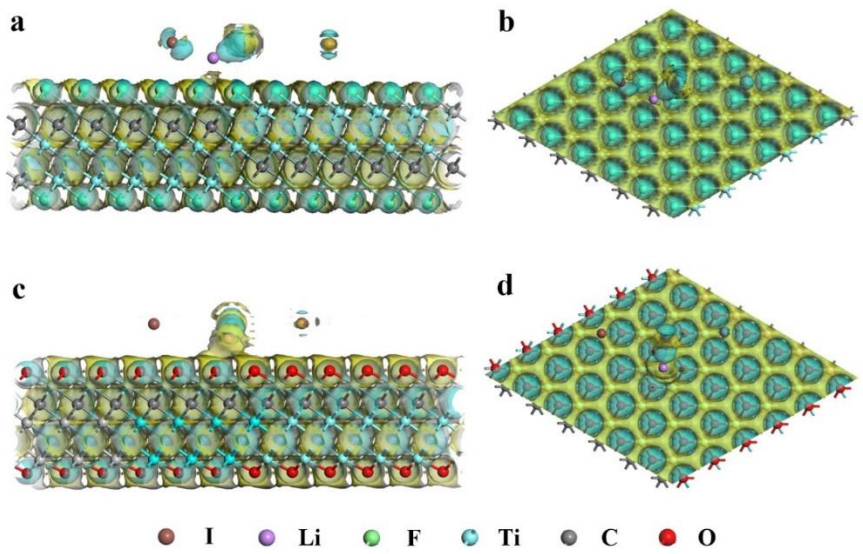

***Figure 4.24**. a) Side view and b) top view of the difference in charge density for the optimized structure of LiI_3 adsorbed on $Ti_3C_2F_2$ MXene. c) Side view and d) top view of the difference in charge density for the optimized structure of LiI_3 adsorbed on $Ti_3C_2O_2$ MXene. Yellow and blue color indicate the charge depletion and accumulation, respectively.*

4.4 Conclusions

In summary, we have discovered that the synergistic optimization of a CC-I/MXene cathode in conjunction with a composite polymer electrolyte can significantly suppress the self-discharge and enhance the reversible capacity of Li-I batteries. The MXene sheets wrapped on the CC-I electrode possess a high binding energy with iodine species, which successfully restrains them in the cathode. The PETEA-based polymer matrix in the *in situ* prepared CPE not only immobilizes the iodine species against dissolution and diffusion, but also forms a stable Li anode/CPE interface to suppress the growth of Li dendrites. $NaNO_3$ particles acts as a catalyst to efficiently improve the Coulombic efficiency of batteries by enhancing the transformation kinetics of LiI_3 in the cathode, and also improve the mechanical strength of CPE. The CC-I/MXene and CPE cooperatively enables a quasi-solid-state Li-I battery with high energy/power density, excellent cycling performance and good flexibility. This work opens a new path to inspire the development of high-

performance Li-I batteries and other novel Li-based rechargeable batteries (*e.g.* Li-oxygen, Li-sulfur, and Li-selenium batteries).

Chapter 5 High-performance potassium-sulfur batteries enabled by MXene-based dendrite-free potassium metal anodes

5.1 Introduction

The soaring demands from the electrification of road transportation and grid-scale energy storage require rechargeable batteries with high energy density and low cost.[146] Although lithium-ion batteries have achieved tremendous successes in commercial applications, they are constrained by limited and localized resources of lithium in the earth's crust.[182] As an alkali metal with chemical similarity to lithium, potassium (K) is about three orders of magnitude more abundant than lithium geographically.[183] Furthermore, the K^+/K couple exhibits the lowest redox potential in nonaqueous media (*e. g.*, propylene carbonate) compared with other alkaline metal ions, which endows potassium-based batteries with high operating voltage and energy density.[184] Potassium ions also possess a higher transference number and ionic conductivity than sodium ions and lithium ions due to potassium's weak Lewis acidity and low desolvation energy, which is expected to facilitate fast diffusion kinetics in batteries.[185] These advantages make potassium-based batteries as high-performance and low-cost rechargeable battery system for large-scale energy storage applications.

Among the anode candidates of potassium-based batteries, K metal has attracted special attention due to its lower potential (-2.93 V *vs.* the standard hydrogen electrode (SHE)) and higher specific capacity (~687 mAh g^{-1}) compared to other anode materials including carbonaceous, alloying, and intercalation compounds.[186, 187] The utilization of K metal anodes can also eliminate ancillary current collectors in anodes, and thus dramatically increase the energy density of batteries. Moreover, K metal anodes enable the application of unpotassiated cathodes for high-energy-density battery systems based on conversion chemistry, *e. g.*, potassium-oxygen (K-O_2) and potassium-sulfur (K-S) batteries.[188]

However, reversible plating and stripping of K metal in electrolytes remains a major challenge. It is well-known that the highly reactive K metal spontaneously reacts with electrolyte compounds to form a solid electrolyte interphase (SEI) on its surface.[189] Due to the "hostless" nature of potassium metal, such an SEI film can be easily broken by mechanical deformation during K deposition/stripping process, which promotes non-uniform ionic flux and leads to the growth of K dendrites.[190] The resulting K dendrites can penetrate the separator, and result in an internal short circuit, causing safety hazards (e. g., combustion and explosion).[191] Furthermore, dendrite growth can expose a large surface area of fresh K metal, leading to a continuous breakdown/re-construction of SEI during cycling, and finally forming isolated electrochemically inactive "dead K". These dramatically decrease the Coulombic efficiency and lifespan of K metal batteries.[186] In the case of K-O_2 and K-S batteries, inhomogeneous K deposition will also enlarge the reaction area with soluble intermediate products (i. e., oxygen species and polysulfides), which aggravates their shuttling and further deteriorates the battery performance.[192]

To date, the research on K metal anodes is still in its infancy. Several works have been reported on restraining dendrite growth on K metal anodes by replacing K metal with a K-Na alloy,[186, 193] surface engineering on K metal[190] or stabilizing the SEI by optimizing liquid electrolyte composition.[194] However, the employment of liquid-state K-Na alloy anodes may induce severe safety concerns. Meanwhile, the surface engineering or electrolyte optimization alone cannot suppress the huge volumetric change during K plating/stripping.[153] In contrast, confining K metal into a three-dimensional (3D) matrix is expected to accommodate the volumetric changes at the electrode level, and simultaneously decrease local current density by spreading ion flow laterally, thus blocking the growth of K dendrites. Herein, for the first time, we present a defect-rich and nitrogen-containing MXene ($Ti_{3-x}CNT_y$, labeled as DN-MXene, where T represents surface

functional groups, x and y are adjustable numbers)/carbon nanotube (CNT) free-standing scaffold as a K metal host to control nucleation behavior and suppress dendritic growth. This porous scaffold with abundant interconnected voids enables massive loading of metallic K and preserves a constant electrode dimension during plating/stripping. Owing to the high electronic transport and fast K ion diffusion,[195, 196] the as-prepared scaffold efficiently reduces the effective local current density and facilitates a uniform K ionic flux. More importantly, as verified by theoretical calculations and experimental investigations, the DN-MXene sheets in the scaffold possess high potassium-philic characteristic. This enables them to act as "seed points" to initiate the K nucleation during cycling, which effectively prevents the direct plating of K outside of the scaffold. As a result, the as-prepared K metallic anode (K@DN-MXene/CNT) exhibits a dendrite-free morphology with high Coulombic efficiency (~98.6%), low overpotential and long cycle life during repeated K plating/striping process. When applied in K-S batteries, the as-assembled full cell shows an enhanced specific capacity and cycling performance compared with cells using bare K anodes.

5.2 Experimental section

5.2.1 Sample preparation

Synthesis of the defect-rich and N-containing MXene sheets: Ti_3AlCN with a particle size of < 38 μm was synthesized according to the previous report.[13] Then, 3 g of as-prepared Ti_3AlCN powder was etched in a mixture of 3 g lithium fluoride (LiF, Alfa Aesar) and 30 mL 9 M hydrochloric acid (HCl, Fisher Scientific) at ~35 ºC for 24 hours to extract the Al atoms and obtain multilayered $Ti_{3-x}CNT_y$ suspension. The obtained suspension was repeatedly rinsed with distilled water and centrifuged (3500 rpm) until the pH of the supernatant was higher than 5.

Preparation of the free-standing DN-MXene/CNT scaffold and CNT scaffold: The CNTs was purchased from Shenzhen Nanotech Port Co. Ltd., China. DN-MXene/CNT porous scaffold was prepared by a filtration method. Briefly, 10 mL $Ti_{3-x}CNT_y$ MXene aqueous suspension (~1 mg mL^{-1}) was added dropwise into 40 mL CNT aqueous suspension (~1 mg mL^{-1}). The obtained mixture was then sonicated for 20 min under Ar atmosphere followed by filtration with a Celgard 3501 membrane. Porous DN-MXene/CNT scaffold can be obtained after rinsing with distilled water several times followed by freeze drying. In comparison, the CNT scaffold can be prepared by the same method without adding DN MXene sheets. The weight of the as-fabricated scaffolds was about ~4 mg cm^{-2}.

Preparation of the K@MXene/CNT: To prepare K@DN-MXene/CNT anodes, a melt-infusion process was performed in an Ar-filled glove box (Universal 2440/750) with a moisture/oxygen concentration below 0.1 ppm. K metal was firstly heated over 70 ºC on a hot plate. Subsequently, DN-MXene/CNT matrix was immersed into the molten potassium, held for 20 seconds and then cooled to room temperature to obtain K@DN-MXene/CNT anode. The mass loading of K was measured by weighting the mass change before and after melt-infusion process, which is about 70 wt%.

5.2.2 Characterization and electrochemical tests

Characterizations: The XRD patterns of the as-prepared samples were collected by using Bruker D8 discover XRD with Cu Kα radiation (40 KV and 40 mA). Raman spectra of samples were measured using a Renishaw inVia Raman spectrometer system (Gloucestershire, UK). X-ray photoelectron spectroscopy (XPS) measurements were performed on a Kratos XSAM-800 spectrometer. The morphology of the samples was observed using field emission scanning electron microscope (FE-SEM, Zeiss Supra 55VP) and High angle annular dark field (HAADF)-scanning

transmission electron microscopy (STEM) (JEOL JEM-ARM200) operated at an accelerating voltage of 200 kV. Atomic force microscopy (AFM) measurements were performed on a Dimension 3100 SPM by using a tapping mode.

Assembly and testing of batteries: CR2032 coin cells were assembled in an Ar-filled glove box. 0.8 M KPF_6 in EC/DEC (1: 1, v/v) or 0.8 M KFSI in EC/DEC (1: 1, v/v) was selected as electrolyte. To study the electrochemical deposition of K, different scaffolds and current collectors (DN-MXene/CNT, CNT, Cu foil, and Al foil) were assembled into coin cells with K metal foil as counter/reference electrode and glass fiber membrane (Whatman GF/A) as separator. Before the tests, the cells were activated by discharging to 0.01 V and then charging to 1 V at a current density of 0.5 mA cm^{-2}. To test the K plating/stripping behavior, metal anodes were first plated on different scaffolds at a current density of 0.5 mA cm^{-2} under a deposition capacity of 1 mAh cm^{-2} and then stripped to 1 V. To test the specific capacity of the as-prepared K@DN-MXene/CNT anode, the K@DN-MXene/CNT anode were assembled into coin cells with cu foil and glass fiber membrane. The symmetric cells were assembled with two pieces of identical electrodes (K@DN-MXene/CNT, K@CNT or bare K foil), in which the K@CNT anode was prepared by electrodepositing 2 mAh cm^{-2} amount of K onto the CNT scaffold at a current density of 0.5 mA cm^{-2}. Cycling performances were studied by galvanostatic cycling measurement consisting of repeated charge (1 h)-discharge (1 h) cycles on symmetric cells at a current density of 0.5 mA cm^{-2}. The rate performances were investigated by galvanostatic cycling measurement consisting of repeated charge (1 h)-discharge (1 h) cycles on symmetric cells at various current densities. The *in situ* optical observations were conducted by using a homemade transparent cell. Such a transparent cell consists of a working electrode (DN-MXene/CNT or Cu) and a K chip acting as counter/reference electrode. After adding 200 μL of electrolyte (0.8 M KPF_6 in EC/DEC (1:1 v/v)), this cell was sealed with a cover

glass window. The cell was connected with a CHI660E electrochemical station for K plating experiments. The K deposition processes were observed by an optical microscope (OLS-4000 OLYMPUS).

For K-S full cells, SPAN as cathode material was synthesized according to the previous report.[40] Briefly, polyacrylonitrile and sulfur with a mass ratio of 1:4 were ground and transferred into a sealed vessel. The SPAN samples can be obtained by heating the mixture at 155 ºC for 1 h and 450 ºC for 5 h in Ar atmosphere with a heating rate of 5 ºC min^{-1}. The cathodes consisted of 80% SPAN active material, 10% conductive agent (carbon black) and 10% polyvinylidene fluoride (PVDF) as binder. The as-developed SPAN cathode was coupled with K@DN-MXene/CNT (or bare K metal foil) anodes, glass fiber separator and 0.8 M KPF_6 in EC/DEC electrolyte. The mass loading of sulfur and electrolyte/sulfur ratio in each cell was uniformly set at as 1.2 mg cm^{-2} and ~40 μL mg^{-1}, respectively. Before the cycling and rate tests, the as-assembled K-S cells were first activated by pre-cycling at 0.5 C (1 C = 250 mA g^{-1} based on the mass of sulfur) between 0.8 and 2.8 V on a Land 2001 A battery testing system at 25 ºC. Cyclic voltammograms (CVs) of the assembled cells were tested using a VMP3 electrochemical workstation (BioLogic, France) at a scanning rate of 0.1 mV s^{-1}. Electrochemical impedance spectra (EISs) of cells were examined using the VMP3 multichannel electrochemical station in a frequency range of 10^{-2} to 10^{5} Hz by applying a disturbance amplitude of 5 mV. The cells after designated cycling tests were transferred into a glove box and disassembled for post mortem analysis.

5.2.3 ***Theoretical calculations***: All structure relaxation and electronic structure calculations were performed using density functional theory (DFT) with the projector-augmented wave method. The exchange-correlation functional of Perdew, Burke, and Enzerhof (PBE) was employed to analyze the exchange and correlation potentials. The cut-off energy level was set as 500 eV, the SCF

tolerance level was set as 1.0×10^{-5} au in geometry optimization, while the SCF tolerance was set as 1.0×10^{-6} for energy calculation. The semi-empirical London dispersion corrections of Grimme *et al.* were applied to account for the van der Waals dispersion interactions.[164]

5.3 Results and discussion

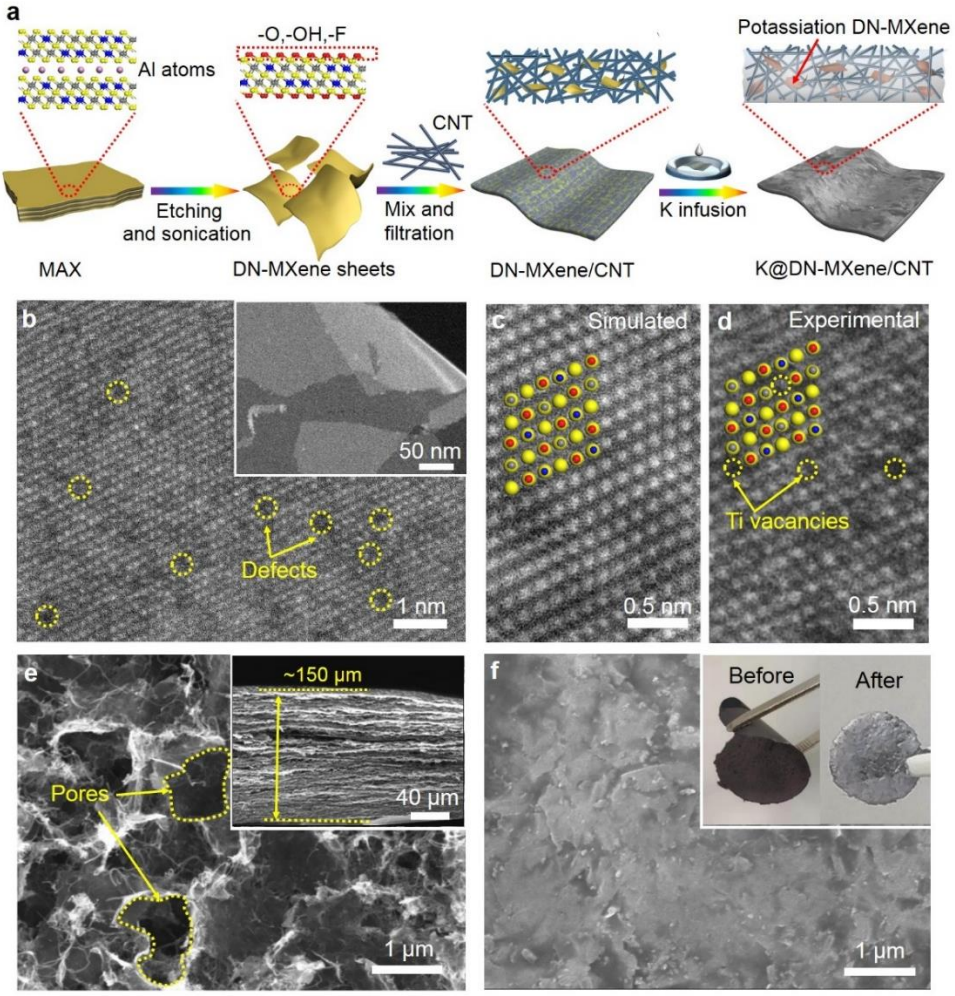

Figure 5.1. *Schematic illustration and morphological characterizations.* ***(a)*** *Schematic illustration for the preparation of the DN-MXene/CNT scaffold and K@DN-MXene/CNT metallic anodes;* ***(b)*** *High-magnification HAADF-STEM images of DN-MXene sheets;* ***(c)*** *The simulated and* ***(d)*** *corresponding experimental atomic-resolution HAADF-STEM images of the DN-MXene sheets; Ti: yellow atoms, C: grey atoms, N: blue atoms, Ti vacancy: circles, surface groups: red atoms.* ***(e)*** *Top-view and cross-sectional (shown in inset) SEM images of the DN-MXene/CNT scaffold;* ***(f)*** *Top-view SEM image of a K@DN-MXene/CNT metallic anode; Optical images of DN-MXene/CNT free-standing scaffold before (left) and after (right) the infusion process are shown in inset.*

Synthesis and characterization. Figure 5.1a illustrates the preparation method of the DN-MXene/CNT free-standing scaffold. Briefly, delaminated DN-MXene sheets (Figure 5.2) were obtained by extracting aluminum atoms from MAX precursor (Ti_3AlCN) followed by sonication. As shown in the high-resolution N 1s XPS spectrum in Figure 5.3, peaks at ~396.6 eV and ~397.2 eV can be assigned to the TiCN and N-Ti-T_x bonds, respectively, which confirms the formation of the DN-MXene.[197] High angle annular dark field (HAADF) scanning transmission electron microscopy (STEM) analysis was performed to resolve the crystal structure and defects of the as-prepared $Ti_{3-x}CNT_y$ MXene sheets. Figure 5.1b presents HAADF-STEM images of DN-MXene sheets. Combined with atomic force microscopy (AFM) result in Figure 5.4, the as-obtained DN-MXene shows an ultrathin sheet morphology with a thickness of around 2 nm. Noticeably, massive defects (including Ti vacancies and Ti vacancy clusters) appear in DN-MXene due to the introduction of nitrogen. Figure 5.1c and d show the simulated and experimental atomic-resolution HAADF-STEM images acquired along the c axis of the $Ti_{3-x}CNT_y$ MXene sheet, respectively, which are overlaid with the projected atomic structure models. The yellow atoms arranged in a hexagonal pattern directly correspond to the stacked Ti atoms in sub-layers. Both simulated and experimental images display slight lattice distortion, compared with N-free titanium carbide MXene in the previously reported literature[198], which may result from the substitution of carbon by nitrogen in the DN-MXene sub-layers.[199] Additionally, abundant Ti vacancies unambiguously exist in the experimental atomic-resolution HAADF-STEM image of the as-obtained $Ti_{3-x}CNT_y$ MXene (Figure 5.1d), which can benefit K metal deposition when applied in batteries, as discussed below.

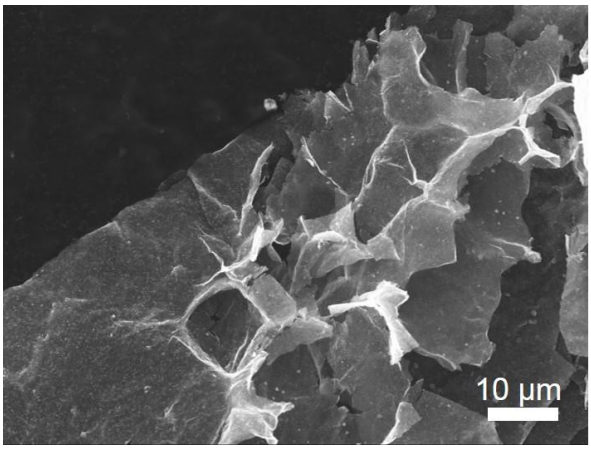

Figure 5.2 *The SEM image of the as-prepared $Ti_{3-x}CNT_y$ MXene sheets. Scale bar is 10 µm.*

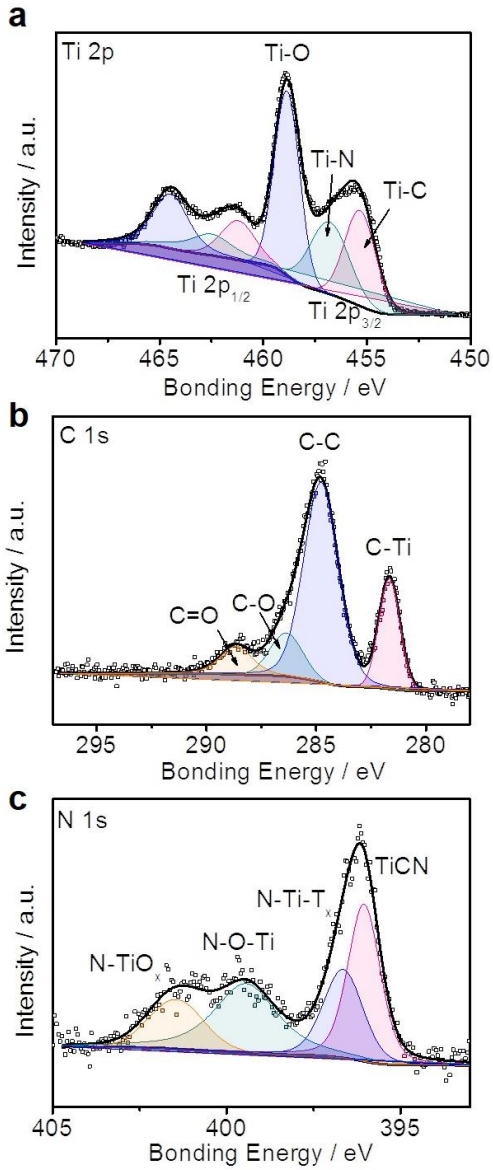

Figure 5.3 *High resolution XPS spectra of* ***a*** *Ti 2p,* ***b*** *C 1s, and* ***c*** *N 1s of the DN-MXene/CNT scaffold.*

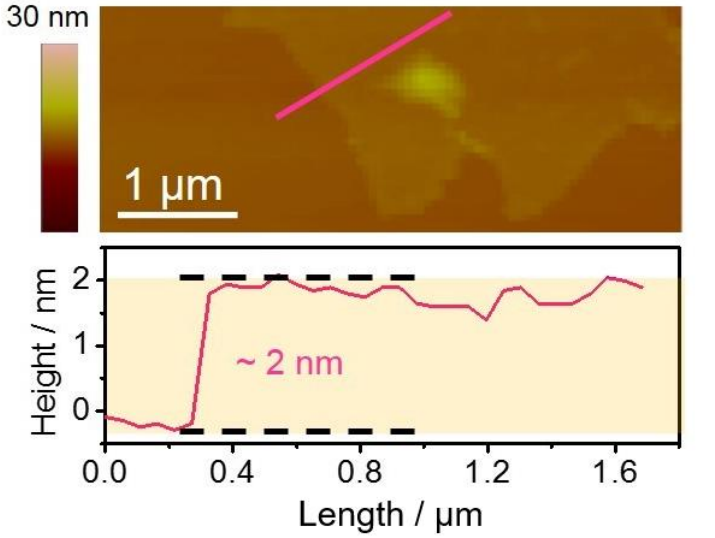

Figure 5.4 *AFM image and corresponding height profiles of the as-obtained* $Ti_{3-x}CNT_y$ *MXene sheet.*

After mixing DN-MXene sheets with CNTs, the free-standing scaffolds were prepared by a simple filtration method (Figure 5.1a, right panel). The top-view (Figure 5.1e) and cross-sectional (the inset in Figure 5.1e and Figure 5.5) morphologies of the DN-MXene/CNT scaffold were observed by scanning electron microscopy (SEM). It is clearly observed that CNTs are homogeneously distributed on the DN-MXene sheets, offering a three-dimensional network for high electron-conducting and fast ionic-transport paths. Additionally, the DN-MXene/CNT scaffold with a thickness of ~150 μm presents a porous structure with massive interconnected voids, while the CNT-only scaffolds prepared by same method show relatively dense and compact structure (Figure 5.6). This elucidates that a small amount of two-dimensional DN-MXene sheets (~20 wt%) added into the skeleton can greatly improve the porosity of the one-dimensional CNT-based scaffold, which is beneficial for the K metal loading that could improve the energy density

of K metal-based batteries. Furthermore, the X-ray diffraction (XRD) and Raman results shown in Figure 5.7 confirms the successful preparation of DN-MXene/CNT scaffolds.

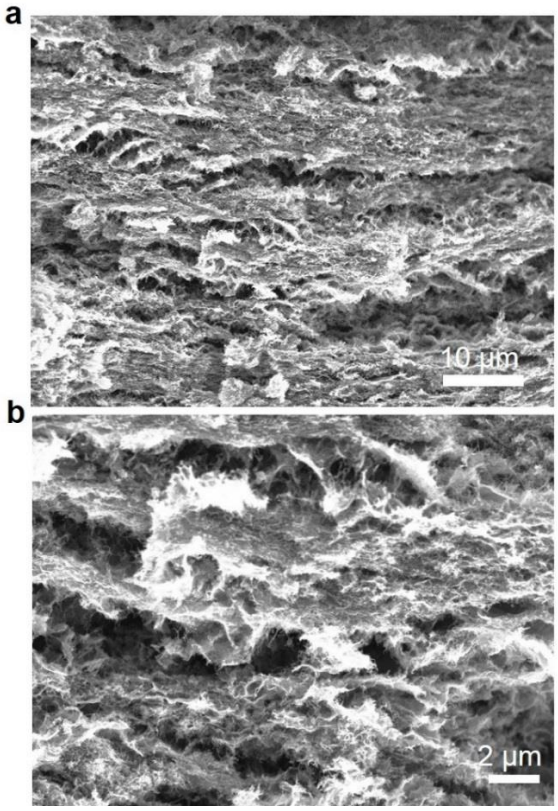

Figure 5.5. *The cross-sectional morphologies of the DN-MXene/CNT scaffold.*

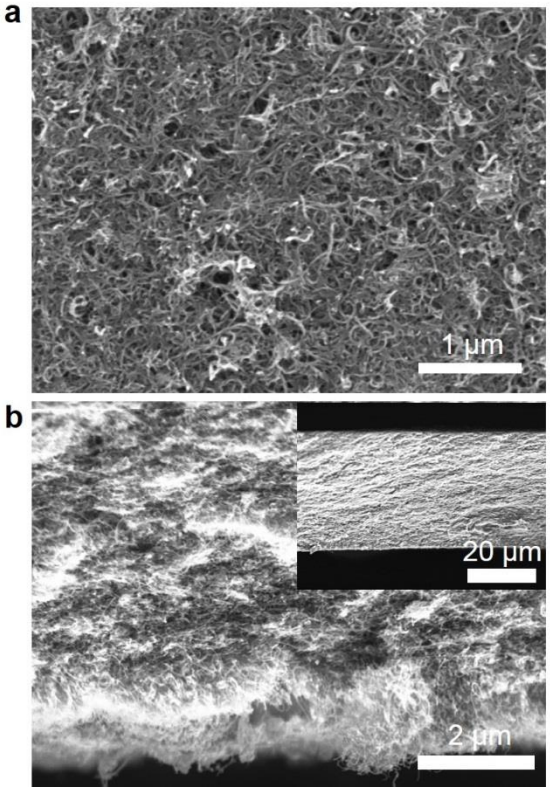

Figure 5.6. *The (**a**) top-view and (**b**) cross-sectional morphologies of the CNT scaffold.*

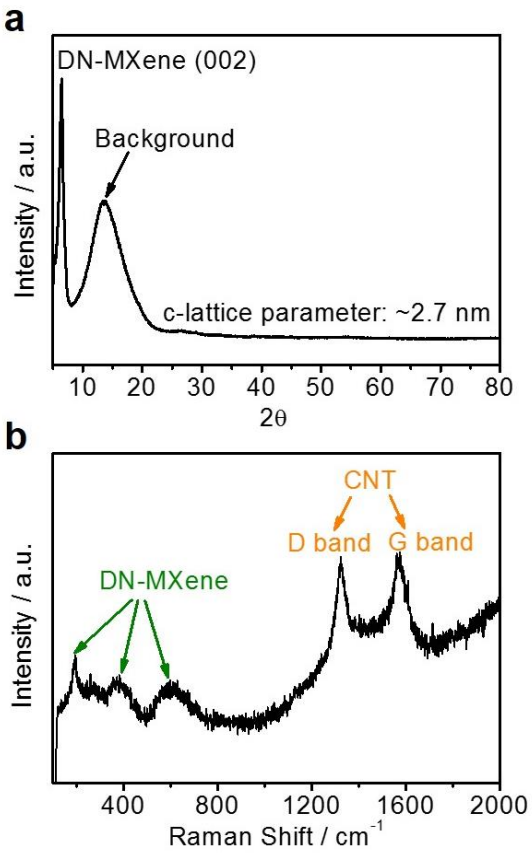

Figure 5.7. *(**a**) XRD and (**b**) Raman spectra of the DN-MXene/CNT scaffold. (Supplementary Note 2.)*

Subsequently, taking advantage of the low melting point of K (~63 ºC), solid K metal was heated to melt into liquid-state, which can directly absorb onto the scaffold (Figure 5.1a and Figure 5.8). The optical image (left inset of Figure 5.1f) of the as-prepared DN-MXene/CNT scaffold exhibits excellent bending ability, which makes it a promising flexible host for K metal. After the K infusion, the anode surface presents an obvious metallic luster, indicating the successful loading of metallic K into the porous structure of the scaffold (the right inset of Figure 5.1f). Furthermore, SEM image of a K@DN-MXene/CNT composite anode verifies that K metal is uniformly distributed in the pores of the scaffold (Figure 5.1f). The K@DN-MXene/CNT composite anodes

prepared by this melt infusion strategy can be directly coupled with K-free cathodes to construct high-performance full batteries.

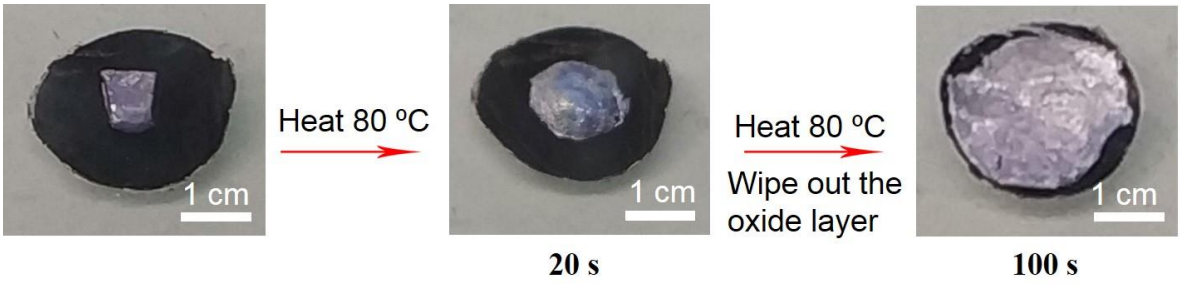

Figure 5.8. *The optical images showing that K metal melting and diffusion on the DN-MXene/CNT scaffold.*

Density functional theory (DFT) calculations and characterizations of potassium-philic property. DFT calculations were conducted to further investigate the interaction between K atoms and different scaffolds/current collectors. As shown in Figure 5.9a-c and Figure 5.10a-c, the binding energies of K atoms absorbed on Cu foil, Al foil, and CNT scaffold are calculated to be -0.13, -0.51, and -0.84 eV, respectively. As verified by the discharge profile and XRD results (Figure 5.11), K atoms preferably intercalate into the interlayer space of DN-MXene sheets before the plating of K metal, which is consistent with the previous reports.[136] Considering the possible surface functionalities, MXenes terminated with -OH, =O, and -F were modeled.[200] As shown in Figure 5.12, the binding energies between K-intercalated Ti_3CNT_x MXenes and K atoms are 1.91 eV (Ti_3CNO_2), 1.86 eV ($Ti_3CN(OH)_2$), and 1.88 eV (Ti_3CNF_2), which are larger than their nitrogen-free counterparts (Figure 5.13), demonstrating that the substitution of carbon by nitrogen can significantly enhance the interaction with K atoms. Furthermore, when introducing one Ti vacancy into N-containing MXene layer, the binding energies further increase to 2.27 eV ($Ti_{3-x}CNO_2$), 2.1 eV ($Ti_{3-x}CN(OH)_2$), and 2.04 eV ($Ti_{3-x}CNF_2$), which are much larger than those of the Al, Cu and CNT. This indicates that K atoms prefer to nucleate on the K-intercalated DN-MXene

sheets rather than CNTs or other current collectors. Thus, this potassium-philicity of DN-MXene enables the preferential nucleation of K metal during plating, which makes DN-MXene as an ideal "seed point" for the development of dendrite-free metal anode.

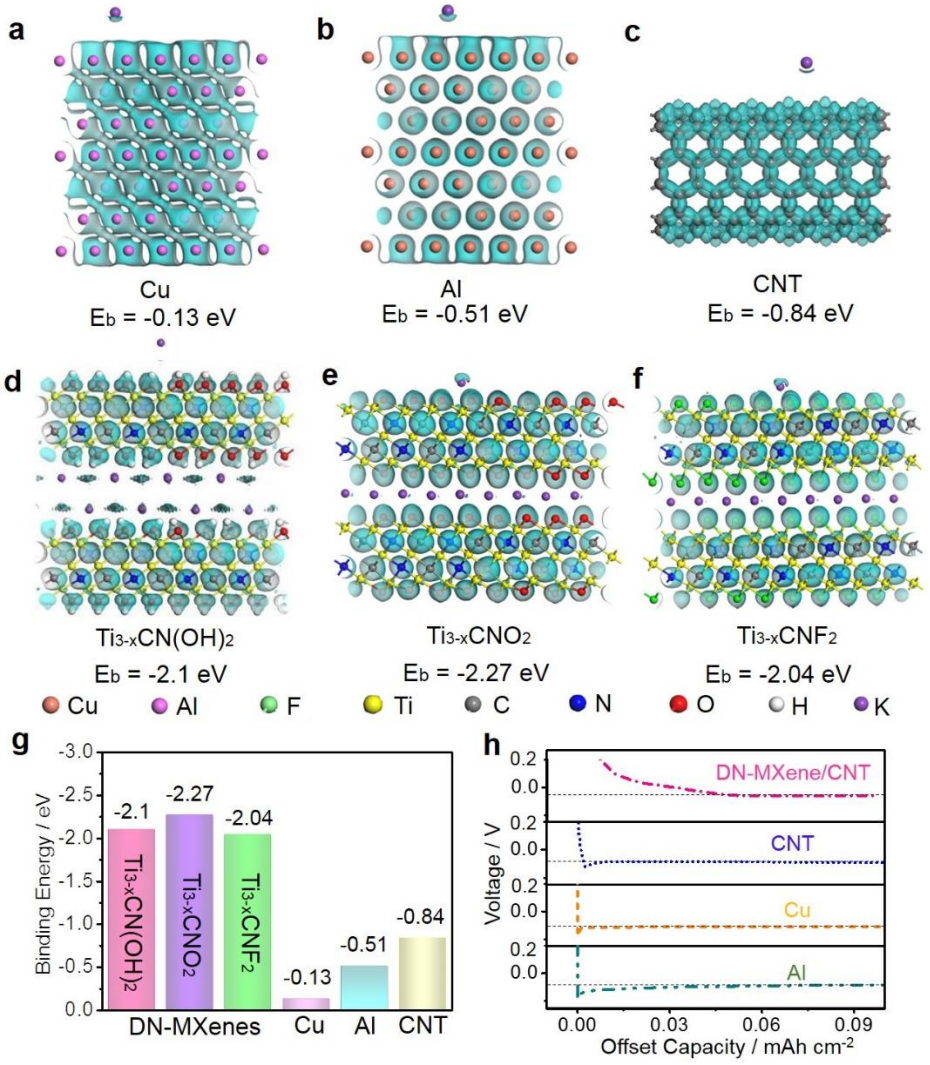

***Figure 5.9**. Density functional theory calculations and corresponding experimental characterizations. The deformation charge density of K atoms absorbed on **(a)** Cu, **(b)** Al, **(c)** CNT, **(d)** $Ti_{3-x}CN(OH)_2$, **(e)** $Ti_{3-x}CNO_2$ and **(f)** $Ti_{3-x}CNF_2$; **(g)** The calculated binding energies of K atoms with different scaffolds or current collectors; **(h)** The voltage profiles of K nucleation on MXene/CNT scaffold, CNT scaffold, Cu foil, and Al foil at a current density of 0.05 mA cm^{-2}.*

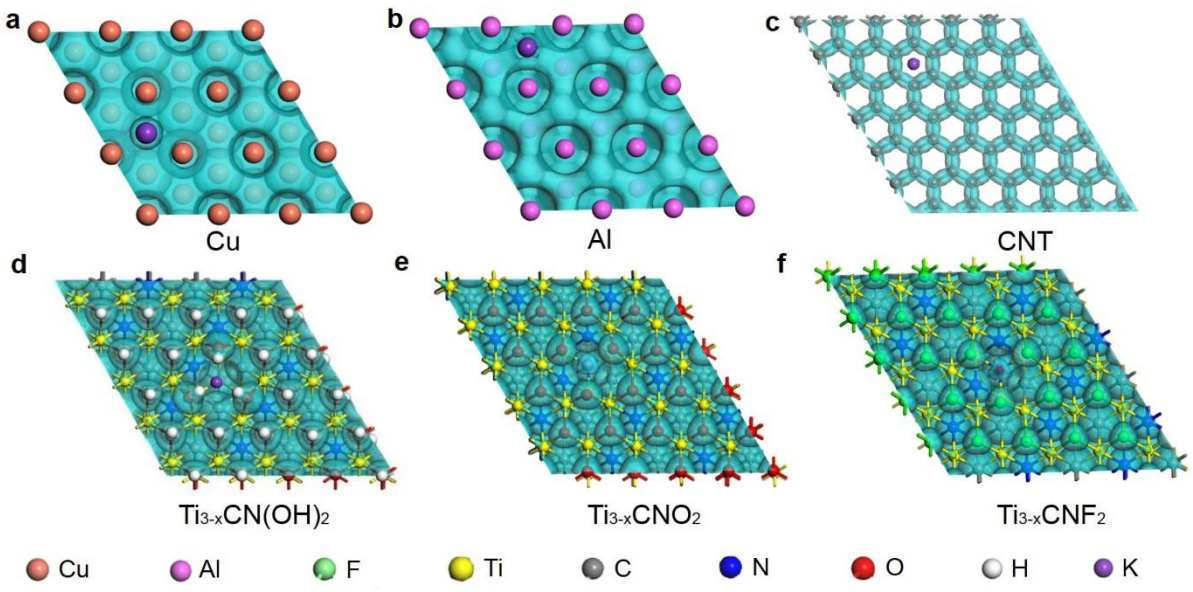

Figure 5.10. *The deformation charge density of K atoms absorbed on* ***(a)*** *Cu,* ***(b)*** *Al,* ***(c)*** *CNT, and* ***(d)*** *$Ti_{3-x}CN(OH)_2$,* ***(e)*** *$Ti_{3-x}CNO_2$,* ***(f)*** *$Ti_{3-x}CNF_2$.*

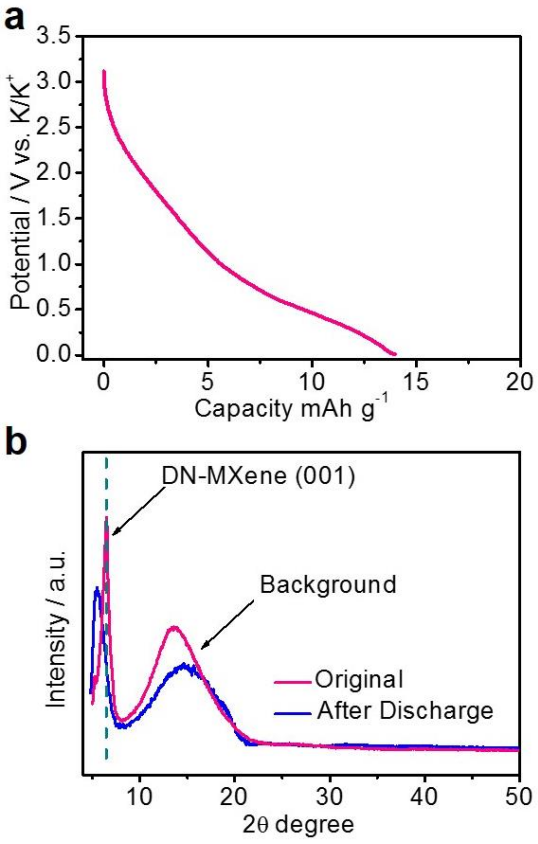

Figure 5.11. ***(a)*** *The discharge profile of the DN-MXene/CNT scaffold at a current density of 0.05 mA cm^{-2};* ***(b)*** *The corresponding XRD patterns of the DN-MXene/CNT scaffold before and after discharge.*

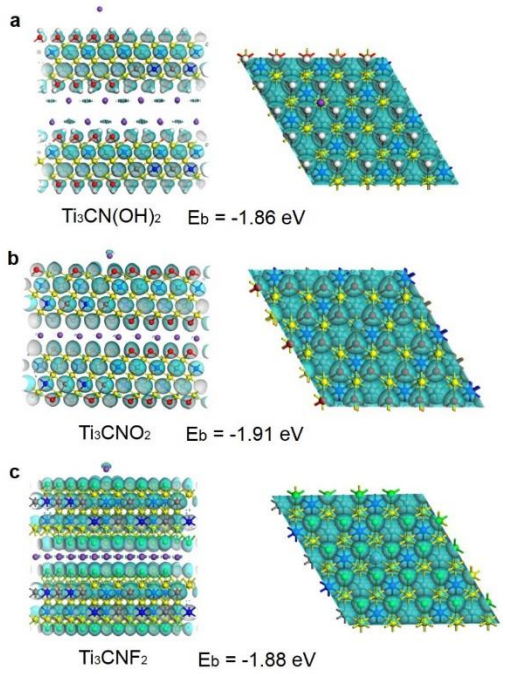

Figure 5.12. *The deformation charge density of K atoms absorbed on the defect-free (**a**) $Ti_3CN(OH)_2$, (**b**) Ti_3CNO_2, (**c**) Ti_3CNF_2 MXenes.*

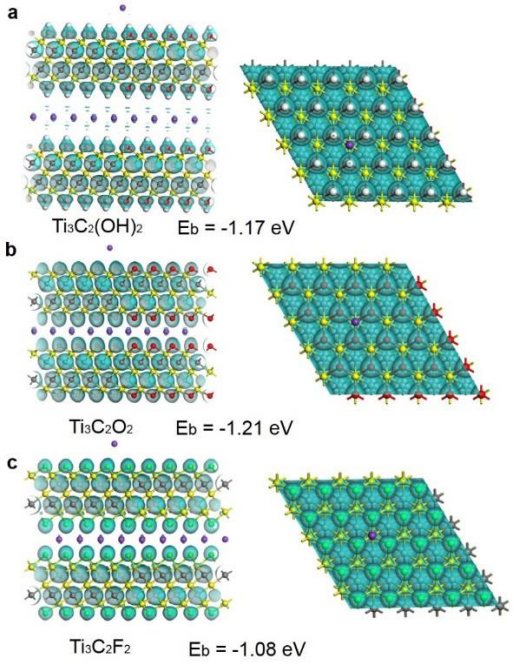

Figure 5.13. *The deformation charge density of K atoms absorbed on the N-free defect-free (**a**) $Ti_3C_2(OH)_2$, (**b**) $Ti_3C_2O_2$, (**c**) $Ti_3C_2F_2$ MXenes.*

To validate the potassium-philic properties of the as-prepared DN-MXene sheets, the nucleation overpotentials of scaffolds/current collectors were tested at a current density of 0.05 mA cm^{-2}. All the voltage profiles exhibit a voltage dip at the beginning of K plating, followed by a flat voltage plateau with lower potential. The value of the K metal nucleation overpotential can be defined as the difference between the bottom of the voltage dip and the flat part of the voltage plateau.[201] As shown in Figure 5.9h, the K nucleation overpotentials of CNT, Cu and Al are 33, 65 and 103 mV, respectively. In contrast, the nucleation overpotential of DN-MXene/CNT is much lower (~6 mV), indicating the reduced resistance for metallic K to nucleate on the as-prepared porous scaffold. This value is also higher than that of N-free $Ti_3C_2T_x$ MXene/CNT scaffold (Figure 5.14a), which is highly consistent with the theoretical calculation results.

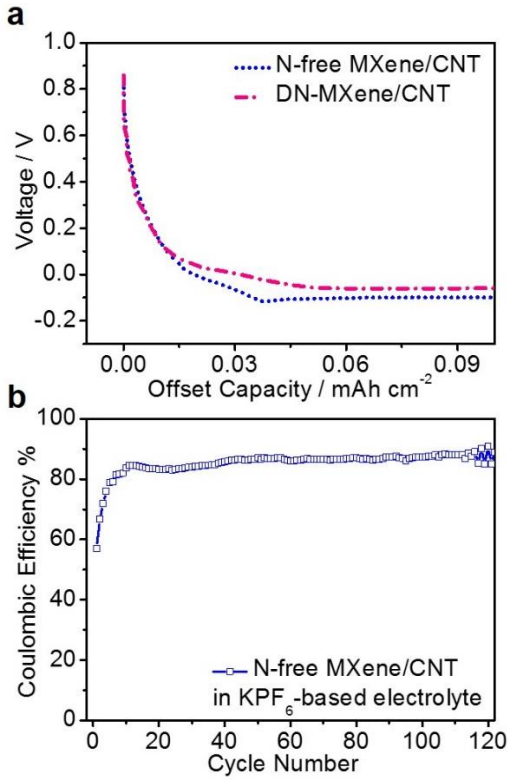

Figure 5.14. *(**a**) The overpotentials of N-free MXene/CNT scaffold and DN-MXene/CNT scaffold at a current density of 0.05 mA cm^{-2}. (**b**) The Coulombic efficiency of K plating/stripping on the N-free $Ti_3C_2T_x$ MXene/CNT scaffold at a current density of 0.5 mA cm^{-2} in the KPF_6-based electrolyte.*

Electrochemical performance evaluation. The K plating/stripping on different scaffolds and current collectors (DN-MXene/CNT, CNT, Cu and Al) was further studied by using a two-electrode cell configuration. Figure 5.15a shows the Coulombic efficiencies (the ratio of K stripping capacity to K plating capacity) of the different scaffolds and current collectors in 0.8 M potassium hexafluorophosphate (KPF_6) dissolved in ethylene carbonate (EC): diethyl carbonate (DEC) (1:1, v/v). It is noted that all the scaffolds and current collectors present relatively lower Coulombic efficiencies in the initial cycles, which is due to the formation of SEI layer and continuous consumption of electrolyte.[187] Subsequently, the Cu and Al foils exhibit low Coulombic efficiencies (~50% for Cu and ~65% for Al) and short lifespans (20 cycles for Cu and 60 cycles for Al), which can be attributed to the dendrite growth and continuous breakdown/reconstruction of SEI layer.[202] CNT scaffolds delivered an average Coulombic efficiency of ~80% during the cycling process, which could be ascribed to the high specific surface area of the conductive CNT scaffold that significantly reduces local current density.[203] However, the cell using CNT scaffolds still suffers from limited cycling life with Coulombic efficiency dropping dramatically beyond 80 cycles. Noticeably, DN-MXene/CNT scaffolds can achieve improved Coulombic efficiency (~93.1%) and cycling stability (120 cycles), which is also higher than that of N-free MXene/CNT scaffold (Figure 5.14b). This indicates that DN-MXene/CNT scaffolds can effectively reduce the local current density, regulate the flux of K ions and suppress the growth of the dendrites. The corresponding voltage profiles for K plating/stripping on different scaffolds and current collectors are shown in Figure 5.15b. The DN-MXene/CNT exhibits a small voltage gap between charge and discharge plateaus (~0.19 V) compared with those of CNT matrix (~0.28 V), Al foil (~0.30 V), and Cu foil (~0.34 V) at the 20^{th} cycle, indicating the reduced polarization of the as-prepared DN-MXene/CNT scaffolds. Such a small polarization is ascribed

to the fact that the DN-MXene can guide homogeneous K plating in the CNT matrix, and therefore suppress the side reactions with electrolyte.

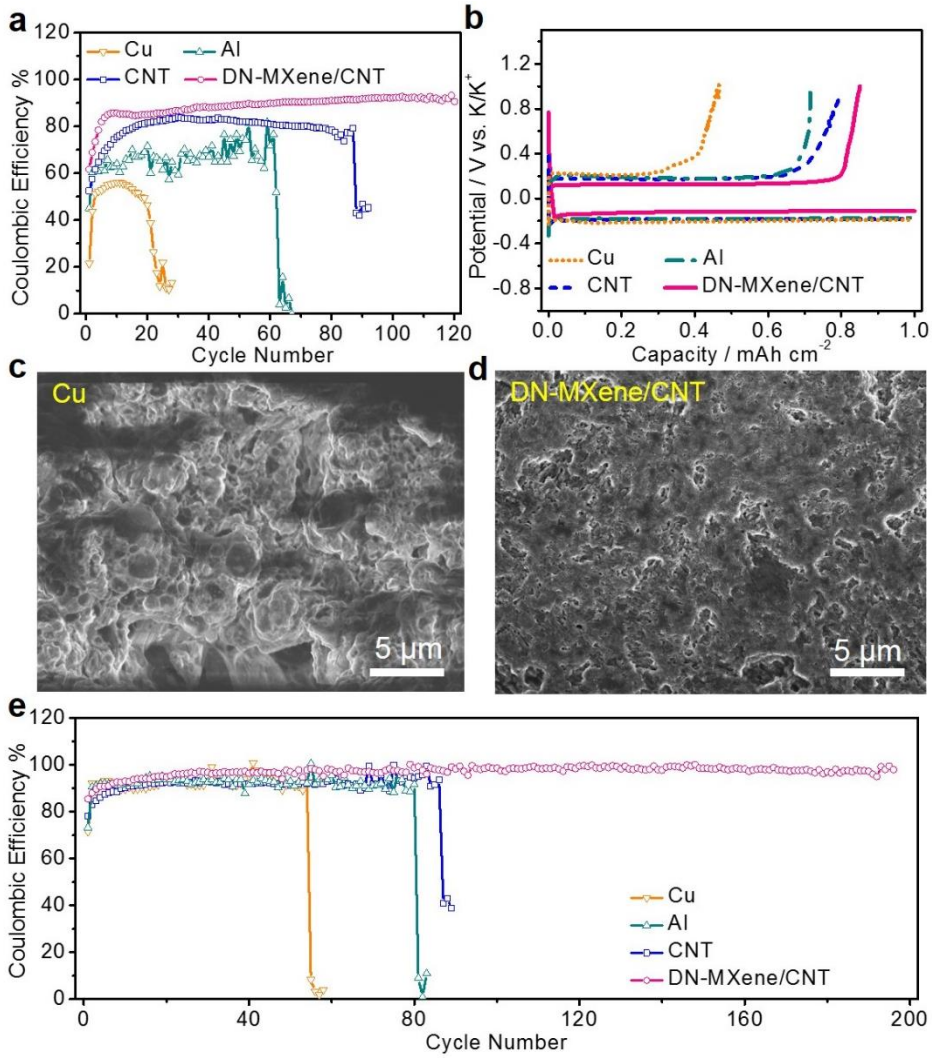

Figure 5.15. *Electrochemical performances of DN-MXene/CNT scaffold. (**a**) The Coulombic efficiencies of K plating/stripping on different scaffolds and current collectors at a current density of 0.5 mA cm^{-2} in KPF_6-based electrolyte; (**b**) The corresponding voltage profiles of K plating/stripping on different scaffolds and current collectors at the 20th cycle in KPF_6-based electrolyte; (**c-d**) Top-view SEM images of K deposition onto (**c**) Cu and (**d**) DN-MXene/CNT at a current density of 0.5 mA cm^{-2} with a plating capacity of 5 mAh cm^{-2} in KPF_6-based electrolyte; (**e**) The Coulombic efficiencies of K plating/stripping on different scaffolds and current collectors at a current density of 0.5 mA cm^{-2} in KFSI-based electrolyte.*

The morphologies of K deposited scaffolds and current collectors were further observed by SEM characterizations. Direct K deposition onto Cu (Figure 5.15c) and Al (Figure 5.16a) foils results in uneven surface and mossy K dendrites.[204] Moreover, as shown in the cross-sectional images, the deposited K metal is highly porous and loose on Cu (Figure 5.17a) and Al foils (Figure 5.17b), and the thicknesses of the deposited K metal are ~200 and 160 μm, respectively, far exceeding the theoretical thickness (~85 μm). When employing CNT scaffolds, the surface of the electrode becomes smoother compared with Cu and Al foils (Figure 5.16b). However, an obvious porous structure and mossy dendrites are still observed on the CNT scaffolds (Figure 5.17c), which is the result of the direct nucleation of K on the top surface of the CNT scaffold and non-uniform distribution of K ionic flux during cycling. In contrast, K metal is well-confined in the DN-MXene/CNT scaffold with a smooth morphology (Figure 5.15d). The porous structure of DN-MXene/CNT scaffold is densely filled with metallic K, and no dendrites can be observed outside the DN-MXene/CNT scaffold (the cross-sectional and mapping images in Figure 5.17d and 5.18, respectively). Such a dendrite-free surface morphology can significantly alleviate interfacial side reactions between the metallic K and electrolytes, thus improving the Coulombic efficiency and cycle life. *Ex situ* SEM characterization was also performed to confirm the nucleation and deposition of K metal on the DN-MXene/CNT scaffold. With plating capacities increasing from 0 to 1, 2.5, and 5 mAh cm^{-2}, it is clearly seen that the K metal is nucleated and deposited inside of the DN-MXene/CNT scaffold (Figure 5.19), which is highly consistent with the DFT calculation results in Figure 5.9. Additionally, the Coulombic efficiency of DN-MXene/CNT scaffold can be further improved to ~98.6 % over 200 cycles by using an optimized electrolyte (0.8 M potassium bis(fluoroslufonyl)imide (KFSI) in EC: DEC (1:1, v/v)) (Figure 5.15e and 5.20), exceeding the previously reported values (Table 5.1). This is because the cleavage of the S-F bond of the KFSI

salts facilitates the formation of a fluorine-rich SEI layer on K metal anode, which leads to reversible plating/stripping and suppresses dendrites. Therefore, the nucleation guidance from the DN-MXene sheets in the scaffold plays an important role in achieving the dendrite-free surface morphology.

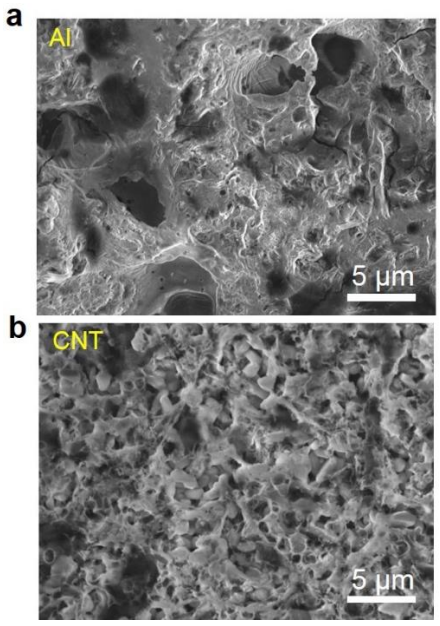

Figure 5.16. *Top-view SEM images of K deposition onto (**a**) Al and (**b**) CNT at a current density of 0.5 mA cm^{-2} with a plating capacity of 5 mAh cm^{-2} in KPF_6-based electrolyte.*

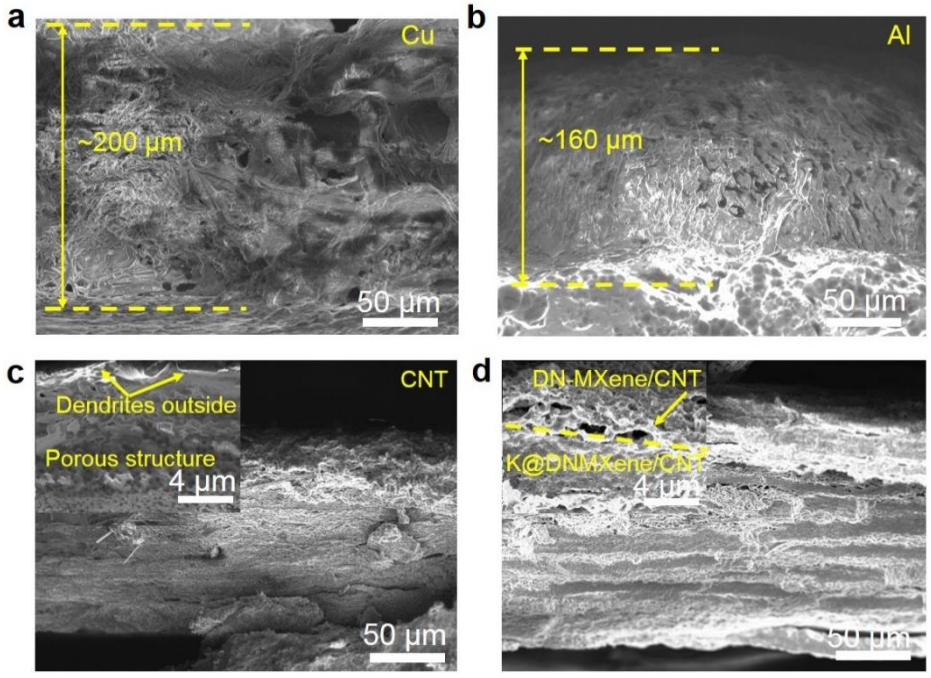

Figure 5.17. *The cross-sectional morphologies of K deposited on* ***(a)*** *Cu,* ***(b)*** *Al,* ***(c)*** *CNT, and* ***(d)*** *DN-MXene/CNT at a current density of 0.5 mA cm^{-2} with a plating capacity of 5 mAh cm^{-2} in KPF_6-based electrolyte.*

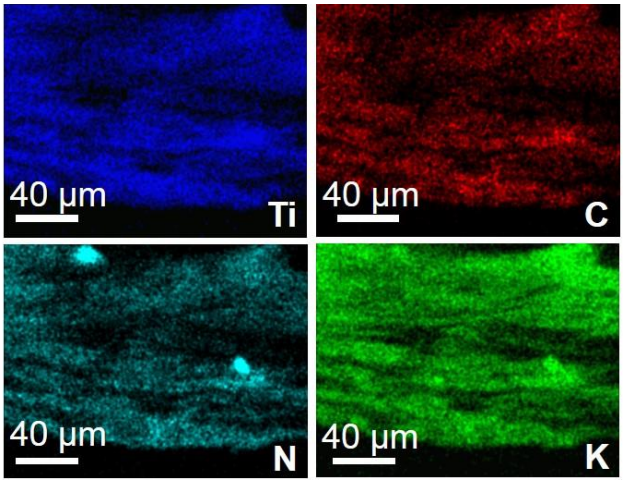

Figure 5.18. *The elemental mapping images of Ti, C, N, and K taken from the cross-sectional area of the K deposited DN-MXene/CNT scaffold.*

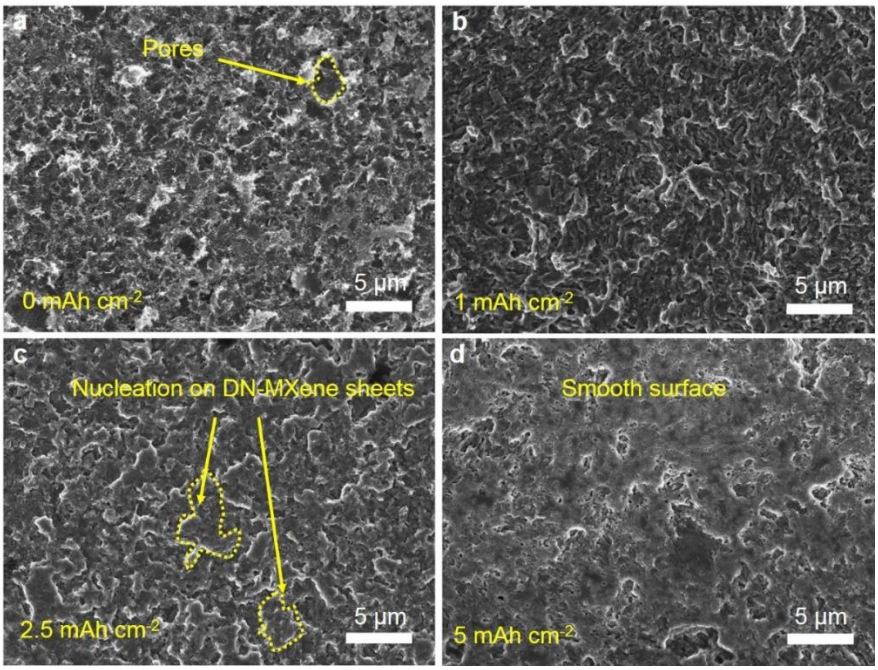

Figure 5.19. *SEM images of the DN-MXene/CNT scaffold after plating K in KPF_6-based electrolyte with capacities of* ***(a)*** *0 mAh cm^{-2},* ***(b)*** *1 mAh cm^{-2},* ***(c)*** *2.5 mAh cm^{-2},* ***(d)*** *5 mAh cm^{-2}.*

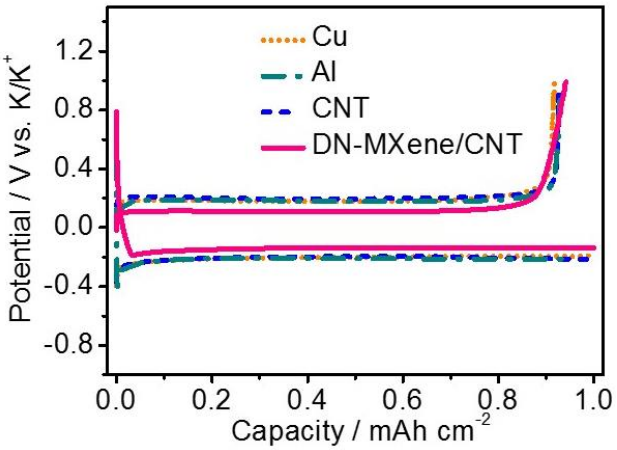

Figure 5.20. *The voltage profiles of K plating/stripping on different scaffolds and current collectors at the 20th cycle in KFSI-based electrolyte.*

In situ XRD was employed to investigate K deposition on Cu current collectors and DN-MXene/CNT scaffolds during the first plating process. As shown in the *in situ* XRD patterns (Figure 5.21) and the corresponding color plots (Figure 5.22a), a characteristic diffraction peak at ~29.6º is assigned to the K_2CO_3 (112) plane (PDF no. 04-010-2694), which is a decomposition product of the electrolyte.[136] This peak gradually increases in the cell using Cu current collector (Figure 5.22a), indicating the formation of thick SEI layers due to serious dendrite growth.[205] In comparison, the K_2CO_3 (112) peak remains low without obvious change in the cell when using the DN-MXene/CNT scaffold, suggesting that employment of DN-MXene/CNT scaffold can effectively minimize side reactions (Figure 5.22b). Furthermore, the *in situ* optical microscopy visualization was conducted to study the surface morphologies of Cu current collector and DN-MXene/CNT scaffold during the K metal deposition process. As shown in Figure 5.22c, mossy K dendrites appear on the surface of Cu current collector during the 30 min plating process, while the surface of DN-MXene/CNT remains smooth and flat, suggesting a dendrite-free potassium surface upon plating. The Sand's time was further measured by using Cu foil and DN-MXene/CNT

scaffold (Figure 5.23). The Sand's time is determined where the apparent voltage divergence occurs due to complete ion depletion and rapid dendrite growth.[206] The DN-MXene/CNT scaffold delivers a prolonged sand's time of ~12 h, which is 6 times longer than that of Cu foils (~2 h). According to the space charge model[204] and equation (6-1)[207]:

$$\tau = \pi D \left(\frac{C_0 e(\mu_a + \mu_{k^+})}{2J\mu_a} \right)^2 \qquad (6-1)$$

where τ is the Sand's time, which is a time when the K dendrite start to grow. *D* is the diffusion coefficient, e is the elementary charge. C_0 is the initial concentration of K salt. μ_a and μ_{k^+} are the anionic and K^+ mobility, respectively, and *J* is the effective electrode current density. The increased Sand's time of the DN-MXene/CNT scaffold confirms the fast K^+ transport of scaffold and enhanced specific surface area that reduces the local current density.

Table 5.1. *Summary of the Coulombic efficiencies and cycling performances of K metal deposition on current collectors/ scaffolds.*

Coulombic efficiencies	Electrolyte	Cycling performances	Preparation method	Current density (mA cm^{-2})	Ref.
~50 %	KPF_6-EC/DEC	20 cycles	deposit K on Cu with modified electrolyte	0.05	187
~98 %	KFSI-DME	100 cycles	deposit K on Cu with modified electrolyte	0.5	187
~40 %	KTFSI-DME	20 cycles	deposit K on Cu	0.1	194
~96 %	KTFSI-DME	40 cycles	deposit K on Cu with artificial SEI	0.1	194

93 %	KPF_6-EC/DEC	-	deposit K on PM/NiO	0.4	[204]
~93.1 %	KPF_6-EC/DEC	120 cycles	deposit K on DN-MXene/CNT	0.5	This work
~98.6 %	KFSI-EC/DEC	200 cycles	deposit K on DN-MXene/CNT	0.5	This work

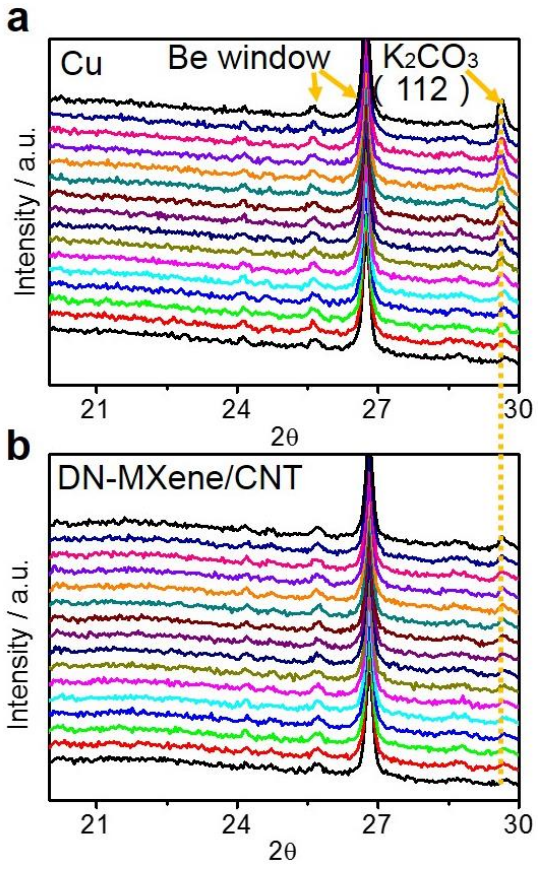

Figure 5.21. *In situ XRD analysis of the K deposition on* ***(a)*** *Cu and* ***(b)*** *DN-MXene/CNT scaffold.*

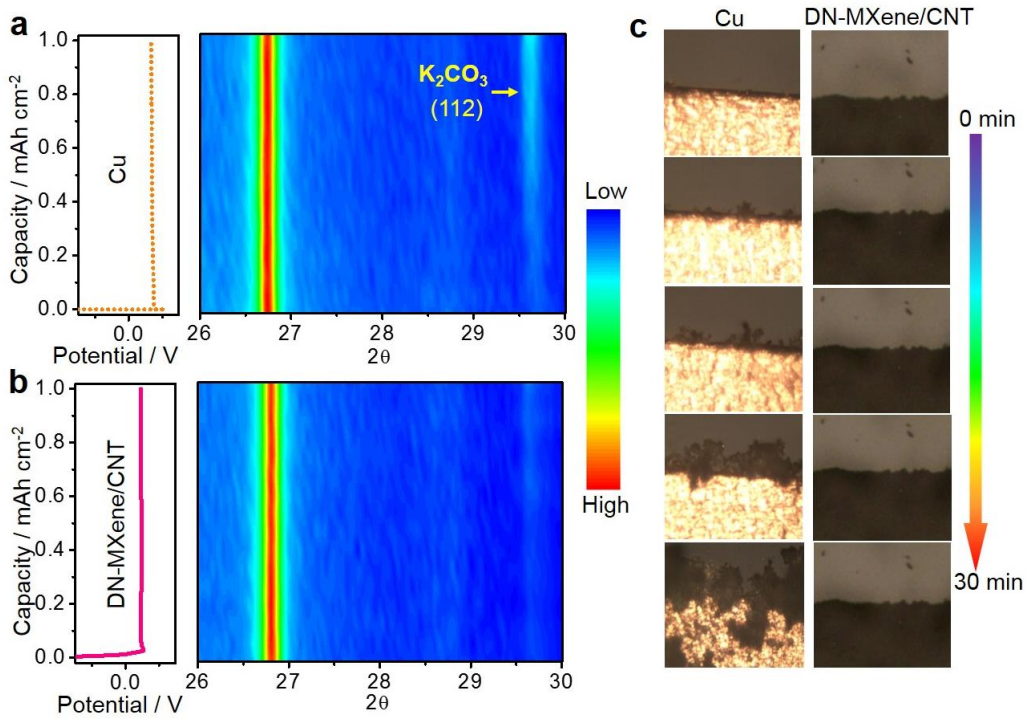

***Figure 5.22**. Mechanism investigation in KPF_6-based electrolyte. Contour plots of in situ XRD patterns for the K deposited on the (**a**) Cu and (**b**) DN-MXene/CNT scaffold. The corresponding electroplating curves are shown on the left; the high-intensity peak at around 26.8° is assigned to the Be window. (**c**) In situ optical microscopy visualization of K deposited on the Cu foil scaffold (left panel) and DN-MXene/CNT (right panel) at a current density of 2 mA cm^{-2}.*

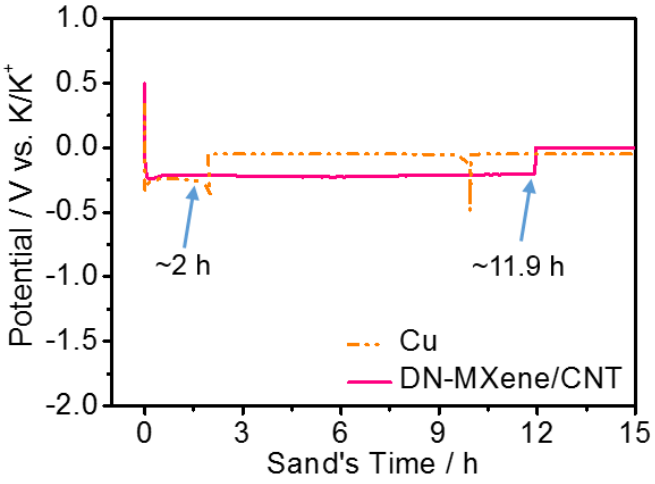

***Figure 5.23.** The voltage profiles of K plating on Cu foil and DN-MXene/CNT scaffold at a constant current density of 2 mA cm^{-2}, blue arrows indicate the characteristic Sand's time when dendrite formation starts, as denoted by the voltage divergence.*

To further measure the long-term galvanostatic cycling performance of DN-MXene/CNT scaffolds, symmetric cells were assembled by using two identical K@DN-MXene/CNT electrodes prepared by the melt infusion strategy. Noticeably, the K@DN-MXene/CNT anodes show a higher specific capacity compared with bare K anodes (shown in Figure 5.24). The symmetric cells with two identical K@CNT electrodes (or two bare K foils) were also assembled for comparison. As presented in Figure 5.25a, a negative voltage value indicates the K plating, while the positive voltage value refers to K stripping.[208] The voltage hysteresis of the bare K||bare K cell significantly increases from ~0.62 V at the initial cycle to ~1.13 V at 60 h, mainly due to the accumulated thick SEI caused by nonuniform K deposition and dendrite growth. Furthermore, the voltage hysteresis suddenly drops to around 0.2 V at 75 h, which indicates a short-circuit induced by dendrite growth (inset of Figure 5.25a, Figure 5.25b).[209] The K@CNT||K@CNT cell shows an average overpotential of ~0.45 V and short-circuits at ~220 h (Figure 5.25a-b). In contrast, the K@DN-MXene/CNT||K@DN-MXene/CNT cell delivers a flat voltage plateaus during both K plating and stripping processes (Figure 5.26) with a reduced voltage hysteresis of ~0.3 V, which remains steady without obvious oscillation during 300 h cycling (Figure 5.25b). Additionally, the cycle life of K@DN-MXene/CNT||K@DN-MXene/CNT cell can be further improved to 1000 h in KFSI-based electrolyte (Figure 5.27), which validates the excellent reversibility of the DN-MXene/CNT scaffold. Furthermore, the symmetric cell with K@DN-MXene/CNT electrodes also has superior rate performance. The K@DN-MXene/CNT||K@DN-MXene/CNT cell delivered voltage hysteresis of 0.11, 0.16, 0.24, 0.31, 0.40 V, when current densities increase from 0.1 mA cm^{-2} to 0.2, 0.5, 1, and 2 mA cm^{-2}, respectively (Figure 5.25c). These values are much lower than those of K@CNT||K@CNT cells and K||K cells. Therefore, the DN-MXene/CNT scaffold with high electronic conductivity and fast K ion diffusion can effectively reduce local current density and

regulate the K metal deposition at high current densities. The electrochemical impedance spectroscopy (EIS) spectra of the symmetric cells after 10 cycles are shown in Figure 5.25d. The K@DN-MXene/CNT||K@DN-MXene/CNT cell shows the lowest interfacial resistance among the three symmetric cells, which is in good agreement with their stable cycling performances.

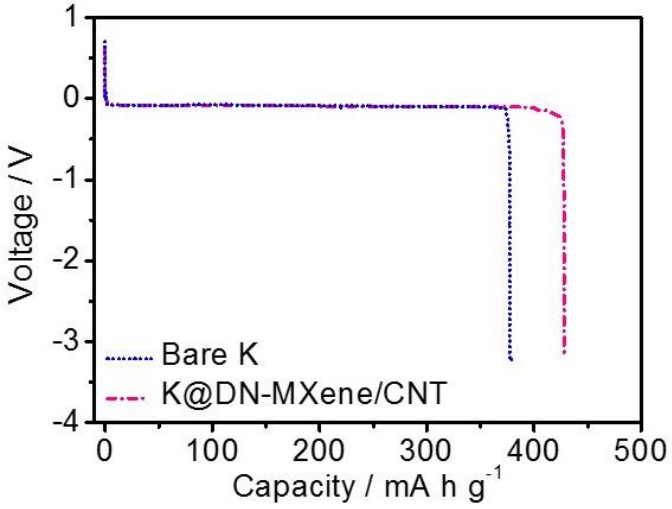

Figure 5.24. *The voltage profiles of stripping K metal in K@DN-MXene/CNT||Cu and bare K||Cu cells at a current density of 0.05 mA cm^{-2} in KPF_6 electrolyte. The capacities were calculated based on the mass of the anode.*

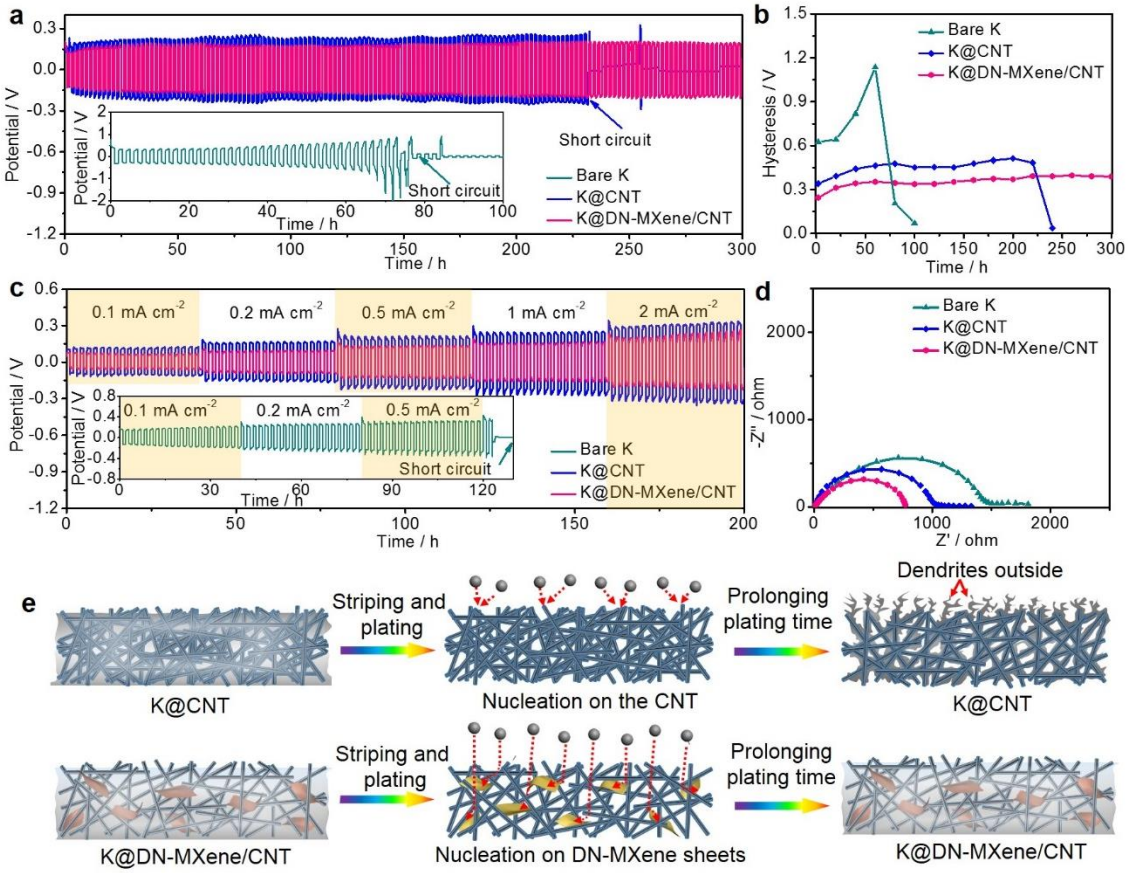

Figure 5.25. *The electrochemical performances of symmetric cells in KPF_6-based electrolyte. (**a**) Voltage profiles of symmetric cells with K@DN-MXene/CNT, K@CNT, or bare K metal anodes at a current density of 0.5 mA cm^{-2}, and (**b**) Corresponding voltage hysteresis of the as-assembled symmetric cells during cycling; (**c**) Rate performances of three symmetric cells at different current densities; (**d**) The EIS spectra of three symmetric cells after 10h charge-10h discharge cycles at 0.5 mA cm^{-2}; (**e**) Schematic illustration of plating/stripping of K metal on CNT scaffold (upper panels) and DN-MXene/CNT scaffold (lower panels).*

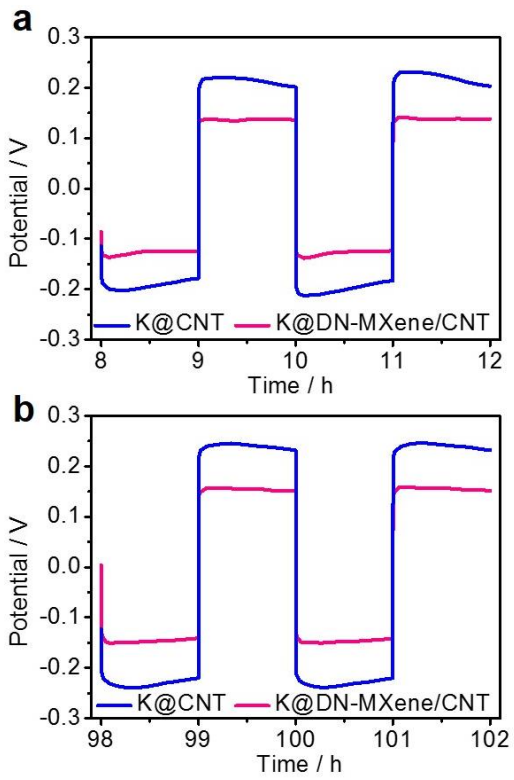

Figure 5.26. *The enlarged voltage profiles of K@DN-MXene/CNT||K@DN-MXene/CNT and K@CNT||K@CNT symmetric cells at a current density of 0.5 mA cm^{-2}.*

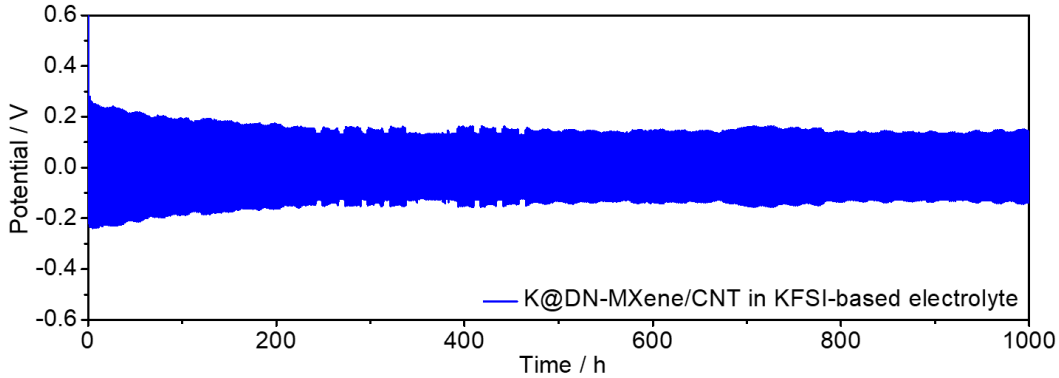

Figure 5.27. *The cycling stability of K@DN-MXene/CNT||K@DN-MXene/CNT symmetric cell at a current density of 0.5 mA cm^{-2} in the KFSI-based electrolyte.*

Figure 5.25e demonstrates a schematic illustration of K metal deposition behaviors on CNT and DN-MXene/CNT scaffolds. For the K@CNT anode, K atoms incline to directly nucleate and plate

onto the CNTs randomly during the repeated plating/stripping process. This leads to a porous deposit and dendritic growth outside of the scaffold, thus decreasing the Coulombic efficiency and the cycle life of K@CNT anode (Figure 5.25e, upper panels). With the introduction of highly electronically conductive DN-MXene sheets into the scaffold, the potassium-philic DN-MXene sheets act as "seed points" to trigger nucleation and guide homogeneous ionic flux during cycling, which results in the uniform K metal deposition without dendrite formation (Figure 5.25e, lower panels).

Potassium-sulfur battery performance. As a proof of concept, K-S cells were assembled using the K@DN-MXene/CNT composite as anode and sulfur-poly(acrylonitrile) (SPAN) as cathode. To determine the effect of the DN-MXene/CNT scaffold, optically transparent devices were fabricated by immersing a K@DN-MXene/CNT anode (or bare K metal foil) in KPF_6-based electrolyte together with the same amount of SPAN powder on the bottom of the vessels. The liquid electrolyte turns yellow after aging for 24 h at room temperature (Figure 5.28a), and a strong peak at 220~260 nm related to S^{2-} and S_2^{2-} appears in the corresponding ultraviolet-visible spectrum[182]. Such a distinct color change implies that the elemental sulfur from the SPAN powder continuously dissolves into the liquid electrolyte, and then electrochemically reacts with K metal to form soluble K polysulfides with dark color. This is consistent with the self-discharge phenomenon observed in batteries.[161] In the device assembled with K@DN-MXene/CNT anode, however, the liquid electrolyte remains clear (Figure 5.28a) with a much lower polysulfide peak in the UV-vis spectrum (Figure 5.28a, inset). This verifies that the shuttle effect of soluble polysulfides can be effectively suppressed by employing a DN-MXene/CNT host in K metallic anodes.[210]

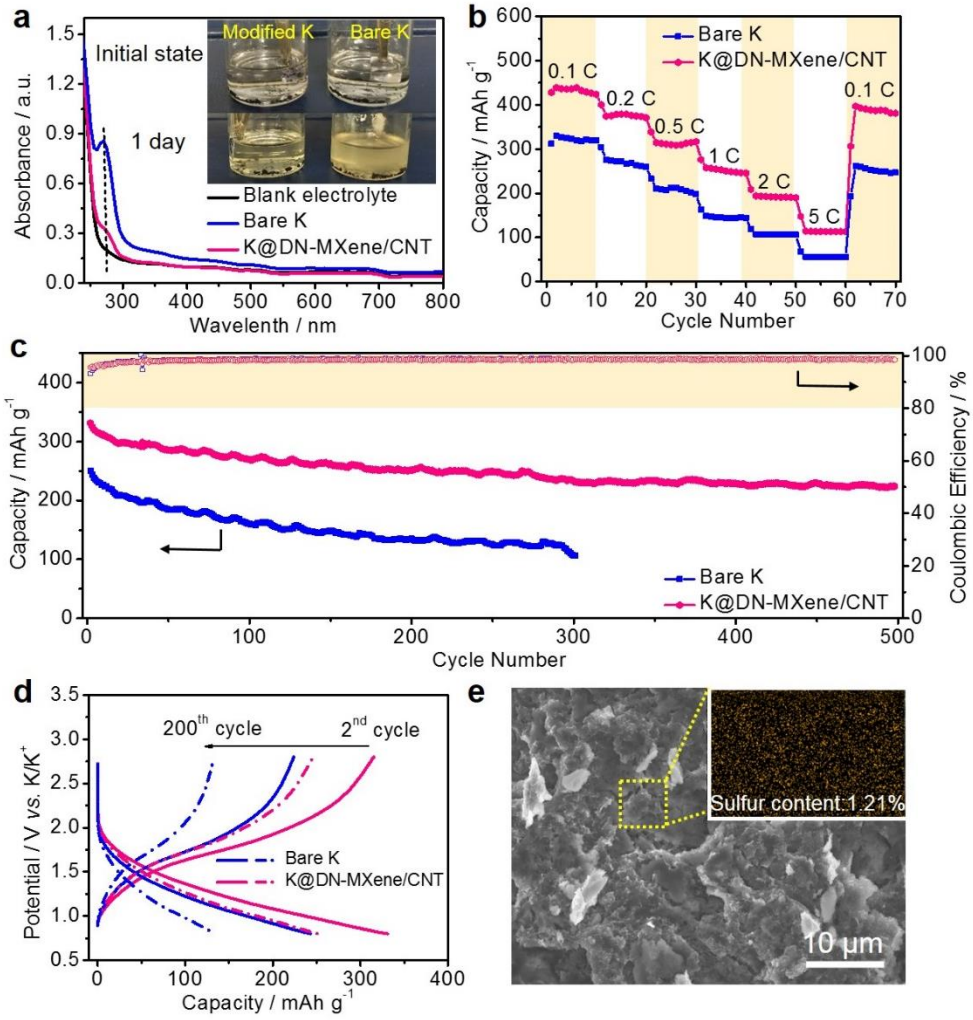

Figure 5.28. *Electrochemical performances of K@DN-MXene/CNT||SPAN and bare K||SPAN K-S batteries.* ***(a)*** *Digital images (shown in inset) and the corresponding UV-vis spectra of liquid electrolytes in optically transparent devices assembled with K@DN-MXene/CNT anode (or bare K foil) and SPAN powder immersed in liquid electrolytes;* ***(b)*** *Rate performances of K@DN-MXene/CNT||SPAN and bare K||SPAN K-S batteries;* ***(c)*** *Cycling performances of K@DN-MXene/CNT||SPAN and bare K||SPAN K-S batteries at a current density of 0.5 C, and* ***(d)*** *Corresponding discharging-charging profiles at the 2nd cycle and 200th cycle; The specific capacity is calculated based on the mass of sulfur.* ***(e)*** *The EIS spectra of two K-S batteries after different cycles at 0.5 C.*

Figure 5.28b shows the rate performances of K-S batteries. Meanwhile, the corresponding voltage profiles are shown in Figure 5.29. The K@DN-MXene/CNT||SPAN cell exhibits specific capacities of 436, 375, 312, 256, and 193 mAh g^{-1} (based on the mass of sulfur) at current densities

of 0.1 C, 0.2 C, 0.5 C, 1 C, and 2 C, respectively. Even at a high current density of 5 C, the cell still maintains a capacity of 113 mAh g^{-1}, which is much higher than that of K-S batteries with bare K foils. Figure 5.28c demonstrates the cycling performances of K-S batteries. The K@DN-MXene/CNT||SPAN cell can deliver an initial discharge capacity of 638 mAh g^{-1} at 0.5 C, which is related to an activation process, including the cleavage of C-S bonds and re-arrangement of sulfur atoms (Figure 5.30a).[211, 212] The corresponding cyclic voltammograms (CV) are shown in Figure 5.30b, in which an irreversible peak at ~1.25 V can be observed in the first cycle and disappears in the following cycles. Moreover, the peak located at ~1.79 V can be assigned to the oxidation of the polysulfides during the charge process.[212] The galvanostatic profiles of a K@DN-MXene/CNT||SPAN cell are shown in Figure 5.28d. The sloping curves during the discharge process are ascribed to the reaction between potassium and sulfur with varying chain lengths.[213] A reversible capacity of 331 mAh g^{-1} was achieved in the subsequent cycles. Even after 500 cycles, a capacity of ~230 mAh g^{-1} can be retained (Figure 5.28c). In contrast, K-S batteries with bare K anodes suffer from a severe capacity fading and internal short-circuiting after ~300 cycles, which is due to the continuous dendrite growth, severe shuttle effect, and electrolyte consumption during plating/stripping of K metal.[214]

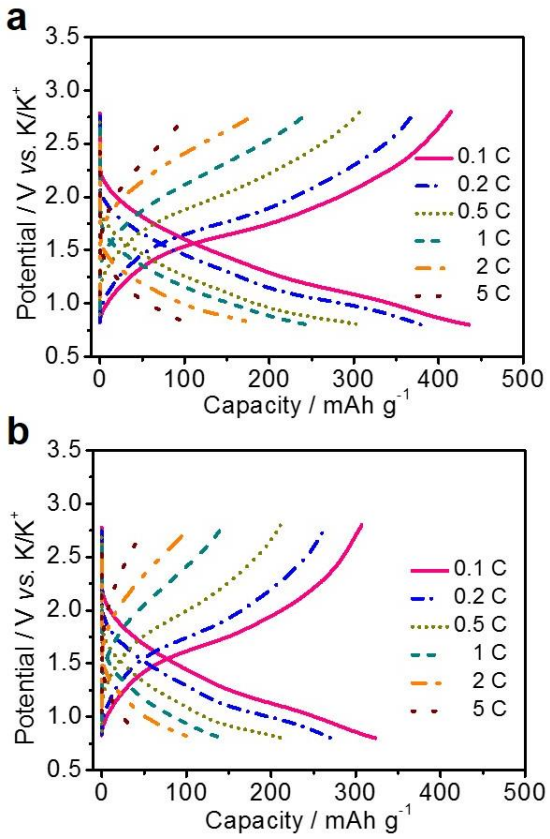

Figure 5.29. *The voltage profiles of* ***(a)*** *K@DN-MXene/CNT||SPAN cell and* ***(b)*** *bare K||SPAN cell at different current densities. The specific capacity is calculated based on the mass of sulfur.*

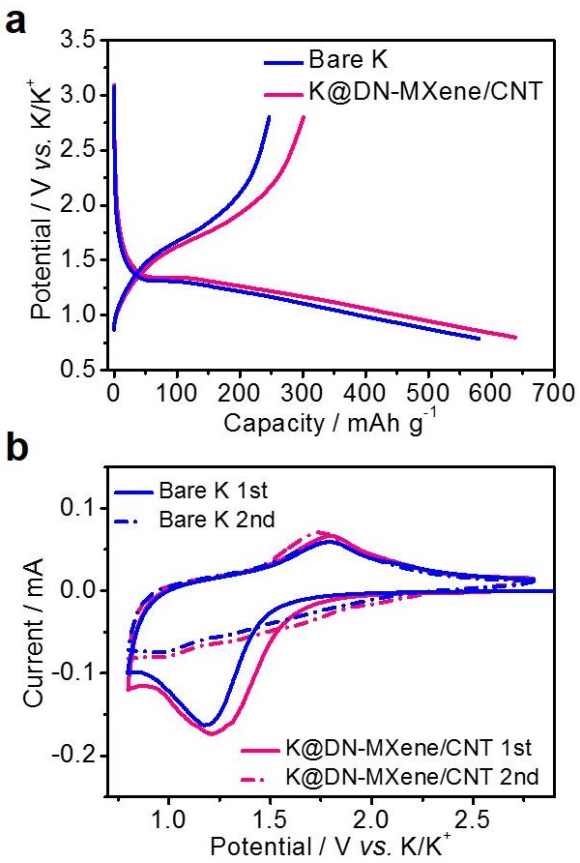

Figure 5.30. *(**a**) The initial voltage profiles of K@DN-MXene/CNT||SPAN and bare K||SPAN cells at a current density of 0.5 C. (**b**) The CV curves of K@DN-MXene/CNT||SPAN and bare K||SPAN cells at a scan rate of 0.1 mV s^{-1}. The specific capacity is calculated based on the mass of sulfur.*

EIS was measured to study the interfacial behavior of K-S batteries. Figure 5.31a shows the EIS spectra of the K@DN-MXene/CNT||SPAN and bare K||SPAN cells after different numbers of cycles. The as-obtained EIS spectra can be simulated via an equivalent circuit (Figure 5.31b), and the simulation results are presented in Table 5.2. Notably, the solid/electrolyte interface resistance (R_f) of bare K||SPAN cell increases from ~282 Ω to ~779 Ω after 10 cycles, which is associated with the dendrite growth on the K anode and deteriorated SEI film as well as the severe shuttle effect in the batteries. In contrast, after employing the DN-MXene/CNT scaffold, the K-S batteries deliver a lower value of R_f (~137 Ω after 1st cycle), which increases slightly to ~177 Ω after the 10th cycle. This indicates a stable solid/electrolyte interface and suppressed shuttle effect, which

contribute to the excellent long-term cycling stability shown in Figure 5.28c. Furthermore, the morphologies of K anodes disassembled from K-S batteries after 50 cycles were characterized by SEM (Figure 5.28e and Figure 5.32). It can be observed that the K@DN-MXene/CNT anode after 50 cycles still maintained smooth surface with a low sulfur content of 1.21 %. However, numerous dead K metal and porous dendrites were found on the surface of the bare K anode after 50 cycles, and the sulfur content on its surface was as high as 6.87 %. These results imply that the DN-MXene/CNT scaffold can not only efficiently suppress the formation "dead K" and dendrites resulting from the inhomogeneous deposition, but also reduce the reaction area with polysulfides, and therefore restrain the shuttle effect (Figure 5.33).

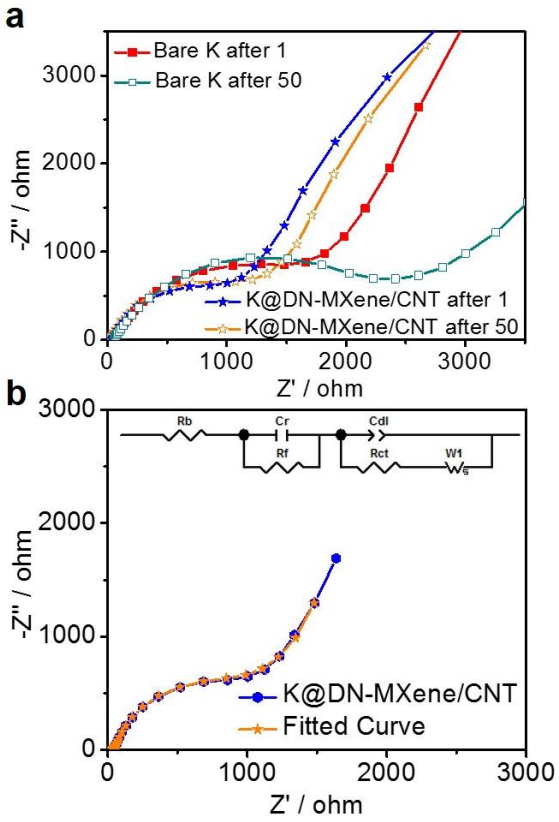

Figure 5.31. *(**a**) The EIS spectra of the K@DN-MXene/CNT||SPAN and bare K||SPAN cells after 1 cycle and 50 cycles. (**b**) Experimental and simulation EIS curves of the K@DN-MXene/CNT||SPAN cell after 1 cycle; Inset is the corresponding equivalent circuit diagram.*

Table 5.2. *The EIS results obtained from Figure 5.31.*

Battery sample	After 1st cycle			After 10th cycle		
	R_b (Ω)	R_{ct} (Ω)	R_f (Ω)	R_b (Ω)	R_{ct} (Ω)	R_f (Ω)
Bare K|SPAN	24	1294	282.5	45	1473	779
K@MXene/CNT|SPAN	12.7	897.5	137.2	32.1	1070	177.9

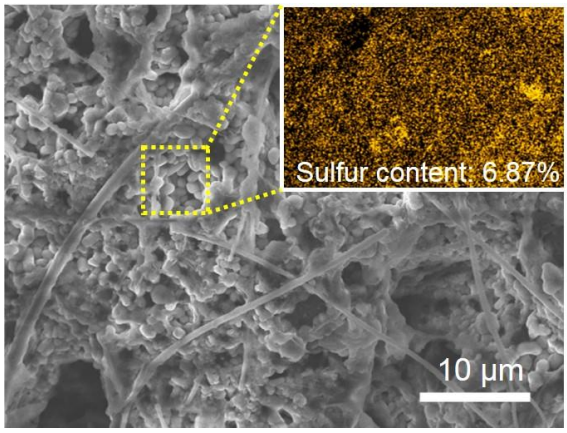

Figure 5.32. *The top-view morphology of the bare K anode disassembled from a K-S battery after 50 cycles. The elemental mapping and content of sulfur are shown in inset.*

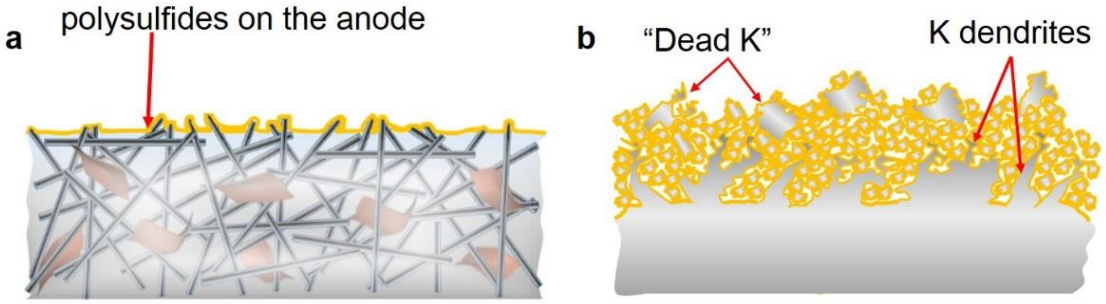

Figure 5.33. *The schematic illustration of* ***(a)*** *K@DN-MXene/CNT and* ***(b)*** *bare K anodes recovered from the cycled K-S batteries.*

5.4 Conclusions

We have rationally designed and prepared a free-standing DN-MXene/CNT scaffold as a matrix for dendrite-free K metallic anodes. Due to the high electronic conductivity and fast K ion diffusion, such DN-MXene/CNT scaffolds can efficiently reduce local current density and facilitate homogeneous K ionic flux, leading to improved rate performance. Furthermore, as validated by DFT calculations and experimental investigations, DN-MXene sheets with potassium-philic characteristic can induce the nucleation of K atoms, therefore suppressing dendritic growth during plating/stripping process. When applying the K@DN-MXene/CNT metal anodes in K-S batteries, the matrix can significantly protect the K metal from the shuttle effect of polysulfides by suppressing dendrite growth, which significantly improves the electrochemical performances of the K-S batteries. This work could open up a new path to inspire the development of K metal anodes and high-performance K-based batteries.

Chapter 6. High-performance Lithium-sulfur/ion batteries enabled by MXene interlayer

6.1 Introduction

Recently, soaring demand for the renewable energy and electrification of road transportation require high-performance energy storage technologies.[1] Consequently, various energy storage devices, such as lithium-ion batteries, sodium-ion batteries, and lithium-sulfur batteries, *etc.,* have been developed. Among them, organic lithium-sulfur (Li-S) battery is one of the attractive candidates for the large-scale energy storage technology because of their high energy density (more than 500 Wh kg^{-1}) and abundant sulfur resources.[215] For example, Li-S batteries tested in ether-based electrolyte can deliver a much higher specific capacity and energy density compared with the present commercial batteries.[216] However, organic Li-S batteries suffer from several intrinsic drawbacks.[217] The dendrites formation on lithium metal anode may pierce the separator, leading to short circuit and safety issues. Furthermore, a series of intermediate polysulfides tend to dissolve in ether-based electrolyte and shuttle to the anode side. This not only leads to low Coulombic efficiency and capacity fading, but also deteriorates the anode/electrolyte interface, leading to short lifespan. Moreover, the highly inflammable ether-based electrolyte used in Li-S batteries may result in safety concerns, which hinder the large-scale application of organic Li-S batteries.[130, 218]

Replacement of organic electrolyte by its aqueous counterpart has been proposed to develop aqueous Li-S batteries. Employment of aqueous electrolyte not only eliminates toxicity concerns resulted from the organic electrolytes, but also avoid using lithium metal anode, thus preventing the safety issues. For example, a Li-ion/polysulfide battery system has been fabricated by using potassium (poly)sulfide as anolyte, Li_2SO_4 solution as electrolyte.[219, 220] Subsequently, elemental sulfur was employed as anode to couple with $LiMn_2O_4$ cathode.[221] The reaction in these battery

systems is related to extensive speciation and a complex equilibrium of H_2S, HS^-, S_4^-, OH^-, and H_2O ($4S + 2e^- = S_4^{2-}$; $S_4^{2-} + 4H_2O + 6e^- = 4HS^- + 4OH^-$).[222] However, HS^- is highly soluble in aqueous electrolyte, which may lead to parasitic shuttle effect and capacity fading. To solve this issue, water-in-bisalt (WiBS) aqueous electrolyte was developed. Such an electrolyte not only enhances the voltage window, enabling the utilization of sulfur anode and transition metal oxide cathode, but also suppresses the dissolution of short-chain lithium polysulfides.[223]

MXenes with the chemical formula of $M_{n+1}X_nT_x$ (where the M represents early transition metal, X is carbon and/or nitrogen, T represents the surface functional groups:-O, -OH, and –F) are a large family of early transition metal carbides/nitrides, which can be prepared by selectively etching "A" elements (such as Al, Si, *etc.*) from laminated carbides or carbonitrides ("MAX" phases).[224] MXenes with unique chemical/physical properties are considered as promising materials in many fields. Particularly, in the Li-S batteries, a strong Ti-S bond can be formed between the MXenes and polysulfides, which can effectively suppress the shuttling of polysulfides and improve the electrochemical performance of Li-S batteries.[131, 225]

Herein, we report the development of high-performance aqueous lithium-sulfur/ion (Li-SI) battery enabled by highly concentrated electrolyte and free-standing $Ti_3C_2T_x$ MXene interlayer. The highly concentrated electrolyte can enhance the electrochemical window, which enables the lithiation/delithiation reaction of sulfur anode and $LiMn_2O_4$ cathode. Additionally, the electrolyte can also suppress the dissolution of polysulfides and slow the diffusion of polysulfides, preventing the loss of active materials. Furthermore, the as-developed free-standing MXene paper has been applied as an interlayer between anode and separator, which can effectively trap polysulfides and intermediate products, thus preventing the shuttle effect during the cycling. Due to the synergistical

optimization effect, the as-assembled aqueous rechargeable batteries can deliver enhanced specific capacity (~715 mAh g^{-1} at a current density of 0.2 C) and improved cycling performance.

6.2 Experimental section

6.2.1 Synthesis of sulfur@biocarbon (S@C)

The biocarbon materials derived from biomass were synthesized as sulfur hosts. Firstly, spongy precursors can be obtained by soaking sterculia lychnophora in warm distilled water for at least 1 hour. Then, a freeze-dry method was used to remove the water in the precursors, and the dried precursors were ground to powder, which was further mixed with $KHCO_3$ with a mass ratio of 1:4. The mixture was heated at 800 ºC for 5 hours under Ar atmosphere. Afterwards, the as-prepared products were rinsed by diluted HCl and distilled water and then dried at 80 ºC overnight to obtain biocarbon materials. Sulfur@carbon (S@C) anode materials were synthesized by melt diffusion method. The sulfur powder (99.99%, Sigma-Aldrich) and the as-obtained biocarbon materials were homogenously mixed with the mass ratio of 1:1 (S:biocarbon). Then, the S@C can be obtained by heating the mixture at 155 ºC, in which sulfur was incorporated into the porous carbon matrix by melt diffusion. Sulfur anodes were prepared by compressing S@C composite and poly(vinylidenedifluoride) (PTFE, 5 wt % aqueous solution) (mass ratio, 9:1) on a titanium mesh (200 mesh). The diameter of sulfur anode was 0.7 cm and the areal loading of sulfur was around 1~2 mg cm^{-2}.

6.2.2 Synthesis of MXene and MXene interlayer

Ti_3AlC_2 "MAX" was prepared according to the previous reported literature.[226] Then, the Al atoms in Ti_3AlC_2 powder can be removed by slowly adding 3 g of Ti_3AlC_2 powder into a mixture of lithium fluoride (LiF, 3 g, Alfa Aesar) and hydrochloric acid (HCl, 30 mL, 9 M, Fisher Scientific)

at ~35 ºC for 24 hours under stirring to obtain exfoliated $Ti_3C_2T_x$ suspension. The as-obtained suspension was washed with distilled water and centrifuged (3500 rpm) for several times until the pH value of the supernatant was higher than 5. Free-standing MXene paper can be synthesized by a filtration method. Typically, 5 mL $Ti_3C_2T_x$ MXene suspension (~2 mg mL^{-1}) was sonicated for 20 min under Ar atmosphere followed by vacuum filtration on a Celgard 3501 membrane. The free-standing MXene paper can be obtained by repeatedly rinsing with distilled water for several times followed by freeze-dry process. The weight of the as-developed free-standing MXene paper was about ~0.6 mg cm^{-2}.

6.2.3 Structure and morphology characterizations

The XRD characterizations of the samples were conducted on a Bruker D8 discover XRD with Cu Kα radiation (40 KV and 40 mA) with a step scan of 0.02º, 5º ~ 80º 2θ ranges and step time of 0.5 s. The morphologies of the specimens were characterized by using a field emitting scanning electron microscope (FE-SEM) (Zeiss Supra 55VP, Germany). Raman spectra were collected by using a Renishaw inVia Raman spectrometer system (Gloucestershire, UK) equipped with a Leica DML Bmicroscope (Wetzlar, Germany) and a 17 mW at 633 nm Renishaw helium neon laser source. Thermogravimetric/differential thermal analysis (TG/DTA) was performed on a 2960 SDT system. X-ray photoelectron spectroscopy (XPS) measurements were carried out on a Kratos XSAM-800 spectrometer with an Mg Ka radiation source.

6.2.4 Electrochemical characterizations

The highly concentrated aqueous electrolyte was prepared by dissolving 7 mol kg^{-1} lithium trifluoromethane sulfonate (LiOTf, ~99%, Sigma-Aldrich) and 21 mol kg^{-1} lithium bis(trifluoromethanesulfonyl)imide (LiTFSI, ~99%, Sigma-Aldrich) in water. Cyclic

voltammograms (CVs) of anode and cathode were collected by using three electrode configurations on a VMP3 electrochemical workstation at a scan rate of 0.2 mV s^{-1}. Electrochemical cells were assembled in a glass cell with either S@C or $LiMn_2O_4$ as working electrode, a saturated silver/silver chloride (Ag/AgCl) as reference electrode, and Pt wire as counter electrode.

For the full cell tests, a stainless-steel coin cell was assembled with S@C anode, $LiMn_2O_4$ cathode, MXene interlayer, and filter paper as separator. Galvanostatic charge-discharge measurements were tested on Neware battery testing systems. Before the cycling and rate tests, the as-developed Li-SI cells were first activated by charging to 2 V and discharging to 0.1 V for three times at 0.5 C rate (1 C = 1675 mA g^{-1} based on the mass of sulfur) at 25 ºC. Electrochemical impedance spectra (EISs) of cells were also collected in a frequency range of 10^{-2} to 10^5 Hz by applying a disturbance amplitude of 5 mV.

6.3 Results and discussion

The biocarbon can be prepared by annealing the mixture of biomass powder and potassium hydrogen carbonate ($KHCO_3$) at 850 ºC for 5 hours. FE-SEM image of biocarbon is presented in Figure 6.1a, in which the as-obtained carbon materials exhibit a porous morphology with pore sizes from ~500 nm to ~1 μm. This architecture not only allows the incorporation of large amount of sulfur into carbon matrix, but also benefits for the rapid diffusion of electrolyte, thus enabling a fast reaction kinetics.[227] After the melting diffusion treatment, no obvious sulfur aggregation can be observed on the surface of carbon, suggesting the successful incorporation of elemental sulfur into the porous structure of carbon (Figure 6.1b). Figure 6.2 shows the TGA curves of the S@C electrode materials under N_2 atmosphere from room temperature to 800 ºC. The weight loss (~50

wt% of the total mass) in temperature range of 100 ~ 400 °C corresponds to the evaporation of sulfur.

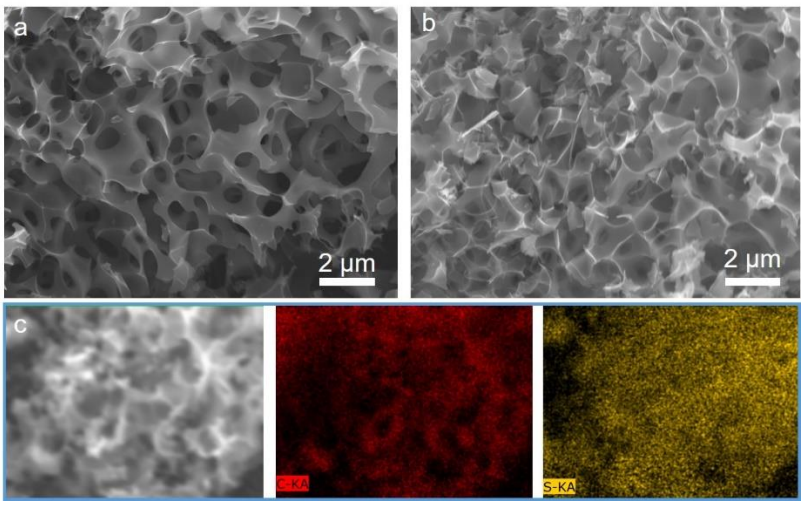

Figure 6.1. *Characterizations of biocarbon and S@C composites.* ***a****) the FE-SEM image of the biocarbon materials;* ***b****) the FE-SEM image of the S@C anode materials;* ***c****) the EDS elemental mapping of the C and S in S@C anode materials.*

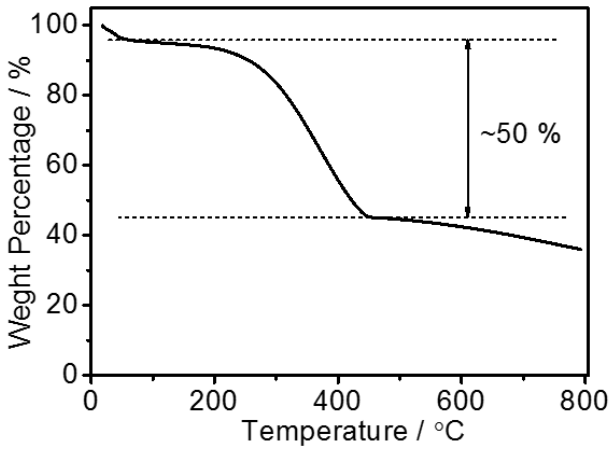

Figure 6.2. *The TGA curves of the S@C anode materials.*

As the polysulfides are highly sensitive, they would react with water molecules in diluted electrolyte to form H_2S, HS^-, and Li_2S_4-anolyte, which may shuttle into the electrolyte, leading to capacity fading and loss of active materials.[219, 223] In this regard, highly concentrated electrolyte

has been prepared by dissolving 7 mol kg^{-1} lithium trifluoromethane sulfonate (LiOTf) and 21 mol kg^{-1} lithium bis(trifluoromethanesulfonyl)imide (LiTFSI) in water. The electrochemical windows of the concentrated electrolyte and diluted electrolyte were investigated by linear sweep voltammetry (LSV) with stainless steel meshes as working electrodes (Fiugre 6.3a). In diluted electrolyte, Li^+ remains well hydrated in its primary solvation sheath with large amount of free water molecules, and the potential of lithium salt decomposition is below that of water splitting, which leads to preferential reduction of water.[228] Therefore, the diluted electrolyte present a relatively narrow voltage window of ~1.75 V. In contrast, when the salt concentration increases, the onsets of oxygen evolution reaction (OER)/hydrogen evolution reaction (HER) occur at 4.5/2.0 V with an enhanced voltage window of ~2.5 V, which suggests the suppressed water splitting in concentrated electrolyte. This stable electrochemical window enables the employments of sulfur anodes and transition metal oxide cathodes (shown later). Additionally, the concentrated electrolyte can also suppress the dissolution of short-chain polysulfides, preventing the shuttle effect. As shown in Figure 6.3b, after adding the polysulfides (Li_2S) to the electrolytes, the diluted electrolyte turned to brown immediately, while the polysulfides are immiscible with the concentrated electrolyte and the diffusion of them has been suppressed.

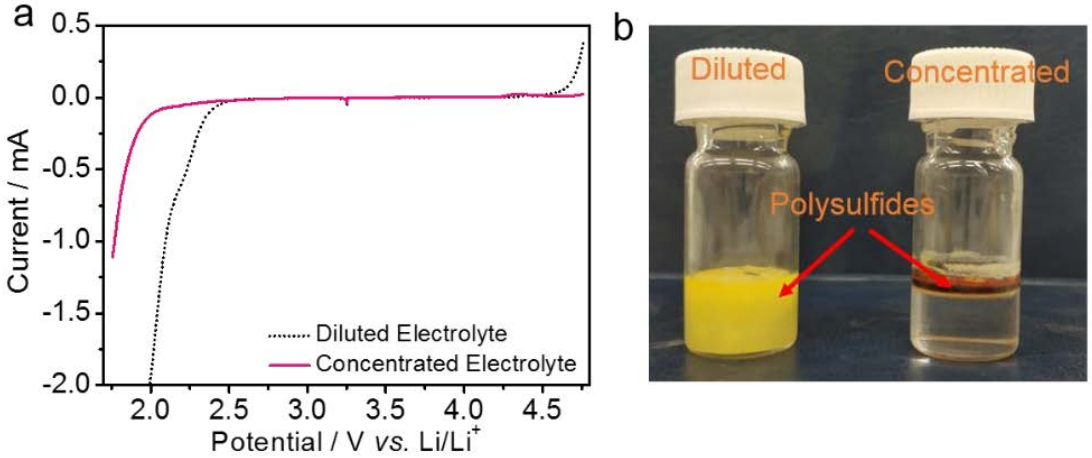

Figure 6.3. a) *The stable voltage windows of diluted and concentrated electrolytes on stainless steel mesh electrode. Linear sweep voltammetry was carried out at a scan rate of 10 mV* s^{-1}*;* ***b)*** *The optical images of polysulfides dissolution/diffusion in diluted and concentrated electrolytes.*

When using the concentrated electrolyte, the electrochemical behavior of a S@C anode was investigated by conducting cyclic voltammetry (CV) within the voltage range of 2.25~3.25 V *vs.* Li/Li^+ (-1~0 V *vs.* Ag/AgCl). As shown in Figure 6.4a, compared with Li-S batteries with nonaqueous electrolyte, the S@C anode only presents a pair of redox peaks at 2.55/2.72 V *vs.* Li/Li^+ in concentrated aqueous electrolyte, which is higher than that tested in nonaqueous solutions.[229] This single-state redox reaction can be ascribed to the reduction/oxidation of elemental sulfur. According to the previously reported literature, this process undergoes a solid-liquid reaction with ultrafast kinetics.[223] To couple with S@C anode, a $LiMn_2O_4$ (LMO) cathode has been prepared. The Morphology and X-ray diffraction (XRD) of $LiMn_2O_4$ materials are shown in Figure 6.5, in which the $LiMn_2O_4$ powder shows a typical spinel structure.[230] As shown in Figure 6.4b, cyclic voltammetry of $LiMn_2O_4$ cathode was also performed within the voltage range of 3.25~4.45 V *vs.* Li/Li^+ (0~1.2 V *vs.* Ag/AgCl). The commercial $LiMn_2O_4$ cathode presents two reversible redox couples at 4.38/3.82 and 4.22/3.74 V *vs.* Li/Li^+ at the scan rate of 0.2 mV s^{-1}, which can be ascribed to the two-step intercalation/extraction of Li ions into/from spinel structure. This result is highly consistent with previously reported literatures.[221, 231, 232]

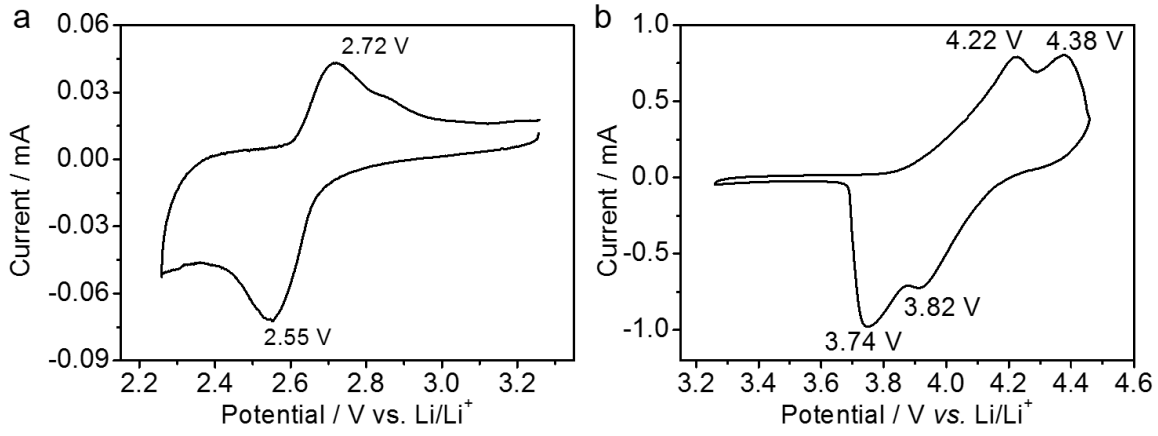

Figure 6.4. *The Cyclic voltammetry (CV) curves of* ***a)*** *S@C anode and* ***b)*** *$LiMn_2O_4$ cathode in concentrated electrolyte at a scan rate of 0.2 mV s^{-1}.*

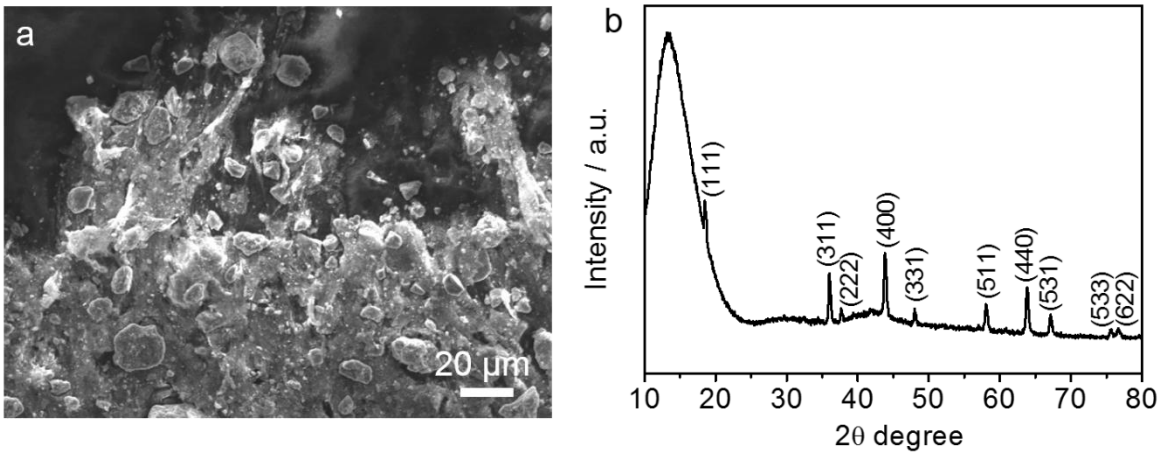

Figure 6.5. a) *The FE-SEM image of the commercial $LiMn_2O_4$ cathode materials;* ***b)*** *the XRD pattern of the $LiMn_2O_4$ cathode materials.*

To further optimize the electrochemical performance of the Li-SI batteries, a free-standing MXene paper has been applied as interlayer between separator and the S@C anode. Briefly, the MXene paper can be prepared by vacuum filtration process (see details in experimental section). Figure 6.6a displays the surface morphology of the free-standing MXene paper. Due to the two-dimensional property of MXene, the exfoliated MXene sheets can be easily stacked with each other to form a free-standing MXene paper. This architecture not only acts as a physical barrier to block the polysulfides, but also presents a strong chemical bonding with polysulfides, thus significantly restrain the shuttle effect in the batteries.[233] The optical image of MXene paper is shown in inset of Figure 6c. Such a MXene paper with diameter of 1 cm can be directly used in the batteries without any further process.

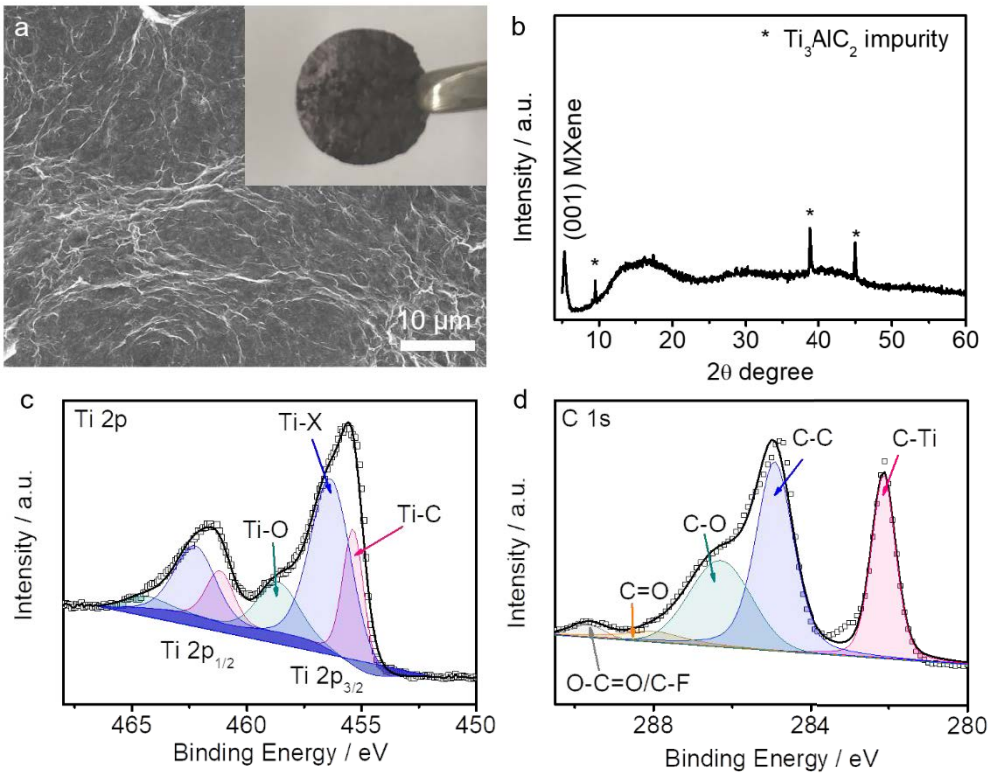

Figure 6.6. a*) The top-view FE-SEM image of the as-prepared MXene paper, the inset image shows the optical image of the free-standing MXene paper;* ***b****) The XRD pattern of the as-prepared MXene paper; high resolution XPS spectrum of* ***c****) Ti 2p and* ***d****) C 1s in the MXene paper.*

Further characterizations have been conducted to study the phase and chemical composition of the MXene paper. Figure 6.6b shows the XRD pattern of the MXene paper, in which the peak at about 6º is attributed to the (001) plane of the MXene. Noticeably, three peaks at ~10º, 39º, and 45º are attributed to the Ti_3AlC_2 MAX impurity. X-ray photoelectron spectroscopy (XPS) was also applied to study the chemical composition of the MXene paper. As shown in Figure 6.6c, the Ti 2p spectrum (Figure 2c) have a Ti $2p_{3/2}$ part at ~455.5 eV, and a Ti $2p_{1/2}$ part at 461.8 eV, respectively. In the Ti $2p_{3/2}$, a deconvoluted peak at 455.3 eV is corresponding to Ti-C bonds, while other peaks at 456.5 and 458.7 eV can be assigned to Ti-X bonds and Ti-O surface bonds, respectively. Similarly, three deconvoluted peaks at 461.1, 462.2 and 464.5 eV can also be observed in the Ti $2p_{1/2}$ part. These results confirm the successful synthesis of MXene paper

without any compositional change. The C 1s XPS spectrum of MXene paper (Figure 6.6d) can be fitted into five peaks at 282.1, 284.8, 286.1, 288.3 and 289.2 eV. The peak at 282.1 eV is related to the C-Ti bond. The peaks located at 284.8 eV and 286.1 eV correspond to C-C and C-O, respectively. The other two peaks are ascribed to C=O (288.3 eV) and O-C=O/C-F (289.2 eV), respectively.

To investigate the electrochemical performance of the aqueous Li-SI batteries, the full cells have been assembled by using S@C anode, $LiMn_2O_4$ cathode, MXene interlayer, and highly concentrated electrolyte. For comparison, the Li-SI batteries without MXene interlayer (LMO|| S@C) have also been assembled. Figure 6.7a presents the schematic illustration of the battery configuration with MXene interlayer. Such an interlayer is expected to restrain the migration of polysulfides by both physical and chemical adsorption, thus facilitating the utilization of active materials and improving the cycling performance. The mass ratio of cathode and anode was set as around 2.5:1. The as-assembled cells were tested in an electrochemical window of 0.1~2.0 V. Figure 6.7b presents the galvanostatic charge-discharge profiles of Li-SI batteries with/without MXene interlayer at a current density of 0.2 C (1 C = 1675 mA g^{-1}, based on the mass of sulfur). It can be noted that Li-SI batteries exhibit plateaus at ~1.75/1.50 V during charge/discharge processes with a polarization of ~0.25 V. Additionally, the LMO||S@C delivered a discharge capacity of ~365 mAh g^{-1} at a current density of 0.2 C. When employing the MXene interlayer, a higher discharge capacity of ~715 mAh g^{-1} can be achieved at 0.2 C, which suggests that MXene interlayer used in aqueous Li-SI batteries can effectively immobilize the shuttling of polysulfides.

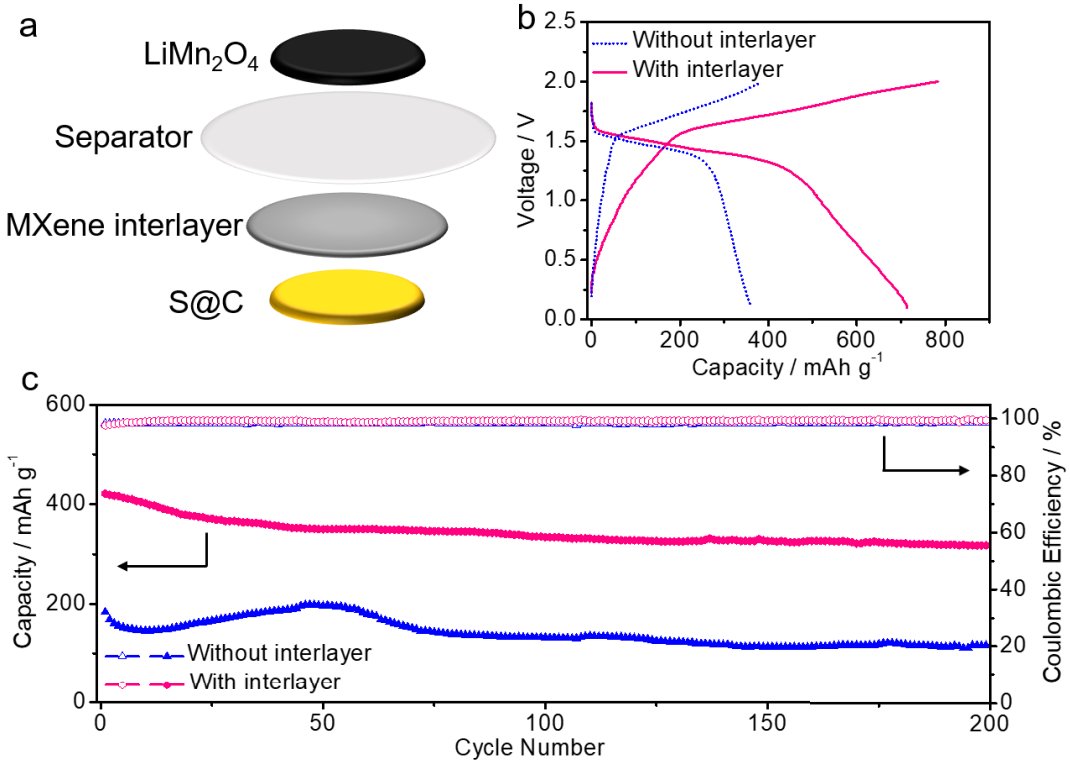

Figure 6.7. a) *The schematic illustration of the battery configuration of the S@C/MXene||LMO cell;* ***b)*** *The charge/discharge profiles of the Li-SI batteries with/without interlayer at the current density of 0.2 C;* ***c)*** *the cycling performance of the batteries with/without MXene interlayer at the current density of 0.5 C.*

The cycle life is an important criterion in Li-S batteries. In traditional aqueous Li-S batteries, the polysulfides can extract the water molecule to form Li_2S_4-anolyte, HS^-, and H_2S, which tend to dissolve into the electrolyte, leading to serious self-discharge and continuous capacity fading.[219, 234] In contrast, when using the as-prepared highly concentrated electrolyte, the reaction of polysulfides to Li_2S_4-anolyte, HS^- has been suppressed due to the limited free water molecules.[223] Furthermore, the concentrated electrolyte can also slow the diffusion of the intermediate products (Figure 6.3b). Therefore, Li-SI batteries with concentrated electrolyte showed a capacity of ~116 mAh g^{-1} after 200 cycles (shown in Figure 6.7c). The employment of MXene interlayer can further enhance the cycling stability of the batteries. Noticeably, Li-SI batteries with MXene interlayer (S@C/MXene||LMO) can still deliver ~317 mAh g^{-1} after 200 cycles. This value is higher than

those of previously reported configurations (MWCNTs@S@PPy|saturated lithium acetate|$LiMn_2O_4$: ~108 mAh g^{-1} at 0.5 A g^{-1} after 120 cycles; C/polysulfide|0.5 M Li_2SO_4|$LiMn_2O_4$: ~105 mAh g^{-1} at 0.5 C after 120 cycles; SBA-15/polysulfide|2.5 M Li_2SO_4|$LiMn_2O_4$: ~78 mAh g^{-1} at 2 C after 50 cycles).[220, 221, 235]

Electrochemical impedance spectroscopy (EIS) was also carried out to study the interfacial behavior of the aqueous Li-SI batteries. Figure 6.8 presents the EIS spectra of Li-SI batteries after 200 cycles. According to the simulated equivalent circuit shown in the inset of Figure 6.8, the intersection of the diagram with the real axis represents a bulk resistance (R_b), which is a sum of the resistances of electrodes and electrolyte/separator. Noticeably, the LMO||S@C cell showed a higher R_b value (~64 Ω) than their counterparts with interlayer (~32 Ω), indicating that the shuttling intermediate products in the electrolyte may largely increase the resistence of battery systems. Considering the roughness of the surface, The CPE 1 and CPE 2 were used in the simulated equivalent circuit. In high frequency area, the depressed semicircle is assigned to the interfacial resistance (R_f) and CPE 1 (the constant phase elements), and the depressed semicircle in medium frequency area is related to the charge transfer resistance (R_{ct}) and CPE 2. In low frequency area, the slope line is equivalent to the Warburg impedance (Z_w), which refers to the kinetics transformation. For the S@C/MXene||LMO batteries, the solid electrolyte interface resistance (R_f) is about ~103 Ω, which is smaller than that of LMO||S@C cell. This suggests the inhibition of the polysulfides shuttling and a stable solid/electrolyte interface, which facilitate the enhanced cycling performance (shown in Figure 6.7c).

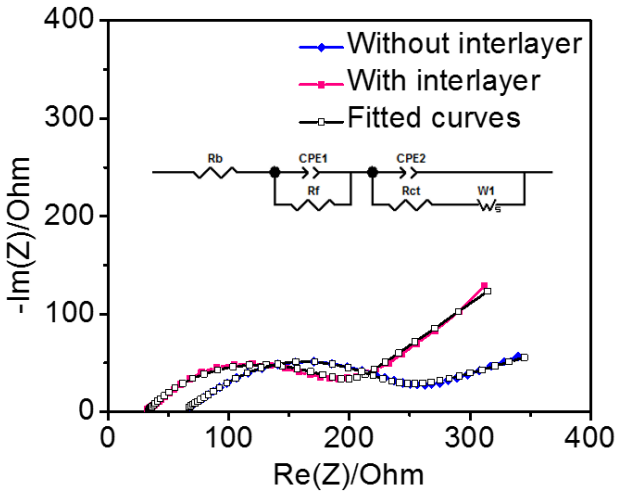

Figure 6.8. *The EIS spectra of the batteries with/without MXene interlayer, the inset shows the simulated equivalent circuit.*

6.4 Conclusions

In summary, we have developed an aqueous lithium-sulfur/ion battery enabled by the highly concentrated electrolyte and free-standing MXene interlayer. The concentrated electrolyte with limited free water molecule can effectively suppress the side reaction and slow the diffusion of the intermediate products. In the meanwhile, the free-standing MXene interlayer is able to prevent the loss of the active materials by chemical and physical adsorption. Due to the synergistically optimization effect, the concentrated electrolyte and MXene interlayer enables an aqueous lithium-sulfur/ion battery with optimized capacity and cycling performance. This work opens a new path to inspire the development of aqueous rechargeable batteries based on conversion chemistry as well as the various applications of MXene materials.

Chapter 7 Conclusions and future perspective

Tremendous efforts have been devoted to research on MXene-based materials for energy storage devices to achieve superior electrochemical performances, including high energy density, high power density and long cycle life. In this thesis, we have developed various energy storage devices enabled by two-dimensional MXenes, which greatly improve their electrochemical performances. The preparation methods, properties of composite materials, and applications (including lithium-sulfur batteries, lithium-iodine batteries, and K metal batteries) were systematically discussed. Typically, most MXenes can be prepared by selectively extracting the "A" atoms from the corresponding MAX phase precursors using HF acid. In addition to HF acid, LiF/HCl and concentrated NaOH have also been used to remove the "A" layers. Both preparation methods can yield MXenes, but the morphologies and surface functional groups of the obtained MXenes are different, which provides unique impacts on the properties of the MXene materials. Hence, further investigation is necessary to develop MXenes with different surface functional groups and architectures for various applications. Although MXene electrodes deliver an inclined charge-discharge profile and relatively low initial Coulombic efficiency, MXene-based composites with enhanced interlayer spacing and excellent electronic conductivity show great promise for high power-density batteries. In addition to lithium ions, sodium, potassium, and other multivalent ions can also be intercalated into MXene interlayers, indicating the potential utilization of MXenes in other battery systems (*e.g.*, sodium-ion batteries, potassium-ion batteries, aluminum-ion batteries and hybrid capacitors, *etc.*).[103] On the other hand, the surface functional groups on the MXene sheets can effectively immobilize polysulfides or iodide species, suppressing the shuttle effect during charge-discharge process in batteries based on conversion chemistry. Additionally, MXenes can confine metal anode (including lithium, sodium, and potassium, *etc.*) and prevent the

growth of dendrites, which improves the performances of metal anodes in batteries. These features endow MXenes with great potential for application in lithium-sulfur batteries.

Despite these advantages, some challenges still need to be overcome for the practical application of MXenes. First, new preparation methods are needed to synthesize MXenes with specific surface terminations because the current preparation methods lead to arbitrarily functionalized MXenes with more than one type of surface termination.[16] On the other hand, HF acid is highly corrosive, and it is much safer to fabricate MXenes by fluoride-free strategies. According to theoretical calculations, lithium ions can migrate more easily on bare Ti_3C_2 due to the lower energy barrier and shorter diffusion pathway compared with its fluorinated or hydroxylated derivatives. However, it has been difficult to prepare MXenes without terminations until now. Thus, it is promising to synthesize and employ bare MXenes without surface functional groups as electrode materials. Second, similar to other 2D materials, the restacking of MXene layers tends to decrease the specific surface area and number of active sites, leading to capacity fading in lithium-ion batteries. Thus, in addition to the HF-etched and DMSO-intercalated MXenes, other intercalants should be utilized to act as pillars to prevent the restacking of MXene layers.[28] However, large intercalated molecules may excessively increase the interlayer spacing and hinder charge transfer, which may be unfavorable for energy storage. Hence, intercalation with large molecules still needs to be fully investigated. In addition, the incorporation of high-capacity active materials with MXenes can effectively improve the energy density of batteries without sacrificing the power density since MXenes can provide facile electron conduction pathways. The fabrication of hierarchical few-layer MXene architectures are also attractive because the increased surface area and exposed active sites can result in enhanced electrochemical performance. Furthermore, MXene flakes with a vertically aligned architecture can remarkably improve ion/electron transport. Advanced

technologies, such as electrospinning, electrophoretic deposition and electrochemical deposition, could be used to fabricate vertically aligned MXene arrays. Third, considering the numerous types of MXenes that have been predicted, we should continue to theoretically and experimentally explore new types of 2D MXenes. For instance, theoretical calculations predicted that boron (B) can substitute carbon/nitrogen to occupy octahedral interstitial sites in MXenes, and calculated Mo_2B_2 and Fe_2B_2 exhibit low diffusion barriers and high theoretical capacities in lithium-ion batteries.[104] Finally, studies of MXene materials for use in lithium-sulfur batteries are still in their infancy, and only a few MXenes have been reported to serve as sulfur hosts; therefore, it is promising to examine more MXenes as hosts and/or separator components for lithium-sulfur batteries. Moreover, the corresponding theoretical calculations are also required to understand the mechanism of immobilizing polysulfides.

To date, MXenes and MXene-based composites have undoubtedly exhibited many advantages as electrode materials for lithium-based batteries. The abundant surface functional groups and excellent electronic conductivity of MXenes, as well as synergistic optimization effects in MXene-based composites, comprehensively contribute to the excellent electrochemical performances. In the future, both theoretical studies and experimental research should be conducted together to understand the mechanisms underlying the superior performance of MXenes.

APPENDIX: NOMENCLATURE

Abbreviations/Symbols	Full name
a.u.	Arbitrary unit
Ar	Argon
BET	Brunauer-Emmett-Teller
BJH	Barrett-Joyner-Halenda
CB	Carbon black
CNT	carbon nanotube
CV	Cyclic Voltammetry
C-rate	Current rate
DI	de-ionized
DEC	Diethyl carbonate
EC	Ethylene carbonate
EIS	Electrochemical Impedance Spectroscopy
EVs	Electric vehicles
FE-SEM	Field-Emission Scanning Electron Microscopy
FTIR	Fourier transform infrared spectroscopy
g	Gram
MXene	Transition metal carbides/nitrides
h	Hour
Hz	Hertz
I	Intensity
HEVs	Hybrid electric vehicles

HRTEM	High-resolution transmission electronic spectroscopy
JCPDS	Joint Committee on Powder Diffraction Standards
Li	Lithium
K	Potassium
LIBs	Lithium-ion Batteries
M	Molar concentration
mAh g^{-1}	Milli ampere hour per gram
h	hour
mm	Millimeter
nm	Nanometer
NMP	1-methyl-2-pyrrolidinone
PC	Propylene carbonate
PVDF	Poly(vinylidene difluoride)
R_{ct}	Charge transfer resistance
R_{Ω}	Ohmic resistance
SAED	Selected area electron diffraction
SEI	Solid Electrolyte Interface
SEM	Scanning electron Microscopy
PIBs	Potassium-ion Batteries
TEM	Transmission electron microscopy
TGA	Thermogravimetric analysis
XRD	X-ray diffraction
º	Degree

Ω	Ohm
ºC	Degree Celsius
*Z*w	Warburg impedance
LiTFSI	Lithium bis(trifluoromethanesulfonyl)imide
LiOTf	Lithium trifluoromethane sulfonate
PTFE	Poly(vinylidenedifluoride)
DOL	1,2-dioxolane
DME	Dimethoxymethane

REFERENCES

1. Armand, M.; Tarascon, J.-M., Building better batteries. *Nature* 2008, 451, 652.
2. Wang, G.; Yang, J.; Park, J.; Gou, X.; Wang, B.; Liu, H.; Yao, J., Facile synthesis and characterization of graphene nanosheets. *J. Phys. Chem. C* 2008, 112, 8192-8195.
3. Wang, G.; Shen, X.; Yao, J.; Park, J., Graphene nanosheets for enhanced lithium storage in lithium ion batteries. *Carbon* 2009, 47, 2049-2053.
4. Stankovich, S.; Dikin, D. A.; Piner, R. D.; Kohlhaas, K. A.; Kleinhammes, A.; Jia, Y.; Wu, Y.; Nguyen, S. T.; Ruoff, R. S., Synthesis of graphene-based nanosheets via chemical reduction of exfoliated graphite oxide. *Carbon* 2007, 45, 1558-1565.
5. Dikin, D. A.; Stankovich, S.; Zimney, E. J.; Piner, R. D.; Dommett, G. H.; Evmenenko, G.; Nguyen, S. T.; Ruoff, R. S., Preparation and characterization of graphene oxide paper. *Nature* 2007, 448, 457.
6. Liu, H.; Neal, A. T.; Zhu, Z.; Luo, Z.; Xu, X.; Tománek, D.; Ye, P. D., Phosphorene: an unexplored 2D semiconductor with a high hole mobility. *ACS Nano* 2014, 8, 4033-4041.
7. Zou, F.; Hu, X.; Li, Z.; Qie, L.; Hu, C.; Zeng, R.; Jiang, Y.; Huang, Y., MOF-derived porous $ZnO/ZnFe_2O_4$/C octahedra with hollow interiors for high-rate lithium-ion batteries. *Adv. Mater.* 2014, 26, 6622-6628.
8. Pumera, M.; Sofer, Z.; Ambrosi, A., Layered transition metal dichalcogenides for electrochemical energy generation and storage. *J. Mater. Chem. A* 2014, 2, 8981-8987.
9. Chhowalla, M.; Shin, H. S.; Eda, G.; Li, L.-J.; Loh, K. P.; Zhang, H., The chemistry of two-dimensional layered transition metal dichalcogenide nanosheets. *Nat. Chem.* 2013, 5, 263.
10. Coleman, J. N.; Lotya, M.; O'Neill, A.; Bergin, S. D.; King, P. J.; Khan, U.; Young, K.; Gaucher, A.; De, S.; Smith, R. J.; Shvets, I. V.; Arora, S. K.; Stanton, G.; Kim, H.-Y.; Lee, K.; Kim, G. T.; Duesberg, G. S.; Hallam, T.; Boland, J. J.; Wang, J. J.; Donegan, J. F.; Grunlan, J. C.; Moriarty, G.; Shmeliov, A.; Nicholls, R. J.; Perkins, J. M.; Grieveson, E. M.; Theuwissen, K.; McComb, D. W.; Nellist, P. D.; Nicolosi, V., Two-dimensional nanosheets produced by liquid exfoliation of layered materials. *Science* 2011, 331, 568-571.
11. Naguib, M.; Kurtoglu, M.; Presser, V.; Lu, J.; Niu, J.; Heon, M.; Hultman, L.; Gogotsi, Y.; Barsoum, M. W., Two-dimensional nanocrystals produced by exfoliation of Ti_3AlC_2. *Adv. Mater,* 2011, 23, 4248-4253.
12. Peng, Q. M.; Guo, J. X.; Zhang, Q. R.; Xiang, J. Y.; Liu, B. Z.; Zhou, A. G.; Liu, R. P.; Tian, Y. J., Unique lead adsorption behavior of activated hydroxyl group in two-dimensional titanium carbide. *J. Am. Chem. Soc.* 2014, 136, 4113-4116.
13. Naguib, M.; Mashtalir, O.; Carle, J.; Presser, V.; Lu, J.; Hultman, L.; Gogotsi, Y.; Barsoum, M. W., Two-dimensional transition metal carbides. *ACS Nano* 2012, 6, 1322-1331.
14. Anasori, B.; Xie, Y.; Beidaghi, M.; Lu, J.; Hosler, B. C.; Hultman, L.; Kent, P. R. C.; Gogotsi, Y.; Barsoum, M. W., Two-dimensional, ordered, double transition metals carbides (MXenes). *ACS Nano* 2015, 9, 9507-9516.
15. Ghidiu, M.; Naguib, M.; Shi, C.; Mashtalir, O.; Pan, L. M.; Zhang, B.; Yang, J.; Gogotsi, Y.; Billinge, S. J. L.; Barsoum, M. W., Synthesis and characterization of two-dimensional Nb_4C_3 (MXene). *Chem. Commun.* 2014, 50, 9517-9520.
16. Jing, Y.; Zhou, Z.; Cabrera, C. R.; Chen, Z., Graphene, inorganic graphene analogs and their composites for lithium ion batteries. *J. Mater. Chem. A* 2014, 2, 12104-12122.
17. Khazaei, M.; Arai, M.; Sasaki, T.; Estili, M.; Sakka, Y., Two-dimensional molybdenum carbides: potential thermoelectric materials of the MXene family. *Phys. Chem. Chem. Phys.* 2014, 16, 7841-7849.
18. Anasori, B.; Lukatskaya, M. R.; Gogotsi, Y., 2D metal carbides and nitrides (MXenes) for energy storage. *Nat. Rev. Mater.* 2017, 2, 16098.
19. Ren, W.; Qin, M.; Zhu, Z.; Yan, M.; Li, Q.; Zhang, L.; Liu, D.; Mai, L., Activation of sodium storage sites in Prussian blue analogues via surface etching. *Nano Lett.* 2017, 17, 4713-4718.

20. Naguib, M.; Mochalin, V. N.; Barsoum, M. W.; Gogotsi, Y., 25th anniversary article: MXenes: a new family of two-dimensional materials. *Adv. Mater.* 2014, 26, 992-1005.
21. Wang, X.; Shen, X.; Gao, Y.; Wang, Z.; Yu, R.; Chen, L., Atomic-scale recognition of surface structure and intercalation mechanism of Ti_3C_2X. *J. Am. Chem. Soc.* 2015, 137, 2715-2721.
22. Chaudhari, N. K.; Jin, H.; Kim, B.; San Baek, D.; Joo, S. H.; Lee, K., MXene: an emerging two-dimensional material for future energy conversion and storage applications. *J. Mater. Chem. A* 2017, 5, 24564-24579.
23. Zhang, X.; Zhang, Z.; Zhou, Z., MXene-based materials for electrochemical energy storage. *J. Energy Chem.* 2017, 27, 73-85.
24. Dong, Y.; Mallineni, S. S. K.; Maleski, K.; Behlow, H.; Mochalin, V. N.; Rao, A. M.; Gogotsi, Y.; Podila, R., Metallic MXenes: A new family of materials for flexible triboelectric nanogenerators. *Nano Energy* 2018, 44, 103-110.
25. Ran, J.; Gao, G.; Li, F. T.; Ma, T. Y.; Du, A.; Qiao, S. Z., Ti_3C_2 MXene co-catalyst on metal sulfide photo-absorbers for enhanced visible-light photocatalytic hydrogen production. *Nat. Commun.* 2017, 8, 13907.
26. Zhao, L.; Dong, B.; Li, S.; Zhou, L.; Lai, L.; Wang, Z.; Zhao, S.; Han, M.; Gao, K.; Lu, M.; Xie, X.; Chen, B.; Liu, Z.; Wang, X.; Zhang, H.; Li, H.; Liu, J.; Zhang, H.; Huang, X.; Huang, W., Interdiffusion reaction-assisted hybridization of two-dimensional metal–organic frameworks and $Ti_3C_2T_x$ nanosheets for electrocatalytic oxygen evolution. *ACS Nano* 2017, 11, 5800-5807.
27. Ling, C.; Shi, L.; Ouyang, Y.; Chen, Q.; Wang, J., Transition metal-promoted V_2CO_2 (MXenes): a new and highly active catalyst for hydrogen evolution reaction. *Adv. Sci.* 2016, 3, 1600180.
28. Lukatskaya, M. R.; Mashtalir, O.; Ren, C. E.; Dall'Agnese, Y.; Rozier, P.; Taberna, P. L.; Naguib, M.; Simon, P.; Barsoum, M. W.; Gogotsi, Y., Cation intercalation and high volumetric capacitance of two-dimensional titanium carbide. *Science* 2013, 341, 1502-1505.
29. Ling, Z.; Ren, C. E.; Zhao, M.-Q.; Yang, J.; Giammarco, J. M.; Qiu, J.; Barsoum, M. W.; Gogotsi, Y., Flexible and conductive MXene films and nanocomposites with high capacitance. *P. Natl. Acad. Sci.* 2014, 111, 16676-16681.
30. Lukatskaya, M. R.; Bak, S. M.; Yu, X. Q.; Yang, X. Q.; Barsoum, M. W.; Gogotsi, Y., Probing the mechanism of high capacitance in 2D titanium carbide using in situ X-Ray absorption spectroscopy. *Adv. Energy Mater.* 2015, 5, 1500589.
31. Chen, Y. Z.; Wang, C.; Wu, Z. Y.; Xiong, Y.; Xu, Q.; Yu, S. H.; Jiang, H. L., From bimetallic metal-organic framework to porous carbon: high surface area and multicomponent active dopants for excellent electrocatalysis. *Adv. Mater.* 2015, 27, 5010-5016.
32. Ghidiu, M.; Lukatskaya, M. R.; Zhao, M. Q.; Gogotsi, Y.; Barsoum, M. W., Conductive two-dimensional titanium carbide 'clay' with high volumetric capacitance. *Nature* 2014, 516, 78-81.
33. Zhao, M.-Q.; Ren, C. E.; Ling, Z.; Lukatskaya, M. R.; Zhang, C.; Van Aken, K. L.; Barsoum, M. W.; Gogotsi, Y., Flexible MXene/carbon nanotube composite paper with high volumetric capacitance. *Adv. Mater,* 2015, 27, 339-345.
34. VahidMohammadi, A.; Hadjikhani, A.; Shahbazmohamadi, S.; Beidaghi, M., Two-dimensional vanadium carbide (MXene) as a high-capacity cathode material for rechargeable aluminum batteries. *ACS Nano* 2017, 11, 11135-11144.
35. Xie, Y.; Dall'Agnese, Y.; Naguib, M.; Gogotsi, Y.; Barsoum, M. W.; Zhuang, H. L.; Kent, P. R., Prediction and characterization of MXene nanosheet anodes for non-lithium-ion batteries. *ACS Nano* 2014, 8, 9606-9615.
36. Xie, Y.; Naguib, M.; Mochalin, V. N.; Barsoum, M. W.; Gogotsi, Y.; Yu, X.; Nam, K.-W.; Yang, X.-Q.; Kolesnikov, A. I.; Kent, P. R., Role of surface structure on Li-ion energy storage capacity of two-dimensional transition-metal carbides. *J. Am. Chem. Soc.* 2014, 136, 6385-6394.
37. Guo, X.; Zhang, J.; Song, J.; Wu, W.; Liu, H.; Wang, G., MXene encapsulated titanium oxide nanospheres for ultra-stable and fast sodium storage. *Energy Storage Materials* 2018, 14, 306-313.
38. Bao, W.; Tang, X.; Guo, X.; Choi, S.; Wang, C.; Gogotsi, Y.; Wang, G., Porous cryo-dried MXene for efficient capacitive deionization. *Joule* 2018, 2, 778-787.

39. Shahzad, F.; Alhabeb, M.; Hatter, C. B.; Anasori, B.; Man Hong, S.; Koo, C. M.; Gogotsi, Y., Electromagnetic interference shielding with 2D transition metal carbides (MXenes). *Science* 2016, 353, 1137-1140.
40. El-Kady, M. F.; Strong, V.; Dubin, S.; Kaner, R. B., Laser scribing of high-performance and flexible graphene-based electrochemical capacitors. *Science* 2012, 335, 1326-1330.
41. Naguib, M.; Gogotsi, Y., Synthesis of two-dimensional materials by selective extraction. *Acc. Chem. Res.* 2015, 48, 128-135.
42. Mashtalir, O.; Naguib, M.; Mochalin, V. N.; Dall'Agnese, Y.; Heon, M.; Barsoum, M. W.; Gogotsi, Y., Intercalation and delamination of layered carbides and carbonitrides. *Nat. Commun.* 2013, 4, 1716.
43. Naguib, M.; Unocic, R. R.; Armstrong, B. L.; Nanda, J., Large-scale delamination of multi-layers transition metal carbides and carbonitrides "MXenes". *Dalton Trans.* 2015, 44, 9353-9358.
44. Maleski, K.; Mochalin, V. N.; Gogotsi, Y., Dispersions of two-dimensional titanium carbide MXene in organic solvents. *Chem. Mater.* 2017, 29, 1632-1640.
45. Ghidiu, M.; Kota, S.; Halim, J.; Sherwood, A. W.; Nedfors, N.; Rosen, J.; Mochalin, V. N.; Barsoum, M. W., Alkylammonium cation intercalation into Ti_3C_2 (MXene): Effects on properties and ion-exchange capacity estimation. *Chem. Mater.* 2017, 29, 1099-1106.
46. Alhabeb, M.; Maleski, K.; Mathis, T. S.; Sarycheva, A.; Hatter, C. B.; Uzun, S.; Levitt, A.; Gogotsi, Y., Selective etching of silicon from Ti_3SiC_2 (MAX) to obtain 2D titanium carbide (MXene). *Angew. Chem. Int. Ed.* 2018, 57, 5444-5448.
47. Li, T.; Yao, L.; Liu, Q.; Gu, J.; Luo, R.; Li, J.; Yan, X.; Wang, W.; Liu, P.; Chen, B., Fluorine-free synthesis of high-purity $Ti_3C_2T_x$ (T= OH, O) via alkali treatment. *Angew. Chem. Int. Ed.* 2018, 57, 6115-6119.
48. Alhabeb, M.; Maleski, K.; Anasori, B.; Lelyukh, P.; Clark, L.; Sin, S.; Gogotsi, Y., Guidelines for synthesis and processing of two-dimensional titanium carbide ($Ti_3C_2T_x$ MXene). *Chem. Mater.* 2017, 29, 7633-7644.
49. Hope, M. A.; Forse, A. C.; Griffith, K. J.; Lukatskaya, M. R.; Ghidiu, M.; Gogotsi, Y.; Grey, C. P., NMR reveals the surface functionalisation of Ti_3C_2 MXene. *Phys. Chem. Chem. Phys.* 2016, 18, 5099-5102.
50. Sang, X.; Xie, Y.; Lin, M.-W.; Alhabeb, M.; Van Aken, K. L.; Gogotsi, Y.; Kent, P. R. C.; Xiao, K.; Unocic, R. R., Atomic defects in monolayer titanium carbide ($Ti_3C_2T_x$) MXene. *ACS Nano* 2016, 10, 9193-9200.
51. Xuan, J.; Wang, Z.; Chen, Y.; Liang, D.; Cheng, L.; Yang, X.; Liu, Z.; Ma, R.; Sasaki, T.; Geng, F., Organic-base-driven intercalation and delamination for the production of functionalized titanium carbide nanosheets with superior photothermal therapeutic performance. *Angew. Chem. Int. Ed.* 2016, 55, 14569-14574.
52. Urbankowski, P.; Anasori, B.; Makaryan, T.; Er, D.; Kota, S.; Walsh, P. L.; Zhao, M.; Shenoy, V. B.; Barsoum, M. W.; Gogotsi, Y., Synthesis of two-dimensional titanium nitride Ti_4N_3 (MXene). *Nanoscale* 2016, 8, 11385-11391.
53. Xu, C.; Wang, L.; Liu, Z.; Chen, L.; Guo, J.; Kang, N.; Ma, X.-L.; Cheng, H.-M.; Ren, W., Large-area high-quality 2D ultrathin Mo_2C superconducting crystals. *Nat. Mater.* 2015, 14, 1135-1141.
54. Xiao, X.; Yu, H.; Jin, H.; Wu, M.; Fang, Y.; Sun, J.; Hu, Z.; Li, T.; Wu, J.; Huang, L.; Gogotsi, Y.; Zhou, J., Salt-templated synthesis of 2D metallic MoN and other nitrides. *ACS Nano* 2017, 11, 2180-2186.
55. Ren, C. E.; Zhao, M.-Q.; Makaryan, T.; Halim, J.; Boota, M.; Kota, S.; Anasori, B.; Barsoum, M. W.; Gogotsi, Y., Porous two-dimensional transition metal carbide (MXene) flakes for high-performance Li-ion storage. *ChemElectroChem* 2016, 3, 689-693.
56. Halim, J.; Lukatskaya, M. R.; Cook, K. M.; Lu, J.; Smith, C. R.; Naslund, L.-A.; May, S. J.; Hultman, L.; Gogotsi, Y.; Eklund, P.; Barsoum, M. W., Transparent conductive two-dimensional titanium carbide epitaxial thin films. *Chem. Mater.* 2014, 26, 2374-2381.
57. Feng, A.; Yu, Y.; Wang, Y.; Jiang, F.; Yu, Y.; Mi, L.; Song, L., Two-dimensional MXene Ti_3C_2 produced by exfoliation of Ti_3AlC_2. *Mater. Des.* 2017, 114, 161-166.
58. Yang, J.; Naguib, M.; Ghidiu, M.; Pan, L.-M.; Gu, J.; Nanda, J.; Halim, J.; Gogotsi, Y.; Barsoum, M. W., Two-dimensional Nb-based M_4C_3 solid solutions (MXenes). *J. Am. Ceram. Soc.* 2016, 99, 660-666.

59. Halim, J.; Kota, S.; Lukatskaya, M. R.; Naguib, M.; Zhao, M.-Q.; Moon, E. J.; Pitock, J.; Nanda, J.; May, S. J.; Gogotsi, Y.; Barsoum, M. W., Synthesis and characterization of 2D molybdenum carbide (MXene). *Adv. Func. Mater.* 2016, 26, 3118-3127.
60. Naguib, M.; Halim, J.; Lu, J.; Cook, K. M.; Hultman, L.; Gogotsi, Y.; Barsoum, M. W., New two-dimensional niobium and vanadium carbides as promising materials for Li-ion batteries. *J. Am. Chem. Soc.* 2013, 135, 15966-15969.
61. Zhou, J.; Zha, X.; Chen, F. Y.; Ye, Q.; Eklund, P.; Du, S.; Huang, Q., A Two-dimensional zirconium carbide by selective etching of Al_3C_3 from nanolaminated $Zr_3Al_3C_5$. *Angew. Chem. Int. Ed.* 2016, 128, 5092-5097.
62. Zhou, J.; Zha, X.; Zhou, X.; Chen, F.; Gao, G.; Wang, S.; Shen, C.; Chen, T.; Zhi, C.; Eklund, P.; Du, S.; Xue, J.; Shi, W.; Chai, Z.; Huang, Q., Synthesis and electrochemical properties of two-dimensional hafnium carbide. *ACS Nano* 2017, 11, 3841-3850.
63. Lai, S.; Jeon, J.; Jang, S. K.; Xu, J.; Choi, Y. J.; Park, J.-H.; Hwang, E.; Lee, S., Surface group modification and carrier transport properties of layered transition metal carbides (Ti_2CT_x, T:–OH,–F and–O). *Nanoscale* 2015, 7, 19390-19396.
64. Tang, Q.; Zhou, Z.; Shen, P., Are MXenes promising anode materials for Li ion batteries? Computational studies on electronic properties and Li storage capability of Ti_3C_2 and $Ti_3C_2X_2$ (X = F, OH) monolayer. *J. Am. Chem. Soc.* 2012, 134, 16909-16916.
65. Khazaei, M.; Arai, M.; Sasaki, T.; Chung, C.-Y.; Venkataramanan, N. S.; Estili, M.; Sakka, Y.; Kawazoe, Y., Novel electronic and magnetic properties of two-dimensional transition metal carbides and nitrides. *Adv. Func. Mater.* 2013, 23, 2185-2192.
66. Khazaei, M.; Ranjbar, A.; Arai, M.; Yunoki, S., Topological insulators in the ordered double transition metals $M_2'M''C_2$ MXenes (M′= Mo, W; M″= Ti, Zr, Hf). *Phys. Rev. B* 2016, 94, 125152.
67. Li, L., Lattice dynamics and electronic structures of $Ti_3C_2O_2$ and $Mo_2TiC_2O_2$ (MXenes): The effect of Mo substitution. *Comp. Mater. Sci.* 2016, 124, 8-14.
68. Karlsson, L. H.; Birch, J.; Halim, J.; Barsoum, M. W.; Persson, P. O. A., Atomically resolved structural and chemical investigation of single MXene sheets. *Nano Lett.* 2015, 15, 4955-4960.
69. Harris, K. J.; Bugnet, M.; Naguib, M.; Barsoum, M. W.; Goward, G. R., Direct measurement of surface termination groups and their connectivity in the 2D MXene V_2CT_x using NMR spectroscopy. *J. Phys. Chem. C* 2015, 119, 13713-13720.
70. Wang, H.-W.; Naguib, M.; Page, K.; Wesolowski, D. J.; Gogotsi, Y., Resolving the structure of $Ti_3C_2T_x$ MXenes through multilevel structural modeling of the atomic pair distribution function. *Chem. Mater.* 2015, 28, 349-359.
71. Magne, D.; Mauchamp, V.; Célérier, S.; Chartier, P.; Cabioc'h, T., Spectroscopic evidence in the visible-ultraviolet energy range of surface functionalization sites in the multilayer Ti_3C_2 MXene. *Phys. Rev. B* 2015, 91, 201409.
72. Xie, Y.; Kent, P. R. C., Hybrid density functional study of structural and electronic properties of functionalized $Ti_{n+1}X_n$ (X = C, N) monolayers. *Phys. Rev. B* 2013, 87, 235441.
73. Enyashin, A. N.; Ivanovskii, A. L., Two-dimensional titanium carbonitrides and their hydroxylated derivatives: Structural, electronic propertis and stability of MXenes $Ti_3C_{2-x}N_x(OH)_2$ from DFTB calculations. *J. Solid State Chem.* 2013, 207, 42-48.
74. Enyashin, A. N.; Ivanoyskii, A. L., Structural and electronic properties and stability of MXenes Ti_2C and Ti_3C_2 functionalized by methoxy groups. *J. Phys. Chem. C* 2013, 117, 13637-13643.
75. Yu, T.; Zhao, Z.; Liu, L.; Zhang, S.; Xu, H.; Yang, G., TiC_3 monolayer with high specific capacity for sodium-ion batteries. *J. Am. Chem. Soc.* 2018, 140, 5962-5968.
76. Lipatov, A.; Lu, H.; Alhabeb, M.; Anasori, B.; Gruverman, A.; Gogotsi, Y.; Sinitskii, A., Elastic properties of 2D $Ti_3C_2T_x$ MXene monolayers and bilayers. *Sci. Adv.* 2018, 4, eaat0491.
77. Borysiuk, V. N.; Mochalin, V. N.; Gogotsi, Y., Bending rigidity of two-dimensional titanium carbide (MXene) nanoribbons: A molecular dynamics study. *Comp. Mater. Sci.* 2018, 143, 418-424.
78. Borysiuk, V. N.; Mochalin, V. N.; Gogotsi, Y., Molecular dynamic study of the mechanical properties of two-dimensional titanium carbides $Ti_{n+1}C_n$ (MXenes). *Nanotechnol.* 2015, 26, 265705.

79. Kurtoglu, M.; Naguib, M.; Gogotsi, Y.; Barsoum, M. W., First principles study of two-dimensional early transition metal carbides. *Mrs Commun.* 2012, 2, 133-137.
80. Khazaei, M.; Arai, M.; Sasaki, T.; Chung, C. Y.; Venkataramanan, N. S.; Estili, M.; Sakka, Y.; Kawazoe, Y., Novel electronic and magnetic properties of two-dimensional transition metal carbides and nitrides. *Adv. Func. Mater.* 2013, 23, 2185-2192.
81. Hu, T.; Zhang, H.; Wang, J.; Li, Z.; Hu, M.; Tan, J.; Hou, P.; Li, F.; Wang, X., Anisotropic electronic conduction in stacked two-dimensional titanium carbide. *Sci. Rep.* 2015, 5, 16329.
82. Dillon, A. D.; Ghidiu, M. J.; Krick, A. L.; Griggs, J.; May, S. J.; Gogotsi, Y.; Barsoum, M. W.; Fafarman, A. T., Highly conductive optical quality solution-processed films of 2D titanium carbide. *Adv. Func. Mater.* 2016, 26, 4162-4168.
83. Dong, Y.; Chertopalov, S.; Maleski, K.; Anasori, B.; Hu, L.; Bhattacharya, S.; Rao, A. M.; Gogotsi, Y.; Mochalin, V. N.; Podila, R., Saturable absorption in 2D Ti_3C_2 MXene thin films for passive photonic diodes. *Adv. Mater,* 2018, 30, 1705714.
84. Chertopalov, S.; Mochalin, V. N., Environment-sensitive photoresponse of spontaneously partially oxidized Ti_3C_2 MXene thin films. *ACS Nano* 2018, 12, 6109-6116.
85. Xie, X.; Zhao, M.-Q.; Anasori, B.; Maleski, K.; Ren, C. E.; Li, J.; Byles, B. W.; Pomerantseva, E.; Wang, G.; Gogotsi, Y., Porous heterostructured MXene/carbon nanotube composite paper with high volumetric capacity for sodium-based energy storage devices. *Nano Energy* 2016, 26, 513-523.
86. Zhang, C. F.; Beidaghi, M.; Naguib, M.; Lukatskaya, M. R.; Zhao, M. Q.; Dyatkin, B.; Cook, K. M.; Kim, S. J.; Eng, B.; Xiao, X.; Long, D. H.; Qiao, W. M.; Dunn, B.; Gogotsi, Y., Synthesis and charge storage properties of hierarchical niobium pentoxide/carbon/niobium carbide (MXene) hybrid materials. *Chem. Mater.* 2016, 28, 3937-3943.
87. Naguib, M.; Come, J.; Dyatkin, B.; Presser, V.; Taberna, P.-L.; Simon, P.; Barsoum, M. W.; Gogotsi, Y., MXene: a promising transition metal carbide anode for lithium-ion batteries. *Electrochem. Commun.* 2012, 16, 61-64.
88. Come, J.; Naguib, M.; Rozier, P.; Barsoum, M. W.; Gogotsi, Y.; Taberna, P. L.; Morcrette, M.; Simon, P., A non-aqueous asymmetric cell with a Ti_2C-based two-dimensional negative electrode. *J. Electrochem. Soc.* 2012, 159, A1368-A1373.
89. Liang, X.; Garsuch, A.; Nazar, L. F., Sulfur cathodes based on conductive MXene nanosheets for high-performance lithium–sulfur batteries. *Angew. Chem. Int. Ed.* 2015, 54, 3907-3911.
90. Kajiyama, S.; Szabova, L.; Iinuma, H.; Sugahara, A.; Gotoh, K.; Sodeyama, K.; Tateyama, Y.; Okubo, M.; Yamada, A., Enhanced Li-ion accessibility in MXene titanium carbide by steric chloride termination. *Adv. Energy Mater.* 2017, 7, 1601873.
91. Er, D.; Li, J.; Naguib, M.; Gogotsi, Y.; Shenoy, V. B., Ti_3C_2 MXene as a high capacity electrode material for metal (Li, Na, K, Ca) ion batteries. *ACS Appl. Mater. Interfaces* 2014, 6, 11173-11179.
92. Sun, D. D.; Wang, M. S.; Li, Z. Y.; Fan, G. X.; Fan, L. Z.; Zhou, A. G., Two-dimensional Ti_3C_2 as anode material for Li-ion batteries. *Electrochem. Commun.* 2014, 47, 80-83.
93. Kim, S. J.; Naguib, M.; Zhao, M. Q.; Zhang, C. F.; Jung, H. T.; Barsoum, M. W.; Gogotsi, Y., High mass loading, binder-free MXene anodes for high areal capacity Li-ion batteries. *Electrochim. Acta* 2015, 163, 246-251.
94. Zhao, S.; Meng, X.; Zhu, K.; Du, F.; Chen, G.; Wei, Y.; Gogotsi, Y.; Gao, Y., Li-ion uptake and increase in interlayer spacing of Nb_4C_3 MXene. *Energy Storage Materials* 2017, 8, 42-48.
95. Hu, J.; Xu, B.; Ouyang, C.; Yang, S. A.; Yao, Y., Investigations on V_2C and V_2CX_2 (X = F, OH) mono layer as a promising anode material for Li ion batteries from first-principles calculations. *J. Phys. Chem. C* 2014, 118, 24274-24281.
96. Xia, Y.; Mathis, T. S.; Zhao, M.-Q.; Anasori, B.; Dang, A.; Zhou, Z.; Cho, H.; Gogotsi, Y.; Yang, S., Thickness-independent capacitance of vertically aligned liquid-crystalline MXenes. *Nature* 2018, 557, 409.
97. Zhao, M. Q.; Xie, X.; Ren, C. E.; Makaryan, T.; Anasori, B.; Wang, G.; Gogotsi, Y., Hollow MXene spheres and 3D macroporous MXene frameworks for Na-ion storage. *Adv. Mater.* 2017, 29, 1702410.

98. Lin, Z.; Sun, D.; Huang, Q.; Yang, J.; Barsoum, M. W.; Yan, X., Carbon nanofiber bridged two-dimensional titanium carbide as a superior anode for lithium-ion batteries. *J. Mater. Chem. A* 2015, 3, 14096-14100.
99. Mashtalir, O.; Lukatskaya, M. R.; Zhao, M. Q.; Barsoum, M. W.; Gogotsi, Y., Amine-assisted delamination of Nb_2C MXene for Li-ion energy storage devices. *Adv. Mater.* 2015, 27, 3501-3506.
100. Zheng, W.; Zhang, P.; Chen, J.; Tian, W.; Zhang, Y.; Sun, Z., In situ synthesis of CNTs@Ti_3C_2 hybrid structures by microwave irradiation for high-performance anodes in lithium ion batteries. *J. Mater. Chem. A* 2018, 6, 3543-3551.
101. Byeon, A.; Zhao, M. Q.; Ren, C. E.; Halim, J.; Kota, S.; Urbankowski, P.; Anasori, B.; Barsoum, M. W.; Gogotsi, Y., Two-dimensional titanium carbide MXene as a cathode material for hybrid magnesium/lithium-ion batteries. *ACS Appl. Mater. Interfaces* 2017, 9, 4296-4300.
102. Ma, Z.; Zhou, X.; Deng, W.; Lei, D.; Liu, Z., 3D porous MXene (Ti_3C_2)/reduced graphene oxide hybrid films for advanced lithium storage. *ACS Appl. Mater. Interfaces* 2018, 10, 3634-3643.
103. Chen, C.; Boota, M.; Xie, X.; Zhao, M.; Anasori, B.; Ren, C. E.; Miao, L.; Jiang, J.; Gogotsi, Y., Charge transfer induced polymerization of EDOT confined between 2D titanium carbide layers. *J. Mater. Chem. A* 2017, 5, 5260-5265.
104. Lin, Z. Y.; Sun, D. F.; Huang, Q.; Yang, J.; Barsoum, M. W.; Yan, X. B., Carbon nanofiber bridged two-dimensional titanium carbide as a superior anode for lithium-ion batteries. *J. Mater. Chem. A* 2015, 3, 14096-14100.
105. Mashtalir, O.; Lukatskaya, M. R.; Zhao, M.-Q.; Barsoum, M. W.; Gogotsi, Y., Amine-assisted delamination of Nb_2C MXene for Li-ion energy storage devices. *Adv. Mater.* 2015, 27, 3501-3506.
106. Luo, J.; Tao, X.; Zhang, J.; Xia, Y.; Huang, H.; Zhang, L.; Gan, Y.; Liang, C.; Zhang, W., Sn^{4+} ion decorated highly conductive Ti_3C_2 MXene: promising lithium-ion anodes with enhanced volumetric capacity and cyclic performance. *ACS Nano* 2016, 10, 2491-2499.
107. Luo, J.; Zhang, W.; Yuan, H.; Jin, C.; Zhang, L.; Huang, H.; Liang, C.; Xia, Y.; Zhang, J.; Gan, Y.; Tao, X., Pillared structure design of MXene with ultralarge interlayer spacing for high-performance lithium-ion capacitors. *ACS Nano* 2017, 11, 2459-2469.
108. Zou, G.; Zhang, Z.; Guo, J.; Liu, B.; Zhang, Q.; Fernandez, C.; Peng, Q., Synthesis of MXene/Ag composites for extraordinary long cycle lifetime lithium storage at high rates. *ACS Appl. Mater. Interfaces* 2016, 8, 22280-22286.
109. Zhang, C. F.; Kim, S. J.; Ghidiu, M.; Zhao, M. Q.; Barsoum, M. W.; Nicolosi, V.; Gogotsi, Y., Layered orthorhombic Nb_2O_5@$Nb_4C_3T_x$ and TiO_2@$Ti_3C_2T_x$ hierarchical composites for high performance Li-ion batteries. *Adv. Func. Mater.* 2016, 26, 4143-4151.
110. Ahmed, B.; Anjum, D. H.; Hedhili, M. N.; Gogotsi, Y.; Alshareef, H. N., H_2O_2 assisted room temperature oxidation of Ti_2C MXene for Li-ion battery anodes. *Nanoscale* 2016, 8, 7580-7587.
111. Zhao, M.-Q.; Torelli, M.; Ren, C. E.; Ghidiu, M.; Ling, Z.; Anasori, B.; Barsoum, M. W.; Gogotsi, Y., 2D titanium carbide and transition metal oxides hybrid electrodes for Li-ion storage. *Nano Energy* 2016, 30, 603-613.
112. Ahmed, B.; Anjum, D. H.; Gogotsi, Y.; Alshareef, H. N., Atomic layer deposition of SnO_2 on MXene for Li-ion battery anodes. *Nano Energy* 2017, 34, 249-256.
113. Huang, J.; Meng, R.; Zu, L.; Wang, Z.; Feng, N.; Yang, Z.; Yu, Y.; Yang, J., Sandwich-like $Na_{0.23}TiO_2$ nanobelt/Ti_3C_2 MXene composites from a scalable in situ transformation reaction for long-life high-rate lithium/sodium-ion batteries. *Nano Energy* 2018, 46, 20-28.
114. Chen, C.; Xie, X.; Anasori, B.; Sarycheva, A.; Makaryan, T.; Zhao, M.; Urbankowski, P.; Miao, L.; Jiang, J.; Gogotsi, Y., MoS_2-on-MXene heterostructures as highly reversible anode materials for lithium-ion batteries. *Angew. Chem. Int. Ed.* 2018, 57, 1846-1850.
115. Zheng, M.; Guo, R.; Liu, Z.; Wang, B.; Meng, L.; Li, F.; Li, T.; Luo, Y., MoS_2 intercalated p-Ti_3C_2 anode materials with sandwich-like three dimensional conductive networks for lithium-ion batteries. *J. Alloys Compd.* 2018, 735, 1262-1270.
116. Shen, C.; Wang, L.; Zhou, A.; Zhang, H.; Chen, Z.; Hu, Q.; Qin, G., MoS_2-decorated Ti_3C_2 MXene nanosheet as anode material in lithium-ion batteries. *J. Electrochem. Soc.* 2017, 164, A2654-A2659.

117. Wu, Y.; Nie, P.; Wu, L.; Dou, H.; Zhang, X., 2D MXene/SnS_2 composites as high-performance anodes for sodium ion batteries. *Chem. Eng. J.* 2018, 334, 932-938.
118. Wang, F.; Wang, Z.; Zhu, J.; Yang, H.; Chen, X.; Wang, L.; Yang, C., Facile synthesis SnO_2 nanoparticle-modified Ti_3C_2 MXene nanocomposites for enhanced lithium storage application. *J. Mater. Sci.* 2017, 52, 3556-3565.
119. Du, F.; Tang, H.; Pan, L. M.; Zhang, T.; Lu, H. M.; Xiong, J.; Yang, J.; Zhang, C., Environmental friendly scalable production of colloidal 2D titanium carbonitride MXene with minimized nanosheets restacking for excellent cycle life lithium-ion batteries. *Electrochim. Acta* 2017, 235, 690-699.
120. Wu, X. H.; Wang, Z. Y.; Yu, M. Z.; Xiu, L. Y.; Qiu, J. S., Stabilizing the MXenes by carbon nanoplating for developing hierarchical nanohybrids with efficient lithium storage and hydrogen evolution capability. *Adv. Mater.* 2017, 29, 1607017.
121. Pang, Q.; Liang, X.; Kwok, C.; Nazar, L. F., The importance of chemical interactions between sulfur host materials and lithium polysulfides for advanced lithium-sulfur batteries. *J. Electrochem. Soc.* 2015, 162, A2567-A2576.
122. Bao, W.; Su, D.; Zhang, W.; Guo, X.; Wang, G., 3D metal carbide@mesoporous carbon hybrid architecture as a new polysulfide reservoir for lithium-sulfur batteries. *Adv. Func. Mater.* 2016, 26, 8746-8756.
123. Bao, W.; Xie, X.; Xu, J.; Guo, X.; Song, J.; Wu, W.; Su, D.; Wang, G., Confined sulfur in 3D MXene/reduced graphene oxide hybrid nanosheets for lithium–sulfur battery. *Chem. Eur. J.* 2017, 23, 12613-12619.
124. Liang, X.; Rangom, Y.; Kwok, C. Y.; Pang, Q.; Nazar, L. F., Interwoven MXene nanosheet/carbon-nanotube composites as Li–S cathode hosts. *Adv. Mater.* 2017, 29, 1603040.
125. Sim, E. S.; Yi, G. S.; Je, M.; Lee, Y.; Chung, Y.-C., Understanding the anchoring behavior of titanium carbide-based MXenes depending on the functional group in LiS batteries: A density functional theory study. *J. Power Sources* 2017, 342, 64-69.
126. Zhao, Y.; Zhao, J., Functional group-dependent anchoring effect of titanium carbide-based MXenes for lithium-sulfur batteries: A computational study. *Appl. Surf. Sci.* 2017, 412, 591-598.
127. Rao, D.; Zhang, L.; Wang, Y.; Meng, Z.; Qian, X.; Liu, J.; Shen, X.; Qiao, G.; Lu, R., Mechanism on the improved performance of lithium sulfur batteries with MXene-based additives. *J. Phys. Chem. C* 2017, 121, 11047-11054.
128. Guo, X.; Li, K.; Bao, W.; Zhao, Y.; Xu, J.; Liu, H.; Wang, G., Highly reversible lithium polysulfide semiliquid battery with nitrogen-rich carbon fiber electrodes. *Energy Technol.* 2018, 6, 251-256.
129. Bao, W.; Liu, L.; Wang, C.; Choi, S.; Wang, D.; Wang, G., Facile synthesis of crumpled nitrogen-doped MXene nanosheets as a new sulfur host for lithium–sulfur batteries. *Adv. Energy Mater.* 2018, 8, 1702485.
130. Fang, R.; Zhao, S.; Sun, Z.; Wang, D. W.; Cheng, H. M.; Li, F., More reliable lithium-sulfur batteries: status, solutions and prospects. *Adv. Mater.* 2017, 29, 1606823.
131. Song, J.; Su, D.; Xie, X.; Guo, X.; Bao, W.; Shao, G.; Wang, G., Immobilizing polysulfides with MXene-functionalized separators for stable lithium–sulfur batteries. *ACS Appl. Mater. Interfaces* 2016, 8, 29427-29433.
132. Lin, C.; Zhang, W.; Wang, L.; Wang, Z.; Zhao, W.; Duan, W.; Zhao, Z.; Liu, B.; Jin, J., A few-layered Ti_3C_2 nanosheet/glass fiber composite separator as a lithium polysulphide reservoir for high-performance lithium-sulfur batteries. *J. Mater. Chem. A* 2016, 4, 5993-5998.
133. Sun, C.; Shi, X.; Zhang, Y.; Liang, J.; Qu, J.; Lai, C., $Ti_3C_2T_x$ MXene interface layer driving ultra-stable lithium-iodine batteries with both high iodine content and mass loading. *ACS Nano* 2020, 14, 1176-1184.
134. Li, B.; Zhang, D.; Liu, Y.; Yu, Y.; Li, S.; Yang, S., Flexible Ti_3C_2 MXene-lithium film with lamellar structure for ultrastable metallic lithium anodes. *Nano Energy* 2017, 39, 654-661.
135. Li, J.; Yuan, X.; Lin, C.; Yang, Y.; Xu, L.; Du, X.; Xie, J.; Lin, J.; Sun, J., Achieving high pseudocapacitance of 2D titanium carbide (MXene) by cation intercalation and surface modification. *Adv. Energy Mater.* 2017, 7, 1602725.

136. Naguib, M.; Adams, R. A.; Zhao, Y.; Zemlyanov, D.; Varma, A.; Nanda, J.; Pol, V. G., Electrochemical performance of MXenes as K-ion battery anodes. *Chem. Commun.* 2017, 53, 6883-6886.
137. Ming, F.; Liang, H.; Zhang, W.; Ming, J.; Lei, Y.; Emwas, A.-H.; Alshareef, H. N., Porous MXenes enable high performance potassium ion capacitors. *Nano Energy* 2019, 62, 853-860.
138. Lian, P.; Dong, Y.; Wu, Z.-S.; Zheng, S.; Wang, X.; Wang, S.; Sun, C.; Qin, J.; Shi, X.; Bao, X., Alkalized Ti_3C_2 MXene nanoribbons with expanded interlayer spacing for high-capacity sodium and potassium ion batteries. *Nano Energy* 2017, 40, 1-8.
139. Zhu, J.; Schwingenschlögl, U., P and Si functionalized MXenes for metal-ion battery applications. *2D Mater.* 2017, 4, 025073.
140. Zhao, R.; Di, H.; Hui, X.; Zhao, D.; Wang, R.; Wang, C.; Yin, L., Self-assembled Ti_3C_2 MXene and N-rich porous carbon hybrids as superior anodes for high-performance potassium-ion batteries. *Energy Environ. Sci.* 2020, 13, 246-257.
141. Sun, N.; Zhu, Q.; Anasori, B.; Zhang, P.; Liu, H.; Gogotsi, Y.; Xu, B., MXene-bonded flexible hard carbon film as anode for stable Na/K-ion storage. *Adv. Func. Mater.* 2019, 29, 1906282.
142. Li, J.; Rui, B.; Wei, W.; Nie, P.; Chang, L.; Le, Z.; Liu, M.; Wang, H.; Wang, L.; Zhang, X., Nanosheets assembled layered MoS_2/MXene as high performance anode materials for potassium ion batteries. *J. Power Sources* 2019, 449, 227481.
143. Huang, H.; Cui, J.; Liu, G.; Bi, R.; Zhang, L., Carbon-coated $MoSe_2$/MXene hybrid nanosheets for superior potassium storage. *ACS Nano* 2019, 13, 3448-3456.
144. Tian, Y.; An, Y.; Xiong, S.; Feng, J.; Qian, Y., A general method for constructing robust, flexible and freestanding MXene@metal anodes for high-performance potassium-ion batteries. *J. Mater. Chem. A* 2019, 7, 9716-9725.
145. Andre, D.; Meiler, M.; Steiner, K.; Wimmer, C.; Soczka-Guth, T.; Sauer, D. U., Characterization of high-power lithium-ion batteries by electrochemical impedance spectroscopy. I. Experimental investigation. *J. Power Sources* 2011, 196, 5334-5341.
146. Schmuch, R.; Wagner, R.; Hörpel, G.; Placke, T.; Winter, M., Performance and cost of materials for lithium-based rechargeable automotive batteries. *Nat. Energy* 2018, 3, 267.
147. Wang, Y.; Sun, Q.; Zhao, Q.; Cao, J.; Ye, S., Rechargeable lithium/iodine battery with superior high-rate capability by using iodine–carbon composite as cathode. *Energy Environ. Sci.* 2011, 4, 3947-3950.
148. Gong, D.; Wang, B.; Zhu, J.; Podila, R.; Rao, A. M.; Yu, X.; Xu, Z.; Lu, B., An iodine quantum dots based rechargeable sodium–iodine battery. *Adv. Energy Mater.* 2017, 7, 1601885.
149. Kim, S.; Kim, S.-K.; Sun, P.; Oh, N.; Braun, P. V., Reduced graphene oxide/LiI composite lithium ion battery cathodes. *Nano Lett.* 2017, 17, 6893-6899.
150. Zhao, Y.; Wang, L.; Byon, H. R., High-performance rechargeable lithium-iodine batteries using triiodide/iodide redox couples in an aqueous cathode. *Nat. Commun.* 2013, 4, 1896.
151. Su, Z.; Wei, Z.; Lai, C.; Deng, H.; Liu, Z.; Ma, J., Robust pseudo-capacitive Li-I_2 battery enabled by catalytic, adsorptive N-doped graphene interlayer. *Energy Storage Materials* 2018, 14, 129-135.
152. Su, D.; Zhou, D.; Wang, C.; Wang, G., Toward high performance lithium–sulfur batteries based on Li2S cathodes and beyond: status, challenges, and perspectives. *Adv. Func. Mater.* 2018, 28, 1800154.
153. Zheng, G.; Lee, S. W.; Liang, Z.; Lee, H.-W.; Yan, K.; Yao, H.; Wang, H.; Li, W.; Chu, S.; Cui, Y., Interconnected hollow carbon nanospheres for stable lithium metal anodes. *Nat. Nanotechnol.* 2014, 9, 618.
154. Zhang, Q.; Wu, Z.; Liu, F.; Liu, S.; Liu, J.; Wang, Y.; Yan, T., Encapsulating a high content of iodine into an active graphene substrate as a cathode material for high-rate lithium–iodine batteries. *J. Mater. Chem. A* 2017, 5, 15235-15242.
155. Su, Z.; Tong, C.-J.; He, D.-Q.; Lai, C.; Liu, L.-M.; Wang, C.; Xi, K., Ultra-small B_2O_3 nanocrystals grown in situ on highly porous carbon microtubes for lithium–iodine and lithium–sulfur batteries. *J. Mater. Chem. A* 2016, 4, 8541-8547.
156. Wang, H.; Zhang, G.; Ke, L.; Liu, B.; Zhang, S.; Deng, C., Understanding the effects of 3D porous architectures on promoting lithium or sodium intercalation in iodine/C cathodes synthesized via a biochemistry-enabled strategy. *Nanoscale* 2017, 9, 9365-9375.

157. Zhao, Q.; Lu, Y.; Zhu, Z.; Tao, Z.; Chen, J., Rechargeable lithium-iodine batteries with iodine/nanoporous carbon cathode. *Nano Lett.* 2015, 15, 5982-5987.
158. Lu, K.; Hu, Z.; Ma, J.; Ma, H.; Dai, L.; Zhang, J., A rechargeable iodine-carbon battery that exploits ion intercalation and iodine redox chemistry. *Nat. Commun.* 2017, 8, 527.
159. Li, K.; Lin, B.; Li, Q.; Wang, H.; Zhang, S.; Deng, C., Anchoring iodine to N-doped hollow carbon fold-hemisphere: toward a fast and stable cathode for rechargeable lithium–iodine batteries. *ACS Appl. Mater. Interfaces* 2017, 9, 20508-20518.
160. Liu, F.-C.; Liu, W.-M.; Zhan, M.-H.; Fu, Z.-W.; Li, H., An all solid-state rechargeable lithium-iodine thin film battery using LiI(3-hydroxypropionitrile)$_2$ as an I^- ion electrolyte. *Energy Environ. Sci.* 2011, 4, 1261-1264.
161. Zhou, D.; Chen, Y.; Li, B.; Fan, H.; Cheng, F.; Shanmukaraj, D.; Rojo, T.; Armand, M.; Wang, G., A stable quasi-solid-state sodium–sulfur battery. *Angew. Chem. Int. Ed.* 2018, 57, 10168-10172.
162. Liu, M.; Zhou, D.; He, Y.-B.; Fu, Y.; Qin, X.; Miao, C.; Du, H.; Li, B.; Yang, Q.-H.; Lin, Z., Novel gel polymer electrolyte for high-performance lithium–sulfur batteries. *Nano Energy* 2016, 22, 278-289.
163. Abraham, K.; Jiang, Z.; Carroll, B., Highly conductive PEO-like polymer electrolytes. *Chem. Mater.* 1997, 9, 1978-1988.
164. Grimme, S., Semiempirical GGA-type density functional constructed with a long-range dispersion correction. *J. Comp. Chem.* 2006, 27, 1787-1799.
165. Jiang, Q.; Kurra, N.; Alhabeb, M.; Gogotsi, Y.; Alshareef, H. N., All pseudocapacitive mxene-RuO_2 asymmetric supercapacitors. *Adv. Energy Mater.* 2018, 8, 1703043.
166. Sherwood, P. M., X-ray photoelectron spectroscopic studies of some iodine compounds. *J. Chem. Soc., Faraday Trans.* 1976, 72, 1805-1820.
167. Gardner, J. M.; Abrahamsson, M.; Farnum, B. H.; Meyer, G. J., Visible light generation of iodine atoms and I−I bonds: sensitized I^- oxidation and I_3^- photodissociation. *J. Am. Chem. Soc.* 2009, 131, 16206-16214.
168. Wang, W.; Liu, W.; Zeng, Y.; Han, Y.; Yu, M.; Lu, X.; Tong, Y., A novel exfoliation strategy to significantly boost the energy storage capability of commercial carbon cloth. *Adv. Mater.* 2015, 27, 3572-3578.
169. Croce, F.; Focarete, M. L.; Hassoun, J.; Meschini, I.; Scrosati, B., A safe, high-rate and high-energy polymer lithium-ion battery based on gelled membranes prepared by electrospinning. *Energy Environ. Sci.* 2011, 4, 921-927.
170. Zhou, D.; Liu, R.; Zhang, J.; Qi, X.; He, Y.-B.; Li, B.; Yang, Q.-H.; Hu, Y.-S.; Kang, F., In situ synthesis of hierarchical poly (ionic liquid)-based solid electrolytes for high-safety lithium-ion and sodium-ion batteries. *Nano Energy* 2017, 33, 45-54.
171. Bai, P.; Li, J.; Brushett, F. R.; Bazant, M. Z., Transition of lithium growth mechanisms in liquid electrolytes. *Energy Environ. Sci.* 2016, 9, 3221-3229.
172. Zhou, D.; Liu, R.; He, Y. B.; Li, F.; Liu, M.; Li, B.; Yang, Q. H.; Cai, Q.; Kang, F., SiO_2 hollow nanosphere-based composite solid electrolyte for lithium metal batteries to suppress lithium dendrite growth and enhance cycle life. *Adv. Energy Mater.* 2016, 6, 1502214.
173. Etacheri, V.; Marom, R.; Elazari, R.; Salitra, G.; Aurbach, D., Challenges in the development of advanced Li-ion batteries: A review. *Energy Environ. Sci.* 2011, 4, 3243-3262.
174. Wang, J.; Polleux, J.; Lim, J.; Dunn, B., Pseudocapacitive contributions to electrochemical energy storage in TiO_2 (anatase) nanoparticles. *J. Phys. Chem. C* 2007, 111, 14925-14931.
175. Zhang, S. S., A new finding on the role of $LiNO_3$ in lithium-sulfur battery. *J. Power Sources* 2016, 322, 99-105.
176. Geyer, A.; Alicke, B.; Konrad, S.; Schmitz, T.; Stutz, J.; Platt, U., Chemistry and oxidation capacity of the nitrate radical in the continental boundary layer near Berlin. *J. Geophys. Res. Atmos.* 2001, 106, 8013-8025.
177. Wayne, R. P.; Barnes, I.; Biggs, P.; Burrows, J.; Canosa-Mas, C.; Hjorth, J.; Le Bras, G.; Moortgat, G.; Perner, D.; Poulet, G., The nitrate radical: Physics, chemistry, and the atmosphere. *Atmos. Environ.* 1991, 25, 1-203.

178. Tomat, R.; Rigo, A., Electrochemical oxidation of aliphatic hydrocarbons promoted by inorganic radicals. II. NO_3 radicals. *J. Appl. Electrochem.* 1986, 16, 8-14.
179. Štangar, U. L.; Orel, B.; Vuk, A. Š.; Sagon, G.; Colomban, P.; Stathatos, E.; Lianos, P., In situ resonance raman microspectroscopy of a solid-state dye-sensitized photoelectrochemical cell. *J. Electrochem. Soc.* 2002, 149, E413-E423.
180. Jung, N.; Crowther, A. C.; Kim, N.; Kim, P.; Brus, L., Raman enhancement on graphene: adsorbed and intercalated molecular species. *ACS Nano* 2010, 4, 7005-7013.
181. Shen, C.; Ge, M.; Zhang, A.; Fang, X.; Liu, Y.; Rong, J.; Zhou, C., Silicon (lithiated)–sulfur full cells with porous silicon anode shielded by Nafion against polysulfides to achieve high capacity and energy density. *Nano Energy* 2016, 19, 68-77.
182. Xu, X.; Zhou, D.; Qin, X.; Lin, K.; Kang, F.; Li, B.; Shanmukaraj, D.; Rojo, T.; Armand, M.; Wang, G., A room-temperature sodium–sulfur battery with high capacity and stable cycling performance. *Nat. Commun.* 2018, 9, 3870.
183. Hwang, J. Y.; Myung, S. T.; Sun, Y. K., Recent progress in rechargeable potassium batteries. *Adv. Func. Mater.* 2018, 28, 1802938.
184. Eftekhari, A.; Jian, Z.; Ji, X., Potassium secondary batteries. *ACS Appl. Mater. Interfaces* 2016, 9, 4404-4419.
185. Zhao, S.; Yan, K.; Munroe, P.; Sun, B.; Wang, G., Construction of hierarchical $K_{1.39}Mn_3O_6$ spheres via AlF_3 coating for high-performance potassium-ion batteries. *Adv. Energy Mater.* 2019, 9, 1803757.
186. Xue, L.; Gao, H.; Zhou, W.; Xin, S.; Park, K.; Li, Y.; Goodenough, J. B., Liquid K–Na alloy anode enables dendrite-free potassium batteries. *Adv. Mater,* 2016, 28, 9608-9612.
187. Xiao, N.; McCulloch, W. D.; Wu, Y., Reversible dendrite-free potassium plating and stripping electrochemistry for potassium secondary batteries. *J. Am. Chem. Soc.* 2017, 139, 9475-9478.
188. Cong, G.; Wang, W.; Lai, N.-C.; Liang, Z.; Lu, Y.-C., A high-rate and long-life organic–oxygen battery. *Nat. Mater.* 2019, 18, 390-396.
189. Ji, B.; Zhang, F.; Song, X.; Tang, Y., A novel potassium-ion-based dual-ion battery. *Adv. Mater.* 2017, 29, 1700519.
190. Gu, Y.; Wang, W.-W.; Li, Y.-J.; Wu, Q.-H.; Tang, S.; Yan, J.-W.; Zheng, M.-S.; Wu, D.-Y.; Fan, C.-H.; Hu, W.-Q., Designable ultra-smooth ultra-thin solid-electrolyte interphases of three alkali metal anodes. *Nat. Commun.* 2018, 9, 1339.
191. Hwang, J.-Y.; Kim, H. M.; Yoon, C. S.; Sun, Y.-K., Toward high-safety potassium–sulfur batteries using a potassium polysulfide catholyte and metal-free anode. *ACS Energy Lett.* 2018, 3, 540-541.
192. McCulloch, W. D.; Ren, X.; Yu, M.; Huang, Z.; Wu, Y., Potassium-ion oxygen battery based on a high capacity antimony anode. *ACS Appl. Mater. Interfaces* 2015, 7, 26158-26166.
193. Ding, Y.; Guo, X.; Qian, Y.; Zhang, L.; Xue, L.; Goodenough, J. B.; Yu, G., A liquid-metal-enabled versatile organic alkali-ion battery. *Adv. Mater.* 2019, 31, 1806956.
194. Xiao, N.; Gourdin, G.; Wu, Y., Simultaneous stabilization of potassium metal and superoxide in $K–O_2$ batteries on the basis of electrolyte reactivity. *Angew. Chem. Int. Ed.* 2018, 57, 10864-10867.
195. Chen, X.; Kong, Z.; Li, N.; Zhao, X.; Sun, C., Proposing the prospects of Ti_3CN transition metal carbides (MXenes) as anodes of Li-ion batteries: A DFT study. *Phys. Chem. Chem. Phys.* 2016, 18, 32937-32943.
196. Zhang, X.; Lv, R.; Wang, A.; Guo, W.; Liu, X.; Luo, J., MXene aerogel scaffolds for high-rate lithium metal anodes. *Angew. Chem. Int. Ed.* 2018, 57, 15028-15033.
197. Hantanasirisakul, K.; Alhabeb, M.; Lipatov, A.; Maleski, K.; Anasori, B.; Salles, P.; Ieosakulrat, C.; Pakawatpanurut, P.; Sinitskii, A.; May, S. J., Effects of synthesis and processing on optoelectronic properties of titanium carbonitride MXene. *Chem. Mater.* 2019, 31, 2941-2951.
198. Sang, X.; Xie, Y.; Lin, M.-W.; Alhabeb, M.; Van Aken, K. L.; Gogotsi, Y.; Kent, P. R.; Xiao, K.; Unocic, R. R., Atomic defects in monolayer titanium carbide ($Ti_3C_2T_x$) MXene. *ACS Nano* 2016, 10, 9193-9200.

199. Enyashin, A.; Ivanovskii, A., Two-dimensional titanium carbonitrides and their hydroxylated derivatives: Structural, electronic properties and stability of MXenes $Ti_3C_{2-x}N_x(OH)_2$ from DFTB calculations. *J. Solid State Chem.* 2013, 207, 42-48.
200. Anasori, B.; Lukatskaya, M. R.; Gogotsi, Y., 2D metal carbides and nitrides (MXenes) for energy storage. *Nat. Rev. Mater.* 2017, 2, 16098.
201. Sun, B.; Li, P.; Zhang, J.; Wang, D.; Munroe, P.; Wang, C.; Notten, P. H.; Wang, G., Dendrite-free sodium-metal anodes for high-energy sodium-metal batteries. *Adv. Mater.* 2018, 30, 1801334.
202. Lin, D.; Liu, Y.; Liang, Z.; Lee, H.-W.; Sun, J.; Wang, H.; Yan, K.; Xie, J.; Cui, Y., Layered reduced graphene oxide with nanoscale interlayer gaps as a stable host for lithium metal anodes. *Nat. Nanotechnol.* 2016, 11, 626.
203. Xu, Y.; Li, T.; Wang, L.; Kang, Y., Interlayered dendrite-free lithium plating for high-performance lithium-metal batteries. *Adv. Mater.* 2019, 31, 1901662.
204. Li, Y.; Zhang, L.; Liu, S.; Wang, X.; Xie, D.; Xia, X.; Gu, C.; Tu, J., Original growth mechanism for ultra-stable dendrite-free potassium metal electrode. *Nano Energy* 2019, 62, 367-375.
205. Qian, J.; Henderson, W. A.; Xu, W.; Bhattacharya, P.; Engelhard, M.; Borodin, O.; Zhang, J.-G., High rate and stable cycling of lithium metal anode. *Nat. Commun.* 2015, 6, 6362.
206. Wu, T.-H.; Zhang, Y.; Althouse, Z. D.; Liu, N., Nanoscale design of zinc anodes for high-energy aqueous rechargeable batteries. *Mater. Today Nano* 2019, 6, 100032.
207. Brissot, C.; Rosso, M.; Chazalviel, J.-N.; Lascaud, S., Dendritic growth mechanisms in lithium/polymer cells. *J. Power Sources* 1999, 81, 925-929.
208. Liu, Y.; Lin, D.; Liang, Z.; Zhao, J.; Yan, K.; Cui, Y., Lithium-coated polymeric matrix as a minimum volume-change and dendrite-free lithium metal anode. *Nat. Commun.* 2016, 7, 10992.
209. Zhou, D.; Tkacheva, A.; Tang, X.; Sun, B.; Shanmukaraj, D.; Li, P.; Zhang, F.; Armand, M.; Wang, G., Stable conversion chemistry-based lithium metal batteries enabled by hierarchical multifunctional polymer electrolytes with near-single ion conduction. *Angew. Chem. Int. Ed.* 2019, 58, 6001-6006.
210. Jayaprakash, N.; Shen, J.; Moganty, S. S.; Corona, A.; Archer, L. A., Porous hollow carbon@sulfur composites for high-power lithium–sulfur batteries. *Angew. Chem. Int. Ed.* 2011, 50, 5904-5908.
211. Hwang, T. H.; Jung, D. S.; Kim, J.-S.; Kim, B. G.; Choi, J. W., One-dimensional carbon–sulfur composite fibers for Na–S rechargeable batteries operating at room temperature. *Nano Lett.* 2013, 13, 4532-4538.
212. Liu, Y.; Wang, W.; Wang, J.; Zhang, Y.; Zhu, Y.; Chen, Y.; Fu, L.; Wu, Y., Sulfur nanocomposite as a positive electrode material for rechargeable potassium–sulfur batteries. *Chem. Commun.* 2018, 54, 2288-2291.
213. Wei, S.; Ma, L.; Hendrickson, K. E.; Tu, Z.; Archer, L. A., Metal–sulfur battery cathodes based on PAN–sulfur composites. *J. Am. Chem. Soc.* 2015, 137, 12143-12152.
214. Jian, Z.; Luo, W.; Ji, X., Carbon electrodes for K-ion batteries. *J. Am. Chem. Soc.* 2015, 137, 11566-11569.
215. Zhang, S. S., Liquid electrolyte lithium/sulfur battery: Fundamental chemistry, problems, and solutions. *J. Power Sources* 2013, 231, 153-162.
216. Ji, X.; Lee, K. T.; Nazar, L. F., A highly ordered nanostructured carbon–sulphur cathode for lithium–sulphur batteries. *Nat. Mater.* 2009, 8, 500-506.
217. Evers, S.; Nazar, L. F., New approaches for high energy density lithium–sulfur battery cathodes. *Acc. Chem. Res.* 2013, 46, 1135-1143.
218. Peng, H. J.; Huang, J. Q.; Cheng, X. B.; Zhang, Q., Review on high-loading and high-energy lithium–sulfur batteries. *Adv. Energy Mater.* 2017, 7, 1700260.
219. Demir-Cakan, R.; Morcrette, M.; Leriche, J.-B.; Tarascon, J.-M., An aqueous electrolyte rechargeable Li-ion/polysulfide battery. *J. Mater. Chem. A* 2014, 2, 9025-9029.
220. Demir-Cakan, R.; Morcrette, M.; Tarascon, J.-M., Use of ion-selective polymer membranes for an aqueous electrolyte rechargeable Li-ion-polysulphide battery. *J. Mater. Chem. A* 2015, 3, 2869-2875.

221. Wu, X.; Yuan, X.; Yu, J.; Liu, J.; Wang, F.; Fu, L.; Zhou, W.; Zhu, Y.; Zhou, Q.; Wu, Y., A high-capacity dual core–shell structured MWCNTs@S@PPy nanocomposite anode for advanced aqueous rechargeable lithium batteries. *Nanoscale* 2017, 9, 11004-11011.
222. Peramunage, D.; Licht, S., A solid sulfur cathode for aqueous batteries. *Science* 1993, 261, 1029-1032.
223. Yang, C.; Suo, L.; Borodin, O.; Wang, F.; Sun, W.; Gao, T.; Fan, X.; Hou, S.; Ma, Z.; Amine, K., Unique aqueous Li-ion/sulfur chemistry with high energy density and reversibility. *P. Natl. Acad. Sci.* 2017, 114, 6197-6202.
224. Ling, Z.; Ren, C. E.; Zhao, M.-Q.; Yang, J.; Giammarco, J. M.; Qiu, J.; Barsoum, M. W.; Gogotsi, Y., Flexible and conductive MXene films and nanocomposites with high capacitance. *P. Natl. Acad. Sci.* 2014, 111, 16676-16681.
225. Dong, Y.; Zheng, S.; Qin, J.; Zhao, X.; Shi, H.; Wang, X.; Chen, J.; Wu, Z.-S., All-MXene-based integrated electrode constructed by Ti_3C_2 nanoribbon framework host and nanosheet interlayer for high-energy-density Li–S batteries. *ACS Nano* 2018, 12, 2381-2388.
226. Guo, X.; Zhang, W.; Zhang, J.; Zhou, D.; Tang, X.; Xu, X.; Li, B.; Liu, H.; Wang, G., Boosting sodium storage in two-dimensional phosphorene/$Ti_3C_2T_x$ MXene nanoarchitectures with stable fluorinated interphase. *ACS Nano* 2020, 14, 3651-3659.
227. Peng, X.-X.; Lu, Y.-Q.; Zhou, L.-L.; Sheng, T.; Shen, S.-Y.; Liao, H.-G.; Huang, L.; Li, J.-T.; Sun, S.-G., Graphitized porous carbon materials with high sulfur loading for lithium-sulfur batteries. *Nano Energy* 2017, 32, 503-510.
228. Suo, L.; Borodin, O.; Gao, T.; Olguin, M.; Ho, J.; Fan, X.; Luo, C.; Wang, C.; Xu, K., "Water-in-Salt" electrolyte enables high voltage aqueous Li-ion chemistries. *Science* 2015, 350, 938-943.
229. Manthiram, A.; Fu, Y.; Chung, S.-H.; Zu, C.; Su, Y.-S., Rechargeable lithium–sulfur batteries. *Chem. Rev.* 2014, 114, 11751-11787.
230. Kim, D. K.; Muralidharan, P.; Lee, H.-W.; Ruffo, R.; Yang, Y.; Chan, C. K.; Peng, H.; Huggins, R. A.; Cui, Y., Spinel $LiMn_2O_4$ nanorods as lithium ion battery cathodes. *Nano Lett.* 2008, 8, 3948-3952.
231. Li, W.; McKinnon, W. R.; Dahn, J. R., Lithium intercalation from aqueous solutions. *J. Electrochem. Soc.* 1994, 141, 2310-2316.
232. Schlörb, H.; Bungs, M.; Plieth, W., Synthesis and electrochemical studies of manganese oxides with spinel structure in aqueous electrolyte (9 M KOH). *Electrochim. Acta* 1997, 42, 2619-2625.
233. Bao, W.; Shuck, C. E.; Zhang, W.; Guo, X.; Gogotsi, Y.; Wang, G., Boosting performance of Na–S batteries using sulfur-doped $Ti_3C_2T_x$ MXene nanosheets with a strong affinity to sodium polysulfides. *ACS Nano* 2019, 13 (10), 11500-11509.
234. Yun, S.; Park, S. H.; Yeon, J. S.; Park, J.; Jana, M.; Suk, J.; Park, H. S., Materials and device constructions for aqueous lithium–sulfur batteries. *Adv. Func. Mater.* 2018, 28, 1707593.
235. Shao, J.; Li, X.; Zhang, L.; Qu, Q.; Zheng, H., Core–shell sulfur@polypyrrole composites as high-capacity materials for aqueous rechargeable batteries. *Nanoscale* 2013, 5, 1460-1464.